Plasma Physics Reports, Vol. 27, No. 4, 2001, pp. 273–277. From Fizika Plazmy, Vol. 27, No. 4, 2001, pp. 291–295.

Formation of Electron Transport Barriers under ECR Control of the *q*(*r*) Profile in the T-10 Tokamak

K. A. Razumova*, V. V. Alikaev*, I. S. Bondarenko, A. A. Borschegovskiĭ*, V. A. Vershkov*,
A. V. Gorshkov*, Yu. V. Gott*, Yu. N. Dnestrovskij*, V. V. Dreval*, M. M. Dremin*,
L. G. Eliseev*, G. S. Kirnev*, A. Ya. Kislov*, I. V. Klimanov*, A. S. Kozachok**,
A. D. Komarov**, V. A. Krupin*, L. I. Krupnik**, S. V. Krylov*, S. E. Lysenko*,
A. A. Medvedev*, A. V. Melnikov*, T. B. Myalton*, G. E. Notkin*, A. Yu. Novikov*,
Yu. D. Pavlov*, D. P. Petrov*, V. I. Poznyak*, I. N. Roy*, P. V. Savrukhin*,
V. V. Sannikov*, S. V. Soldatov*, A. V. Sushkov*, V. M. Trukhin*,
S. M. Khrebtov**, V. V. Chistyakov*, and D. A. Shelukhin***

**Russian Research Centre Kurchatov Institute, pl. Kurchatova 1, Moscow, 123182 Russia*
e-mail: razumova@nfi.kiae.ru
***Ukrainian Scientific Center Kharkov Institute of Physics and Technology, Kharkov, 61108 Ukraine*

Received September 7, 2000; in final form, October 17, 2000

Abstract—The formation of transport barriers under electron cyclotron resonance heating and current drive in the T-10 tokamak is studied. In regimes with off-axis co-ECCD and $q_L < 4$ at the limiter, a spontaneous transition to improved confinement accompanied by the formation of two electron transport barriers is observed. The improvement resembles an L–H transition. It manifests itself as density growth, a decrease in the D_α emission intensity, and an increase in the central electron and ion temperatures. Two deep wells on the potential profile (the first one at $r/a_L \approx 0.6$, where a_L is the limiter radius, and the second one near the edge) arise during the transition. The internal barrier is formed when $dq/dr \sim 0$ with $q \approx 1$ in the barrier region. *© 2001 MAIK "Nauka/Interperiodica".*

Previous T-10 experiments [1] showed that an electron internal transport barrier (EITB) can arise when a $q(r)$ profile with $dq/dr \sim 0$ is formed near a rational surface. Such a profile was created by using the electron cyclotron current drive (ECCD) in the co- or counter-direction with respect to the main plasma current (co-CD or counter-CD, respectively). The electron-cyclotron (EC) current was generated with the help of a gyrotron setup operating at a frequency of $f = 140$ GHz. X-mode microwave radiation was launched at an angle of 21° with respect to the major radius of the torus and was absorbed at the second harmonic of the EC frequency. The total absorbed power P_{EC} was as high as 0.7–0.8 MW. The resonance region could be shifted along the major radius by varying the toroidal magnetic field B_t. In order to make the EC current comparable with the plasma current I_p, the experiments were conducted at moderate plasma currents ($I_p \leq 160$ kA) and, consequently, at high q_L values at the limiter. In these regimes, an EITB was formed at $\rho \equiv r/a_L \leq 0.3$. The improvement of confinement was either steady-state or periodical. In the regimes with an EITB at $q_L > 4$, we observed an increase in the electron temperature in the plasma core (on the inside of the barrier); however, there was no evidence of improved confinement at the plasma edge.

However, for $q_L < 4$, the EITB formation in the plasma core was accompanied by improved confinement at the plasma edge, independently of the EITB position. Figure 1 shows that, even during small periodical improvements of confinement (humpbacks), the increase in the central electron temperature $T_e(0)$ is accompanied by effects typical of an L–H transition at the edge: the density near the limiter increases, the D_α line emission intensity decreases, and β_p increases in phase with increasing $T_e(0)$.

Recent experiments in T-10 were performed at high currents I_p ($q_L = 2.2$–3) and with the EC resonance position r_{EC} shifted inward. An EITB formed with co-ECCD was quasi-steady. The regime in which the barrier was formed at $\rho = 0.6$ ($I_p = 280$ kA, $B_t = 2.14$ T, $n_e = 1.4 \times 10^{19}$ m^{-3}, $P_{EC} = 0.8$ MW, $r_{EC} = -(16$–$17)$ cm, and $a_L = 30$ cm) was studied in more detail. Such a regime could be realized at lower toroidal fields; this allowed us to measure the plasma potential profile evolution in different parts of the plasma column during the barrier formation using heavy ion beam probing (HIBP) [2]. We also used a multichannel soft X-ray (SXR) camera and ECE and Thomson scattering diagnostics to measure the electron temperature T_e. The values of $\beta_p + l_i/2$ and β_p were determined from diamagnetic and loop

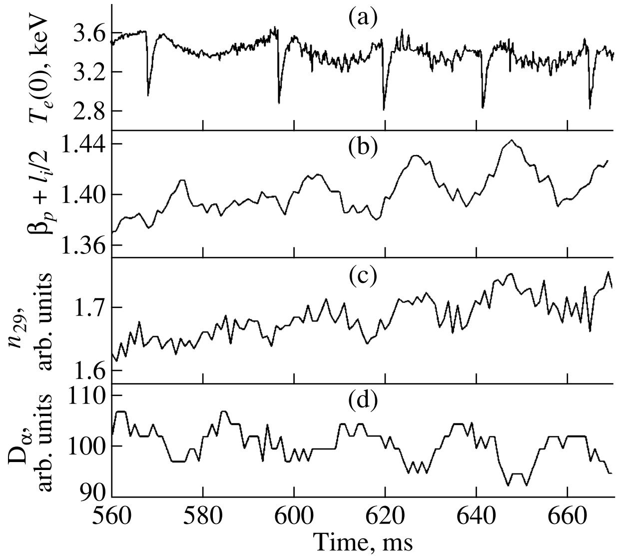

Fig. 1. Periodical increases in (a) the central electron temperature, (b) the $\beta_p + l_i/2$ value, and (c) line-averaged density at the outer chord $r = 29$ cm during humpbacks, accompanied by (d) drops in the D_α line emission intensity (shot no. 20194, $B_t = 2.44$ T, $I_p = 180$ kA, and $\bar{n}_e = 1.7 \times 10^{19}$ m^{-3}; on-axis counter-CD).

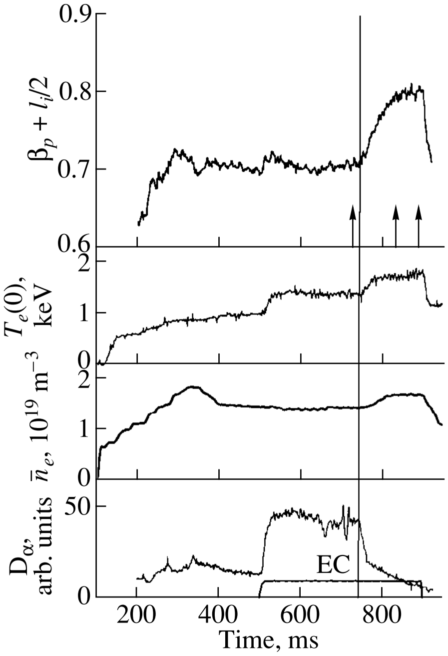

Fig. 2. Time evolution of the plasma parameters in the regime with simultaneous formation of an internal barrier at $r = 17$ cm and L–H transition (shot no. 24273, $B_t = 2.14$ T, and $I_p = 280$ kA; off-axis co-CD).

measurements, n_e was measured using radiointerferometry, the ion temperature $T_i(0)$ was measured using a charge exchange analyzer, and the D_α emission was recorded using a monochromator.

The waveforms of the plasma parameters in this regime are shown in Fig. 2. After the EC pulse starts, a spontaneous transition to improved confinement occurs with some delay. We see that the increase in T_e, n_e, and β_p is accompanied by a decrease in the D_α emission intensity. The simultaneous growth of T_e and n_e is caused by the formation of two transport barriers. The formation of an IETB at $\rho = 0.6$ results in the steep temperature gradient ∇T_e in the narrow barrier region (Fig. 3a), while the density gradient in this region is small, $\nabla n_e \sim 0$. Another barrier with the steep density gradient ∇n_e is formed at the edge, in the immediate vicinity of the limiter (Fig. 4).

The spatiotemporal characteristics of the plasma electric potential are shown in Figs. 3b and 4b. The potential is measured with respect to its level before the transition. We see that, during the EITB formation, the potential rapidly decreases ($\Delta\phi \simeq 1$–1.2 kV) in the narrow ($\Delta r = 1$ cm) region near $\rho = 0.6$, which coincides with the region with an increased ∇T_e. The local potential well is conserved for the entire EITB formation phase. As the plasma parameters approach their steady-state values, the well becomes shallower; however, the slope of the potential profile in the EITB region is still positive.

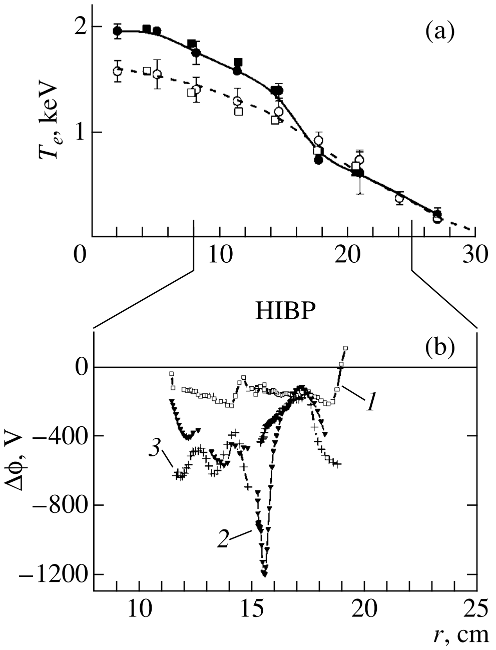

Fig. 3. (a) The electron temperature profile measured by Thomson scattering (circles) and second-harmonic ECE (squares) and (b) the relative plasma potential profile in two similar shots with EITBs (*1*) before, (*2*) during, and (*3*) after the barrier formation. The instants of the potential measurements are shown by arrows in Fig. 2 (shot nos. 24264–24273, $B_t = 2.14$ T, $I_p = 280$ kA, and $E_{HIBP} = 170$ keV).

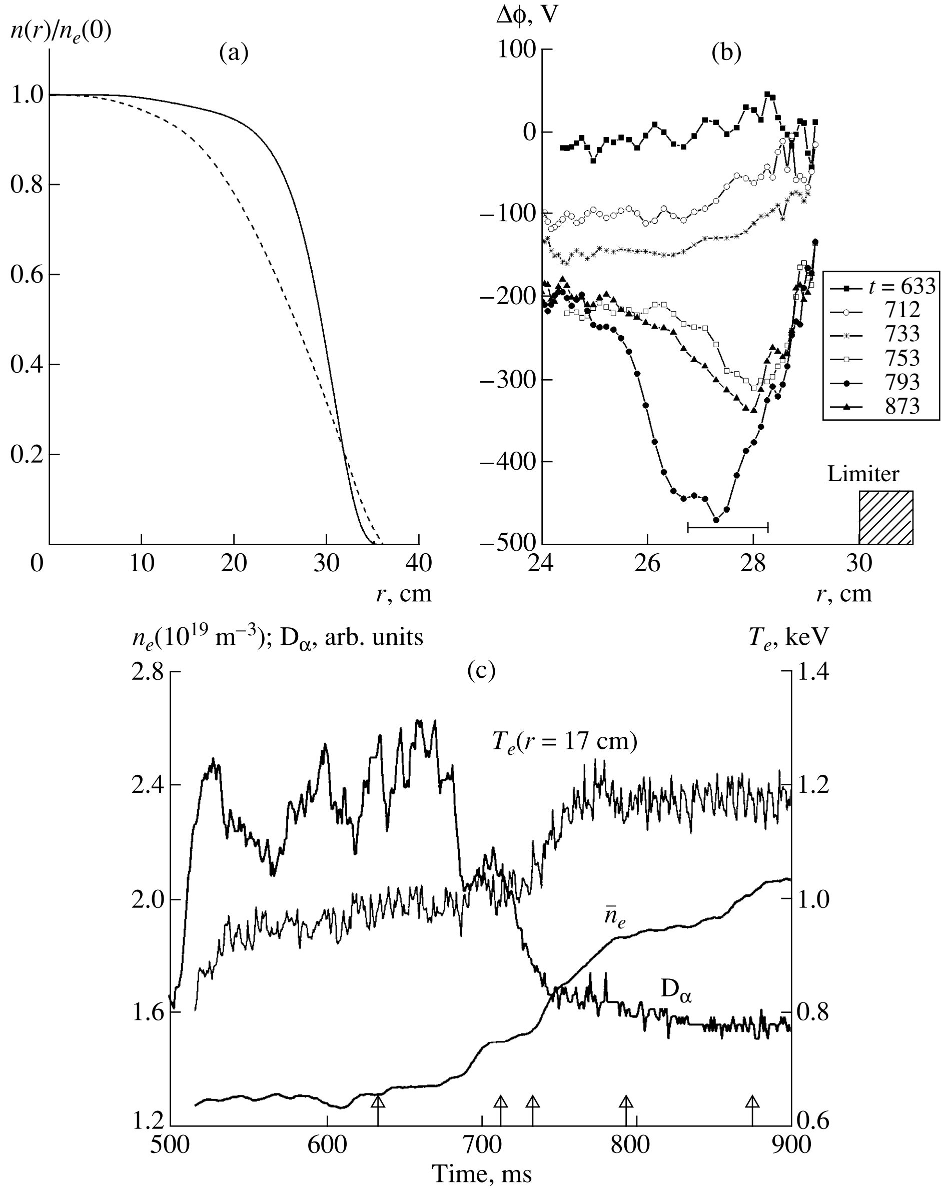

Fig. 4. Profiles of (a) the electron density at t = 630 ms (dashed line) and t = 800 ms (solid line) and (b) relative plasma potential and (c) the time evolution of the plasma parameters in shot no. 26176, where an edge potential well was measured. Arrows in plot (c) show the instants of the potential measurements. A horizontal bar in plot (b) shows the radial uncertainty of the potential profile measurements.

The EITB formation in these regimes is always accompanied by the formation of an external barrier. The edge well is not so deep, but its temporal evolution is similar to that of the internal well. The steep n_e gradient and the decrease in the D_α emission intensity resemble those accompanying the L–H transition.

Since the density was rather low, the energy exchange between the ions and electrons was weak. However, the central ion temperature increased during the barrier formation (Fig. 5). Estimates show that the ion confinement time in the core increased by a factor of 1.5.

The improvement of confinement due to the barrier formation is accompanied by a flattening of the $q(r)$ profile. Figure 6 shows the $q(r)$ profiles for the same shot as in Fig. 2. The profiles are calculated using the experimental $T_e(r)$ and $n_e(r)$ profiles before and after the transition. As in [1], the $q(r)$ profile is flattened near the EITB; in our case, the barrier lies in the region where $q(r) \approx 1$. Note that no negative shear is required for the barrier formation.

An internal barrier could also be obtained at $q_L \leq 4$ and under on-axis EC power deposition [3]; however, in this case, the central electron temperature increased

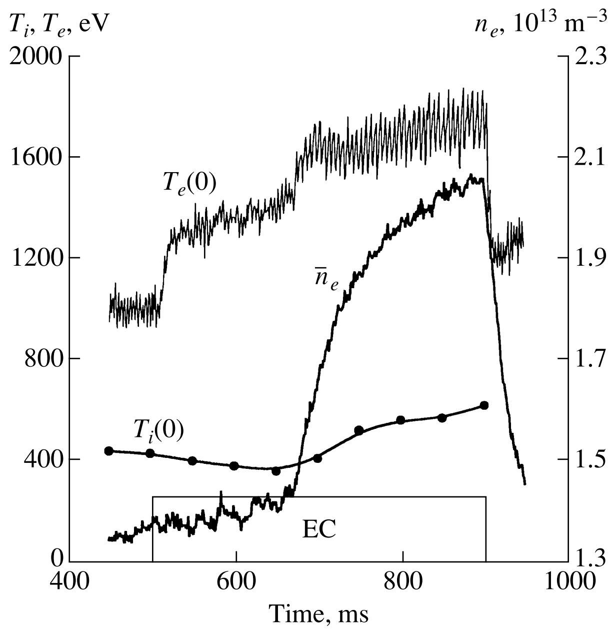

Fig. 5. Temporal evolution of the central electron and ion temperatures and the line-averaged density during the EITB formation at t = 660 ms (shot no. 26353, B_t = 2.10 T, and I_p = 270 kA).

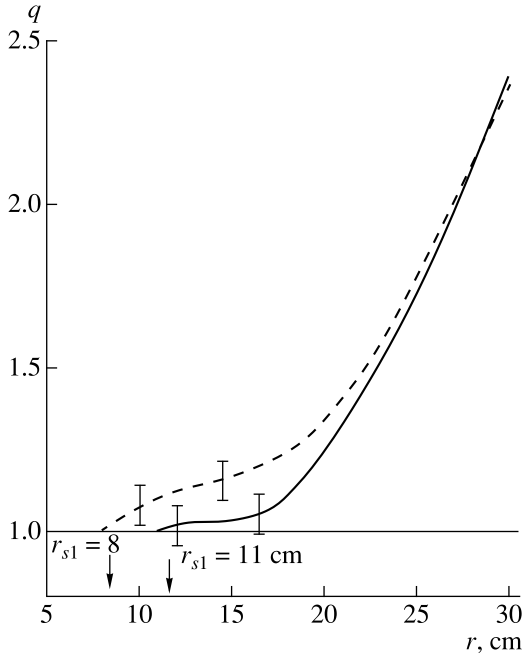

Fig. 6. Calculated $q(r)$ profile before (dashed curve) and after (solid curve) the EITB formation for the plasma parameters from Figs. 2–5 (shot no. 24264). Vertical bars show an uncertainty in determining q related to the T_e measurement errors. Arrows show the radii of sawtooth inversion before and after the barrier formation.

only slightly. Possibly, very strong heat losses during sawtooth oscillations impede the increase in ∇T_e near $q(r) = 1$ (although there is some indirect evidence of the formation of a small barrier in this region).

Apparently, sawtooth oscillations under power deposition at $\rho = 0.6$ also restricted the increase in the central electron temperature; nevertheless, a large temperature gradient was formed.

In T-10 experiments, only ECR heating was used; in this case, no angular momentum was introduced to the plasma and all the power was deposited into the electron component. The change in the ion temperature is the secondary effect as compared to electron processes. Therefore, we may state that we observed *electron* transport barriers.

We propose the following explanation of the phenomena observed.

Usually, the interaction between magnetic islands increases the heat fluxes and leads to the dependence of the transport coefficients on the global plasma parameters (the profile self-consistency [4]).

The zero shear $S \equiv r/q\, dq/dr \approx 0$ for q values close to a certain resonant value under electron heating may stabilize some MHD perturbations related to the electron transport. The transport reduces, but remains much greater than the neoclassical one.

The electron flux reduces, while the ion flux remains unchanged. This leads to the appearance of a potential well in the region where the electron transport is reduced; as a result, the fluxes equalize.

The arising electric field (~1 kV/cm) drives the poloidal $\mathbf{E} \times \mathbf{B}$ plasma drift. The drift velocity varies sharply along the radius and may even change its direction (the sheared $\mathbf{E} \times \mathbf{B}$ flow). This may stabilize the ion temperature gradient mode [5] (and, probably, some other modes) and, hence, improve ion confinement.

The simultaneous formation of two barriers apparently indicates that the plasma edge and core are strongly coupled (probably, via toroidal coupling).

CONCLUSIONS

(i) For first time, the plasma potential profile is measured in a wide radial region.

(ii) At low q_L values at the plasma edge, two potential wells appear simultaneously.

(iii) The internal potential well is apparently related to the formation of an internal transport barrier because, in this region, improved electron confinement is observed.

(iv) The external barrier exhibits the features of an L–H transition.

ACKNOWLEDGMENTS

This work was supported in part by the Russian Foundation for Basic Research (project nos. 98-02-

16277, 99-02-18457, and 00-15-96536) and the Ministry of Science and Technology of the Russian Federation (grant no. 363).

REFERENCES

1. K. A. Razumova, V. V. Alikaev, A. A. Borschegovskii, *et al.*, Plasma Phys. Controlled Fusion **42**, 973 (2000).
2. A. V. Melnikov, L. G. Eliseev, L. I. Krupnik, and S. M. Khrebtov, in *Proceedings of the 26th European Conference on Controlled Fusion and Plasma Physics, Maastricht, 1999* [ECA, **23J**, 829 (1999)].
3. V. V. Alikaev, A. A. Borshchegovskiĭ, V. A. Vershkov, *et al.*, Fiz. Plazmy **26**, 979 (2000) [Plasma Phys. Rep. **26**, 917 (2000)].
4. B. B. Kadomtsev, Fiz. Plazmy **13**, 771 (1987) [Sov. J. Plasma Phys. **13**, 443 (1987)].
5. V. S. Chan and DIII-D Team, in *Proceedings of the 16th International Conference on Fusion Energy, Montreal, 1996* (IAEA, Vienna, 1997), Vol. 1, p. 95.

Translated by the authors

Plasma Physics Reports, Vol. 27, No. 4, 2001, pp. 278–292. Translated from Fizika Plazmy, Vol. 27, No. 4, 2001, pp. 296–310.
Original Russian Text Copyright © 2001 by Andreev, Veĭsman, Goreslavskiĭ, Chegotov.

PLASMA KINETICS

Residual Electron Momentum and Energy in a Gas Ionized by a Short High-Power Laser Pulse

N. E. Andreev*, M. E. Veĭsman*, S. P. Goreslavskiĭ, and M. V. Chegotov***

**Institute for High Energy Densities, Associated Institute for High Temperatures, Russian Academy of Sciences, Izhorskaya ul. 13/19, Moscow, 127412 Russia*

***Moscow Engineering Physics Institute (Technical University), Kashirskoe sh. 31, Moscow, 115409 Russia*

Received June 1, 2000; in final form, September 19, 2000

Abstract—A study is made of the nonadiabatic dynamics of photoelectrons produced during interaction of an elliptically polarized, high-power laser pulse with a gas. Expressions for the so-called residual momentum and energy of the electrons (i.e., the mean electron momentum and energy after the passage of the pulse through the gas) are derived. The residual electron momentum and energy are investigated analytically as functions of the gas and laser parameters. A relationship is established between the residual energy and the electron temperature tensor. *© 2001 MAIK “Nauka/Interperiodica”.*

1. INTRODUCTION

In recent years, the problem of residual electron energy (REE) (i.e., the problem of what fraction of the energy acquired by an electron at the top of a laser pulse remains in an electron after the passage of a laser pulse) has been extensively discussed in the literature [1, 2]. For a laser pulse propagating through a preionized gas, the REE is negligible. However, for a pulse propagating in a gas and ionizing it, this energy may become substantial because of the nonadiabatic motion of an electron produced during a short-term ionization event in a laser field. As a femtosecond laser pulse propagates in a low-density plasma, the electron heating due to inverse-bremsstrahlung absorption is insignificant; consequently, after the passage of the pulse, the electron energy is mainly determined by the REE.

The study of REE is particularly important for developing X-ray lasers in which a multiply ionized plasma that is strongly nonequilibrium with respect to ionization and recombination serves as an active medium [2]. In such lasers, the degree to which the plasma is nonequilibrium with respect to these processes should be as high as possible; i.e., it is necessary to produce plasmas with the maximum possible ion charge number and minimum possible REE. This problem can be resolved by ionizing a gas with a short (about one hundred femtoseconds) intense ($I_0 > 10^{15}$ W cm^{-2}) laser pulse.

Here, we apply the so-called “two-stage” ionization model. According to this model, the transition of an electron from the bound state to the state of free motion is described in terms of quantum mechanics (by the theory of tunneling ionization) and its subsequent motion in the laser field is described by the classical equations [3, 4]. However, in contrast to [1–3], we assume that free electrons are produced with a nonzero initial momentum $\mathbf{p}_*$ with the probability determined by the corresponding quantum-mechanical distribution (cf. [4]). The momentum and energy of an electron produced in such a manner are governed by its interaction with the laser field and can be deduced from the classical relativistic equations of motion. Then, we can average the resulting electron momentum and energy over the electron ensemble. The relationships between the residual electron momentum (REM), REE, and electron temperature can be derived by comparing the results obtained by one-particle and hydrodynamic approaches.

In the particular case of a linearly polarized laser pulse and under the assumption that the electrons are born with a zero initial momentum, formulas (12) and (13) for the longitudinal momentum and mean energy of an electron (see below) yield formula (13) from [2]. Our purpose here is to generalize the theory of REE developed by Pulsifer *et al.* [2] so as to take into account the distribution of the produced free electrons over their initial momenta and to consider relativistic laser pulses with an arbitrary elliptic polarization. We show that the ensemble-averaged energy and momentum of a free electron in a laser field consist of two parts: first, strongly oscillating components Q_{van} and $\mathbf{P}_{\mathrm{van}}$, which vanish after the pulse leaves the plasma, and, second, weakly oscillating components Q_{fin} and $\mathbf{P}_{\mathrm{fin}}$, which are just the REE and REM after the passage of the pulse. The formulas derived here for Q_{fin} and $\mathbf{P}_{\mathrm{fin}}$ make it possible to clarify the dependence of the REE and REM on the main gas and laser parameters: the ionization potentials, the laser intensity, the degree of elliptic polarization of the laser field, the laser wavelength, and the pulse shape. We show that, when the ionization front duration is as long as several laser field periods, the REE Q_{fin} is substantially higher than the energy $P_{\text{fin}}^2/(2m)$; consequently, Q_{fin} can be regarded as the energy of *disordered* electron motion. We find that the REE is expressed in terms of the sum of the transverse (with respect to the x-axis along which the pulse propagates) pressure tensor elements Π_{yy} and Π_{zz}: $Q_{\text{fin}} = (\Pi_{yy} + \Pi_{zz})/(2n_e) \equiv (T_{yy} + T_{zz})/2$, where n_e is the electron density and T_{yy} and T_{zz} are the electron temperature tensor elements.[1]

2. IONIZATION MODEL

We treat the problem in a one-dimensional approximation; i.e., we consider the electron motion in the vicinity of the laser-pulse axis, assuming that the pulse is wide enough to neglect both transverse electron drift[2] and laser-light diffraction. We also consider a gas with a sufficiently low density such that the nonlinear processes distorting the pulse shape [8–10] occur on time scales much longer than the pulse duration. In this case, the laser field strength along the propagation direction of the pulse depends on the x coordinate only through the combination $x/c–t$, so that the shape of the propagating pulse can be assumed to be unchanged. Consequently, for convenience, we can consider the electron motion near the point $x = 0$, keeping in mind that the results obtained will also pertain to the remaining electrons, because they move in the same field that is only shifted in phase with respect to the point $x = 0$.

At $x = 0$, the rapidly oscillating component $\tilde{\mathbf{E}}(t)$ of the electric field of the laser pulse can be represented as

$$\tilde{\mathbf{E}}(t) = E(t)[\mathbf{e}_y\cos(\omega_0 t) + \eta\mathbf{e}_z\sin(\omega_0 t)],$$
$$E(t) = E_0\exp[-(t/\sigma_t)^2], \qquad (1)$$
$$E_0 = \sqrt{(8\pi/c)I_0/(1+\eta^2)}, \quad \sigma_t = \tau_{FWHM}/\sqrt{2\ln 2},$$

where $\mathbf{e}_y$ and $\mathbf{e}_z$ are unit vectors in the y and z directions, $\eta \in [-1, 1]$ is the degree of elliptic polarization ($\eta = 0$ and $|\eta| = 1$ correspond to linear and circular polarizations, respectively), $E(t)$ is the laser field amplitude, E_0 is the maximum laser field amplitude, I_0 is the peak intensity of the pulse, and τ_{FWHM} is the full width at half-maximum (FWHM) of the pulse.

For the above laser pulse parameters, the gas is ionized on a time scale much shorter than the pulse duration. The ionization can be assumed to proceed via the tunneling mechanism when the Keldysh parameter [11] is much smaller than unity, $\gamma = \omega_0\sqrt{2mJ_k}/eE(t^*) \ll 1$,[3] where m and e are the mass of an electron and the absolute value of its charge, ω_0 is the laser frequency, $E(t^*)$ is the electric field amplitude of the laser wave at the time t^* of an ionization event, and J_k is the ionization potential of an ion in the $(k – 1)$th ionization state. For the short ($\tau_{FWHM} < 1$ ps) laser pulses under consideration, the electron–ion collision time in a low-density ($n_e < 10^{19}$ cm^{-3}) gas is longer than the pulse duration; consequently, the processes of recombination and impact ionization do not come into play throughout the pulse.

Under the conditions of tunneling ionization, we can assume that the electron shells are ionized successively (starting from the shell farthest from the nucleus). In this case, the number N of electrons originating by the time t per unit volume in the vicinity of the point x under consideration is determined by the equations

$$\frac{\partial N}{\partial t} = S = \sum_{k=1}^{z_n} kS_k = \sum_{k=1}^{z_n} W_k n_{k-1},$$
$$\frac{\partial n_k}{\partial t} = S_k, \quad S_k = -W_{k+1}n_k + W_k n_{k-1}, \qquad (2)$$
$$k = 1, \ldots, z_n - 1, \quad S_{z_n} = W_{z_n} n_{z_n - 1},$$
$$n_0 = n_{at} - \sum_{k=1}^{z_n} n_k,$$

where n_k is the density of the ions in the kth ionization state ($k = 0$ corresponds to a neutral atom), which are heavy enough to be regarded as immobile; W_{k+1} is the ionization rate of these ions; $n_{at} = \sum_{k=0}^{z_n} n_k$ is the total ion density (including neutrals); and z_n is the nuclear charge.

Under our conditions, the rate at which an electron produced via tunneling ionization of an ion collides with the potential barrier formed by both the electric field of this ion and the laser field is much higher than the laser frequency. Therefore, we can search for the tunneling ionization rate in the adiabatic approximation [13], i.e., by substituting the absolute value of the instantaneous laser field, $|\tilde{\mathbf{E}}(t)| = E(t)\sqrt{\cos^2(\omega_0 t) + \eta^2\sin^2(\omega_0 t)}$, into the formula for the ionization rate in a constant electric field, which is equal to the tunneling ionization rate in a circularly polarized field. For arbitrary atoms, the latter rate is described by the Ammosov–Delone–Kraĭnov (ADK) formula [14]. Consequently, in the adiabatic

---

[1] In [5, 6], it was shown that, in this case, free electrons moving in the y and z directions obey Maxwellian velocity distributions with temperatures T_{yy} and T_{zz}.

[2] Simple estimates made in [7] show that the transverse electron drift can be ignored under the condition $\sigma_r/\lambda_0 > 80(\sigma_t/1\text{ ps})\sqrt{I_0/10^{17}\text{ W cm}^{-2}}$, where λ_0 is the laser wavelength and σ_r and σ_t are the characteristic width and duration of the pulse, respectively.

[3] More precise conditions for tunneling ionization are determined by Ilkov *et al.* [12], who showed that the tunneling mechanism is dominant when $\gamma \le 0.5$.

approximation, the total ionization rate in the field of an arbitrarily polarized laser pulse has the form

$$W_k(t) = \omega_a \frac{e^1 k^2}{2\pi n_*^4}\left(\frac{4e^1 k^3 E_a}{n_*^4|\tilde{\mathbf{E}}(t)|}\right)^{2n_*-1} \times \exp\left\{-\frac{2}{3}\left(\frac{k}{n_*}\right)^3 \frac{E_a}{|\tilde{\mathbf{E}}(t)|}\right\}, \qquad (3)$$

where $n_* = k\sqrt{J_H/J_k}$ is the principal quantum number of an ion in the $(k-1)$th ionization state with the ionization potential J_k, J_H is the ionization potential of a hydrogen atom, $\omega_a \approx 4.1 \times 10^{16}$ s^{-1} is the atomic frequency, $E_a \approx 5.1 \times 10^9$ V cm^{-1} is the atomic electric field, and $e^1 = \exp(1)$. In deriving formula (3), we assumed that the orbital and magnetic quantum numbers are both zero; this assumption is justified, e.g., in [15].

In order to take into account the distribution of the produced electrons over the initial momenta, we need to know not only the total ionization rate W_k but also the differential ionization cross section $\Gamma_k(\mathbf{p}_*)$, i.e., the probability $W_k(t) = \int \Gamma_k(t, \mathbf{p}_*) d^3\mathbf{p}_*$ for an electron with the initial momentum $\mathbf{p}_*$ to originate in a unit momentum interval per unit time. To determine $\Gamma_k(\mathbf{p}_*)$, we turn to the results obtained by Goreslavsky and Popruzhenko [4], who proposed a formula for the distribution of the ionization-produced electrons over their initial velocities. Strictly speaking, this formula applies to a zero-range atomic potential (i.e., to a potential in the form of a δ function). However, the results obtained by Delone and Kraĭnov [15], who derived the Coulomb correction to the ionization probability with allowance for the long-term nature of the atomic potential, show that the coefficient in front of the exponential function in the expression for the differential ionization cross section is independent of the initial momentum of an ionization-produced electron. In view of this fact and taking into account that the distribution derived in [4] correctly reflects the exponential dependence of the differential ionization cross section on the initial electron velocity, we can extend this distribution to the case of a complex atom. In this way, we choose the coefficient in front of the exponential function so as to describe the total ionization rate by the ADK formula (3). As a result, we obtain

$$\Gamma_k(\mathbf{p}_*, t)d^3\mathbf{p} = \frac{1}{\pi}\frac{E_a}{|\tilde{\mathbf{E}}(t)|}\sqrt{\frac{J_k}{J_H}}\,W_k(|\tilde{\mathbf{E}}(t)|) \times \exp\left[-\frac{p_{*\perp}^2}{2mJ_H}\frac{E_a}{|\tilde{\mathbf{E}}(t)|}\sqrt{\frac{J_k}{J_H}}\right]\delta(p_{*\tilde{\mathbf{E}}})\,dp_{*\tilde{\mathbf{E}}}\,\frac{d^2p_{*\perp}}{2mJ_H}, \qquad (4)$$

where $W_k(|\tilde{\mathbf{E}}(t)|)$ is defined by formula (3) and the δ function reflects the fact that the electron momentum $p_{*\tilde{\mathbf{E}}}$ in the instantaneous direction of the laser field at the time of an ionization event is equal to zero [4]. In the plane perpendicular to this direction, the electrons obey a two-dimensional isotropic distribution over the initial momenta $p_{*\perp}$.

It should be noted that formulas (3) and (4) are valid under the condition $\alpha_k \equiv (J_H/J_k)^{3/2}E/E_a \ll 1$, which may fail to hold for strong laser fields. In sufficiently strong fields, the ionization can exhibit the phenomenon of *stabilization.* In other words, for $\alpha_k > 1$, the stronger the laser field, the lower both the ionization probability per unit time and the total ionization probability are (see, e.g., [15–19]). In [16–19], the stabilization of ionization was calculated for laser pulses with sharp fronts (the rise time of the front being ten atomic times $\tau_a = 1/\omega_a$ or shorter). On the other hand, Kulander *et al.* [18] noted that, for pulses with smoother fronts, the stabilization effect is less pronounced because the rapid ionization of atoms occurs at the pulse front, where $\alpha_k \ll 1$. Our simulations for light gases that are completely ionized by laser pulses with nonrelativistic intensities (except, possibly, for the 1S electron shell) showed that a pulse with a duration longer than ten laser field periods will completely ionize ions in the $(k-1)$th ionization state by the time at which $\alpha_k \gtrsim 10^{-1}$; by this time, the relative concentration of these ions, n_{k-1}/n_{at}, will become lower than 10^{-2} [20]. Consequently, for stronger laser fields, the uncertainty in determining the probability W_k will affect the final results only slightly. Thus, we can conclude that, in our analysis of pulses with rise times longer than several laser field periods, the stabilization effect is insignificant.

Another restriction on formulas (3) and (4) is that they are written in the nonrelativistic limit and are inapplicable to ions with high ionization potentials (i.e., ions that are ionized by relativistic laser fields) [15]. Consequently, in applying our model to relativistic laser pulses, we must assume that the gas atoms are light enough for the plasma to be produced at the *pulse front*; in other words, we must work under the condition $eE(t_{z_{\max}})/(m\omega_0) \ll c$, where $t_{z_{\max}}$ is the time at which the ions with the charge number $z_{\max} - 1$ are ionized at the highest rate and $z_{\max}$ is the maximum charge of the ions that can be produced during the ionization of a given gas by a given laser pulse. Of course, this restriction does not refer to nonrelativistic pulses. Under the condition $eE(t_{z_{\max}})/(m\omega_0) \ll c$, we can also assume that $|\mathbf{p}_*/(mc)| \ll 1$.

3. ENERGY AND MOMENTUM OF THE IONIZATION-PRODUCED ELECTRONS

The ensemble-averaged momentum **P**(t) and energy $Q(t)$ transferred from the laser field to the electrons that originate by the time t in the vicinity of the point x under consideration, both divided by the number of these electrons, are equal to

$$\mathbf{P}(t) = N^{-1}(t)\int\limits_{-\infty}^{t}\int \mathbf{P}(t, t^*, \mathbf{p}_*)\Gamma(t^*, \mathbf{p}_*)d^3\mathbf{p}_*dt^*,$$
$$Q(t) = N^{-1}(t)\int\limits_{-\infty}^{t}\int Q(t, t^*, \mathbf{p}_*)\Gamma(t^*, \mathbf{p}_*)d^3\mathbf{p}_*dt^*. \tag{5}$$

Here, $\mathbf{P}(t, t^*, \mathbf{p}_*)$ and $Q(t, t^*, \mathbf{p}_*)$ are the instantaneous (at the time t) momentum and energy of an electron that originates with the momentum $\mathbf{p}_*$ at the time t^* and $\Gamma(t, \mathbf{p}_*) = \sum_{k=1}^{z_n}\Gamma_k(t, \mathbf{p}_*)n_{k-1}(t)$ where Γ_k and n_{k-1} are determined by formulas (2)–(4).

Assuming that the laser field envelope changes insignificantly over the laser field period[4] and applying the approach described in [21] (see also [22]), we can write the instantaneous (at the time t) momentum and energy of an electron in the field of a plane, elliptically polarized laser wave (the wave parameters are assumed to depend on the variables x and t only through the combination $x - ct$) in terms of the longitudinal (along the x-axis) displacement $\delta(t, t^*)$ of the electron from the point x at which it is born at the time t^*. Note that, by definition, we have $\delta(t^*, t^*) = 0$.

The kinetic energy $Q(t, t^*, \mathbf{p}_*)$ of an electron originating with the momentum $\mathbf{p}_*$ at the time t^* is related to the projection of its momentum onto the propagation direction of the pulse (the x-axis) by

$$Q(t, t^*, \mathbf{p}_*) = cP_x(t, t^*, \mathbf{p}_*) + mc^2(\kappa_* - 1), \tag{6}$$

where $\kappa_* = \gamma_* - p_{x*}/(mc)$, $\gamma_* = \sqrt{1 + (\mathbf{p}_*/mc)^2}$, and $\mathbf{p}_*^2 = p_{x*}^2 + p_{y*}^2 + p_{z*}^2$.

Now, the momentum of an electron can be written as

$$\mathbf{P}(t, t^*, \mathbf{p}_*) = \mathbf{P}_{\text{van}}(t, t^*, \mathbf{p}_*) + \mathbf{P}_{\text{fin}}(t^*, \mathbf{p}_*),$$

where the components $\mathbf{P}_{\text{van}}$ and $\mathbf{P}_{\text{fin}}$ have the form

$$P_{y_{\text{fin}}} = p_{y*}(\kappa_*/\gamma_*)^2 + 2\kappa_*\sqrt{mQ_p(\phi^*)}\sin(\phi^*),$$
$$P_{y_{\text{van}}} = -2\kappa_*\sqrt{mQ_p(\phi)}\sin(\phi), \tag{7}$$

$$P_{z_{\text{fin}}} = p_{z*}(\kappa_*/\gamma_*)^2 - 2\eta\kappa_*\sqrt{mQ_p(\phi^*)}\cos(\phi^*),$$
$$P_{z_{\text{van}}} = 2\eta\kappa_*\sqrt{mQ_p(\phi)}\cos(\phi), \tag{8}$$

$$P_{x_{\text{fin}}} = 2\frac{\kappa_*}{c}Q_p(\phi^*)[\sin^2(\phi^*) + \eta^2\cos^2(\phi^*)]$$
$$+\frac{1}{2}\left[\frac{\kappa_*^3}{\gamma_*^4}\left(\frac{p_{y*}^2}{mc} + \frac{p_{z*}^2}{mc}\right) + \frac{mc}{\kappa_*} - mc\kappa_*\right]$$
$$+2\sqrt{\frac{Q_p(\phi^*)}{mc^2}}\frac{\kappa_*^2}{\gamma_*^2}[p_{y*}\sin(\phi^*) - 2\eta p_{z*}\cos(\phi^*)],$$
$$P_{x_{\text{van}}} = 2\frac{\kappa_*}{c}Q_p(\phi)[\sin^2(\phi) + \eta^2\cos^2(\phi)]$$
$$-2\frac{\kappa_*}{c}\sqrt{Q_p(\phi)Q_p(\phi^*)}[\sin(\phi)\sin(\phi^*)$$
$$+\eta^2\cos(\phi)\cos(\phi^*)]. \tag{9}$$

Here, $\phi^* = \omega_0 t^*$ is the field phase at which an electron originates in the vicinity of the point x under consideration, $\phi = \omega_0(t - \delta(t, t^*)/c)$ is the field phase at the point at which the electron occurs at the time t, and $Q_p(\phi) = m(eE(\phi)/2m\omega_0)^2$ is the averaged oscillatory energy of an electron at the time t. The longitudinal displacement $\delta(t, t^*)$ of an electron from the point at which it is born at the time t^* to the point at which it occurs at the time t satisfies the transcendental algebraic equation presented in Appendix A.

In formulas (7)–(9), the strongly oscillating momentum component $\mathbf{P}_{\text{van}}$ depends on ϕ, while the weakly oscillating component $\mathbf{P}_{\text{fin}}$ depends only on ϕ^* rather than ϕ. As $t \longrightarrow \infty$, we have $\mathbf{P}_{\text{van}} \longrightarrow 0$, because $\phi = t - \delta(t, t^*)/c \longrightarrow \infty$ by virtue of both $d\delta(t, t^*)/dt < c$ and $Q(\phi \longrightarrow \infty) \longrightarrow 0$. Therefore, the component $\mathbf{P}_{\text{van}}$ makes no contribution to the REM. Consequently, the REM is determined by the component $\mathbf{P}_{\text{fin}}$, which is nonzero in the limit $t \longrightarrow \infty$.

Using formulas (5) and taking into account expressions (7)–(9), (3), (4), and (6), we can see that the ensemble-averaged electron momentum and energy satisfy the relationships

$$\mathbf{P}(t) = \mathbf{P}_{\text{van}}(t) + \mathbf{P}_{\text{fin}}(t), \quad Q(t) = Q_{\text{van}}(t) + Q_{\text{fin}}(t).$$

The strongly oscillating components $\mathbf{P}_{\text{van}}(t)$ and $Q_{\text{van}}(t) = cP_{x_{\text{van}}}(t)$ vanish as $t \longrightarrow \infty$, while the weakly oscillating components $\mathbf{P}_{\text{fin}}(t)$ and $Q_{\text{fin}}(t)$ (which oscillate only slightly about their values averaged over the laser field period) remain nonzero after the passage of the pulse. The weakly oscillating components determine the ensemble-averaged momentum and energy that the laser field transfers irreversibly in the nonadiabatic interaction to the electrons produced in the vicin-

---

[4] Goreslavsky *et al.* [7] showed that this assumption is valid even for ultrashort laser pulses with a duration of about one laser field period.

ity of the point x by the time t during gas ionization. Hence, after the passage of the pulse (at $t \longrightarrow \infty$ for a Gaussian pulse), the components $\mathbf{P}_{\rm fin}$ and $Q_{\rm fin}$ are just the REM and REE.

Substituting expressions (7)–(9), (3), and (4) into formula (5), we find that the momentum $\mathbf{p}_*$ does not contribute to the projections of the REM $\mathbf{P}_{\rm fin}$ onto the y- and z-axes and that the contribution of $\mathbf{p}_*$ to the x-component of $\mathbf{P}_{\rm fin}$ is determined by the small parameter $|\mathbf{p}_*/(mc)|^2 \ll 1$ and can always be neglected. For this reason, the projections of $\mathbf{P}_{\rm fin}$ onto the coordinate axes,

$$P_{y_{\rm fin}}(t) = 2\sqrt{m}N(t)^{-1} \times \int_{-\infty}^{t}\sum_{k=1}^{z_n} Q_p^{1/2}(t^*)\sin(\omega_0 t^*)n_{k-1}(t^*)W_k(t^*)dt^*, \quad (10)$$

$$P_{z_{\rm fin}}(t) = -\eta 2\sqrt{m}N(t)^{-1} \times \int_{-\infty}^{t}\sum_{k=1}^{z_n} Q_p^{1/2}(t^*)\cos(\omega_0 t^*)n_{k-1}(t^*)W_k(t^*)dt^*, \quad (11)$$

$$P_{x_{\rm fin}}(t) = 2[cN(t)]^{-1}\int_{-\infty}^{t}\sum_{k=1}^{z_n} Q_p(t^*)[\sin^2(\omega_0 t^*) + \eta^2\cos^2(\omega_0 t^*)]n_{k-1}(t^*)W_k(t^*)dt^* \quad (12)$$

have the same form as for $\mathbf{p}_* = 0$.

Formula (5) with expressions (6), (3), and (4) yields the following relationship for $Q_{\rm fin}(t)$:

$$Q_{\rm fin}(t) = cP_{x_{\rm fin}}(t) + Q_*(t), \quad (13)$$

where

$$Q_*(t) = \frac{J_H}{N(t)}\int_{-\infty}^{t}\sum_{k=1}^{z_n}\sqrt{\frac{J_H}{J_k}\frac{E(t^*)}{E_{\rm a}}}[\eta^2\sin^2(\omega_0 t^*) + \cos^2(\omega_0 t^*)]^{1/2}n_{k-1}(t^*)W_k(t^*)dt^*. \quad (14)$$

In formula (13), the term Q_* accounts for the initial velocity distribution of the ionization-produced electrons; setting $\Gamma_k(\mathbf{p}_*, t) \sim \delta(\mathbf{p}_*)$ in expression (4) gives $Q_* = 0$.

In order to investigate how the quantities $\mathbf{P}_{\rm fin}$ and $Q_{\rm fin}$ depend on the parameters of the gas and the laser pulse, it is convenient to eliminate oscillating terms in the integrals in expressions (10)–(14) with the ionization rate and electron density determined by formulas (3) and (2), respectively. Below, the mean electron energy, mean longitudinal (along the x-axis) electron momentum, and the transverse REM will be analyzed separately.

3.1. Averaged Equations for $P_{x_{fin}}$ and Q_{fin}

We start by investigating the mean electron energy and mean longitudinal electron momentum. To do this, we perform the time integration in formulas (12) and (14) over subintervals $[t'; t' + \pi/(2\omega_0)]$, each is as long as one-quarter of the laser field period. For a laser pulse with arbitrary polarization, the integrals over the subintervals are expressed in terms of Bessel functions. In this case, the quantities under consideration cannot be represented simply as power functions of the electric field strength (see [13]). In order to avoid difficulties (which are not, however, of fundamental importance), we consider two opposite limiting cases in which the integrals over the subintervals $[t'; t' + \pi/(2\omega_0)]$ can be expanded in asymptotic or power series, because, on a time scale of about ω_0^{-1}, the field amplitude and electron density change only slightly, and, for a sufficiently high ionization rate, the parameter $\alpha_k \sim 10^{-1}$ is small.

(i) If the polarization of a laser pulse is far from being circular, $3\alpha_k/(1-\eta^2) \ll 1$, formulas (12) and (14) reduce to

$$\bar{P}_{x_{\rm fin}}(t) = \frac{4N^{-1}(t)}{(\hbar\omega_0)^2 c}\sum_{k=1}^{z_n} J_k^3\int_{-\infty}^{t}\bar{W}_k(t')\bar{n}_{k-1}(t')\alpha_k^2(t') \times\left[\eta^2 + \frac{3}{2}\alpha_k(t')R_k(t')\right]dt', \quad (15)$$

$$\bar{Q}_*(t) = N^{-1}(t)\sum_{k=1}^{z_n} J_k\int_{-\infty}^{t}\bar{W}_k(t')\bar{n}_{k-1}(t')\alpha_k(t') \times\left[1 - \frac{3}{2}\alpha_k(t') + O\{\alpha_k^2(t')\}\right]dt', \quad (16)$$

where the coefficient R_k incorporates the first three terms of the corresponding asymptotic series in α_k (see Appendix B). With good accuracy, we can assume for estimates that this coefficient is equal to 0.8, because, in a wide range of the pulse parameters, it lies between 0.7 and 1, provided that the relative densities n_{k-1} of the ions in different ionization states are nonzero. The ionization rate $\bar{W}_k(t')$ averaged over the laser field period [see expression (3)] has the form

$$\bar{W}_k(t') = W_k(E(t'))\sqrt{\frac{3\alpha_k(t')}{\pi(1-\eta^2)}} \times\left[1 + \frac{3}{2}\alpha_k(t')\left(n_* - \frac{13}{8} + \frac{1/2}{1-\eta^2}\right) + O\{\alpha_k^2(t')\}\right], \quad (17)$$

where the density of the ions in the kth ionization state, $\bar{n}_k$, averaged over the laser field period, is calculated from formulas (2), in which W_k and $W_k(E(t'))$ are determined by expressions (17) and (3), respectively. We emphasize that, in contrast to formula (3), expression (17) should be taken with the field amplitude $E(t')$ rather than with the instantaneous value $|\tilde{\mathbf{E}}(t')|$ of the rapidly oscillating field. Note also that, for linear polarization, the averaged ADK formula taken with the instantaneous laser field (as is the case in [1, 2]) may lead to an REE overestimated by a factor of approximately 1.5 [20].

For $\eta = 0$, the first term in formula (17) gives the ADK formula for the rate of tunneling ionization by a linearly polarized laser field [14].[5] The remaining terms in the asymptotic series are negligible for $1 - \eta^2 \gg 3\alpha_k$. Note that, at a fixed peak intensity I_0, in accordance with formulas (17), (3), and (1), the main dependence of $\overline{W}$ on η in the limit $1 - \eta^2 \gg 3\alpha_k$ under consideration is determined by the factor $E^{3/2 - 2n_*}(1 - \eta^2)^{-1/2} \sim (1 + \eta^2)^{n_* - 3/4}(1 - \eta^2)^{-1/2}$.

(ii) For a laser pulse with nearly circular polarization, $3\alpha_k/(1 - \eta^2) \gg 1$, formulas (12) and (14) reduce to

$$\overline{P}_{x_{\rm fin}}(t) = \frac{4N^{-1}(t)}{(\hbar\omega_0)^2 c}\sum_{k=1}^{z_n} J_k^3 \int_{-\infty}^{t} \overline{W}_k(t')\bar{n}_{k-1}(t')\alpha_k^2(t') \times\left[\eta^2 + \frac{(1-\eta^2)\breve{R}_k(t')}{2}\right]dt', \tag{18}$$

$$\overline{Q}_*(t) = N^{-1}(t)\sum_{k=1}^{z_n} J_k \int_{-\infty}^{t} \overline{W}_k(t')\bar{n}_{k-1}(t')\alpha_k(t') \times[1 - (1-\eta^2)/2 + O\{(1-\eta^2)^2\}]dt'. \tag{19}$$

Here, the averaged ionization rates $\overline{W}_k$ have the form

$$\overline{W}_k(t') = W_k(E(t'))\left\{1 - \frac{1-\eta^2}{2}\left[\frac{1}{3\alpha_k(t')} - n_* + \frac{1}{2}\right] + \frac{3}{8}(1-\eta^2)^2\left[\frac{1}{18\alpha_k^2(t')} - \frac{1}{3\alpha_k(t')}\left(n_* + \frac{1}{4}\right) + \frac{n_*^2}{2} - \frac{1}{8}\right] + O\{(1-\eta^2)^3\}\right\}, \tag{20}$$

the densities $\bar{n}_{k-1}$ are calculated from formulas (2) and (20), and $W(t')$ is determined by expression (3) with the field amplitude $E(t')$ in place of the instantaneous field $|\tilde{\mathbf{E}}(t)|$. The coefficient $\breve{R}_k$, which accounts for the power series in $1 - \eta^2$, is presented in Appendix B.

According to formulas (16) and (19), the correction Q_* (caused by the nonzero initial electron momentum $\mathbf{p}_*$) to the REE $Q_{\rm fin}$ depends weakly on the degree of elliptical polarization of laser radiation; i.e., in both of the above cases, the factors in square brackets are close to unity. For a circularly polarized pulse, the ratio $Q_*/(cP_{x_{\rm fin}}) \approx (\hbar\omega_0/2J_k)\gamma \ll 1$ is negligibly small. For a linearly polarized pulse, we have $Q_*/(cP_{x_{\rm fin}}) \approx 0.9\gamma^2$, so that the correction Q_* can be large in the regime close to the regime of tunneling ionization ($\gamma \sim 1$).

Figure 1 illustrates the dependence of the REE $Q_{\rm fin}(t \longrightarrow \infty)$ on the degree η of elliptic polarization of the pulse. The curves were obtained numerically from formulas (3) and (12)–(14) for different gases (hydrogen, helium, and oxygen). The residual energies in hydrogen, helium, and oxygen were normalized, respectively, to their values $Q_{\rm fin}$ = 23, 600, and 1810 eV in the case of a circularly polarized ($\eta = 1$) laser pulse with the parameters $I_0 = 5 \times 10^{18}$ W cm^{-2}, $\lambda_0 = 0.78$ μm, and τ_{FWHM} = 100 fs. The curves symbolized by open circles reflect the residual energies calculated from the averaged formulas (15)–(17) (the lower curve) and formulas (18)–(20) (the upper curve); we can see that

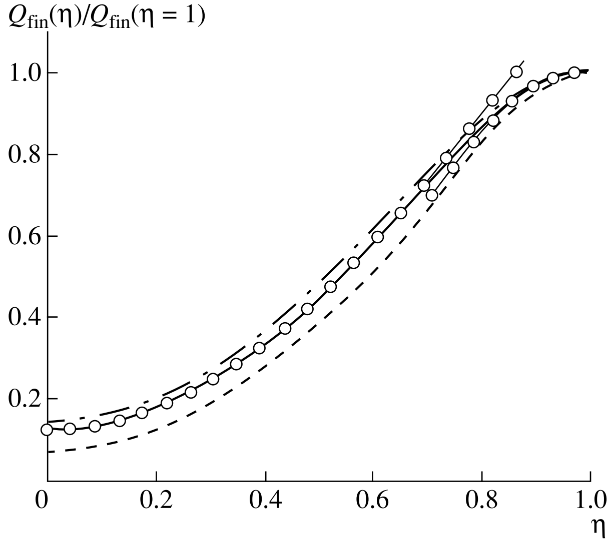

Fig. 1. REE $Q_{\rm fin}(t \longrightarrow \infty)$, normalized to its maximum (at $\eta = 1$) value, versus the degree η of elliptic polarization of a laser pulse with the parameters $I_0 = 5 \times 10^{18}$ W cm^{-2}, λ_0 = 0.78 μm, and τ_{FWHM} = 100 fs for hydrogen (dashed-and-dotted curve), oxygen (dashed curve), and helium (solid curve and curves marked by circles). The solid curve illustrates the results obtained from formulas (2), (3), and (12)–(14). The curves marked by circles show the residual energies calculated from formulas (2), (13), and (15)–(17) (the lower curve) and formulas (2), (13), and (18)–(20) (the upper curve). For hydrogen, helium, and oxygen, the maximum residual energies are equal to $Q_{\rm fin}(\eta = 1)$ = 23, 600, and 1810 eV, respectively.

---

[5] In [14], the corresponding formula is misprinted: the numerical factor $\left(\frac{3e^{1}}{\pi}\right)$ should be raised to a power of 3/2 rather than 1/2.

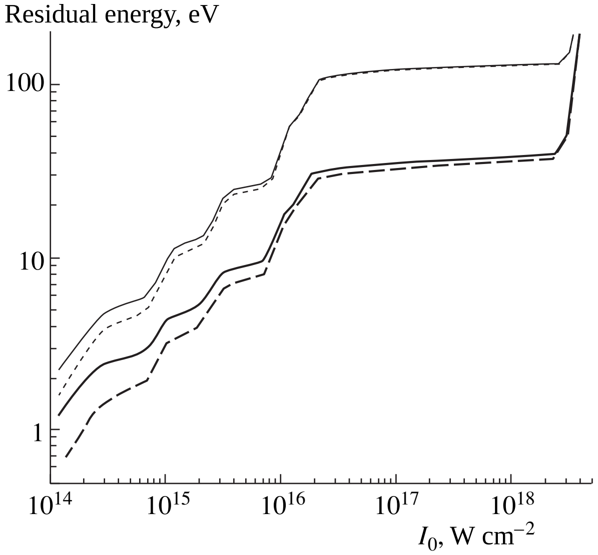

Fig. 2. REE versus the peak intensity I_0 for nitrogen ionized by a laser pulse with the parameters $\lambda_0 = 0.62$ μm and $\tau_{FWHM} = 100$ fs. The heavy curves refer to a linearly polarized pulse ($\eta = 0$), and the light curves refer to an elliptically polarized pulse ($\eta = 0.4$). The solid curves are calculated with allowance for the initial velocity distribution of the ionization-produced electrons, and the dashed curves are obtained under the assumption that the electrons originate with a zero initial velocity.

these formulas give quite reliable results for $\eta < 0.8$ and $\eta > 0.8$, respectively.

Since, for the chosen parameter values, the correction Q_* to the main term $cP_{x_{\rm fin}}$ is small, we can assume that the electrons are produced with a zero initial momentum $\mathbf{p}_*$. From Fig. 1, we can also see that the profiles $Q_{\rm fin}(\eta)/Q_{\rm fin}$ ($\eta = 1$) are similar for different gases.

Figure 2 shows the REE as a function of the peak intensity of a laser pulse in nitrogen, calculated from formulas (12)–(14) with and without allowance for the initial velocity distribution of the ionization-produced electrons (in the latter case, the correction Q_* was set at zero). The steps in the dependence of the REE on I_0 correspond to the successive ionization of different electron shells. We can see that the initial velocity distribution of the ionization-produced electrons makes the largest contribution to the REE in the case of low-intensity laser pulses, for which the Keldysh parameter is relatively large. The higher the degree of elliptic polarization, the smaller the contribution of the initial electron velocity distribution to the REE.

Pronounced peaks in the time evolution of the ionization rate $\bar{S} \equiv S_0$ averaged over the laser field period in helium correspond to the successive ionization of different electron shells (Fig. 3). Replacing the peaks by δ-functions, we obtain from formulas (13), (15), (16), and (18) the following estimates:

$$\overline{Q_{\rm fin}}(t) \approx \left[\sum_{k=1}^{Z_{\max}} \theta(t-t_k)\right]^{-1} \sum_{k=1}^{Z_{\max}} \left[\frac{J_k^3}{(\hbar\omega_0)^2}[4\eta^2\alpha_k^2(t_k) + 5\alpha_k^3(t_k)] + J_k\alpha_k(t_k)\right]\theta(t-t_k),$$

$$\frac{3\alpha_k}{1-\eta^2} \ll 1,$$

$$\overline{Q_{\rm fin}}(t) \approx \left[\sum_{k=1}^{Z_{\max}} \theta(t-t_k)\right]^{-1} [1+\eta^2-0.7(1-\eta^2)^2] \tag{21}$$

$$\times \sum_{k=1}^{Z_{\max}} \frac{2J_k^3}{(\hbar\omega_0)^2}\alpha_k^2(t_k)\theta(t-t_k),$$

$$\frac{3\alpha_k}{1-\eta^2} \gg 1,$$

where t_k is the time at which the ionization rate of the ions in the kth ionization state is the highest, $\alpha_k(t_k) \sim 10^{-1}$ is the value of the parameter α_k at the time t_k, $\theta(t - t_k)$ is the Heaviside step function, and $Z_{\max} \le z_n$ is the number of completely ionized electron shells. The coefficients R_k and $\breve{R}_k$ are set to be equal to 0.83 and $1 - 0.7(1 - \eta^2)$, respectively (see Appendix B). As was shown above, the correction $J_k\alpha_k$, which comes from the initial momentum distribution of the ionization-produced electrons, should be taken into account only for laser pulses with a nearly linear polarization.

Estimates (21) imply that, for laser pulses whose polarization is far from being circular ($\eta < 0.8$), the mean energy of the electrons produced from ionization of the kth shell depends on the field amplitude as $Q_{{\rm fin}_k} \propto \eta^2E^2(t_k) + (J_H/J_k)^{3/2}E_{\rm a}^{-1}E^3(t_k)$; for pulses with nearly circular polarization ($\eta > 0.8$), this dependence is $Q_{{\rm fin}_k} \propto E^2(t_k)$. Also, the above formulas show that the mean electron energy is proportional to the squared laser wavelength.

As the peak intensity I_0 of the pulse increases, the point t_k, corresponding to the time at which the ionization rate of the ions in the kth ionization state is the highest, is displaced toward the pulse front along the temporal profile of the pulse. As a result, for peak intensities I_0 that exceed the ionization threshold I_{th} by a factor of two to three, the REE depends only weakly on I_0. (According to [1], the threshold intensity is the pulse intensity at which the potential barrier for an electron in a laser field becomes lower than the ionization potential; for an ion in the $(k - 1)$th ionization state, we have

$I_{th} \approx 1.4 \times 10^{14}(J_k/J_H)^4k^{-2}$ W cm^{-2}.) For multielectron atoms, the REE changes in a jumplike fashion every time the peak intensity of the pulse increases above the threshold for the ionization of each next low-lying electron shell (Fig. 2).

As the laser pulse duration increases or the pulse front becomes less steep [for example, when pulses with a hyperbolic secant envelope are used in place of Gaussian pulses (1)], the point t_k, corresponding to the time at which the ionization rate of the kth electron shell is the highest, is displaced toward the pulse front along the temporal profile of the pulse. As a result, the REE decreases. However, for longer laser pulses such that the ionization front is longer than ten laser field periods, the REE changes insignificantly as the pulse duration increases. Thus, for a laser pulse with the wavelength $\lambda_0 = 0.78$ μm and the intensity $I_0 = 5 \times 10^{18}$ W cm^{-2}, the REE changes only slightly when $\tau_{FWHM} > 100$ fs.

Our calculations showed that, for laser pulses with a peak intensity above the threshold and a duration longer than a hundred picoseconds, the parameter $\alpha_k(t_k)$ is essentially insensitive to the characteristics of laser radiation. Thus, for helium, this parameter takes on the values $\alpha_1 \sim 0.1$ and $\alpha_2 \sim 0.07$, and, for oxygen, we have $\alpha_1 \sim 0.08$; $\alpha_2 \sim 0.06$; α_3, α_4, $\alpha_5 \sim 0.05$; and $\alpha_6 \sim 0.04$. Having found α_k from Eq. (2) with expression (3) or from relationships (17) and (20), we can use formula (21) to estimate the mean energy Q_{fin_k} of the electrons produced during ionization of the gas atoms up to the kth ionization state. For example, for a helium gas ionized by a linearly polarized laser pulse with the same parameters as in Fig. 1, we arrive at the estimates $Q_{\mathrm{fin}_1} \approx 30$ eV, $Q_{\mathrm{fin}_2} \approx 110$ eV, and $Q_{\mathrm{fin}} = (Q_{\mathrm{fin}_1} + Q_{\mathrm{fin}_2})/2 \approx 70$ eV, which agree satisfactorily with the results calculated from more exact formulas (12)–(14): $Q_{\mathrm{fin}_1} \approx 27$ eV, $Q_{\mathrm{fin}_2} \approx 122$ eV, and $Q_{\mathrm{fin}} \approx 75$ eV.

3.2. Equations for the Transverse REM

Before we proceed with the examination of the transverse REM $\mathbf{P}_{\perp\infty} \equiv \mathbf{e}_y P_{y_{\mathrm{fin}}}(t \longrightarrow \infty) + \mathbf{e}_z P_{z_{\mathrm{fin}}}(t \longrightarrow \infty)$ as a function of the laser and gas parameters, note that the integrals of rapidly oscillating functions in expressions (10) and (11) differ substantially from zero only when the width L_S of the ionization curve $S(t)$ is no longer than several laser field periods. In fact, the ionization-produced electrons move initially in different directions, depending on the laser field phases at which they are ejected from the atomic shells. The total electron momentum can substantially differ from zero only when the number of electrons propagating in one direction is markedly larger than the number of electrons propagating in the opposite direction. This situation is possible only when laser pulses are sufficiently short and/or sufficiently intense to produce the ionization front with a small width L_S. While the absolute value of the transverse REM is a monotonically decreasing function of the width of the ionization front, the direction of the REM is governed by the laser field phases at the times t_k at which the ions in the kth ionization state are ionized with the highest rate: the vector of the residual transverse momentum of the electrons produced from ionization of the kth shell will rotate[6] about the

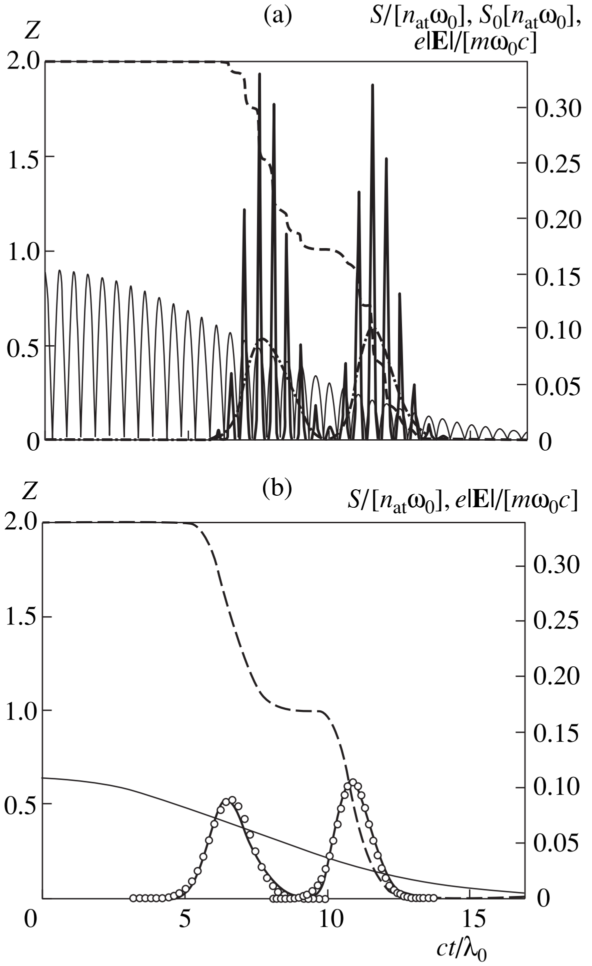

Fig. 3. Dimensionless ionization rate $S(t)/(n_{at}\omega_0)$ (heavy curves), mean ion charge $Z = N/n_{at}$ (dashed and dashed-and-dotted curves), and dimensionless electric field strength $e|\tilde{\mathbf{E}}(t)|/(m\omega_0 c)$ (light curves) for helium ionized by (a) linearly and (b) circularly polarized laser pulses with the parameters $I_0 = 5 \times 10^{16}$ W cm^{-2}, $\lambda_0 = 0.78$ μm, and $\tau_{FWHM} = 30$ fs. In Fig. 3a, the dashed-and-dotted curve is for the zeroth harmonic $S_0 = \bar{S}$ of the ionization rate. In Fig. 3b, the circles illustrate the results from the approximations of the first and second peaks in the ionization curve by Gaussian functions.

---

[6] For a linearly polarized laser pulse, the transverse REM will reverse direction, because it can be oriented either parallel or antiparallel to the electric field.

x-axis (along which the pulse propagates) as the field phase at the time t_k changes (as a result of changes in laser pulse parameters).

In order to justify the above considerations and to analytically investigate the dependence of the transverse REM on the laser and gas parameters, we approximate the term S_k, which incorporates the ionization of the kth electron shell into the total ionization rate S in Eqs. (2), by a smooth curve, e.g., a curve that is described by a Gaussian function $S_k = n_{at}\exp\{-[(t-t_k)/\tau_{S,k}]^2\}/[\sqrt{\pi}\tau_{S,k}]$, where $\tau_{S,k} = L_{S,k}/c$ and $L_{S,k}$ is the characteristic width of the kth ionization front (Fig. 3b). Since the direction of the momentum $\mathbf{P}_{\perp\infty}$ is sensitive to the field phase at the ionization time t_k, we must take into account the phase shift of the oscillating component $\cos(\omega_0 t)$ with respect to the pulse center. For this reason, we specify the electric field of the pulse in the form $\tilde{\mathbf{E}}(t) = E(t)[\mathbf{e}_y\cos(\omega_0 t + \varphi) + \eta\mathbf{e}_z\sin(\omega_0 t + \varphi)]$, in contrast to formulas (1), in which we set $\varphi = 0$. As a result, with allowance for the fact that, on scale lengths $L_{S,k}$, the electric field changes only slightly, we arrive at the expressions

$$
\begin{aligned}
P_{y_{\text{fin}}}(t \longrightarrow \infty) = {} & 2Z_{\max}^{-1}\sum_{k=1}^{Z_{\max}}\sqrt{mQ_p(t_k)} \\
& \times[\sin(\omega_0 t_k + \varphi)e^{-(\omega_0\tau_{S,k}/2)^2}[1-\mu_{k_2}(t_k)] \\
& + \sin(3\omega_0 t_k + 3\varphi)e^{-(3\omega_0\tau_{S,k}/2)^2}[\mu_{k_2}(t_k)-\mu_{k_4}(t_k)] + \dots],
\end{aligned}
\tag{22}
$$

$$
\begin{aligned}
P_{z_{\text{fin}}}(t \longrightarrow \infty) = {} & -2\eta Z_{\max}^{-1}\sum_{k=1}^{Z_{\max}}\sqrt{mQ_p(t_k)} \\
& \times[\cos(\omega_0 t_k + \varphi)e^{-(\omega_0\tau_{S,k}/2)^2}[1+\mu_{k_2}(t_k)] \\
& + \cos(3\omega_0 t_k + 3\varphi)e^{-(3\omega_0\tau_{S,k}/2)^2}[\mu_{k_2}(t_k)+\mu_{k_4}(t_k)] + \dots],
\end{aligned}
\tag{23}
$$

where $Z_{\max} \le z_n$ is the number of completely ionized electron shells. The coefficients $\mu_{k_2} \equiv W_{k_2}/(2W_{k_0})$, $\mu_{k_4} \equiv W_{k_4}/(2W_{k_0})$, etc., incorporate high-frequency harmonics in the spectrum of the ionization source for a laser pulse with a noncircular polarization (Fig. 3a). Here, $W_{k_{2n}} = 2\overline{W_k\cos(2\omega_0 t)}$ $(n = 1, 2\dots)$ denotes the $[2n]$th high-frequency harmonic of the ionization rate W_k, $W_{k_0} = \overline{W}_k$ is the ionization rate averaged over the laser field period [which is calculated from formula (17) when the pulse polarization is far from being circular and from formula (20) when the pulse polarization is nearly circular], and the superior bar stands for averaging over the laser field period. The first of these coefficients takes on the following values: $\mu_{k_2} = 1 - 3\alpha_k R_k/(1-\eta^2)$ when the pulse polarization is far from being circular, $\mu_{k_2} = 1 - \breve{R}_k \approx 0.7(1-\eta^2) \ll 1$ when the pulse polarization is nearly circular, $\mu_{k_2} \approx 0.75$ for a linearly polarized pulse, and $\mu_{k_2} = 0$ for a circularly polarized pulse. The coefficients $\mu_{k_{2n}}$ with $n > 1$ can be expressed in terms of the analogous power series in α_k or $1 - \eta^2$; however, we do not require the exact values of these coefficients, because the first term on the right-hand side of expressions (22) and (23) is much larger than the remaining terms (the exponential functions contain the factor $2n + 1$ and thus rapidly decrease with increasing n).

Formulas (22) and (23) imply that, for singly charged ions (including hydrogen ions) produced by a laser pulse with almost circular polarization ($\mu_{1_2} \ll 1$), the absolute value of the transverse REM,

$$
\begin{aligned}
|\mathbf{P}_{\perp\infty}| = {} & \sqrt{P_{y_{\text{fin}}}^2(t \longrightarrow \infty) + P_{z_{\text{fin}}}^2(t \longrightarrow \infty)} \approx 2\sqrt{mQ_p(t_k)}e^{-(\omega_0\tau_{S,1}/2)^2} \\
& \times\sqrt{\eta^2(1+\mu^2)+(1-\mu^2)+[\eta^2(1+\mu^2)-(1-\mu^2)]\cos(2\omega_0 t_1 + 2\varphi)},
\end{aligned}
\tag{24}
$$

depends weakly on the phase $\omega_0 t_1 + \varphi$ and decreases exponentially with increasing the ionization front width $\tau_{S,1}$ and, accordingly, the pulse duration τ_{FWHM}. As the field phase changes, the vector of the transverse REM rotates about the x-axis such that the angle θ between $\mathbf{P}_{\perp\infty}$ and the y-axis changes according to the law

$$
\theta \approx \arctan\{\eta^{-1}\cot(\omega_0 t_1 + \varphi)(1+\mu_{1_2}/2)/(1-\mu_{1_2}/2)\}, \quad \eta \ne 0.
$$

For a linearly polarized pulse, the transverse REM is oriented parallel to $\mathbf{E}$ (to the y-axis) and, in accordance with formula (22), changes from about $\approx[-2\sqrt{mQ_p(t_1)}e^{-(\omega_0\tau_{S,1}/2)^2}$ to about $2\sqrt{mQ_p(t_1)}e^{-(\omega_0\tau_{S,1}/2)^2}$ as the field phase at the time t_1 changes. In this case, the angle θ takes on two values: $-\pi/2$ and $\pi/2$.

Note that, according to formula (24), the maximum (for a given width $\tau_{S,1}$ of the ionization front) absolute value of the transverse REM, $|\mathbf{P}_{\perp\infty}|$, is proportional to $\eta(1+\mu_{1_2})$ for $\eta > (1-\mu_{1_2})/(1+\mu_{1_2})$ and to $1-\mu_{1_2}$ for $\eta \le (1-\mu_{1_2})/(1+\mu_{1_2})$. Consequently, from the asymptotic expressions for μ_{1_2}, we can see that $|\mathbf{P}_{\perp\infty}|$ increases as η increases from 0 (a linearly polarized pulse) to 1 (a circularly polarized pulse).

The above analytic estimates are illustrated by Fig. 4a, which shows the energy of the ordered transverse electron motion, $(2m)^{-1}|\mathbf{P}_{\perp\infty}|^2$, calculated from formulas (10) and (11) for hydrogen ionized by laser pulses with the parameters $I_0 = 5 \times 10^{17}$ W cm^{-2} and $\lambda_0 = 0.78$ μm and with different polarizations $\eta = 0.1$, 0.5, and 1. In accordance with our analytic estimates, the envelopes of the curves $(2m)^{-1}|\mathbf{P}_{\perp\infty}|^2(\tau_{FWHM})$ are exponentially decreasing functions of τ_{FWHM}. The lower the degree η of elliptic polarization of a laser pulse, the more oscillatory the dependence $(2m)^{-1}|\mathbf{P}_{\perp\infty}|^2(\tau_{FWHM})$ is; recall that this effect stems from the fact that, as τ_{FWHM} changes, the point t_1 is displaced along the temporal profile of the pulse. The dependence $(2m)^{-1}|\mathbf{P}_{\perp\infty}|^2(\tau_{FWHM})$ for helium is shown by the dashed curve in Fig. 4b. We can see that, in contrast to hydrogen, the curve $(2m)^{-1}|\mathbf{P}_{\perp\infty}|^2(\tau_{FWHM})$ for helium decreases nonmonotonically as τ_{FWHM} increases, because the expression for the energy of the ordered transverse electron motion contains the cross terms of the form $\sin(\omega_0 t_k + \varphi)\sin(\omega_0 t_l + \varphi)$ with $k \ne l$ and $\cos(\omega_0 t_n + \varphi)\cos(\omega_0 t_m + \varphi)$ with $m \ne n$, which stem from the summation of the infinite series in the squares of $P_{y_{\text{fin}}}$ and $P_{z_{\text{fin}}}$ [see expressions (22) and (23)].

Unlike the transverse REM, the longitudinal REM and, accordingly, the REE, which is related to the longitudinal REM by expression (13), experience less pronounced variations as τ_{FWHM} changes. This can be illustrated, e.g., by the dashed-and-dotted and dotted curves in Fig. 4b, which correspond, respectively, to the mean energy $P^2_{x_{\text{fin}}}/(2m)(t \longrightarrow \infty)$ of the ordered longitudinal electron motion and the REE $Q_{\text{fin}}(t \longrightarrow \infty)$ for helium. That is why, for ultrashort laser pulses, the transverse REM can be much higher than the longitudinal REM. In contrast, for longer pulses, the longitudinal REM becomes higher than the transverse REM, because the latter approaches zero as the pulse duration increases (Fig. 4b).

Our analytic expressions [formulas (24), (21), and (12)–(14)] and calculated results (Fig. 4) also imply that, for the above laser and gas parameters, the mean residual energy $Q_{\text{dir}} \equiv [P^2_{x_{\text{fin}}}(t \longrightarrow \infty) + |\mathbf{P}_{\perp\infty}|^2]/(2m)$ of the directed electron motion is much lower than the REE $Q_{\text{fin}}(t \longrightarrow \infty)$.

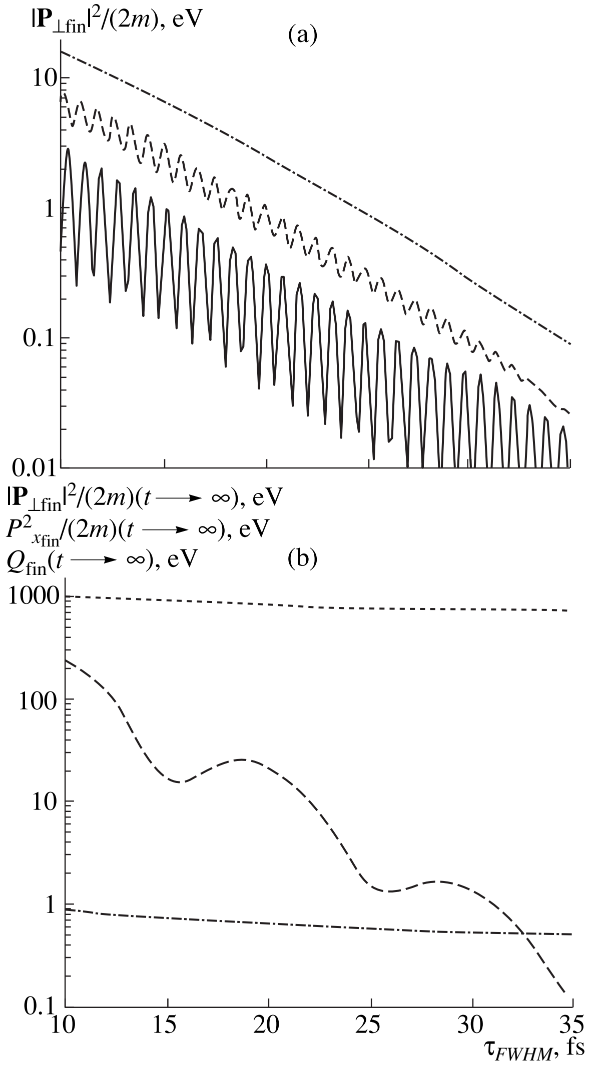

Fig. 4. (a) Dependence of the residual mean energy $|\mathbf{P}_{\perp\text{fin}}|^2/(2m)(t \longrightarrow \infty)$ of the ordered transverse electron motion in hydrogen on the duration of laser pulses with $I_0 = 5 \times 10^{17}$ W cm^{-2} and $\lambda_0 = 0.78$ μm and different polarizations: $\eta = 0.1$ (dashed-and-dotted curve), $\eta = 0.5$ (dashed curve), and $\eta = 1$ (solid curve). (b) Dependence of the residual mean energies ($|\mathbf{P}_{\perp\text{fin}}|^2/(2m)(t \longrightarrow \infty)$) (dashed curve), ($P^2_{x_{\text{fin}}}/(2m)(t \longrightarrow \infty)$) (dashed-and-dotted curve), and $Q_{\text{fin}}(t \longrightarrow \infty)$ (dotted curve) in helium on the duration of a circularly polarized laser pulse with the same parameters.

4. ELECTRON PRESSURE TENSOR IN THE NONRELATIVISTIC COLLISIONLESS LIMIT

Here, we consider the relationship between the REE $Q_{\text{fin}}(t \longrightarrow \infty)$ and the electron pressure tensor Π_{ij} or, equivalently, the electron temperature tensor $T_{ij} \equiv n_e^{-1}\Pi_{ij}$. To do this, we use hydrodynamic equations for a low-density gas ionized by the field of a nonrelativistic laser pulse. The desired hydrodynamic equations can be derived from the following collisionless kinetic equation for the electron velocity distribution function $f(\mathbf{r}, \mathbf{v}, t)$:

$$\frac{\partial f}{\partial t} + v_i \frac{\partial f}{\partial r_i} - \frac{e}{m}\frac{\partial}{\partial v_i}\left\{\left(E_i + \frac{e_{ijl} v_j B_l}{c}\right) f\right\} = \sum_{k=1}^{z_n} \Gamma_k(\mathbf{r}, \mathbf{v}, t) n_{k-1}(t), \tag{25}$$

where e_{ijl} is a completely antisymmetric unit tensor, the subscript i stands for the ith vector component, and E_i and B_l are the corresponding components of the electric $(\tilde{\mathbf{E}})$ and magnetic $(\tilde{\mathbf{B}})$ fields of the pulse. We will derive the hydrodynamic equations for the pressure tensor Π_{ij} in the weakly relativistic limit, because, as was shown in the previous section, the REE is insensitive to relativistic effects if a gas is ionized by a nonrelativistic laser pulse.

Applying the standard method of moments to Eq. (25) yields equations for the hydrodynamic quantities—the electron density $n_e = \int f d^3\mathbf{v}$, electron momentum $\mathbf{P} = n_e^{-1} m \int \mathbf{v} f d^3\mathbf{v}$, and electron pressure tensor $\Pi_{ij} = m\int v'_i v'_j f d^3\mathbf{v}$ (with $v'_i \equiv v_i - V_i$ and $V_i \approx P_i/m$). The corresponding identity transformations put these equations in the form[7]

$$\partial n_e/\partial t + \operatorname{div}(n_e \mathbf{V}) = S, \tag{26}$$

$$\frac{\partial P_i}{\partial t} + V_j \frac{\partial}{\partial x_j} P_i = -eE_i - \frac{P_i S}{n_e} - \frac{e}{c} e_{ijl} V_j B_l - \frac{1}{n_e}\frac{\partial}{\partial r_j}\Pi_{ij}, \tag{27}$$

$$\frac{\partial \Pi_{\alpha\beta}}{\partial t} + \operatorname{div}(\mathbf{V}\Pi_{\alpha\beta} + 2\mathbf{q}_{\alpha\beta}) = mV_\alpha V_\beta S + 2Q'_{\alpha\beta} - \Pi_{\alpha i}\frac{\partial V_\beta}{\partial r_i} - \Pi_{\beta i}\frac{\partial V_\alpha}{\partial r_i} - (e_{\alpha jl}\Pi_{\beta j} + e_{\beta jl}\Pi_{\alpha j})\frac{eB_l}{mc}. \tag{28}$$

Here, $\mathbf{q}_{\alpha\beta} = (m/2)\int v'_\alpha v'_\beta \mathbf{v}' f d^3\mathbf{v}$ is the heat flux vector, the subscripts α and β are fixed, and summation over the repeated Latin indices is used. Using formula (4), we can reduce the quantity $Q'_{\alpha\beta} = m\sum_{k=1}^{z_n} n_{k-1}\int \Gamma_k(\mathbf{v}, \mathbf{r}, t) v_\alpha v_\beta d^3\mathbf{v}$ to

$$Q'_{\alpha\beta} = \frac{1}{2}\begin{pmatrix} 1 & 0 & 0 \\ 0 & \sin^2(\psi) & -\frac{1}{2}\sin(2\psi) \\ 0 & -\frac{1}{2}\sin(2\psi) & \cos^2(\psi) \end{pmatrix} \times \sum_{k=1}^{z_n} n_{k-1} W_k J_H \sqrt{\frac{J_H}{J_k}}\frac{|\tilde{\mathbf{E}}|}{E_{\mathrm{a}}}, \tag{29}$$

where $\psi(t) = \arctan\{\eta \tan(\omega_0 t)\}$ is the angle between the instantaneous electric field $\tilde{\mathbf{E}}$ and the y-axis.

At the initial time (before the pulse starts to ionize the gas), we have $\Pi_{\alpha\beta}(t = 0) = 0$. For $t > 0$, the tensor $\Pi_{\alpha\beta}$ is determined by the source terms—the first and second terms on the right-hand side of Eq. (28). In order to calculate $\Pi_{\alpha\beta}$ in the first approximation, we can use the smallness of the parameters $|\mathbf{V}/c|$, $|\mathbf{V}/c|^2[S/(n_e\omega_0)]^{-1}$, $e^{-(\omega_0\tau_{S,k})^2}[S/(n_e\omega_0)]^{-1}$ and $|\mathbf{V}/c|[S/(n_e\omega_0)]^{-1}(k_0\sigma_r)^{-1}$ in the ionization region (recall that $\tau_{S,k}$ is the characteristic width of the kth ionization front and σ_r is the characteristic transverse size of the pulse); in Eq. (28), we can also neglect the heat flux vector $\mathbf{q}_{\alpha\beta}$ and the terms containing the combinations of $\Pi_{\alpha\beta}$ and $\mathbf{V}$. When the two subscripts $\{\alpha, \beta\}$ do not run the coordinate pairs $\{\alpha = x, \beta = y\}$, $\{\alpha = y, \beta = x\}$, $\{\alpha = x, \beta = z\}$, or $\{\alpha = z, \beta = x\}$, the last term on the right-hand side of Eq. (28) can also be omitted, because it is proportional to $eB_l/(mc)$. As a result, Eq. (28) becomes

$$\Pi_{\alpha\beta}(t) = \int_{-\infty}^{t}[mV_\alpha(t')V_\beta(t')S(t') + 2Q'_{\alpha\beta}(t')]dt'. \tag{30}$$

For $\{\alpha = x, \beta = y\}$ or $\{\alpha = y, \beta = x\}$, we must supplement the right-hand side of Eq. (30) with the term $-(mc)^{-1}\int_{-\infty}^{t}\Pi_{yy}(t')eE_y(t')dt'$, and, for $\{\alpha = x, \beta = z\}$ or $\{\alpha = z, \beta = x\}$, we must add the term $-(mc)^{-1}\int_{-\infty}^{t}\Pi_{zz}(t')eE_y(t')dt'$. However, expressions (35) (see below) imply that these terms both vanish as $t \longrightarrow \infty$.

In the first approximation, the transverse hydrodynamic velocity components V_y and V_z can be calculated by keeping only the first two terms on the right-hand side of Eq. (27). We integrate this equation by part, neglecting the difference $\partial n_e/\partial t - S = \operatorname{div}(n_e\mathbf{V})$ and assuming that $|\partial \ln|\tilde{\mathbf{E}}|/\partial t|$ is much less than $|\partial \ln n_e/\partial t|$.

---

[7] Equations (26) and (27) are also valid in the relativistic limit.

As a result, we obtain from (27) the desired transverse velocity components

$$V_y(t) = e(m\omega_0)^{-1}\left[-E(t)\sin(\omega_0 t) + n_e^{-1}(t)\int_{-\infty}^{t} E(t')\sin(\omega_0 t')S(t')dt'\right],$$
$$V_z(t) = \eta e(m\omega_0)^{-1}\left[E(t)\cos(\omega_0 t) - n_e^{-1}(t)\int_{-\infty}^{t} E(t')\cos(\omega_0 t')S(t')dt'\right]. \tag{31}$$

For our purposes, it is sufficient to calculate the longitudinal hydrodynamic velocity V_x to within terms of the second order in the laser field. Under the condition $\chi \equiv S_0/(n_e\omega_0) \ll 1$, we retain the leading-order terms in the Maxwell equations and the equation of motion (27) to arrive at the following expression for V_x:

$$V_x = -(1-\eta^2)(mc)^{-1}Q_p(t) \times [\cos(2\omega_0 t) - \chi\sin(2\omega_0 t)]. \tag{32}$$

Substituting expressions (31) into formula (30), taking into account expressions (10) and (11) for $P_{y_{\text{fin}}}(t)$ and $P_{z_{\text{fin}}}(t)$, and performing identity transformations, we obtain

$$\frac{1}{2}\Pi_{yy}(t) = n_e(t)\left[Q_{y_{\text{fin}}}(t) - \frac{P^2_{y_{\text{fin}}}(t)}{2m}\right],$$
$$\frac{1}{2}\Pi_{zz}(t) = n_e(t)\left[Q_{z_{\text{fin}}}(t) - \frac{P^2_{z_{\text{fin}}}(t)}{2m}\right], \tag{33}$$
$$\frac{1}{2}\Pi_{yz}(t) = \frac{1}{2}\Pi_{zy}(t) = n_e(t)\left[Q_{yz_{\text{fin}}}(t) - \frac{P_{y_{\text{fin}}}(t)P_{z_{\text{fin}}}(t)}{2m}\right].$$

Here,

$$Q_{y_{\text{fin}}}(t) = 2n_e^{-1}(t)\int_{-\infty}^{t}\sum_{k=1}^{z_n} Q_p(t^*)\sin^2(\omega_0 t^*) \times n_{k-1}(t^*)W_k(t^*)dt^* + Q_{yy*}(t),$$

$$Q_{z_{\text{fin}}}(t) = 2\eta^2 n_e^{-1}(t)\int_{-\infty}^{t}\sum_{k=1}^{z_n} Q_p(t^*)\cos^2(\omega_0 t^*) \times n_{k-1}(t^*)W_k(t^*)dt^* + Q_{zz*}(t), \tag{34}$$

$$Q_{yz_{\text{fin}}}(t) = \eta n_e^{-1}(t)\int_{-\infty}^{t}\sum_{k=1}^{z_n} Q_p(t^*)\sin(2\omega_0 t^*) \times n_{k-1}(t^*)W_k(t^*)dt^* + Q_{yz*}(t),$$

where $Q_{\alpha\beta*} \equiv \int_{-\infty}^{t} Q'_{\alpha\beta}(t^*)dt^*$. The energy Q_{fin} determined by formulas (13) and (14) is equal to $Q_{y_{\text{fin}}} + Q_{z_{\text{fin}}} = Q_{\text{fin}}$, and the REE is $Q_{\text{fin}}(t \longrightarrow \infty)$. The sum of the transverse energies, which are associated with distribution (4) of the ionization-produced electrons over their initial velocities, is equal to one-half of the energy Q_* in expression (14): $Q_{yy*} + Q_{zz*} = Q_*/2$. The remaining half is covered by the longitudinal energy, $Q_{xx*} = Q_*/2$.

The last formulas, together with expressions (33) and (34), determine the relationship between the temperature in the (y, z) plane $T_{\mu\nu} = n_e^{-1}\Pi_{\mu\nu}$ (where $\mu, \nu = y, z$), with the REE and REM.

Analogously, using relationships (32) and (31) and taking into account the above additional terms with $\{\alpha = x, \beta = y\}$ and $\{\alpha = x, \beta = z\}$, we obtain from formula (30) the following expressions:

$$\frac{1}{2}\Pi_{xx}(t) = (1-\eta^2)^2\sum_{k=1}^{z_n}\int_{-\infty}^{t}\frac{2Q_p^2(t^*)}{mc^2}[\cos(2\omega_0 t^*) + \chi(t^*)\sin(2\omega_0 t^*)]^2 n_{k-1}(t^*)W_k(t^*)dt^* + Q_{xx*}(t),$$

$$\Pi_{xy}(t) = (1-\eta^2)(mc^2)^{-1/2}\sum_{k=1}^{z_n}\int_{-\infty}^{z_n} Q_p^{3/2}(t^*)[\sin(3\omega_0 t^*) - \sin(\omega_0 t^*) + 2\chi(t^*)\cos(\omega_0 t^*)]n_{k-1}(t^*)W_k(t^*)dt^* - \Pi_{yy}(t)\sqrt{Q_p(t)/(mc^2)}\sin(\omega_0 t), \tag{35}$$
$$\Pi_{xz}(t) = \eta(1-\eta^2)(mc^2)^{-1/2} \times \sum_{k=1}^{z_n}\int_{-\infty}^{t} Q_p^{3/2}(t^*)[\cos(3\omega_0 t^*) - \cos(\omega_0 t^*) - 2\chi(t^*)\sin(\omega_0 t^*)]n_{k-1}(t^*)W_k(t^*)dt^* + Q_{xz*}(t) + \Pi_{zz}(t)\sqrt{Q_p(t)/(mc^2)}\cos(\omega_0 t).$$

Recall that, since $Q_p(t \longrightarrow \infty) \longrightarrow 0$, the additional terms, which are proportional to Π_{yy} or Π_{zz}, vanish as $t \longrightarrow \infty$.

Now, we consider the electron pressure tensor for moderately short and/or moderately intense laser pulses such that the kth ionization front is no shorter than several laser field periods, so that $\omega_0\tau_{S_k} \gg 1$. For such pulses, formulas (33) and (35) imply that the off-diagonal elements of the pressure tensor as well as the transverse components of the REM are all exponentially small. For laser pulses with different polarizations, the diagonal elements of the pressure tensor and of the temperature tensor $T_{\alpha\alpha} = n_e^{-1}\Pi_{\alpha\alpha}$ can be deduced from formulas (33)–(35) to within unimportant small terms.

(i) When the pulse polarization is far from being circular, $3\alpha_k/(1-\eta^2) \ll 1$, we obtain

$$T_{yy}(t) = 2Q_{y_{\rm fin}}(t) = 12[n_e(t)(\hbar\omega_0)^2]^{-1}$$

$$\times\sum_{k=1}^{z_n} J_k^3\int_{-\infty}^{t}\overline{W}_k(t')\bar{n}_{k-1}(t')\alpha_k^3(t')\frac{R_k(t')}{1-\eta^2}dt' + Q_*(t)/2,$$

$$T_{zz}(t) = 2Q_{z_{\rm fin}}(t) = 8\eta^2[n_e(t)(\hbar\omega_0)^2]^{-1}$$

$$\times\sum_{k=1}^{z_n} J_k^3\int_{-\infty}^{t}\overline{W}_k(t')\bar{n}_{k-1}(t')\alpha_k^2(t') \tag{36}$$

$$\times\left[1-\frac{3}{2}\alpha_k(t')\frac{R_k(t')}{1-\eta^2}\right]dt' + Q_*(t)/2,$$

$$T_{xx}(t) = 8(1-\eta^2)[n_e(t)(\hbar\omega_0)^4 mc^2]^{-1}$$

$$\times\sum_{k=1}^{z_n} J_k^6\int_{-\infty}^{t}\overline{W}_k(t')\bar{n}_{k-1}(t')\alpha_k^4(t')X_k(t')dt' + Q_*(t),$$

where $\overline{W}_k(t')$ is determined by formula (17) and the asymptotic series for X_k and R_k are presented in Appendix B.

(ii) For a pulse with nearly circular polarization, $3\alpha_k/(1-\eta^2) \gg 1$, we have

$$T_{yy}(t) = 2Q_{y_{\rm fin}}(t) = 4[n_e(t)(\hbar\omega_0)^2]^{-1}$$

$$\times\sum_{k=1}^{z_n} J_k^3\int_{-\infty}^{t}\overline{W}_k(t')\bar{n}_{k-1}(t')\alpha_k^2(t')\breve{R}_k(t')dt' + Q_*(t)/2,$$

$$T_{zz}(t) = 2Q_{z_{\rm fin}}(t) = 4\eta^2[n_e(t)(\hbar\omega_0)^2]^{-1}$$

$$\times\sum_{k=1}^{z_n} J_k^3\int_{-\infty}^{t}\overline{W}_k(t')\bar{n}_{k-1}(t')\alpha_k^2(t')[2-\breve{R}_k(t')]dt' + Q_*(t)/2, \tag{37}$$

$$T_{xx}(t) = 4(1-\eta^2)^2[n_e(t)(\hbar\omega_0)^4 mc^2]^{-1}$$

$$\times\sum_{k=1}^{z_n} J_k^6\int_{-\infty}^{t}\overline{W}_k(t')\bar{n}_{k-1}(t')\alpha_k^4(t')dt' + Q_*(t),$$

where $\overline{W}_k(t')$ is determined by formula (20) and the asymptotic series for $\breve{R}_k$ is presented in Appendix B.

Using expressions (36) and (37), we can estimate T_{xx} as

$$(T_{xx}-Q_*)/Q_*$$

$$\sim 7\times10^{-2}(1-\eta^2)^2(J_k/J_H)/[(4\gamma)^4(10\alpha_k)].$$

For ions with low charge numbers and for laser pulses with nearly circular polarization, this ratio is, as a rule, smaller than unity; this indicates that the main contribution to the xx-element of the pressure tensor comes from the distribution of the ionization-produced electrons over their initial velocities. For highly ionized atoms and for laser pulses whose polarization is far from being circular, this ratio can be larger than unity, because, in this case, the xx-element of the pressure tensor is governed mainly by the interaction between the laser field and the electrons as they are ejected from the atoms. Formulas (36) and (37) also allow us to conclude that $T_{xx} \ll T_{yy}$ and $T_{xx} \ll T_{zz}$ (the latter is valid for laser pulses whose polarization is sufficiently far from being linear).

Note also that formulas (15), (18), (36), and (37) give

$$\frac{T_{xx}-Q_*}{\bar{P}_{x_{\rm fin}}^2/m}$$

$$\sim\begin{cases}(1-\eta^2)^2/(\eta^2+3\alpha_k/2) \gtrsim 1, & 1-\eta^2 \gg 3\alpha_k,\\ (1-\eta^2)^2/2 \ll 1, & 1-\eta^2 \ll 3\alpha_k.\end{cases}$$

5. CONCLUSION

We have investigated the REE and REM in gases ionized by elliptically polarized, relativistic, short laser pulses.

We have shown that, for laser pulses with polarization that is not too close to linear, the distribution of the ionization-produced electrons over their initial velocities is unimportant for obtaining the REE and REM, which thus can be determined under the assumption that the electrons are produced with a zero initial velocity, as is usually done in calculations (see, e.g., [2]). For $\gamma \ll 1$, we can, as usual, assume that, during ionization of a gas by a linearly polarized laser pulse, the electrons originate with a zero initial velocity. However, at the boundary of applicability range of the tunneling-ionization model ($\gamma \sim 1$), the initial velocity distribution of the ionization-produced electrons may become important for calculating the REE but again has an insignificant influence on the REM.

Analytic formulas (15)–(24) and (33)–(37) make it possible to study how the main parameters of the gas and the laser pulse affect the REE, the REM, and the electron temperature. We have shown that the transverse REM is essentially nonzero only for very short laser pulses (no longer than one or two tens of laser field periods) and decreases exponentially as the pulse duration increases. The same conclusion is valid for the off-diagonal elements of the electron pressure tensor. For longer laser pulses, only the diagonal elements of the pressure tensor are significantly different from zero.

The diagonal elements of the pressure tensor satisfy the inequalities $\Pi_{xx} \ll \Pi_{yy}$ and $\Pi_{xx} \ll \Pi_{zz}$, and the ratio of Π_{yy} to Π_{zz} is determined by the degree of elliptic polarization η (the pulse is assumed to propagate along the x-axis). The REE is expressed in terms of the pressure tensor elements and REM as $Q_{\text{fin}} = (2n_e)^{-1}(\Pi_{yy} + \Pi_{zz}) - (2m)^{-1}(P^2_{y_{\text{fin}}} + P^2_{y_{\text{fin}}})$. If the laser pulse is not too short, the final energy of the directed electron motion, which is proportional to the squared REM, is much lower than the REE.

We have found that the REE is related to the longitudinal REM by the simple expression (13) and is proportional to the third power of the electric field amplitude (at the time of the most intense ionization) for laser pulses with nearly linear polarization and to the second power of the electric field amplitude for pulses with nearly circular polarization. On the other hand, as the peak pulse intensity I_0 changes, the point corresponding to the time at which the ionization rate is the highest is displaced along the temporal profile of the laser pulse. As a result, for the peak intensity I_0 above the ionization threshold for one-electron atoms, the REE depends weakly on I_0, regardless of the pulse shape. For a gas of multielectron atoms, the dependence of the REE on I_0 is jumplike in character, the number of "jumps" being equal to the number of completely ionized electron shells. We have found that the REE is proportional to the squared laser wavelength. We have also shown that the sharper the pulse front, the higher the REE; in particular, the REE is higher for pulses with the same peak intensity I_0 but with a shorter duration.

ACKNOWLEDGMENTS

We are grateful to V. P. Kraĭnov for valuable discussions. This work was supported in part by the Russian Foundation for Basic Research, project no. 98-02-16263. One of the authors (M.E. Veĭsman) also acknowledges the financial support of the International Soros Science Education Program (ISSEP).

APPENDIX A

The displacement δ of an electron from the point at which it is born is described by the equation

$$
\begin{aligned}
\delta = (m\omega_0 c)^{-1}\Bigg[& 2[\omega_0(t-t^*) - k_0\delta]Q_p(t^*) \\
& \times[\sin^2(\omega_0 t^*) + \eta^2\cos^2(\omega_0 t^*)] \\
& + 4Q_p^{1/2}(t^*)Q_p^{1/2}(t-\delta/c)[\sin(\omega_0 t^*)\cos(\omega_0 t - k_0\delta) \\
& - \eta^2\cos(\omega_0 t^*)\sin(\omega_0 t - k_0\delta)] \\
& - (1/2)(1-\eta^2)Q_p(t-\delta/c)\sin(2\omega_0 t - 2k_0\delta) \\
& - (3/2)(1-\eta^2)Q_p(t^*)\sin(2\omega_0 t^*) \\
& + (1+\eta^2)\int\limits_{t^*}^{t-\delta/c} Q_p(\phi)d\phi\Bigg] + \delta_*(t, t^*, \mathbf{p}_*; \delta),
\end{aligned}
$$

$$
\begin{aligned}
\delta_*(t, t^*, \mathbf{p}_*; \delta) = {} & [c(t-t^*) - \delta] \\
& \times\Bigg[\frac{2Q_p^{1/2}(t^*)}{\sqrt{m}c}\left(\frac{\mathbf{p}_{y*}}{mc}\frac{\kappa_*}{\gamma_*^2}\sin(\omega_0 t^*) - \eta\frac{\mathbf{p}_{z*}}{mc}\frac{\kappa_*}{\gamma_*^2}\cos(\omega_0 t^*)\right) \\
& + \frac{1}{2}\left(\kappa_*^{-2} - 1 + \frac{\kappa_*^2}{\gamma_*^4}\left[\left(\frac{\mathbf{p}_{y*}}{mc}\right)^2 + \left(\frac{\mathbf{p}_{z*}}{mc}\right)^2\right]\right)\Bigg] \\
& + \frac{2Q_p^{1/2}(t-\delta/c)}{\sqrt{m}\omega_0}\Bigg[\frac{\mathbf{p}_{y*}}{mc}\frac{\kappa_*}{\gamma_*^2}\cos(\omega_0(t-t^*) - k_0\delta) \\
& + \eta\frac{\mathbf{p}_{z*}}{mc}\frac{\kappa_*}{\gamma_*^2}\sin(\omega_0(t-t^*) - k_0\delta)\Bigg] \\
& - \frac{2Q_p^{1/2}(t^*)}{\sqrt{m}\omega_0}\Bigg[\frac{\mathbf{p}_{y*}}{mc}\frac{\kappa_*}{\gamma_*^2}\cos(\omega_0 t^*) + \eta\frac{\mathbf{p}_{z*}}{mc}\frac{\kappa_*}{\gamma_*^2}\sin(\omega_0 t^*)\Bigg].
\end{aligned}
$$

In the case at hand, we have $|\mathbf{p}_*/(mc)| \ll 1$. Consequently, for the conditions of tunneling ionization ($\gamma < 1$), we can perform manipulations similar to those in the body of this paper in order to show that $|\delta_*| \ll |\delta - \delta_*|$. Accordingly, in writing Eqs. (7)–(9), we assumed that the displacement δ depends only on t and t^* and is independent of $\mathbf{p}_*$.

APPENDIX B

The coefficient R_k in formulas (15) and (36), the coefficient $\breve{R}_k$ in formulas (18) and (37), and the coefficient X_k in formula (37) for T_{xx} have the form

$$R_k = 1 + \frac{3}{2}\alpha_k\left(2n_* + \frac{1}{1-\eta^2} - \frac{11}{2}\right) + \frac{3\alpha_k^2}{2}\left[\frac{299}{8}\right.$$

$$\left. + 4n_*^2 - 25n_* + \frac{4n_* - 31/2}{1-\eta^2} + \frac{4}{(1-\eta^2)^2}\right] + O\{\alpha_k^3\},$$

$$\breve{R}_k = 1 + \frac{1}{8}\left[2n_* - 1 - \frac{2}{3\alpha_k}\right](1-\eta^2) + O\{(1-\eta^2)^2\},$$

$$X_k = 1 - 6\alpha_k/(1-\eta^2)$$

$$+ (3\alpha_k)^2[(11/2 - 2n_*)/(1-\eta^2) + 2/(1-\eta^2)^2]$$

$$+ O\{\alpha_k^3\}.$$

REFERENCES

1. B. M. Penetrante and J. N. Bardsley, Phys. Rev. A **43**, 3100 (1991).
2. P. Pulsifer, J. P. Apruzese, J. Davis, and P. Kepple, Phys. Rev. A **49**, 3958 (1994).
3. N. H. Burnett and P. B. Corkum, J. Opt. Soc. Am. B **6**, 1195 (1989).
4. S. P. Goreslavsky and S. V. Popruzhenko, Laser Phys. **7**, 700 (1997).
5. V. T. Tikhonchuk and V. Yu. Bychenkov, Laser. Phys. **2**, 525 (1992).
6. N. E. Andreev, M. E. Veĭsman, M. G. Cadjan, and M. V. Chegotov, Fiz. Plazmy **26**, 1010 (2000) [Plasma Phys. Rep. **26**, 947 (2000)].
7. S. P. Goreslavsky, M. V. Fedorov, and A. A. Kil'pio, Laser Phys. **5**, 1020 (1995).
8. M. V. Chegotov, Proc. SPIE **3683**, 33 (1998).
9. N. E. Andreev, L. M. Gorbunov, V. I. Kirsanov, *et al.*, Phys. Plasmas **2**, 2573 (1995).
10. E. Esarey, P. Sprangle, J. Krall, and A. Ting, IEEE Trans. Plasma Sci. **24**, 252 (1996).
11. L. V. Keldysh, Zh. Éksp. Teor. Fiz. **47**, 1945 (1964) [Sov. Phys. JETP **20**, 1307 (1964)].
12. F. A. Ilkov, J. E. Decer, and S. L. Chin, J. Phys. B **25**, 4005 (1992).
13. A. M. Perelomov, V. S. Popov, and M. V. Terent'ev, Zh. Éksp. Teor. Fiz. **50**, 1393 (1966) [Sov. Phys. JETP **23**, 924 (1966)].
14. M. V. Ammosov, N. B. Delone, and V. P. Kraĭnov, Zh. Éksp. Teor. Fiz. **91**, 2008 (1986) [Sov. Phys. JETP **64**, 1191 (1986)].
15. N. B. Delone and V. P. Kraĭnov, Usp. Fiz. Nauk **168**, 531 (1998) [Phys. Usp. **41**, 469 (1998)].
16. M. Dörr, O. Latinne, and C. J. Joachain, Phys. Rev. A **52**, 4289 (1995).
17. R. Grobe and M. V. Fedorov, Phys. Rev. Lett. **68**, 2592 (1992).
18. K. C. Kulander, K. J. Schafer, and J. L. Krause, Phys. Rev. Lett. **66**, 2601 (1991).
19. N. B. Delone and V. P. Kraĭnov, Tr. Inst. Obshch. Fiz. Ross. Akad. Nauk **50**, 34 (1995).
20. N. E. Andreev, M. V. Chegotov, M. E. Veisman, *et al.*, Proc. SPIE **3735**, 234 (1999).
21. P. C. Clemmow and J. P. Dougherty, *Electrodynamics of Particles and Plasmas* (Addison-Wesley, Reading, 1990; Mir, Moscow, 1996).
22. F. V. Hartemann, S. N. Fochs, G. P. Le Sage, *et al.*, Phys. Rev. E **51**, 4833 (1995).

Translated by G.V. Shepekina

Plasma Physics Reports, Vol. 27, No. 4, 2001, pp. 293–302. Translated from Fizika Plazmy, Vol. 27, No. 4, 2001, pp. 311–320.
Original Russian Text Copyright © 2001 by Maĭorov.

Collisional Electron Heating by an Ultraintense Ultrashort Laser Pulse Focused in a Gas

S. A. Maĭorov

Institute of General Physics, Russian Academy of Sciences, ul. Vavilova 38, Moscow, 117942 Russia

Received September 11, 2000; in final form, October 19, 2000

Abstract—Collisional heating of plasma electrons in the field of an ultraintense ultrashort laser pulse is studied. The numerical results obtained by the method of molecular dynamics are compared with the well-known results from kinetic simulations. A model is proposed that provides a good agreement with the results of calculations for both linearly and circularly polarized high-intensity laser pulses. © *2001 MAIK “Nauka/Interperiodica”.*

1. INTRODUCTION

An ultrashort laser pulse focused in a gas produces a plasma with multicharged ions and a relatively low electron temperature. This circumstance opens new possibilities for creating recombination X-ray lasers and X-ray radiation sources [1]. As the directed electron motion in the strong electric field of a laser pulse relaxes toward thermal motion due to elastic collisions of electrons with the ions, the plasma electron temperature increases. The collisional electron heating rate in a strong laser field was first determined by V.P. Silin [2] by solving the Boltzmann–Landau equation under the assumption that the corrections introduced by Coulomb collisions are small.

In this paper, we consider strong high-frequency laser fields such that the laser frequency is higher than the plasma frequency and the electron velocity in a laser field is much higher than the electron thermal velocity. These conditions correspond to experiments with plasmas generated by ultraintense ultrashort laser pulses focused in a gas. The nature of electron–ion (e–i) collisions can be affected by such factors as extremely rapid photoionization of the gas, the periodicity of electron motion in a strong laser field, and small focal spot sizes. Our purpose here is to investigate how these factors influence the collisional electron heating rate.

We consider a fully ionized plasma with the ion density N_i and electron density $N_e = zN_i$, where ze is the ion charge and $-e$ is the charge of an electron. We assume that, at the initial time, the ion temperature is equal to the temperature of the atoms and that the electrons obey a Maxwellian initial energy distribution with a certain temperature T_e governed by the amount by which the absorbed photon energy exceeds the ionization energy.

Let the plasma be affected by a linearly polarized laser wave field $\mathbf{E}(t) = (E_x, 0, 0)$, where

$$E_x(t) = E_0 \cos\omega t. \qquad (1)$$

In a collisionless plasma, the velocity of an electron and its coordinates are equal to

$$\mathbf{v}(t) = \mathbf{v}(0) + \mathbf{v}_E \sin\omega t,$$

$$\mathbf{r}(t) = \mathbf{r}(0) + \mathbf{v}(0)t + \mathbf{r}_E \cos\omega t,$$

where the vectors $\mathbf{v}_E = -e\mathbf{E}_0/m\omega$ and $\mathbf{r}_E = e\mathbf{E}_0/m\omega^2$ determine the oscillatory velocity of the electrons and the amplitude of their oscillations, respectively, and $\mathbf{E}_0 = \mathbf{E}(0)$. Due to the e–i collisions, the directed electron motion in the external electric field (1) becomes stochastic. If the electron oscillatory velocity V_E is much higher than the electron thermal velocity $V_T = \sqrt{T/m}$, then the e–i collision frequency is equal to [2]

$$\nu = \frac{16ze^4N_e}{m^2V_E^3}\left(1 + \ln\frac{V_E}{2V_T}\right)\ln\frac{k_{\max}}{k_{\min}}. \qquad (2)$$

In this case, the collisional electron heating power is equal to [2]

$$W = \frac{8z^2e^4N_eN_i}{mV_E}\left(1 + \ln\frac{V_E}{2V_T}\right)\ln\frac{k_{\max}}{k_{\min}}. \qquad (3)$$

According to [2], the values $k_{\min}$ and $k_{\max}$ are determined by the reciprocal of the Debye radius and the minimum impact parameter, which is found from the condition under which an electron with the velocity V_E can be described either by classical mechanics or by perturbation theory. The Coulomb logarithm satisfies the equality

$$\Lambda = \ln\frac{k_{\max}}{k_{\min}} = \ln\frac{r_D}{\rho_{\min}}. \qquad (4)$$

In expression (2), the logarithm of the ratio of the oscillatory velocity to the thermal velocity stems from the fact that the collision frequency tends to infinity as the directed electron velocity decreases. As a result, the integral over velocities should be truncated at velocities below the thermal velocity. For a circularly polarized laser field, the absolute value of the electron velocity is constant and the logarithm drops out of expression (2) [2].

An analogous formula for the collisional electron heating power in the strong linearly polarized laser wave field was derived by Jones and Lee [3]:

$$W = \frac{8z^2e^4N_eN_i}{mV_E}\ln\frac{V_e}{V_T}\ln\frac{k_{\max}V_T}{\omega}, \tag{5}$$

where the value of $k_{\max}$ is determined from the applicability condition of classical mechanics, $k_{\max} = mV_T/\hbar$.

In the approximate expression derived by Shlessinger and Wright [4] for the collisional electron heating power in a strong linearly polarized laser wave field, the collision frequency is multiplied by the factor that incorporates the difference between the oscillatory and thermal velocities of the electrons:

$$W = \frac{e^2E_0^2}{2m\omega^2}\nu, \tag{6a}$$

$$\nu = \nu_{ei}\left(1 + \frac{V_E^2}{3V_T^2}\right)^{-3/2}, \tag{6b}$$

$$\nu_{ei} = \frac{4\sqrt{2\pi}ze^4N_e}{3\sqrt{m}T^{3/2}}\Lambda, \tag{6c}$$

where Λ is the conventional Coulomb logarithm.

In a collisionless plasma irradiated by a circularly polarized laser pulse with the electric field $\mathbf{E}(t) = (E_x, E_y, 0)$, where

$$E_x(t) = \frac{\sqrt{2}}{2}E_0\cos\omega t,$$

$$E_y(t) = -\frac{\sqrt{2}}{2}E_0\sin\omega t,$$

the electrons move at constant speed $V_E/\sqrt{2}$ along circles of radii $r_E/\sqrt{2}$. In the approximation of instantaneous binary collisions, the interaction of electrons with an immobile ion is taken into account, while the electron–electron interaction is neglected [5], in which case the mean "friction" force exerted by the ions with an impact parameter smaller than $\rho_{\max}$ on an electron has the form [5]

$$F = \frac{4\sqrt{2}\pi z^2e^4N_eN_i}{mV_e}\Lambda,$$

where the Coulomb logarithm is equal to $\lambda = \ln\frac{\sqrt{\rho_\perp^2 + \rho_{\max}^2}}{\rho_\perp} \approx \ln\frac{\rho_{\max}}{\rho_\perp}$ and $\rho_\perp = ze^2/mV^2$ is the impact parameter for which the ion deflects the electron through a right angle. Note that the Coulomb logarithm is not truncated at $\rho_\perp$ because it takes into account all of the e–i collisions with impact parameters $\rho < \rho_{\max}$. The collisional electron heating power is a product of the friction force with the velocity $V_E/\sqrt{2}$ and electron density:

$$W = \frac{4\sqrt{2}\pi z^2e^4N_eN_i}{mV_E}\Lambda. \tag{7}$$

Coulomb logarithm approximation. The Coulomb logarithm Λ is defined in terms of the maximum and minimum impact parameters incorporated into the Landau collision integral [6]: $\Lambda = \ln\rho_{\max}/\rho_{\min}$. For all possible values of the impact parameter ($0 < \rho < +\infty$), the Coulomb collision frequency diverges logarithmically for both short-range and long-range collisions. For short-range collisions, the Coulomb logarithm diverges because the linear expansion fails to apply to the collision integral in this limit; this divergence can be eliminated by choosing the impact parameter in a special way,

$$\rho_{\min} = 1/k_{\max} = \rho_\perp = ze^2/mV^2, \tag{8}$$

which corresponds to an exact solution. In the limiting case of high temperatures such that the impact parameter $\rho_\perp$ is smaller than the de Broglie wavelength $\lambda = h/mV$, the quantum mechanics limit $\rho_{\min} = \lambda/4\pi$ is used (the most thorough treatment of this point is given in [7]). For long-range collisions, the Coulomb logarithm can also be made nondivergent by choosing a finite value of $\rho_{\max}$, i.e., by eliminating (in a physically reasonable manner) long-range collisions from consideration. However, it is not *a priori* clear how to choose the impact parameter $\rho_{\max}$. Initially, most authors (see [8] for the history of this problem) used as the maximum impact parameter the interparticle distance

$$\rho_{\max} = N_i^{-1/3},$$

which determines the upper boundary of the applicability range of the binary-collision approximation. However, after Landau derived the kinetic equation for the plasma, the lower limit of integration was routinely replaced with the Debye radius,

$$\rho_{\max} = r_D = (T_e/4\pi e^2N_e)^{1/2},$$

which indicates that the electron scattering by unscreened fluctuations of the charge density are taken into account.

For a plasma, the Coulomb logarithm is also approximated by the formula [9] that coincides with the approximation proposed by L. Spitzer [10] for singly charged ions. However, the dependence of the Coulomb logarithm on the ion charge *z* may be neglected only for a hot plasma with a low ion charge number. For a cold multicharged plasma with $z \gg 1$, which is of interest for X-ray lasers, taking into account the ions that carry high charges may substantially lower the Coulomb logarithm. Consequently, in describing e–i collisions in a plasma with multicharged ions, we approximate the Coulomb logarithm by

$$\begin{gathered}\Lambda_z = 23.4 - (1/2)\ln N_e + (3/2)\ln T_e - \ln z \\ \text{for} \quad T_e < 50z^2 \text{ eV}, \\ \Lambda_z = 25.3 - (1/2)\ln N_e + \ln T_e - \ln z \\ \text{for} \quad T_e > 50z^2 \text{ eV}.\end{gathered} \tag{9}$$

Sometimes, the Coulomb logarithm is approximated by the formula $\Lambda = (1/2)\ln(1 + 9/4\pi\delta)$, which is written in terms of the Coulomb coupling parameter $\delta = (z + 1)z^3e^6N_e/T_e^3 = 2e^6N_e/T_e^3$ for $z = 1$); below, we will also use a more familiar expression for the coupling parameter, $\Gamma = ze^2 (4\pi N_i/3)^{1/3}/T_e$. This approximation for the Coulomb logarithm was obtained with allowance for the screening of charge density fluctuations by both negative and positive particles and is valid for plasmas with nearly equal masses of positive and negative particles (such as electron–positron plasmas and ion–ion plasmas). It is this approximation that was used by Yakovlenko [11] in order to analyze the results obtained in my paper [8] by numerically simulating Coulomb collisions of electrons with infinitely heavy ions. As a result, the discrepancy between the results of [8] and the conventional theory was underestimated. Note that the method used in [8] to simulate the straight-line motion of particles yielded essentially the same results as those obtained analytically in [7, 12]. Consequently, the results obtained in [8] reflect the long-term and multiparticle nature of Coulomb collisions rather than the numerical technique (as was supposed in [11]).

2. STRAIGHT-LINE MOTION APPROXIMATION

The maximum scale of the charge density fluctuations in a plasma is governed by the electron Debye radius, because the large-scale fluctuations are screened by plasma electrons. Since the electrons are scattered by the charge density fluctuations, the Debye radius can serve as one of the most natural maximum impact parameters for Coulomb collisions in a plasma. However, this is not the case for a plasma affected by an external force that is strong enough to ensure the straight-line motion of particles with an amplitude larger than the Debye radius. The fluctuations of the ion density and the large amplitude of the oscillatory motion of the electron under the action of an external force can strongly influence the nature of Coulomb collisions.

We start by considering atomic density fluctuations in a real gas. The collisional nature of a real gas makes the atomic density fluctuations different from those in an ideal gas. This difference becomes pronounced on spatial scales on the order of the atom mean free path and longer: $\lambda_a = 1/\sigma_a N_a$, where $\sigma_a = \pi d_a^2$ is the gas-kinetic collision cross section, N_a is the atom density, and d_a is the diameter of an atom. In a gas with temperature T_a and atomic mass M, the characteristic relaxation time τ_a of fluctuations is determined by the atom thermal velocity (the speed of sound) $c_s = (\gamma T_a/m_a)^{1/2}$, where $\gamma = 5/3$ is the adiabatic index of an ideal gas:

$$\tau_a = \lambda_a/c_s = 1/\sigma_a N_a c_s.$$

After instantaneous gas ionization followed by instantaneous production of a plasma with the electron temperature T_e and ion charge z, the characteristic relaxation time τ_{ai} of the fluctuations of size λ_a that remained in the gas before ionization is governed by the thermal energy per plasma ion and is equal in order of magnitude to $\tau_{ai} = \lambda_a/c_{pl} = 1/\sigma_a N_a c_{pl}$, where the mass-weighted average speed of sound in a plasma is $c_{pl} = [\gamma(T_a + zT_e)/(M + zm)]^{1/2}$. The duration τ_{las} of an ultraintense ultrashort laser pulse that ionizes the gas is so short that neither the atomic thermal motion nor the plasma oscillations can cause atomic density fluctuations in the gas to relax, because the condition

$$\tau_{\text{las}} \ll \tau_{ai} \ll \tau_a$$

is usually satisfied in experiments with ultrashort laser pulses [1]. Hence, during ultrafast ionization, the atomic density fluctuations in a gas evolve into ion density fluctuations. Since the electrons experience straight-line motion under the action of an external force (the electric field of laser radiation), they cannot screen the ion density fluctuations. Consequently, during ionization, the ion density fluctuations can increase the e–i collision frequency, provided that they occur on a spatial scale substantially longer than that of the space-charge density fluctuations (the Debye radius).

2.1. Dynamic Friction Force and Collisional Heating in the Straight-Line Motion Approximation

There exist systems with the Coulomb potential of interaction among the particles but without screening (e.g., systems of gravitating bodies and systems of immobile ions in semiconductors). For a system without screening, the problem of determining the collision frequency was studied by Kogan [12] in the straight-line motion approximation. He found that the Coulomb collision frequency for the particles moving along straight trajectories should be determined by taking the particle mean free path (the length of the straight portions of particle trajectories) as the maximum impact parameter. Accordingly, for a test particle moving at a constant speed along a straight trajectory among immobile charged particles, the dynamic friction force depends logarithmically on the time Δt that has passed since the test particle started moving [7, 12]:

$$F = \frac{4\pi z^2 e^4 N_i}{mV^2}\ln\frac{\Delta t}{\tau_{\min}}.$$

Here, the time $\tau_{\min}$ is, as usual, determined from the applicability condition of the perturbation theory. While the particle experiences straight-line motion under the action of an external force, the collision frequency is governed precisely by the straight portions of the particle trajectory, in which case Debye screening has no impact on the Coulomb forces, so that the Debye radius cannot serve as the maximum impact parameter. Consequently, with the particle motion in the strong field (1) taken into account, we determine the range of possible values of the impact parameter in terms of the straight portion of a particle trajectory and the squared electron oscillatory velocity averaged over the period of electron oscillations:

$$\rho_{\max} = 2r_E = 2eE_0/m\omega^2, \quad \rho_{\min} = 2ze^2/mV_E^2. \quad (10)$$

In this case, the Coulomb logarithm Λ_E depends only on the frequency of field (1) and its strength:

$$\Lambda_E = \ln\rho_{\max}/\rho_{\min} = \ln(eE_0^3/zm^2\omega^4). \quad (11)$$

The collisional electron heating power can be estimated as a product of the dynamic friction force with the electron velocity and density:

$$W = \frac{16z^2e^4N_eN_i}{mV_E}\ln\frac{eE_0^3}{zm^2\omega^4}. \quad (12)$$

Here, the friction force is calculated from the electron oscillatory velocity averaged over the half-period of the laser field: $\langle V\rangle = V_E/\sqrt{2}$.

2.2. Method of Molecular Dynamics [13]

The method of molecular dynamics (which will be referred to as the MD method) implies a numerical solution of the dynamic equations for a system of $n(1 + z)$ positively and negatively charged particles. In the proposed model, the particles are assumed to be inside a cube at the faces of which the periodic boundary conditions are imposed. The trajectories of n ions and nz electrons are calculated by solving Newton's equations of motion

$$d^2r_k/dt^2 = F_k/m_k, \quad F_k = \sum_{l\neq k}^{n(z+1)} f_{kl},$$
$$k = 1, 2, \ldots, n(z+1).$$

Here, $r_k(t)$ is the position vector of the kth particle with mass m_k and charge q_k. The Coulomb forces f_{kl} of the interaction between the particles that occur at distances smaller than r_0 from each other are assumed to correspond to those of the interaction between uniformly charged, completely interpenetrating spheres of diameter r_0 (the "Coulomb spheres"). Modifying the short-range Coulomb forces in such a manner removes the singularity of the Coulomb potential at infinitely close distances and reduces the equation stiffness caused by the short-range collisions. For the problems at hand, the MD method, which is often referred to as the "method based on *ab initio* principles," should incorporate additional parameters that affect the numerical results. These are the number of particles, $N_p = n(z + 1)$; the radius of Coulomb spheres, r_0; and numerical errors. Since the number of particles in the system to be simulated is relatively small, the way in which the boundary conditions are imposed is also of particular importance. A detailed discussion of these problems goes beyond the scope of our study, so we restrict ourselves to a brief analysis of the most important related physical topics (see also [14]).

Clearly, the applicability condition for the validity of our mathematical model is the smallness of r_0 in comparison with the mean interparticle distance:

$$r_0 \ll N^{-1/3}. \quad (13)$$

Condition (13) is sufficient for determining most plasma parameters. In order to take into account the contribution of short-range collisions between free particles in an ideal plasma, we must impose the condition

$$r_0 \ll \rho_\perp(V_T) = ze^2/mV_T^2.$$

Collisions in a strong laser field should be modeled under a far more stringent requirement:

$$r_0 \ll \rho_\perp(V_E) = ze^2/mV_E^2. \quad (14)$$

The number of particles in the system to be simulated should be such that the collision integral can be approximated in the desired fashion and the surface effects can be neglected. Imposing periodic boundary conditions markedly reduces the influence of the surface effect (or the effect of the finite volume of a calculation cell). The approximation of the collision integral requires that short-range collisions occur on time scales on which the electron temperature (and, accordingly, the electron velocity distribution function) changes insignificantly:

$$znV_E\Delta t \geq \frac{1}{N_i\rho_\perp^2(V_E)}, \quad (15)$$

$$W\Delta t \leq \frac{3}{2}N_eT_e. \quad (16)$$

In numerical simulations, conditions (14)–(16) are often difficult to satisfy, because the computations are very involved. However, we may only impose condition (13) and, for a comparison between the numerical and theoretical results, set $\rho_{\min} = r_0$ in equality (4) and $k_{\max} = 1/\rho_{\min} = 1/r_0$ in expression (5). Of course, the numerical results from MD calculations can only be compared with the results obtained by the kinetic models from which the quantum mechanics limit is eliminated. Additional simulations were carried out in order to determine how the parameters under investigation depend on the values of the quantities r_0 and N_p and to check both the calculation accuracy and the effect of numerical errors on the final results.

At the initial time, all particles are distributed uniformly inside a cubic cell and the electrons and ions fit the Maxwellian initial velocity distribution functions. The size of the cube is chosen so as to ensure the required plasma density. In a system without any correlation between particles in the initial state (the particles are randomly distributed in the cube), the internal energy tends to relax to the Debye energy, so that, on a time scale of about the time required for an electron to pass the mean interparticle distance, the mean electron kinetic energy (or, equivalently, the electron temperature) increases. In order to clarify how this effect influences the electron heating, both the temperature and the internal energy of the system were calculated in the absence of a laser pulse.

2.3. Results of MD Calculations

Simulations were performed for a helium plasma with $z = 2$ and $N_i = 3 \times 10^{19}$ cm^{-3}, the initial electron and ion temperatures being the same, $T_e = T_i = 5$ eV. For such a plasma, the coupling parameter is equal to $\Gamma = 0.3$. The intensity and wavelength of laser radiation, $I = 6 \times 10^{16}$ W/cm^2 and $\lambda_{\text{las}} = 0.248$ μm, were chosen so as to satisfy the conditions for the strong laser field approximation: $V_E/V_T = 7$ and $\omega/\omega_{pl} = 12$. Figures 1–4 illustrate the numerical and analytical time evolutions of the electron temperature and internal energy. The time is expressed in plasma periods, and the potential energy of Coulomb interactions in the system is normalized to the Debye interaction energy per unit volume [15], $E_{\text{cor}} = (\pi\delta)^{1/2}(z + 1)N_iT_e$. For the above plasma parameters, the Debye energy per particle is equal to $U_D = (\pi\delta)^{1/2}T_e \approx 1.2$ eV.

First, we consider the numerical results for a system containing Coulomb spheres of different radii: $r_0/N_i^{-1/3}$ = 0.5, 0.05, 0.005, and 0.0005. The radius $r_0 = 0.005 \cdot N_i^{-1/3}$ is equal to the minimum impact parameter $\rho_{\min} = 2ze^2/mV_E^2$, which is determined by the electron oscillatory velocity. These results are of interest not only from a methodological point of view (the determination of the optimum value of this important numerical parameter) but also from a physical standpoint, because they demonstrate the effect of short-range and long-range collisions on the electron heating rate. Figure 1 shows (a) the electron temperature and (b) the internal energy calculated for Coulomb spheres of different radii in the system under consideration. In the initial stage, the electron temperature somewhat increases because the initial coordinates of the electrons and ions are completely uncorrelated. The temperature acquired by the electrons coincides in order of magnitude with the Debye internal energy of 1.2 eV. For comparison, the

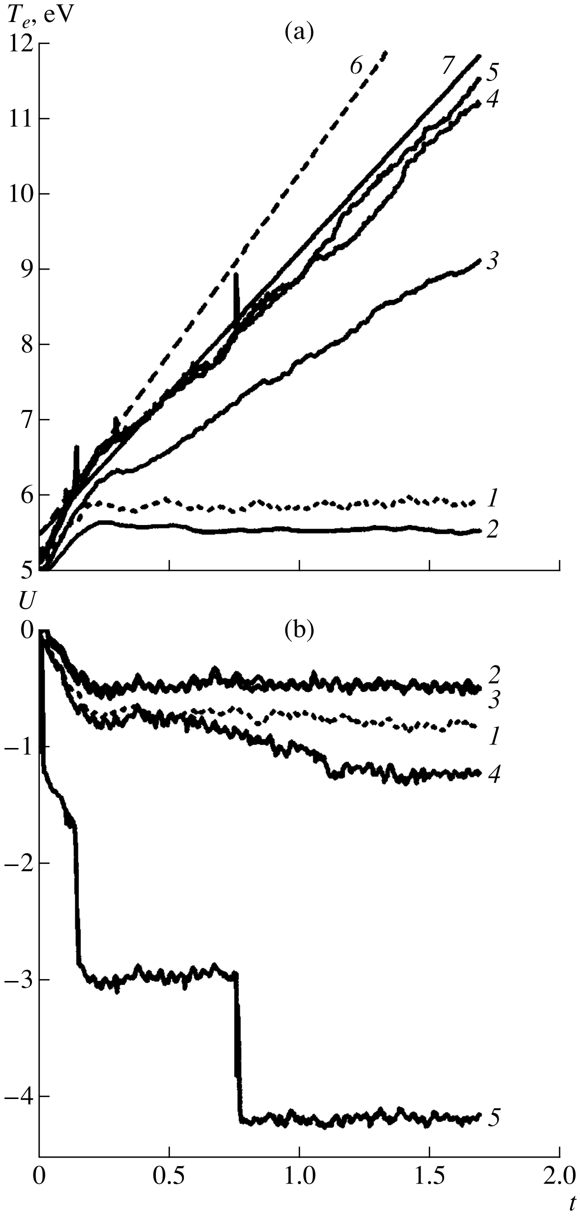

Fig. 1. Time evolutions of (a) the electron temperature and (b) the internal energy of the particles both computed using the MD method for Coulomb spheres of different radii. Curve *1* illustrates the relaxation of the initial state of a helium plasma with $z = 2$ and $\Gamma = 0.3$ in the absence of a laser pulse. Curves *2*, *3*, *4*, and *5* give the results of MD simulations for a system of Coulomb spheres with different radii ($r_0/N_i^{-1/3}$ = 0.5, 0.05, 0.005, and 0.0005, respectively) in a strong laser field. Curve *6* corresponds to the approximate formula (3) derived by Silin [2], and curve *7* is calculated by formula (12) proposed in this paper.

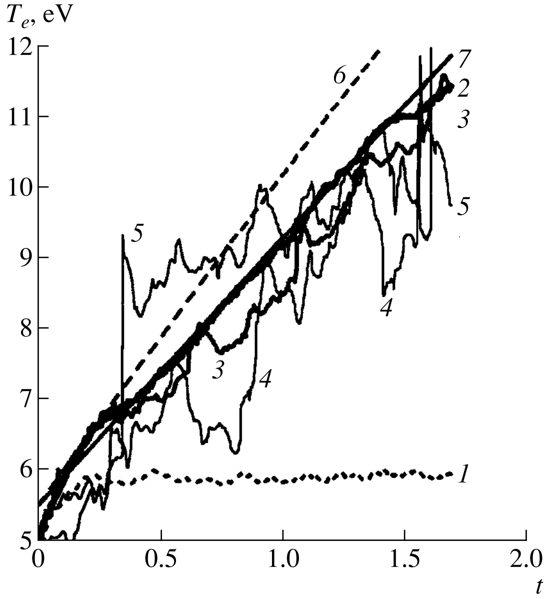

Fig. 2. Time evolutions of the electron temperature obtained from MD simulations for systems with different numbers of particles. Curves *1*, *2*, *3*, *4*, and *5* are for simulations with N_p = 3000, 3000, 300, 30, and 30, respectively. Curve *1* illustrates the relaxation of the initial state of a helium plasma with $z = 2$ and $\Gamma = 0.3$ in the absence of a laser pulse, curve *6* corresponds to the approximate formula (3) derived by Silin [2], and curve *7* is calculated by formula (12) proposed in this paper. Light curves *4* and *5* are computed for different initial coordinates and different velocities of the particles.

dashed curve gives the results from simulations of the relaxation of the same initial state of the system for $r_0 = 0.0005 \cdot N_i^{-1/3}$ but in the absence of a laser pulse. We can see that the stochastic electron heating differs only slightly between the calculations with the smallest radius of the Coulomb spheres, $r_0 = 0.0005 \cdot N_i^{-1/3}$, and with $r_0 = 0.005 \cdot N_i^{-1/3}$. However, the computations with the smallest radius reveal the effect of laser-driven recombination: we can see that the potential energy of the system increases significantly and the kinetic energy profile is peaked. For the same reason, the potential energy of the system also increases considerably, but without having a substantial effect on stochastic electron heating. The binding energy of an electron that has experienced a recombination event is converted into laser field energy.

Figure 2 illustrates the time evolution of the electron temperature calculated for systems with different numbers of particles. The radius of Coulomb spheres was set to be $r_0 = 0.005 \cdot N_i^{-1/3}$, which corresponds to $r_0 = \rho_\perp(V_E) = ze^2/mV_E^2$ (see above) and, according to the previous computations, is small enough for the stochastic heating rate to be calculated correctly. The results obtained show that several thousand particles in a system are quite sufficient to determine the parameters of collisional heating: curve *2*, calculated using the MD model for a system consisting of N_p = 3000 particles, essentially coincides with curve *7*, calculated from formula (12) proposed in this paper.

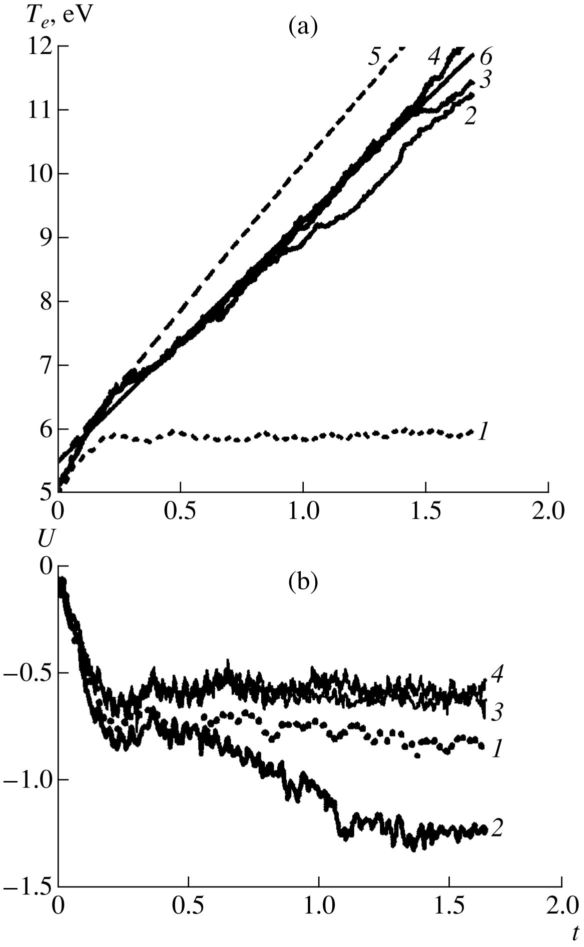

Fig. 3. Time evolutions of (a) the electron temperature and (b) the internal energy of a system of N_p = 3000 particles both computed using the MD method with different accuracies. Curve *5* corresponds to the approximate formula (3) derived by Silin [2], and curve *6* is calculated by formula (12) proposed in this paper.

Figure 3 presents the numerical results obtained for a system consisting of N_p = 3000 particles by integrating the equations of motion with different accuracies. Curves *2*, *3*, and *4* are labeled in order of increasing accuracy: the accuracy of curve *2* is significantly worse than the accuracy inherent in conventional calculations, the accuracy of curve *3* is consistent with the conventional integration steps (as is the case in Figs. 1 and 2), and curve *4* was calculated with increased accuracy. It is of interest to note that the rough computations give a larger absolute value of the potential energy of the system but a lower level of collisional heating; in other words, the stochastic recombination associated with computational errors does not increase the temperature to which the electrons are heated. A comparison between curve *3* (obtained with ordinary accuracy) and curve *4* (obtained with increased accuracy) also exhibits this tendency, which is, however, seen to be less pronounced.

The functional dependence of the collisional heating rate on the laser parameters was studied by performing simulations with different amplitudes r_E of the electron oscillations and with a fixed electron oscillatory velocity V_E. These simulations make it possible to reveal the dependence of the final results on the new parameter—the oscillation amplitude.

Figure 4 shows the representative time evolutions of (a) the electron temperature and (b) the internal energy of the particles calculated for the same oscillatory velocity V_E but for different laser frequencies ω (and, accordingly, for different laser intensities and oscillation amplitudes r_E). As in the previous figures, for comparison, we also plot curve *1*, which was obtained using the MD method and illustrates the relaxation of the initial state of the system with no laser pulse present. The results from MD simulations for laser intensities and wavelengths for which $V_E/V_T = 7$ and $r_E/N_i^{-1/3} = 0.2$, 1, and 4 (and, accordingly, $\omega/\omega_{pl} = 3$, 12, 60) are given by curves *2*, *3*, and *4*, respectively. Curve *3* corresponds to the case when the Debye radius is approximately equal to the oscillation amplitude, and the remaining two curves reflect the limiting (computationally possible) cases when the Debye radius is much larger (curve *2*) and much smaller (curve *4*) than the oscillation amplitude. Curve *5* corresponds to formula (3) derived by Silin [2], and curves *6*, *7*, and *8* correspond to the results obtained from formula (12). The results of MD calculations show the dependence of the heating rate on the oscillation amplitude for a fixed oscillatory velocity. Formulas (3) and (6) show no such behavior. The dependence given by formula (5) differs radically from that obtained using the MD method. The results from MD calculations agree well with the approximate formula (12) derived above under the assumption of straight-line electron motion. The results obtained from simulations with a very small oscillation amplitude (curves *4*, *8*) differ from the theoretical predictions most significantly; this circumstance can be attributed to the correlation effects (see below).

The results from simulations with a circularly polarized laser field (6) also agree well with the theoretical predictions from dependence (7) in which the Coulomb logarithm is taken in the form of (11) rather than (9). Hence, approximation (12) proposed in this paper applies to laser pulses with arbitrary polarization.

Under the conditions adopted in our simulations, approximation (12) does not differ substantially from the approximations derived previously, because the Coulomb logarithm and the logarithm of the ratio of the oscillatory velocity to the thermal velocity are both close to unity. However, for conditions prevailing in real experiments on the interaction of ultraintense laser pulses with gases, this difference can be far more pronounced. The table summarizes the characteristic values of the plasma parameters in experiments aimed at developing advanced recombination X-ray lasers and X-ray radiation sources [1]. For such devices, the table presents the conventional values of the Coulomb logarithm (9) and the values of the Coulomb logarithm that

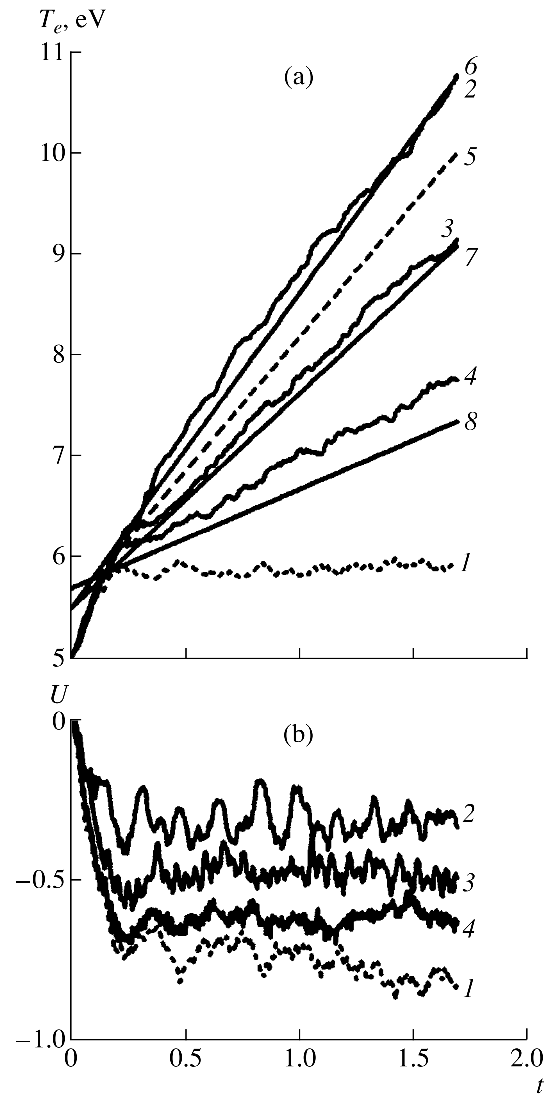

Fig. 4. Time evolutions of (a) the electron temperature and (b) the internal energy of a system. Curve *1* illustrates MD simulations of the relaxation of the initial state of the system in the absence of a laser pulse. Curves *2*, *3*, and *4* give the results of MD simulations for a system in laser fields with different frequencies $\omega/\omega_{pl} = 3$, 12, and 60, respectively (the laser intensity and wavelength are such that the ratio $V_E/V_T = 7$ was the same for all series of simulations). Curve *5* corresponds to Silin's approximate formula [2], which includes only one parameter V_E/V_T and does not differ between the three series of computations. Curves *6*, *7*, and *8* show the calculations by formula (12).

Table

z	T_e, eV	N_i, cm^{-3}	I, W/cm^2	λ_{las}, μm	Λ_z	Λ_E
2	20	3×10^{19}	6×10^{18}	1.05	4.9	14.6
2	50	3×10^{19}	6×10^{18}	1.05	5.4	14.6
2	100	3×10^{19}	6×10^{18}	1.05	6.4	14.6
2	7	10^{17}	10^{18}	0.248	5.8	9.3
2	10	10^{18}	10^{18}	0.248	5.2	9.3
2	30	10^{19}	10^{18}	0.248	5.7	9.3
3	100	10^{18}	10^{17}	0.5	7.6	9.1
10	200	3×10^{19}	10^{18}	0.248	5.5	9.3
10	400	3×10^{19}	10^{18}	0.248	6.5	9.3
10	800	3×10^{19}	10^{18}	0.248	7.6	9.3

Conventional values of the Coulomb logarithm Λ_z (9) and the values of the Coulomb logarithm Λ_E that are calculated from formula (12) proposed in this paper for fully ionized helium, lithium, and neon plasmas (the corresponding atomic numbers are given in the first column) and for different temperatures, densities, laser intensities, and laser wavelengths.

are calculated from formula (12) in the straight-line motion approximation.

3. CORRELATION EFFECTS

The trajectory of an electron oscillating in the laser field is periodically perturbed by remote ions, whose impact parameters change insignificantly due to their thermal motion over the laser field: $\rho \gg V_T/\omega_{\text{las}}$. In this case, the absolute value of the sum of the transverse perturbations of the electron momentum is equal to the sum of the absolute values of the increments in the momentum during one collision event, and, for these long-range collisions, the fraction of the energy of straight-line motion that is converted into thermal energy is proportional to the square of time (or, equivalently, to the number of oscillation periods of the electric field). For uncorrelated collisions, one must sum the squares of the increments in the momentum, in which case the fraction of kinetic energy that is dissipated in the system is linearly proportional to the time. It is of considerable interest to investigate the influence of this effect on the electron heating rate, because the nondiffusive nature of collisions can significantly enhance electron heating.

Recently, when considering the effect of the focusing of an oscillating electron by an immobile point charge with the Coulomb potential, Fraĭman *et al.* [16] predicted that the correlated nature of e–i collisions in a strong laser field should considerably increase the collisional electron heating rate. However, the results from the simulations described here do not confirm this prediction. Presumably, this is because of the collective nature of plasma oscillations (in [16], scattering by a single ion was considered). Let us give a better insight into the effect of the plasma microfields on the probability for an oscillating electron to be attracted by an ion and to experience a strong collision event as a result of which the electron oscillatory velocity becomes stochastic.

3.1. Free Fall of an Electron toward a Point Ion

We consider the problem of the free fall of an initially immobile electron that starts moving at the point $x_0 > 0$ toward an infinitely heavy ion at the point $x = 0$. The equation of electron motion has the form

$$\ddot{x} = -\frac{ze^2 x}{m|x|^3}.$$

Imposing the corresponding initial conditions on this equation, we arrive at the following parametric solution:

$$t(x) = \left(\frac{m}{2ze^2}\right)^{1/2} \int_x^{x_0} \left(\frac{1}{x'} - \frac{1}{x_0}\right)^{-1/2} dx'.$$

Consequently, the time required for an initially immobile electron that starts moving from the point at a distance x_0 from the ion to come into contact with this ion is equal to $t(0) = \frac{\pi}{2}\left(\frac{m x_0^3}{2ze^2}\right)^{1/2}$. In a system of uncorrelated particles, the distribution of the distances between an electron and the nearest ions is governed by the ion density and has the form

$$W(r) = 4\pi r^2 N_i \exp(-r^3/r_0^3),$$

where $r_0 = (3/4\pi N_i)^{1/3}$ is the radius of a spherical ion. If we neglect the forces exerted by the remaining ions on the electron, then the time required for the electron to fall on the nearest ion from the most probable distance $r = (2/3)^{1/3} r_0$ is exactly equal to one-quarter of the plasma oscillation period.

3.2. Applicability Condition of the Single-Ion Approximation

We consider the conditions under which the free fall of an electron on the nearest ion is perturbed by the microfields of the remaining ions such that the electron does not enter the sphere of radius $\rho_{\min} = 2ze^2/mV_E^2$, inside of which the electron oscillatory velocity changes strongly. Assuming that the mean force exerted by the remaining ions on the electron is about the Holtsmark force $F_H = ze^2N_i^{2/3}$ and estimating the time required for the electron to fall on the nearest ion as one-quarter of the plasma oscillation period τ_L, we obtain $F_H\tau_L^2/32m \gg \rho_{\min}$. Combining this inequality with the above expression for the minimum impact parameter yields the condition

$$\frac{1}{2}mV_E^2 \gg \frac{16}{\pi}ze^2N_i^{1/3}. \qquad (17)$$

This condition for the decorrelation of short-range collisions by plasma microfields in a strong ($V_E \gg V_T = \sqrt{T/m}$) laser field is satisfied for an ideal plasma. In fact, condition (17) coincides with the condition that the laser field be strong and holds in all actual situations. Condition (17) also serves as an estimate for the effect of plasma microfields and quite satisfactorily explains why the MD simulations revealed no significant increase in the electron heating rate due to the processes considered in [16]. Note also that the single-ion approximation was also used by Shvets and Fish [17], who, however, took into account only weak collisions. For a rarefied plasma, in which, according to [16], the above effects are easier to observe, condition (17) implies that, in a strong laser field, the plasma microfields have a stronger impact on collisions. However, we emphasize that condition (17) merely indicates that the decorrelation of collisions due to the ion microfields should be taken into account and gives no information about the influence of the microfields on the collisional heating rate.

3.3. Truncation of Strong Collisions in a Small-Size Plasma

Usually, ultraintense laser pulses can be generated not only by shortening the temporal profile of the laser field but also by focusing laser radiation into a very small spot (several microns in diameter). Such a small focal spot of a strong laser field results in the following interesting effect of truncation of strong collisions.

An electron that has experienced a short-range collision with an ion and has acquired a sufficiently large transverse (with respect to the laser field) velocity can leave the small focal region, in which case a thermal electron from the surrounding plasma should inevitably enter this region. Consequently, in the small focal region, the hot electrons (and, accordingly, their strong collisions with ions) do not affect the collisional plasma heating rate. For this reason, the collisional heating should be analyzed without allowance for the range of impact parameters such that the distance on which the hot electrons are decelerated by the thermal electrons (recall that, in collisions with ions, the electron energy changes only slightly) is larger than the diameter of the spot into which laser radiation is focused.

4. CONCLUSION

We have shown that the gas density fluctuations and the periodic (nondiffusive) nature of collisions of an electron moving in a strong laser field with the ions change the collision-related parameters of a plasma created in the interaction of an ultraintense ultrashort laser pulse with a gas.

The approximate formula derived for the collisional electron heating rate agrees well with the results from MD simulations. The new upper limit at which the Coulomb logarithm is proposed to be truncated—the amplitude of electron oscillations in a strong laser field—leads to a new functional dependence of the collisional heating rate on the laser field parameters. The proposed approximate formula applies to laser pulses with arbitrary polarization and does not contain the double logarithm that enters the corresponding formula derived by V.P. Silin [2] for a linearly polarized laser pulse.

ACKNOWLEDGMENTS

I am grateful to V.I. Kogan for bringing paper [12] to my attention. I would like to thank S.V. Bulanov, A.A. Rukhadze, V.P. Silin, and V.T. Tikhonchuk for stimulating discussions and to G.M. Fraĭman for a detailed discussion of the results obtained in papers [16, 18].

REFERENCES

1. N. H. Burnet and G. D. Enright, IEEE J. Quantum Electron. **26**, 1797 (1990); S. C. Rae and K. Burnett, Phys. Rev. A **46**, 2077 (1992); P. Pulsifer, J. P. Apruzese, J. Davis, and P. Kepple, Phys. Rev. A **49**, 2958 (1994); D. Vick, C. E. Capjack, V. Tikhonchuk, and W. Rozmus, Comments. Plasma Phys. Controll. Fusion **17**, 99 (1996).
2. V. P. Silin, Zh. Éksp. Teor. Fiz. **47**, 2254 (1964) [Sov. Phys. JETP **20**, 1510 (1964)].
3. R. D. Jones and K. Lee, Phys. Fluids **25**, 2307 (1982).
4. L. Shlessinger and J. Wright, Phys. Rev. A **20** (5), 1934 (1979).
5. B. A. Trubnikov, in *Reviews of Plasma Physics*, Ed. by M. A. Leontovich (Gosatomizdat, Moscow, 1963; Consultants Bureau, New York, 1963), Vol. 1.
6. E. M. Lifshitz and L. P. Pitaevskiĭ, *Physical Kinetics* (Nauka, Moscow, 1979; Pergamon, Oxford, 1981).

7. D. V. Sivukhin, in *Reviews of Plasma Physics*, Ed. by M. A. Leontovich (Atomizdat, Moscow, 1964; Consultants Bureau, New York, 1968), Vol. 4.
8. S. A. Maĭorov, Kratk. Soobshch. Fiz., Nos. 9–10, 99 (1997).
9. S. I. Braginskii, in *Reviews of Plasma Physics*, Ed. by M. A. Leontovich (Gosatomizdat, Moscow, 1963; Consultants Bureau, New York, 1963), Vol. 1.
10. L. Spitzer, *Physics of Fully Ionized Gases* (Interscience, New York, 1956; Inostrannaya Literatura, Moscow, 1957).
11. S. I. Yakovlenko, Kratk. Soobshch. Fiz., No. 7, 30 (1998).
12. V. I. Kogan, Dokl. Akad. Nauk SSSR **135**, 1374 (1960) [Sov. Phys. Dokl. **5**, 1316 (1961)].
13. R. Hockney and J. Eastwood, *Computer Simulation Using Particles* (McGraw-Hill, New York, 1984; Mir, Moscow, 1987); Ch. K. Birdsall and A. B. Langdon, *Plasma Physics Via Computer Simulations* (McGraw-Hill, New-York, 1985; Énergoatomizdat, Moscow, 1989); A. A. Valuev, G. É. Norman, and V. Yu. Podlipchuk, in *Mathematical Simulation*, Ed. by A. A. Samarskiĭ and N. N. Kalitkin (Nauka, Moscow, 1989), p. 5.
14. S. A. Maĭorov, Kratk. Soobshch. Fiz., No. 1, 33 (1999).
15. L. D. Landau and E. M. Lifshitz, *Statistical Physics* (Nauka, Moscow, 1976; Pergamon, Oxford, 1980).
16. G. M. Fraĭman, A. A. Balakin, and V. A. Mironov, in *Proceedings of the 26th Zvenigorod Conference on Plasma Physics and Controlled Fusion, Zvenigorod, 1999*, p. 234; Zh. Éksp. Teor. Fiz. **115**, 463 (1999) [JETP **88**, 254 (1999)]; Phys. Rev. Lett. **82**, 319 (1999).
17. G. Shvets and H. J. Fish, Phys. Plasmas **4**, 428 (1997).
18. S. A. Maĭorov, in *Proceedings of the 26th Zvenigorod Conference on Plasma Physics and Controlled Fusion, Zvenigorod, 1999,* p. 127; Kratk. Soobshch. Fiz., No. 7, 25 (1999).

Translated by G.V. Shepekina

Plasma Physics Reports, Vol. 27, No. 4, 2001, pp. 303–314. From Fizika Plazmy, Vol. 27, No. 4, 2001, pp. 321–333.
Original English Text Copyright © 2001 by Zhang, Sokolov, Sakai.

Oscillations, Shocks, and Fine Wave Structures Arising during the Coalescence of Two Force-Free Current Loops

H.-M. Zhang*, I. V. Sokolov, and J.-I. Sakai***

**Toyama University, 3190, Gofuku, Toyama, 930-8555 Japan*
***Institute of General Physics, ul. Vavilova 38, Moscow, 117942 Russia*

Received August 23, 2000; in final form, October 10, 2000

Abstract—Two-dimensional numerical simulations of the magnetic reconnection of two parallel force-free current loops are carried out using a high-resolution MHD code in which an *artificial wind* scheme is employed. Two typical cases (namely, co-helicity and counter-helicity reconnection) are investigated. The simulation results show that co-helicity reconnection involves only the reconnection of the poloidal component of the magnetic field, while counter-helicity reconnection involves the reconnection of both the poloidal and axial components of the magnetic field. Therefore, counter-helicity reconnection is much more complicated and violent as compared to co-helicity reconnection. In both cases, jetlike flows are generated. Counter-helicity reconnection is accompanied by oscillations of both the axial magnetic field and the axial component of the velocity. Due to these oscillations, quasi-steady models of a current sheet appear to be inapplicable, because the current sheet structure also changes. The complicated and unsteady structure of the current distribution shows that magnetic reconnection occurs not only in the central sheet between two loops in the earlier stage of the process, but also inside each loop in later stages. Rather complicated flows and waves with fine structures are also generated during reconnection. Some of the waves appear to be shock waves. *© 2001 MAIK "Nauka/Interperiodica".*

1. INTRODUCTION

Magnetic reconnection is the topological change of a magnetic configuration involving the breaking and rejoining of magnetic field lines [1–4]. A local reconnection process often causes macroscopic changes of the magnetic structure [5]. Magnetic reconnection plays an important role in the dynamics of both space and laboratory plasmas. It can also result in releasing the energy stored in the magnetic field and its transformation into kinetic and thermal energies of the plasma in solar flares, auroras, and laboratory plasmas [6–9].

Depending on both the presence or absence of the axial magnetic field and its symmetry or antisymmetry, magnetic reconnection can be classified into three types: null-helicity, co-helicity, and counter-helicity reconnection [10, 11]. Recent experimental studies revealed that the three types of magnetic reconnection differ significantly [12, 13].

To explain the mechanism for explosive solar flares, a loop–loop coalescence model was proposed 40 years ago by Gold and Hoyle [14]. Since their pioneering work, loop coalescence has been thoroughly studied by many authors [15–18]. It is generally believed that the current loop reconnection provides keys for understanding many of the characteristic features of solar flares, such as their short duration, fast plasma heating, high-energy particle acceleration, shock wave formation, variations in the intensity of electromagnetic emissions, as well as the typical evolution of microwave images obtained by satellite observations during flares [19–22].

Computer simulations play an important role in plasma physics and astrophysics. Two- and three-dimensional MHD simulations of the reconnection of two current loops were performed in [23–26]. The results of these simulations allow an understanding of the main physical processes accompanying the loop coalescence. However, due to the low spatial resolution and doubtful nonlinear stability of the codes, these simulations were not able to reveal as many useful results as expected. In order to improve both the resolution and stability of the numerical scheme, a new way for constructing efficient nonoscillatory shock-capturing numerical schemes was recently proposed for hyperbolic systems of the conservation laws, namely, the artificial wind (AW) scheme [27–29]. The basic idea of the AW scheme is to solve the hydrodynamic (or MHD) equations in different steadily moving frames of reference chosen in such a way that the flow is supersonic there, thus resulting in simple upwind formulas for fluxes across control volume faces. This scheme has the main advantages of the total variation diminishing (TVD) and Godunov-type schemes (such as high accuracy and quality of the results) and is free of the main drawbacks of these schemes (such as high complexity and high CPU consumption).

In this paper, a two-dimensional high-resolution MHD code based on the AW scheme is applied to simulate the magnetic reconnection of two parallel force-free loops. The term "loop" or "flux tube" implies a cylindrical magnetic configuration that has typical features of both the Z-pinch and Θ-pinch, because both the axial and poloidal components of the electric current and magnetic field are not equal to zero. As a result, the magnetic field lines and electric current lines have a helical form and, for a force-free configuration, the electric current flows exactly along the magnetic field lines. The theory of such equilibrium configurations is well known [30].

When two force-free configurations are placed not far apart, they interact through the magnetic field, so that this configuration is not in equilibrium. The superposition of two helical magnetic field lines of the two loops gives a null line at some place where all (or some) of the components of the magnetic field vanish. Depending on the signs of the helicities in the loops, three types of current loop reconnection (null-helicity, co-helicity, and counter-helicity) are possible; two of them (namely, co-helicity and counter-helicity reconnections) are investigated in this paper. It should also be mentioned that the local reconnection near null-lines and null-points of the magnetic field involving all three vector components is rather interesting in itself (see, e.g., [31]); however, a detailed analysis of this phenomenon is beyond the scope of this paper.

Simulations demonstrate that counter-helicity reconnection is much more complicated and violent than co-helicity reconnection. This results from the complicated dynamics of the axial-component reconnection. Some of the phenomena typical of this dynamics were considered earlier by different authors mostly for application in toroidal plasma devices [32, 33].

The increased resolution of the present simulations revealed some new effects that were previously concealed or suppressed by numerical dissipation. The axial components of both the magnetic field and velocity suffer weakly damping oscillations. These oscillations (whose frequency varies in space) result in the oscillating structure of the magnetic field in the domain where reconnection takes place. Waves are emitted from this domain, some of which are shock waves. The main purpose of this paper is to investigate these processes in detail, because, for studying charged particle acceleration, hard X-ray emission, and other effects accompanying reconnection, the structure of the electromagnetic fields and the generation of shock waves are of crucial importance.

The paper is organized as follows. In Section 2, the simulation model and numerical scheme are described. The numerical results are presented in Section 3. Section 4 gives the discussion and summary.

2. SIMULATION MODEL AND NUMERICAL SCHEME

In this section, the simulation model, the initial and boundary conditions, and the numerical scheme are described.

A 2D MHD code using the recently proposed AW numerical scheme with splitting over the spatial coordinates (by the Strang scheme) is employed. The AW scheme is based on the fact that the fundamental physical invariance (Galilean or, more generally, Lorentz invariance) allows one to solve the governing equations in different steadily moving frames. The principle of the AW scheme is that the frame of reference may be chosen in such a way that the flow under simulation is supersonic there. The problem of upwinding becomes trivial, and considerably facilitated versions of discontinuity-capturing schemes may be employed. An extra velocity (artificial wind) is added to the velocity of the flow under simulation when the system of coordinates is changed. The AW approach allows one to simplify existing schemes and to obtain new modifications (see [27] for details]). Test ideal MHD simulations show that the AW schemes capture all the structures of MHD waves correctly without producing noticeable oscillations [28, 29].

The following conservative MHD equations are numerically integrated:

$$\frac{\partial \rho}{\partial t} + \frac{\partial}{\partial x_i}(\rho V_i) = 0, \qquad (1)$$

$$\frac{\partial \rho V_i}{\partial t} + \frac{\partial}{\partial x_j}[\rho V_i V_j + (p + B^2)\delta_{ij} - 2B_i B_j] = 0, \qquad (2)$$

$$\frac{\partial B_i}{\partial t} + \frac{\partial}{\partial x_j}(V_j B_i - V_i B_j) = \frac{1}{R_m}\frac{\partial^2 B_i}{\partial x_j^2}, \qquad (3)$$

$$\frac{\partial}{\partial t}\left(\frac{\rho V^2}{2} + \frac{p}{\gamma - 1} + B^2\right) + \frac{\partial}{\partial x_i}\left[V_i\left(\frac{\rho V^2}{2} + \frac{\gamma p}{\gamma - 1} + 2B^2\right) - 2B_i B_j V_j + q_i\right] = 0, \qquad (4)$$

where ρ, V_i, p, and B_i are the density, velocity, pressure, and magnetic field, respectively; γ is the adiabatic constant, which is taken to be $\gamma = 5/3$; R_m is the magnetic Reynolds number; δ_{ij} is a unity tensor; and q_i is the dissipative energy flux. The density, pressure, velocity, and magnetic field are normalized to ρ_0, p_0, $\sqrt{p_0/\rho_0}$, and $B_0 = \sqrt{8\pi p_0}$, respectively. The length is normalized to the loop radius a.

For resistive magnetohydrodynamics with a large but finite value of R_m, the energy equation (4) should be obtained as a sum of the equation for the plasma energy, in which the Joule heating term is represented in the form $(c^2[\nabla \times \mathbf{B}]^2/(4\pi)^2\sigma)$, and the equation for the magnetic energy, which is given by Eq. (3) multiplied by the vector $B_i/(4\pi)$ (here, all of the variables are not normalized and σ is the conductivity). The dissipation of the magnetic field energy is determined by the term $(c^2/(4\pi)^2\sigma)B_i\Delta B_i$. Hence, in Eq. (4) for the total energy, Joule heating is balanced by the magnetic energy dissipation:

$$\begin{aligned}&\frac{c^2}{(4\pi)^2\sigma}[B_i\Delta B_i + [\nabla\times\mathbf{B}]^2]\\ &= \frac{c^2}{(4\pi)^2\sigma}\mathrm{div}[\mathbf{B}\times[\nabla\times\mathbf{B}]].\end{aligned} \tag{5}$$

Therefore, resistive dissipation in the energy equation (4) is present only in the form of an additional dissipative energy flux, which, in normalized variables, may be written as $q_i^{(m)} = R_m^{-1}\partial/\partial x_j(2B_iB_j - B^2\delta_{ij})$. The dissipative energy flux due to heat transfer may also be taken into account in the usual form: $q_i^{(h)} = -\lambda_{ij}\partial/\partial x_j(p/\rho)$. For the sake of simplicity, here we fully neglect the nondiagonal part of the dissipative energy transfer tensor and substitute all the tensors in q_i for those proportional to the unity tensor: $B_iB_j = B^2\delta_{ij}/3$ and $\lambda_{ij} = \lambda_{ll}\delta_{ij}/3$. Numerical simulations show that the influence of the dissipative energy flux is insignificant; hence, we do not try to take it into account more carefully. Finally, we admit the dissipative hydrodynamic flux in the form

$$q_i = \frac{\partial}{\partial x_i}\left(-\frac{B^2}{3R_m} - \lambda\frac{p}{\rho}\right). \tag{6}$$

The magnetic Reynolds number $R_m = 1.3\times10^3$ and two values of the heat transfer constant $\lambda = 0$ and $\lambda = 2.5\times10^{-4}$ were used in simulations.

The motion was assumed to depend on two spatial coordinates x and y. However, all three components of the velocity and magnetic field were involved in the simulation. A uniform 1000 × 1000 grid in the 2D computation domain with a spatial size of $8a\times8a$ was used. In all directions, nonreflective boundary conditions were imposed.

These boundary conditions imply that any perturbation arriving at the boundary from the simulation domain passes freely through the boundary; i.e., they imply that, outside of the computation domain, there is a plasma in which the magnetic field continuously tends to zero at large distances. A test computation carried out with the boundaries being displaced outward (on a 1400 × 1400 grid) showed that the boundaries do not influence significantly the processes under consideration for the chosen simulation time. On the other hand, the boundary conditions undoubtedly affect other, less significant details. For example, the logarithmic divergence of the system energy at large distances and the ability for the outer plasma to flow freely into the computation domain result in the slow growth of the total energy in the computation domain.

A single steady-state current loop satisfies the equilibrium condition if the poloidal and axial magnetic fields are chosen in the form

$$B_\theta = \frac{B_{m0}r/a}{1+(r/a)^2}, \tag{7}$$

$$B_z = \frac{B_{z0}}{1+(r/a)^2}, \tag{8}$$

$$p = \mathrm{const}, \quad \rho = \mathrm{const}. \tag{9}$$

An equilibrium current loop is force-free if $B_{m0} = B_{zm}$ [13].

As the initial condition for the magnetic field, we take the sum of two distributions (7) and (8) for two current loops. The loop axes are parallel to the z-axis and are located at $x_1 = 4.0$ and $y_1 = 2.5$ for the first loop and at $x_2 = 4.0$ and $y_2 = 5.5$ for the second loop. The initial amplitudes of the magnetic field components are $B_{m0} = B_{zm} = 3.0$. The initial pressure and density are $\rho = 1.0$ and $p = 1.0$ throughout the computation domain.

Two runs were carried out for co-helicity and counter-helicity reconnection or, in other words, for partial and complete (including the axial component) reconnection [23], respectively. In the co-helicity $B_{z0} = |B_{z0}|$ case (run A), the axial magnetic fields of both loops are directed along the z-axis ($B_{z0} = \pm|B_{z0}|$), while in the counter-helicity case (run B), the axial magnetic fields of the left and right loop are directed along and opposite the z-axis, respectively ($B_{z0} = |B_{z0}|$). Here, the results of run B are mainly described.

The maximum value of the Alfvén velocity in the initial state is $V_A = 4.24$. The time is normalized to the characteristic Alfvén time $\tau_A = a/V_A$. The typical value of plasma beta ($\beta = pB^{-2}$) is $\beta \sim 0.1$ and $\beta \sim 2.0$ for the loop and ambient medium, respectively.

3. SIMULATION RESULTS

Two parallel loops with antiparallel axial currents repel each other and usually do not reconnect unless they initially move toward each other with a sufficiently high relative velocity. Therefore, we will only consider the case of parallel axial currents.

The main physical picture of the reconnection of two parallel loops with parallel axial currents is known to be as follows. Each of the two current loops is in equilibrium as long as the distance between them is much greater than loop radius a. As the loops approach each other, they are no longer in equilibrium and the whole nonequilibrium system tends to a new equilibrium state. Due to attraction, the two current loops begin to move and approach each other. Then, they meet, merge, and form a new single loop. Simulations were performed to investigate the phenomena accompanying this reconnection process.

First of all, the simulations confirm most of the well-known results, such as the generation of a reverse

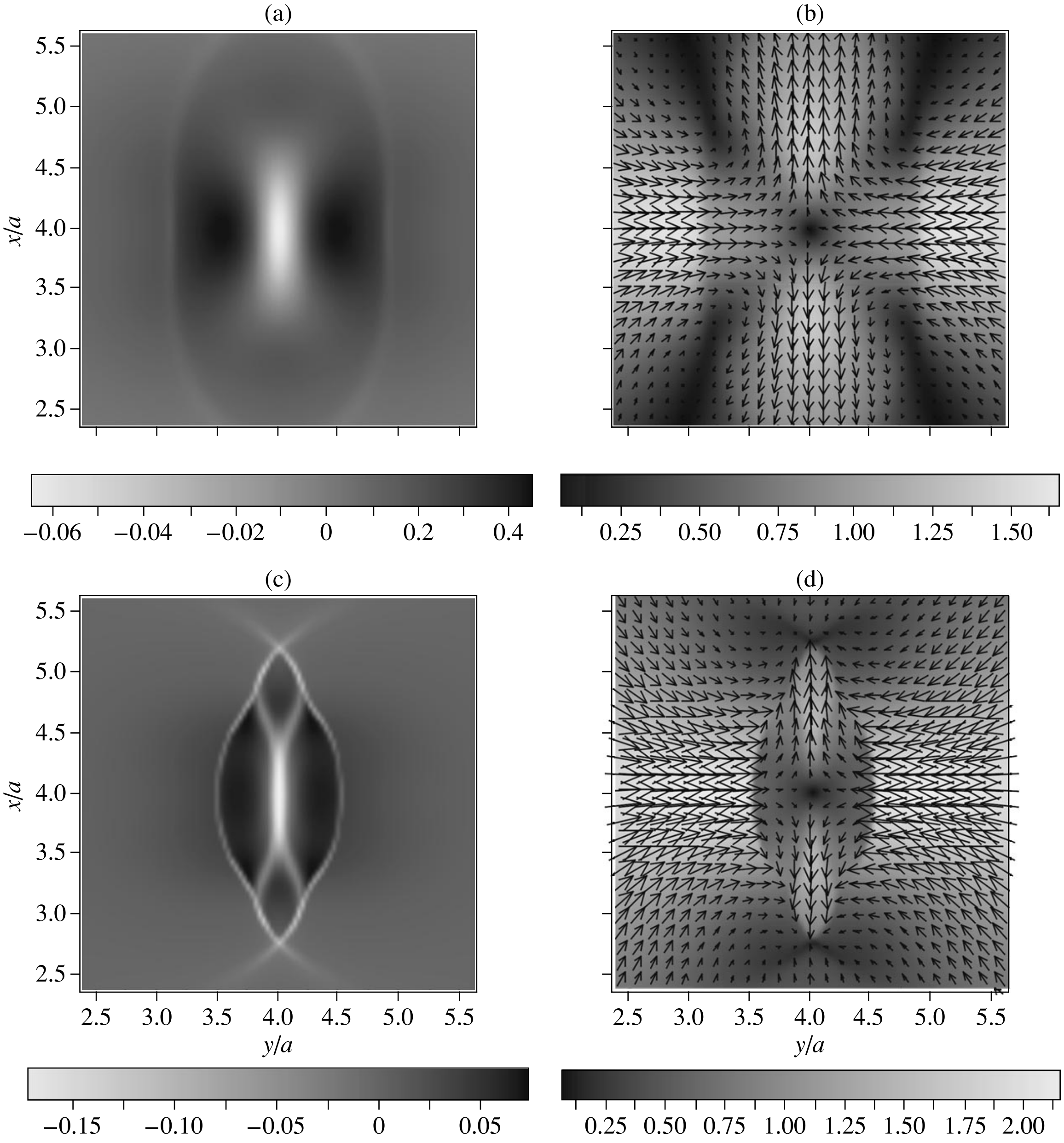

Fig. 1. (a, c) Reverse induced current and (b, d) jetlike flows at the time $t = 2.53\tau_A$ (only the central region $2.25a \le x \le 5.75a$, $2.25a \le y \le 5.75a$ is shown) for (a, b) run A and (c, d) run B. The shade of gray shows the value of the poloidal velocity $(V_x^2 + V_y^2)^{1/2}$; the vectors show the velocity vectors.

current sheet in the region between two loops and an increase in pressure, density, and temperature in the reconnection region. Here, we only focus on the simulation results that appear to be new and interesting.

3.1. Reconnection of the Poloidal Magnetic Field

According to Eqs. (7) and (8), the magnetic field of the current loop has both poloidal and axial components (B_θ and B_z). For convenience of analysis and description, we will discuss the poloidal component reconnection and the axial component reconnection separately. Generally, the simulation results can be described as follows.

In the early stage, when the two loops start approaching each other, the reconnection of the poloidal magnetic field is important. After the loops have met, the reconnection of the poloidal magnetic field proceeds slowly with a typical time much greater than the characteristic Alfvén time. This means that, in the co-helicity reconnection case, only the poloidal field of the two loops undergoes slow reconnection. In contrast, in the case of counter-helicity, the reconnection of the axial magnetic field takes place, so that fast oscillations arise. The oscillation period is governed by the MHD processes and is comparable with the characteristic Alfvén time.

Figure 1 shows the distributions of the induced current j_z and velocity $V_{x,y}$ in the central region of the computation domain ($2.25a \le x \le 5.75a$, $2.25a \le y \le 5.75a$) at the early time $t = 2.53\tau_A$ for the two runs. It is seen that, for both cases, the reverse current is induced in the central region; however, the patterns are different (Figs. 1a, 1c).

Counter-helicity reconnection induces a thinner current sheet. In Fig. 1c, two shock waves are also seen. Figures 1b and 1d show that, in both cases, jetlike flows are formed in the x and $-x$ directions; however, the patterns of these flows in runs A and B are different. Simulations show that the jetlike flows do not propagate very far from the regions where they are generated.

The poloidal field reconnection is illustrated in Fig. 2. As the two current loops approach each other, the original magnetic field lines break and then rejoin to form new ones, the reconnected magnetic field lines being strongly bent. Due to magnetic stress, the magnetic field lines tend to shorten and drive the surrounding plasma to move outward in the x and $-x$ directions. Thus, two jetlike flows are formed. After the magnetic field lines have reached their balance point, the moving plasma turns to drive and stretch the magnetic field lines, which leads to plasma deceleration. Thus, the stress of the frozen magnetic field causes the formation of jetlike flows and, at the same time, prevents them from propagating too far out. As a result, the high pressure and density regions are formed in the vicinity of the stagnation points (see Fig. 8 below).

3.2. Counter-helicity Reconnection and Oscillations of B_z and V_z

A remarkable phenomenon is the oscillations of the axial component of the magnetic field B_z and velocity V_z in the counter-helicity run B.

The evolution of the distributions of the axial magnetic field B_z and the axial velocity V_z in the central region of the computation domain ($2.25a \le x \le 5.75a$, $2.25a \le y \le 5.75a$) are shown in Figs. 3 and 4, respectively. As is seen in Fig. 3a, at the early time $t = 2.53\tau_A$, two loops with antiparallel axial magnetic fields approach each other and move toward the central region. The magnetic field B_z of the left loop is still directed along the z-axis, while in the right loop, it is oppositely directed. At the time $t = 6.78\tau_A$ (Fig. 3b), the magnetic field inside the loops does not change direction, while outside of the loops, regions with the reversed magnetic field B_z appear. Figure 3c shows the distribution of the axial magnetic field at time $t = 11.02\tau_A$. It is seen that the axial magnetic fields inside the loops have changed signs as compared to Fig. 3a. Then, at the time $t = 13.57\tau_A$ (Fig. 1d), the distribution of the axial magnetic field becomes similar to that at $t = 6.78\tau_A$ (Fig. 1b), but the magnetic field direction both inside and outside of the loops is reversed. Thus, the oscillations of the axial magnetic field are generated during the counter-helicity reconnection of two loops.

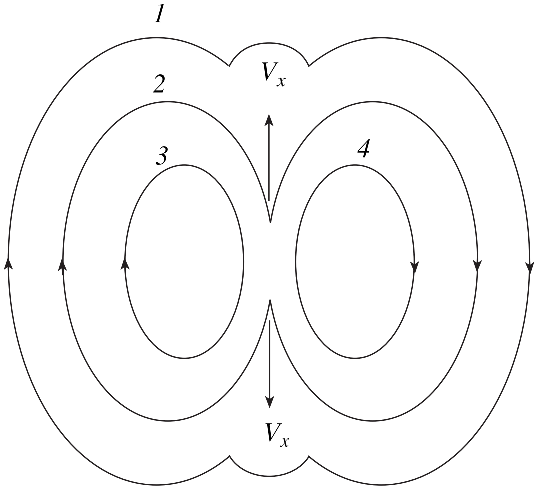

Fig. 2. Schematic of the poloidal magnetic field reconnection and generation of jetlike flows.

The evolution of the axial velocity V_z is shown in Fig. 4. It is seen that the evolution of V_z is similar to that of B_z. What is different is that the regions with opposite signs of V_z occur above and below the center, whereas the regions with opposite signs of B_z occur to the left and right of the center.

The oscillations of B_z and V_z are correlated to each other. In these oscillations, the magnetic energy B_z^2 is converted into plasma kinetic energy $(1/2)\rho V_z^2$ and vice versa. The time variations in the energies $E_{BZ} = \sum_{i,j} B_z^2$ and $E_{VZ} = (1/2)\sum_{i,j}\rho V_z^2$, where $\sum_{i,j}$ is the sum over all the cells within the computation domain, are displayed in Fig. 5. The profiles in Fig. 5 clearly show the interchange between E_{BZ} and E_{VZ}. The oscillation period is about $6.5\tau_A$. In co-helicity reconnection (run A), such oscillations are absent.

The mechanism for the excitation of oscillations during reconnection can be explained as follows. As two current loops approach each other, the B_z reconnection occurs (see Fig. 6). After reconnection, the magnetic field lines appear to be strongly bent. Due to magnetic stress, the magnetic field lines tend to shorten and drive the surrounding plasma to move along the z-axis. After the magnetic field lines have reached their balance point, the moving plasma turns to drive and stretch

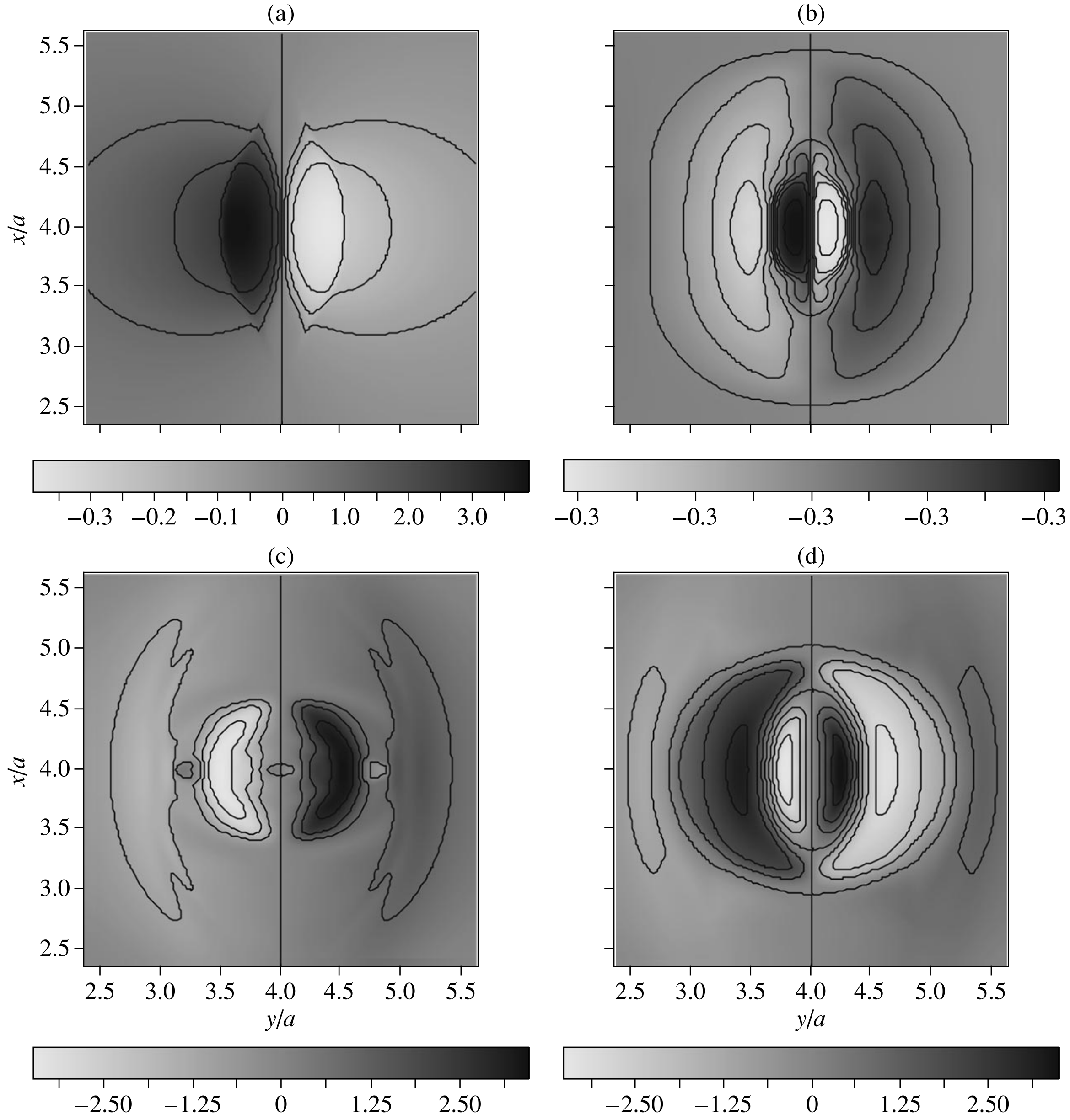

Fig. 3. Time history of the axial magnetic field distribution for run B: (a) $t = 2.53\tau_A$, (b) $t = 6.78\tau_A$, (c) $t = 11.02\tau_A$, and (d) $t = 13.57\tau_A$.

the magnetic field lines, which leads to plasma deceleration. Thus, the interaction between the magnetic field and surrounding plasma leads to oscillations.

In a quite analogous manner, the mechanism for the excitation of toroidal field oscillations accompanying the counter-helicity reconnection of two spheromaks is explained in [32, 33]. Here, we also demonstrate that, inside and outside of the loops, the oscillation periods differ strongly. The helical magnetic field lines far from the loop axis meet each other and reconnect earlier than those close to the axis (see Fig. 2). It is seen from Fig. 3 that the oscillations outside of the loop arise earlier than those inside it.

The poloidal field reconnection leads to the formation of a current sheet. Simulations show that the axial field reconnection can also induce the poloidal current. Figure 7 shows the distributions of the induced current j_x at the times $t = 2.53\tau_A$ and $t = 13.57\tau_A$. It is worth noting that, due to the dependence of the oscillation period on the magnetic field strength and, hence, on the distance from the null-line ($x = 4.0a$, $y = 4.0a$), the pattern of the axial magnetic field may split into several (more than two) domains with different polarities (Fig. 3d). In

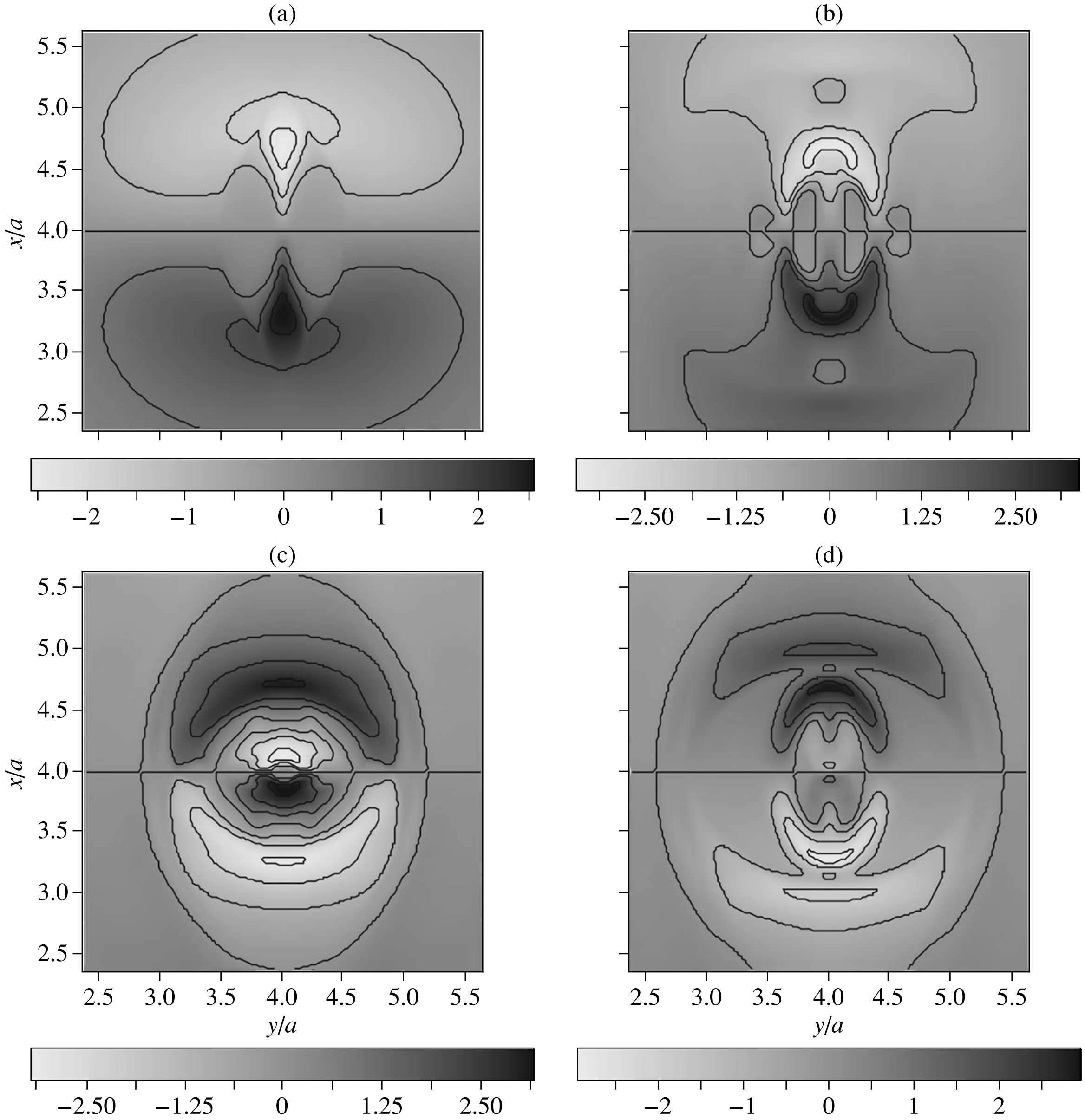

Fig. 4. Time history of the axial velocity distribution for run B: (a) $t = 2.53\tau_A$, (b) $t = 6.78\tau_A$, (c) $t = 11.02\tau_A$, and (d) $t = 13.57\tau_A$.

each pair of antiparallel magnetic field domains, magnetic reconnection can occur (Figs. 3d, 7b). Therefore, the localization of the poloidal electric current does not generally coincide with the axial current sheet. This question will be discussed in more detail in a subsequent publication.

3.3. *Shock Waves and the Fine Structure of the Plasma Flow*

Figures 8 and 9 compare runs A and B. Figure 8 shows the pressure and temperature ($T \propto p/\rho$) distribution in runs A and B at the time $t = 6.78\tau_A$. The maximum values of the pressure and temperature for counter-helicity reconnection (run B) are as high as 26.8 and 10.1, respectively, while for co-helicity reconnection (run A), these values are 3.9 and 2.76, respectively. On the other hand, the reconnection region in run B is more compact than that in run A.

Figure 9 shows the fine structure of the plasma flow and density in the central region at the time $t = 12.21\tau_A$. The complicated pattern of the velocity field distribution, which involves symmetric vortical structures, shows that fairly active processes occur in the reconnection region.

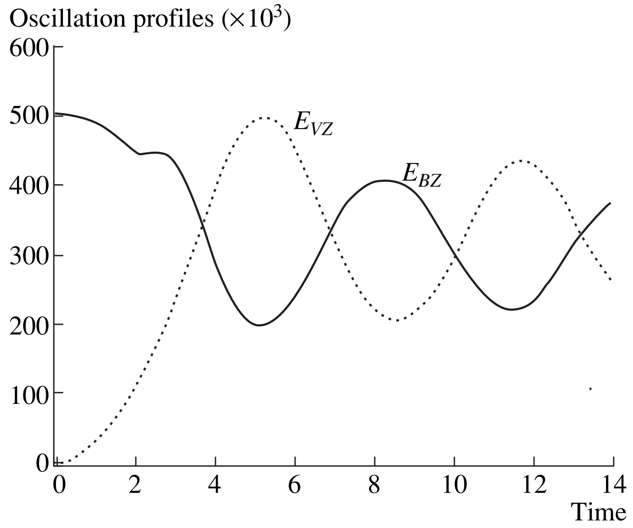

Fig. 5. Oscillations of the axial magnetic field energy ($E_{BZ} = \sum_{ij} B_z^2$) and kinetic energy of plasma motion in the z direction ($E_{VZ} = \sum_{ij}(1/2)\rho V_z^2$) for run B.

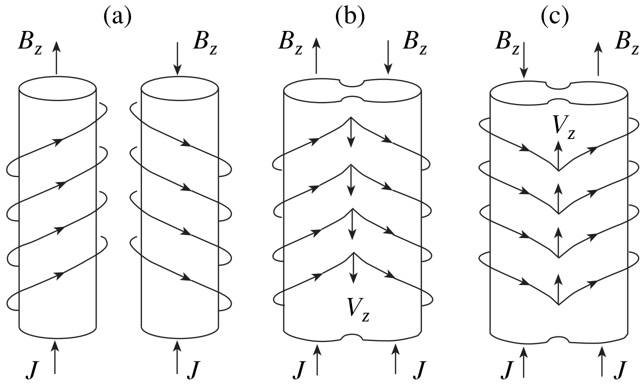

Fig. 6. Schematic of the generation of oscillations of the axial magnetic field and velocity.

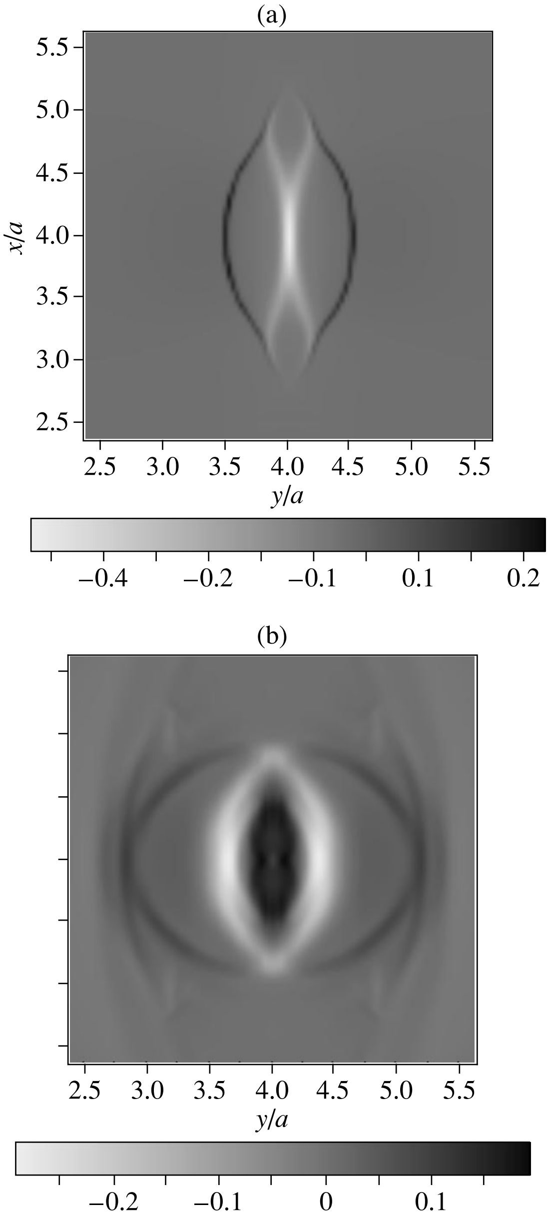

Fig. 7. Induced current j_x arising during the axial magnetic field reconnection for run B: (a) t = 1.53τ_A and (b) t = 13.57τ_A.

An important problem is the mechanism for charged-particle acceleration during magnetic reconnection. It is generally believed that one of the reasons for the generation of fast particles is their acceleration by magnetosonic shock waves. The simulation results show that current loop reconnection can lead to shock wave formation.

First of all, the shock waves moving outward can be clearly seen in Figs. 8 and 10. The shock waves are caused by the relative inward motion of the plasma and high-pressure explosion waves generated in the diffusive reconnection region. In addition to the shock waves, other waves with fine structures are seen in the vicinity of the central diffusive reconnection region (Fig. 11). These waves are caused by the strong inhomogeneity of the pressure and velocity in the diffusive reconnection region. The fine structure of these waves includes shocks, which seems to be interesting because, near the shock front, the electric and magnetic fields change sharply, so that the charged particles are accelerated via the drift acceleration mechanism [34, 35].

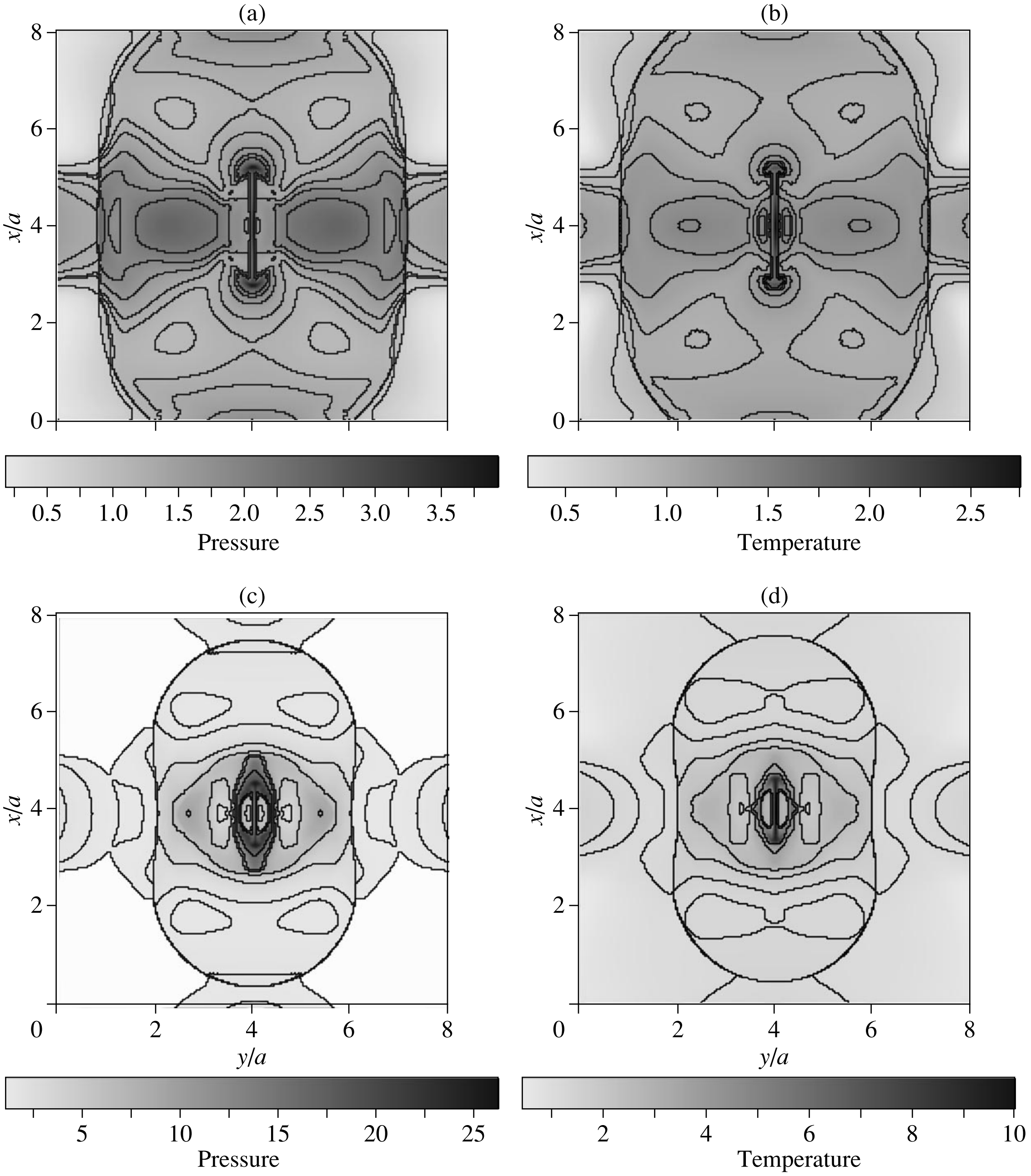

Fig. 8. Distributions of (a, c) density and (b, d) pressure at time $t = 3.43\tau_A$ for (a, b) run A and (b, c) run B.

4. SUMMARY

The coalescence of two parallel force-free current loops is investigated using an MHD code in which the recently proposed AW scheme is employed. The results of simulations shows that co-helicity reconnection involves only the reconnection of the poloidal component of the magnetic field, while counter-helicity reconnection involves the reconnection of both the poloidal and axial components of the magnetic field. In the latter case, the axial magnetic field reconnection occurs in the central diffusive region, in which a series of current sheets (rather than one sheet as is the case of poloidal field reconnection) are formed. Therefore, counter-helicity reconnection is much more complicated and violent as compared to co-helicity reconnection.

In both cases, jetlike flows are formed. However, due to the stress of the frozen-in magnetic field, these flows cannot propagate too far apart.

Counter-helicity reconnection is accompanied by oscillations of the axial magnetic field and the axial

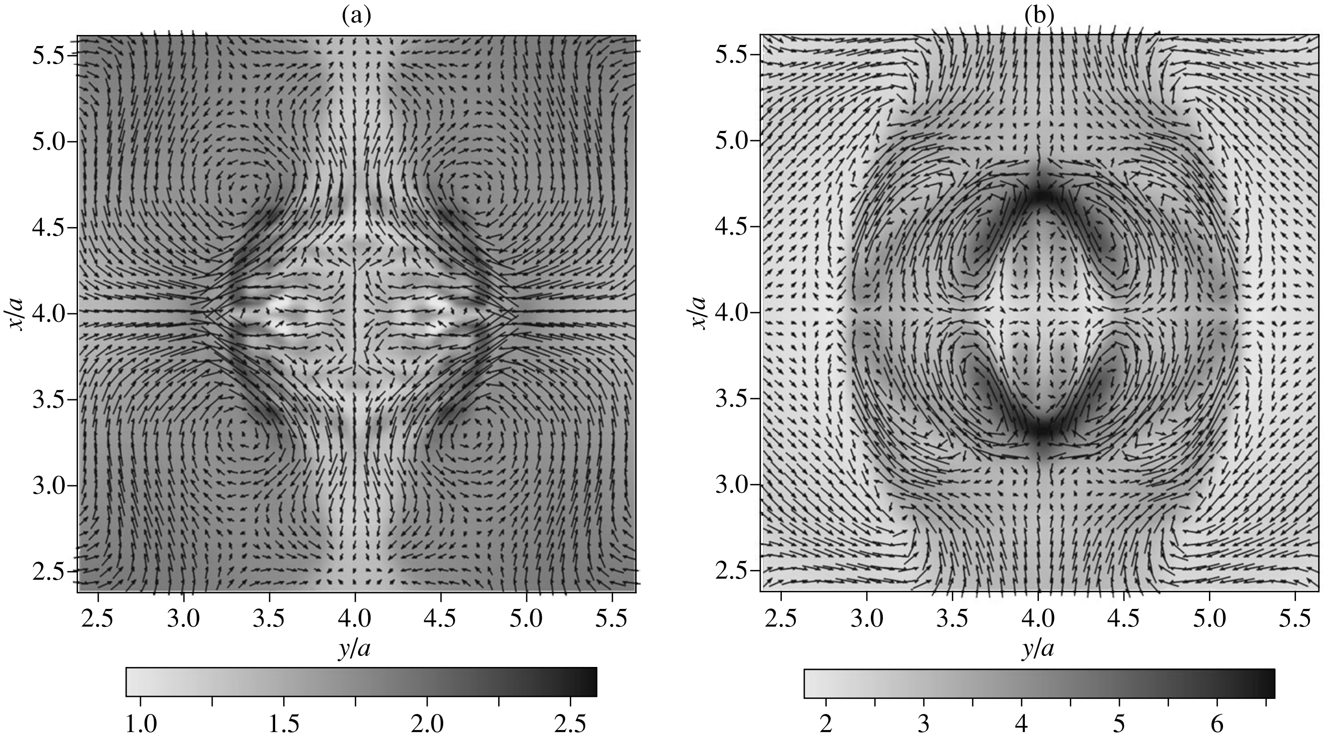

Fig. 9. Distributions of the velocity (vectors) and density (shade of gray) at the time $t = 12.21\tau_A$ for (a) run A and (b) run B.

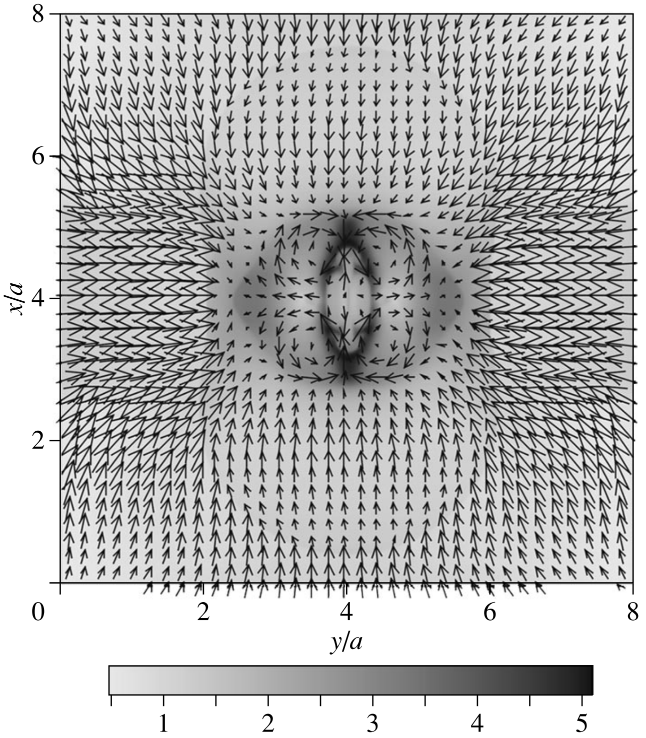

Fig. 10. Distributions of the density (shade of gray) and collapse velocity (V_x, V_y) (vectors) at the time $t = 3.43\tau_A$.

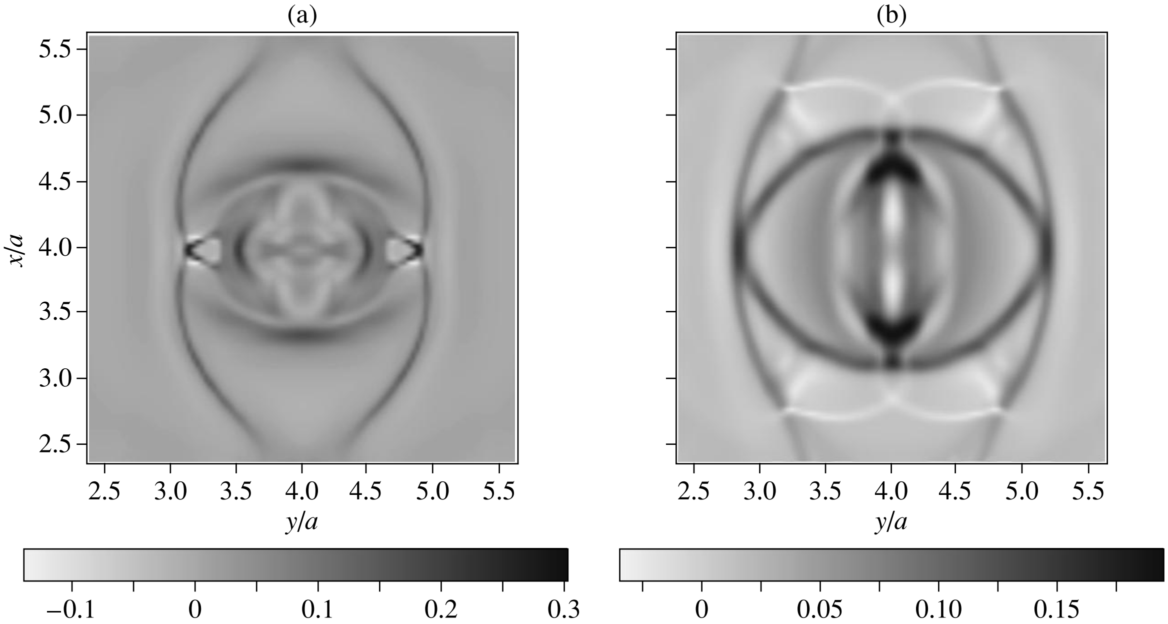

Fig. 11. Current distributions in the central region, demonstrating the presence of shock waves and fine structures, for run B: (a) $t = 11.02\tau_A$ and (b) $t = 13.57\tau_A$.

component of the velocity. Due to these oscillations, quasi-steady models of a current sheet can hardly be applicable, because the structure of the current sheet also changes. The complicated and nonsteady structure of the poloidal current shows that magnetic reconnection occurs not only in the central sheet between two loops in the early stage of the process but also inside each loop in later stages. The plasma and energy of the loops are concentrated in the central region. Complicated flows and waves with fine structures are also generated during reconnection. The fact that some of the waves are shock waves may be used to explain fast particle generation in solar flares.

ACKNOWLEDGMENTS

H.-M. Zhang is grateful to the Japanese Ministry of Education, Science, Sports, and Culture for a scholarship. The work of J.-I. Sakai was supported in part by a Grant-in-Aid for Scientific Research from the Japanese Ministry of Education, Science, Sports, and Culture (no. 11695028). We are grateful to S.V. Bulanov for helpful comments and support. We are also grateful to V.V. Pichushkin for useful discussion.

REFERENCES

1. E. N. Parker, *Cosmical Magnetic Fields* (Clarendon, Oxford, 1979; Mir, Moscow, 1982).
2. E. R. Priest, in *Solar Magnetohydrodynamics*, Ed. by P. Reidel (Kluwer, Dordrecht, 1984).
3. V. M. Vasyliunas, Rev. Geophys. Space Phys. **13**, 303 (1975).
4. S. V. Bulanov, G. T. Dudnikova, T. Zh. Esirkepov, *et al.*, Fiz. Plazmy **22**, 867 (1996) [Plasma Phys. Rep. **22**, 783 (1996)].
5. J. B. Taylor, Rev. Mod. Phys. **58**, 741 (1986).
6. R. M. Kulsrud, Phys. Plasmas **2**, 1735 (1995).
7. S. Tsuneta, Astrophys. J. **456**, 840 (1996); Astrophys. J. Lett. **456**, L63 (1996).
8. M. Yamada, F. M. Levinton, N. Pomphrey, *et al.*, Phys. Plasmas **1**, 3269 (1994).
9. Y. Shi, C. C. Wu, and L. C. Lee, Geophys. Res. Lett. **15**, 295 (1988).
10. E. N. Parker, J. Geophys. Res. **62**, 509 (1957).
11. B. U. O. Sonnerup and D. J. Wang, J. Geophys. Res. **92**, 8621 (1987).
12. M. Yamada, Y. Ono, A. Hayakawa, *et al.*, Phys. Rev. Lett. **65**, 721 (1990).
13. M. Yamada, H. Ji, S. Hsu, *et al.*, Phys. Plasmas **4**, 1936 (1997).
14. T. Gold and F. Hoyle, Mon. Not. R. Astron. Soc. **120**, 89 (1960).
15. J. I. Sakai and C. de Jager, Sol. Phys. **134**, 329 (1991).
16. J. I. Sakai and C. de Jager, Space Sci. Rev. **71**, 1 (1996).
17. T. Shimizu, S. Tsuneta, L. W. Acton, *et al.*, Astrophys. J. **422**, 906 (1994).
18. J. Zhao, J. I. Sakai, and K.-I. Nisikawa, Phys. Plasmas **3**, 844 (1996).
19. T. Tajima, J. I. Sakai, H. Nakajima, *et al.*, Astrophys. J. **321**, 1031 (1987).
20. T. Tajima and J. I. Sakai, Fiz. Plazmy **15**, 1045 (1989) [Sov. J. Plasma Phys. **15**, 606 (1989)].
21. J. I. Sakai, J. Zhao, and K.-I. Nisikawa, Sol. Phys. **154**, 97 (1994).
22. S. Koide and J. I. Sakai, Sol. Phys. **151**, 137 (1994).

23. J. I. Sakai, Sol. Phys. **169**, 367 (1996).
24. T. Fushiki and J. I. Sakai, Sol. Phys. **156**, 265 (1995).
25. J. I. Sakai and C. de Jager, Sol. Phys. **173**, 347 (1997).
26. T. Fushiki and J. I. Sakai, Sol. Phys. **161**, 317 (1995).
27. I. V. Sokolov, E. V. Timofeev, J. I. Sakai, and K. Takayama, Shock Waves **9**, 421 (1999).
28. I. V. Sokolov and J. I. Sakai, J. Plasma Fusion Res. (JPFS Ser. 2), 482 (1999).
29. K. Furusawa, H. M. Zhang, I. V. Sokolov, and J. I. Sakai, in *Proceedings of the Japanese Symposium on Shock Waves, Aoyama Gakuin Univ., Tokyo, 1999*, p. 433.
30. L. D. Landau and E. M. Lifshitz, *Electrodynamics of Continuous Media* (Nauka, Moscow, 1982; Pergamon, New York, 1984).
31. S. V. Bulanov and M. A. Ol'shanetskiĭ, Fiz. Plazmy **11**, 727 (1985) [Sov. J. Plasma Phys. **11**, 425 (1985)].
32. T.-H. Watanabe, T. Sato, and T. Hayashi, Phys. Plasmas **4**, 1297 (1997).
33. Y. Ono, M. Inomoto, T. Okazaki, and Y. Ueda, Phys. Plasmas **4**, 1953 (1997).
34. R. B. Decker, Space Sci. Rev. **48**, 195 (1988).
35. J. A. Miller, P. J. Cargill, A. G. Emslie, *et al.*, J. Geophys. Res. **102**, 14631 (1997).

Translated by the authors

Plasma Physics Reports, Vol. 27, No. 4, 2001, pp. 315–322. Translated from Fizika Plazmy, Vol. 27, No. 4, 2001, pp. 334–342.
Original Russian Text Copyright © 2001 by Bulanov, Echkina, Inovenkov, Pegoraro, Pichushkin.

Three-Dimensional MHD Simulations of Forced Magnetic Reconnection

S. V. Bulanov*, E. Yu. Echkina, I. N. Inovenkov**, F. Pegoraro***, and V. V. Pichushkin****
**Institute of General Physics, Russian Academy of Sciences, ul. Vavilova 38, 117942 Moscow, Russia*
***Moscow State University, Vorob'evy gory, Moscow, 119899 Russia*
****University of Pisa and National Institute of Physics of Matter, Pisa, I-56125 Italy*

Received September 5, 2000; in final form, October 19, 2000

Abstract—Results are presented from MHD simulations of three-dimensional flows of a high-conductivity plasma in the vicinity of a null point of a magnetic field. The excitation of an electric current at the boundary of the computation region results in self-consistent plasma flows and change in the structure of the magnetic field. Generally, in the vicinity of a null point, an MHD singularity arises that manifests itself in the formation of locally plane current sheets. It is shown that the current sheet can be oriented either along the separatrix surface of a magnetic configuration or perpendicular to it, except for axisymmetric configurations (or close to them), when the excitation of an electric current in the direction orthogonal to the separatrix surface does not lead to the formation of a current sheet. *© 2001 MAIK "Nauka/Interperiodica".*

1. INTRODUCTION

It is well known that investigations of the structure of MHD singularities arising in the flows of a highly conducting plasma in the vicinity of critical points of a magnetic field is of great importance for the theory of magnetic reconnection. Reconnection of magnetic field lines plays a key role in various problems of physics of space and laboratory plasmas, including the disruption instability, the nonlinear evolution of magnetic islands in tokamak plasmas, and solar flares and substorms in the Earth's magnetosphere (see [1–6] and the literature cited therein). A rapid change in the topology of a magnetic field during magnetic reconnection is accompanied by the conversion of the magnetic field energy into the energy of the plasma, radiation, and fast electrons and ions. Magnetic reconnection occurs in the vicinity of critical points (or critical lines and surfaces) of a magnetic field. During the self-consistent evolution of the plasma and magnetic field in the vicinity of critical points, highly nonlinear structures (including shock waves and current sheets) are formed.

To analytically describe the local structure of singularities arising near the critical points, self-similar solutions to the MHD equations are commonly used [7–10]. A description of the non-self-similar stage of the development of a singularity requires computer simulations [3, 10–14]. The fundamental result is that the typical structure of an MHD singularity corresponds to a current sheet in which magnetic field reconnection occurs [15]. The overwhelming majority of theoretical studies, numerical simulations, and laboratory experiments concern investigations of two-dimensional (2D) configurations, including the case of three-component magnetic reconnection [10, 12, 16, 17]. At the same time, increasing attention is being given to the 3D magnetic reconnection [3, 6, 9, 10, 12–14, 18–23]. First of all, this stems from the fact that 2D magnetic configurations are structurally unstable; i.e., the topology of a magnetic field in the vicinity of null lines or surfaces changes under the action of arbitrarily small perturbations. This makes the existence of 2D structures in space plasmas problematic. On the other hand, null points in three-dimensional (3D) geometry are structurally stable. An exception is 2D magnetic structures created in laboratory devices, because, in this case, special efforts are taken to create and maintain the high symmetry of magnetic configurations. However, in laboratory plasmas, it is also necessary to take into account the 3D inhomogeneity of a magnetic field, especially when considering the change of the magnetic field topology during the onset of instabilities. In this context, investigations of 3D configurations are of special interest for practical applications. As was shown in [9, 10, 12, 13, 24], 3D description allows one to obtain qualitatively new results. In particular, the formation of current sheets orthogonal to the null lines and parallel to the separatrices of a magnetic field has been predicted.

Although the studies of magnetic reconnection in 3D magnetic configurations have led to a number of important results, many questions related to the influence of the symmetry of the initial configuration and boundary conditions on the formation and stability of current sheets still remain unanswered. In this paper, we present the results of 3D MHD simulations of plasma flows in the vicinity of a null point of a magnetic field. The goal of the study is to investigate the influence of the symmetry of the boundary conditions on the formation of a current sheet.

The paper is organized as follows. In Section 2, we present the basic MHD equations and discuss the structure of a magnetic configuration in the vicinity of a null point. In Section 3, the results from MHD simulations of the formation of a current sheet near a null point of a magnetic field are presented. In the Conclusion, the main results are summarized.

2. MATHEMATICAL MODEL

2.1. Basic MHD Equation

The problem is solved in the MHD approximation. It is assumed that transport coefficients characterizing the plasma (such as the magnetic viscosity ν_m, electric conductivity σ, and thermal conductivity) are constant. The magnetic field is described by the vector potential $\mathbf{B} = \mathrm{rot}\mathbf{A}$, $\mathrm{div}\mathbf{A} = 0$. For numerical simulations, it is convenient to introduce the following dimensionless variables:

$$\tilde{\varrho} = \frac{\varrho}{\varrho_0}, \quad \tilde{\mathbf{B}} = \frac{\mathbf{B}}{B_0}, \quad \tilde{\mathbf{v}} = \frac{\mathbf{v}}{v_a}, \quad \tilde{t} = \frac{t}{t_a}, \qquad \tilde{T} = \frac{T}{T_0}, \quad \tilde{\mathbf{J}} = \frac{4\pi l\mathbf{J}}{cB_0}, \quad \tilde{\mathbf{A}} = \frac{\mathbf{A}}{B_0 l}. \tag{1}$$

Here, ρ_0 and T_0 are the initial values of the density and plasma temperature, respectively; B_0 is the maximum value of the magnetic field; l is the characteristic scale length; $v_a = B_0/(4\pi\rho_0)^{1/2}$ is the Alfvén velocity; and $t_a = l/v_a$ is the Alfvén time. Further, only dimensionless variables will be used and, therefore, the tilde symbol will be omitted.

In the new variables, the system of one-fluid MHD equations takes the form

$$\frac{\partial\varrho}{\partial t} + \mathrm{div}(\varrho\mathbf{v}) = 0, \tag{2}$$

$$\varrho\left(\frac{\partial\mathbf{v}}{\partial t} + (\mathbf{v}\cdot\nabla)\mathbf{v}\right) = -\frac{\beta}{2}\nabla p + \mathrm{curl}\,\mathrm{curl}\mathbf{A}\times\mathrm{curl}\mathbf{A}, \tag{3}$$

$$\frac{\partial\mathbf{A}}{\partial t} = \mathbf{v}\times\mathrm{curl}\mathbf{A} + \nu_m\Delta\mathbf{A}, \tag{4}$$

$$\frac{\varrho}{\gamma-1}\left(\frac{\partial T}{\partial t} + (\mathbf{v}\cdot\nabla)T\right) + p\,\mathrm{div}\mathbf{v} = \mathrm{div}(\kappa\nabla T) + 2\nu_m\frac{(\Delta\mathbf{A})^2}{\beta}, \tag{5}$$

$$p = \rho T. \tag{6}$$

The adiabatic index is chosen to be $\gamma = c_p/c_V = 5/3$. The dimensionless parameter β (the ratio of the plasma pressure to the magnetic pressure at the boundary) is defined as $\beta = 8\pi p_0/B_0^2$, where $p_0 = 2\rho_0 T_0/m$ is the gas-kinetic pressure with m being the mass of the plasma ions. The dimensionless magnetic viscosity (the inverse Lundquist number) $\nu_m = c^2/(4\pi 1\sigma v_a)$ and dimensionless thermal conductivity $\kappa = k/(v_a 1\varrho_0)$ (where k is the dimensional thermal conductivity) are assumed to be constant.

2.2. Structure of a Magnetic Configuration in the Vicinity of a Null Point

Here, we will reproduce the well-known description of the structure of a magnetic field near a null point, which will be used to formulate the problem.

Near an arbitrary point x_0, the magnetic field can be approximated by the first terms of the Tailor series. Without loss of generality, we can set $x_0 = 0$. As a result, we obtain

$$\mathbf{B}(\mathbf{x}, t) = \mathbf{B}(0, t) + (\mathbf{x}\nabla)\mathbf{B}(0, t) + \dots. \tag{7}$$

Below, we will consider the case of a null point of a magnetic field, when $B(0, t) = 0$. We define the matrix of the magnetic field gradients as $\partial B_i/\partial x_j|_{x=0} = A_{ij}$. Then, the magnetic field in the vicinity of a null point can be written as

$$B_i = A_{ij}x_j. \tag{8}$$

We will assume that the matrix A_{ij} is nonzero. Note that the magnetic reconnection near the degenerate critical points of a magnetic field was studied in [25–27].

As is known, the equations for the field lines of the magnetic field (8) are equivalent to the dynamic system

$$\frac{dx_i}{ds} = A_{ij}x_j. \tag{9}$$

The null point corresponds to an equilibrium point. The behavior of trajectories (field lines) is determined by the solutions of the eigenvalue problem for the matrix A_{ij}

$$\det(A_{ij} - \lambda\delta_{ij}) = 0, \tag{10}$$

i.e., the structure of the magnetic field is determined by the eigenvalues λ_α and eigenvectors R_i^α of the matrix A_{ij} ($\alpha = 1, 2, 3$). By virtue of the condition $\mathrm{div}\mathbf{B} = 0$, the trace of the matrix A_{ij} is zero, $A_{kk} = 0$. Depending on the form of the matrix A_{ij}, the equation $A_{ij}x_j = 0$ describes a null plane, line, or point.

Let one of the eigenvalues be zero (e.g., $\lambda_3 = 0$) and the other two be real and opposite in sign ($\lambda_{1,2} = \pm\lambda'$). Then, expression (8) describes the vicinity of an X-type null line. The magnetic field has two separatrix surfaces, which intersect under a certain angle.

If one of the eigenvalues is zero ($\lambda_3 = 0$) and the other two are imaginary and complex conjugate ($\lambda_{1,2} = \pm i\lambda'$), expression (8) describes an O-type null line. When all the eigenvalues λ_α ($\alpha = 1, 2, 3$) are real and nonzero, expression (8) describes the vicinity of a null point that is analogous to a saddle point on a plane. In this case, there is one direction along which the field lines enter the vicinity of this point (or emerge from it) and a separatrix plane along which the field lines emerge from the vicinity of the null point (or enter it). The position of the separatrix plane is determined by the direction of two eigenvectors corresponding to two eigenvalues of the same sign.

If two eigenvalues are complex conjugate ($\lambda_{1,2} = \lambda' \pm i\lambda''$) and one eigenvalue is real ($\lambda_3 = -2\lambda'$), then there is also a separatrix surface in the vicinity of a null point. The magnetic field lines look like spirals (with varying pitch and radius) approaching the separatrix surface or moving away from it.

In this paper, we consider plasma flows near a magnetic null point that is characterized by real eigenvalues. Note that this case corresponds to an initial configuration with a potential magnetic field.

3. RESULTS OF MHD SIMULATIONS OF THE FORMATION OF CURRENT SHEETS IN 3D MAGNETIC CONFIGURATIONS

3.1. Initial Magnetic Configurations

Simulations are performed in a cubic computation region $G = \{-1 \le x \le 1, -1 \le y \le 1, -1 \le z \le 1\}$, in which the plasma and magnetic field evolve self-consistently. At the initial instant, the magnetic field described by the vector potential $\mathbf{A}(x, y, z)$ is potential; i.e., the electric current density is zero and the plasma in the equilibrium state is characterized by a constant density $\rho(0) = 1$ and pressure $p(0) = 1$ and zero initial velocity $\mathbf{v}(0) = 0$. In this case, the magnetic field can be described by expression (8) with a diagonal matrix of the field gradients $A_{ij} = \mathrm{diag}\{a, b, -(a+b)\}$; i.e.,

$$\mathbf{B} = ax\mathbf{e}_x + by\mathbf{e}_y - (a+b)z\mathbf{e}_z. \tag{11}$$

The equilibrium is disrupted by inducing an electric current along the z-axis at the boundary of the computation region.

Three cases corresponding to different initial configurations of the magnetic field were considered. In the first and second cases, the induced electric current was parallel to the separatrix plane, and, in the third case, the excited current was orthogonal to the separatrix plane.

In the first case, the components of the matrix A_{ij} are chosen to be $a = 1.65$ and $b = -1.35$, so that the separatrix surface is parallel to the z-axis and lies in the $x = 0$ plane. In the second case, $a = 0.25$ and $b = -0.75$ and the separatrix surface is parallel the z-axis and lies in the $y = 0$ plane. In the third case, $a = 1.3$ and $b = 0.7$ and the separatrix surface is perpendicular to the z-axis and lies in the $z = 0$ plane.

3.2. Boundary Conditions

As was mentioned above, the equilibrium is disrupted by inducing an electric current at the boundary of the computation region. In this case, the excited nonlinear MHD perturbations propagate in the computation region toward the z-axis. It is well known that, in a plane 2D magnetic field, linear MHD perturbations in a cold plasma are split into Alfvén and magnetosonic modes. In a 3D magnetic configuration, the situation is much more complicated because such splitting is absent.

In simulations, the z-component of the vector potential at the boundary is set to be

$$A_z(x, y, t) = A_z(x, y, t=0) + f(t + \ln(r)), \quad r^2 = x^2 + y^2, \tag{12}$$

where the coordinates x and y belong to the boundary ($x = \pm 1$ and $y = \pm 1$). The function $f(\xi)$, which has the form

$$f(\xi) = \begin{cases} -\tilde{E}(\xi - 1), & \xi > 1 \\ 0, & \xi < 1, \end{cases} \tag{13}$$

describes the gradual switching-on of the electric current. Here, $\tilde{E}$ is the dimensionless electric field (see also [11, 13]).

Thus, for a magnetic configuration given by expression (11), the electric current induced at the boundary of the computation region may be either parallel or perpendicular to the separatrix surface of the magnetic field.

At the boundary regions where the plasma flows into the computation region, we set $\rho = 1$, $p = 1$, $T = 1$; at the other boundary regions, the conditions for the plasma to freely flow out from the computation region are imposed.

Below, we present the results of simulations for the dimensionless magnetic viscosity $\nu_m = 0.006$, the electric field $\tilde{E} = 0.06$, the pressure corresponding to $\beta = 0.012$, and the dimensionless thermal conductivity $\kappa = 0.01$.

3.3. Simulation Results

The complete set of 3D MHD equations (1)–(5) was solved numerically.

The first series of calculations was carried out for a magnetic field given by expression (11) with $a = 1.65$ and $b = -1.35$. The separatrix plane of the magnetic field lies in the $x = 0$ plane. Since the z-component of the magnetic field gradient is equal to $-(a+b) = 0.3$ and the ratio $\frac{|a+b|}{a} = 0.18$ is much less than unity, the magnetic configuration under study is weakly nonuniform along the z-axis. In other words, this is a weakly perturbed null line parallel to the z-axis. Figure 1a shows the structure of the magnetic field lines at the initial instant.

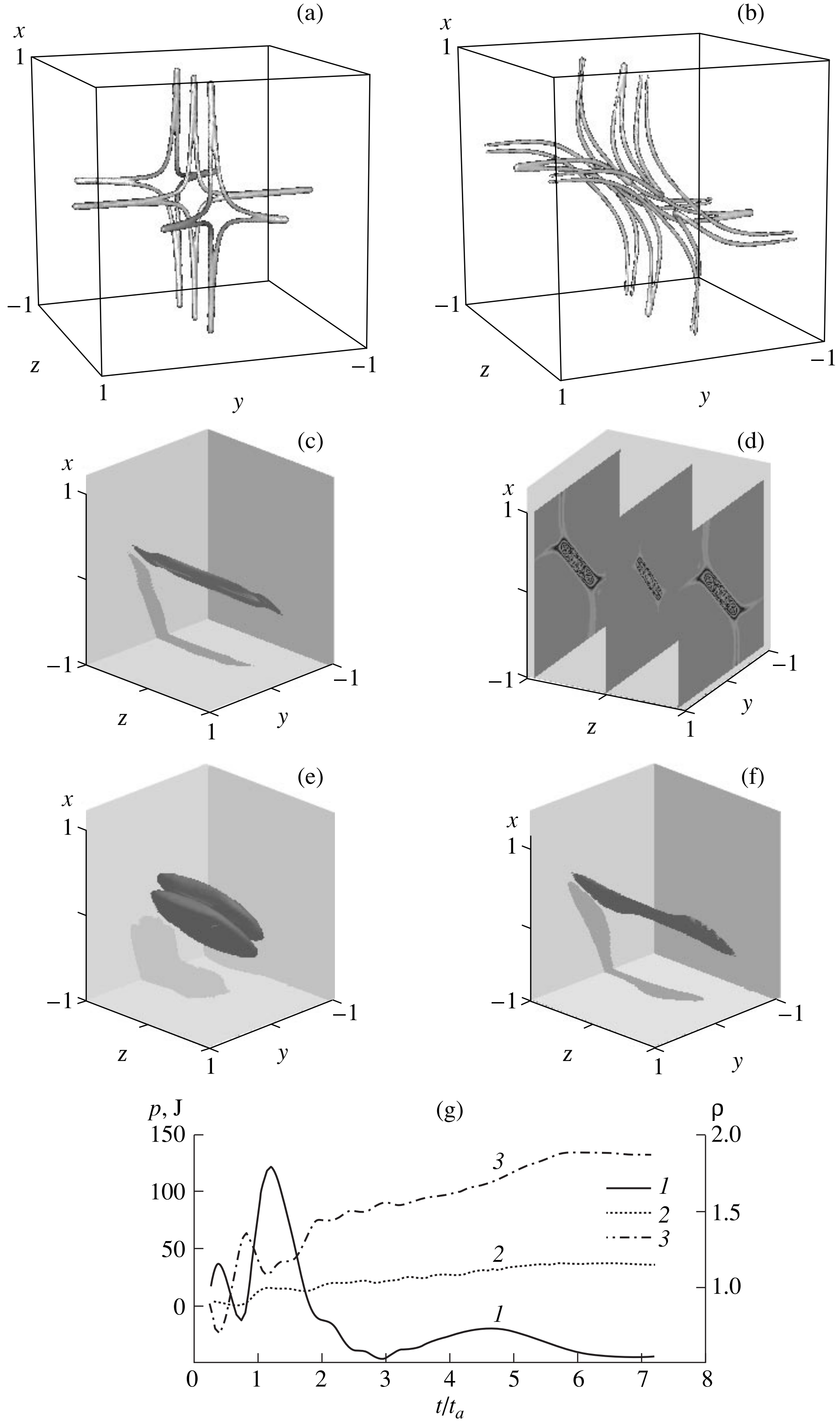

Fig. 1. The magnetic field structure and the distribution of the main plasma parameters for $a = 1.65$ and $b = -1.35$ ($\mathbf{B} = 1.65x\mathbf{e}_x - 1.35y\mathbf{e}_y - 0.3z\mathbf{e}_z$; at the initial instant, the separatrix surface is parallel to the z-axis and lies in the $x = 0$ plane and the induced electric current is parallel to the separatrix plane). The magnetic field structure at (a) $t = 0$ and (b) $t = 8$; (c) isosurface of the electric current density ($J = 72$) at $t = 8$; (d) distributions of the electric current density in different planes $z =$ const; (e) isosurface of the plasma density ($\rho = 0.51$); (f) isosurface of the plasma pressure ($p = 27$); and (g) time evolution of the plasma parameters: (*1*) plasma density ρ, (*2*) plasma pressure p, and (*3*) electric current density J.

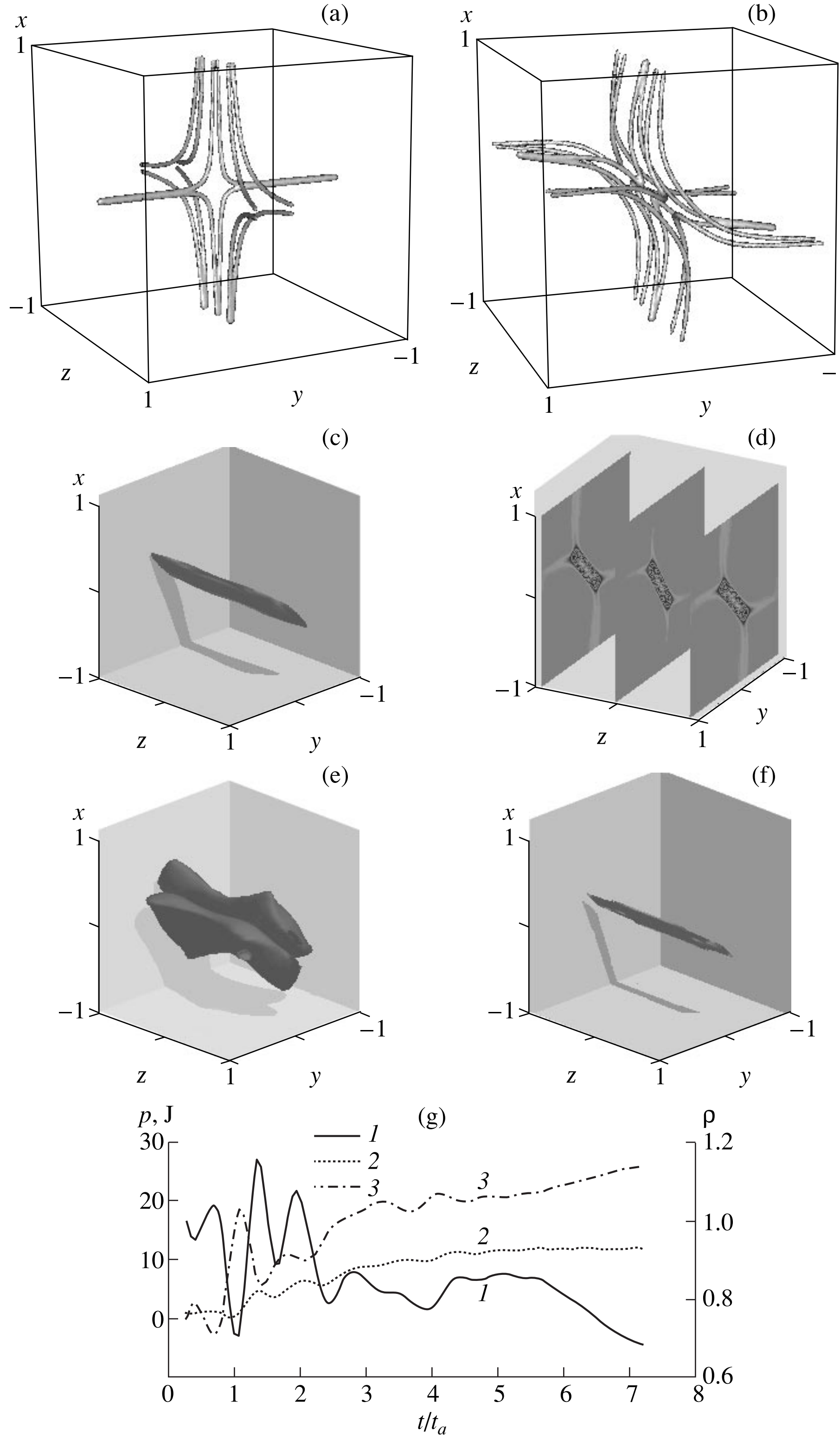

Fig. 2. The magnetic field structure and the distribution of the main plasma parameters for $a = 0.25$ and $b = -0.75$ ($\mathbf{B} = 0.25x\mathbf{e}_x - 0.75y\mathbf{e}_y - 0.5z\mathbf{e}_z$; at the initial instant, the separatrix surface is parallel to the z-axis and lies in the $y = 0$ plane and the induced electric current is parallel to the separatrix plane). The magnetic field structure at (a) $t = 0$ and (b) $t = 8$; (c) isosurface of the electric current density ($J = 16$) at $t = 8$; (d) distributions of the electric current density in different planes $z = \text{const}$; (e) isosurface of the plasma density ($\rho = 0.44$); (f) isosurface of the plasma pressure ($p = 8.66$); and (g) time evolution of the plasma parameters: (*1*) plasma density ρ, (*2*) plasma pressure p, and (*3*) electric current density J.

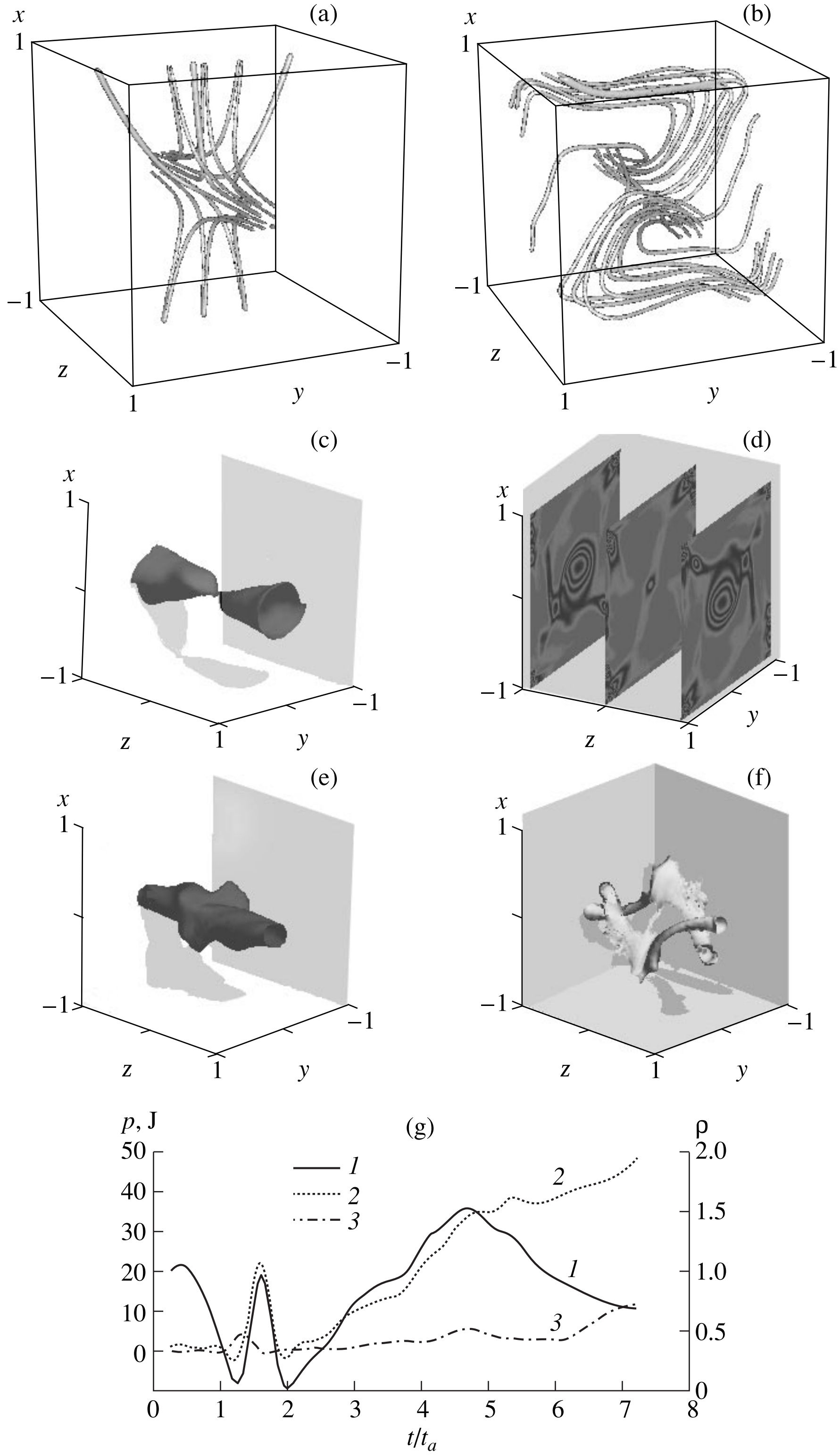

Fig. 3. The magnetic field structure and the distribution of the main plasma parameters for $a = 1.3$ and $b = 0.7$ ($\mathbf{B} = 1.3x\mathbf{e}_x + 0.7\,y\mathbf{e}_y - 2z\mathbf{e}_z$; at the initial instant, the separatrix surface is parallel to the z-axis and lies in the $z = 0$ plane and the induced electric current is orthogonal to the separatrix plane). The magnetic field structure at (a) $t = 0$ and (b) $t = 8$; (c) isosurface of the electric current density ($J = 21.1$) at $t = 8$; (d) distributions of the electric current density in different planes z = const; (e) isosurface of the plasma density ($\rho = 0.78$); (f) isosurface of the plasma pressure ($p = 52.34$); and (g) time evolution of the plasma parameters: (*1*) plasma density ρ, (*2*) plasma pressure p, and (*3*) electric current density J.

A cylindrical MHD wave that is excited at $t = 0$ at the boundary of the computation region starts propagating toward the null line. After the wave has reached the center of the computation region, the structure of the magnetic field changes (see Fig. 1b) and a current sheet is formed. A quasi-steady configuration is formed at $t = 4$. Figures 1c and 1d show an isosurface of the electric current density and the distributions of the electric current density in different planes z = const at $t = 8$. It is seen that a current sheet is formed in the vicinity of the null point. The central part of the current sheet is mainly stretched along the z-axis. The geometrical characteristics (width and thickness) of the current sheet are similar to those in a 2D magnetic configuration.

The spatial distribution of the plasma density (Fig. 1e) is characterized by the presence of two local maxima. As was already shown in 2D simulations [12], such a configuration takes place for small values of the thermal conductivity. Figure 1f illustrates the distribution of the plasma pressure, and Fig. 1g shows the time evolution of the plasma parameters at the null point of the magnetic field. The time during which the MHD wave propagates from the boundary to the null point is equal to two Alfvén times. It is seen that the electric current increases up to $t = 6$ and, then, varies only slightly. During this stage, the pressure continues to grow slowly due to low thermal conductivity.

The second series of calculations was performed for a magnetic field given by expression (11) with $a = 0.25$ and $b = –0.75$. In this case, the separatrix surface of the magnetic field lies in the $y = 0$ plane. Since the z-component of the magnetic field gradient is equal to $–(a + b) = 0.5 < 1$ and the ratio $\frac{|a+b|}{a} = 2$ is larger than unity, the magnetic configuration under study is highly nonuniform. In other words, this is a perturbed null line directed along the z-axis. Figure 2a shows the structure of the magnetic field lines at the initial instant.

A cylindrical MHD wave that is excited at the initial instant at the boundary of the computation region starts propagating toward the null line. After the wave has reached the center of the computation region, a current sheet is formed there. A quasi-steady configuration is established at $t = 4$. Figure 2b shows the magnetic field lines at $t = 8$. It is seen that the separatrix is bent and the current sheet is formed along it. Figures 2c and 2d show an isosurface of the electric current density and the distributions of the electric current density in different planes z = const at $t = 8$. A current sheet is seen to form in the vicinity of the null point. The central part of the current sheet is mainly stretched along the z-axis. The current sheet has a characteristic 3D shape. As in the previous case, the spatial distribution of the plasma density is characterized by the presence of two maxima (Fig. 2e). Figure 2f illustrates the distribution of the plasma pressure. Figure 2g shows the time evolution of the plasma parameters at the null point of the magnetic field. As previously, the time during which the MHD wave propagates from the boundary to the null point is equal to two Alfvén times; however, there is no sharp increase in the electric current density.

The third series of calculations was performed for a magnetic field given by expression (11) with $a = 1.3$ and $b = 0.7$. The separatrix surface lies in the $z = 0$ plane, and the electric current induced at the boundary of the computation region is orthogonal to this surface. Since the z-component of the magnetic field gradient is equal to $–(a + b) = –2$ and the ratio $\frac{|a+b|}{a} \simeq 1.5$ is larger than unity, the magnetic configuration under study is a highly nonuniform 3D configuration. Figure 3a shows the structure of the field lines at the initial instant.

As previously, a quasi-cylindrical MHD wave excited at the initial instant propagates toward the null point. However, in contrast to the previous cases, where the electric current was parallel to the separatrix surface, no current sheet is formed in the vicinity of the null point. Figure 3c shows an isosurface of the electric current. It is seen that the current is concentrated in a spatially nonuniform region. Due to the plasma rotation, the magnetic field lines become twisted and the plasma is expelled from the computation region. Figure 3g shows the time evolution of the plasma parameters at the null point of the magnetic field. The time during which the MHD wave propagates to the null point increases in comparison with the previous cases. No substantial increase in the electric current density in the null point is observed. The plasma pressure increases due to Joule heating.

4. CONCLUSION

This paper presents the results of the first numerical simulations of local configurations arising during magnetic field reconnection in 3D geometry.

In contrast to [14, 18], the structure of an MHD singularity is revealed and investigated in detail. It is shown that the structure of the singularity substantially depends on how the induced electric current is directed with respect to the magnetic field. Here, the decisive factor is the mutual orientation of the electric current and the separatrix surface of the magnetic field. Previously, based on an analysis of self-similar solutions to MHD equations [9–11], it was predicted that the development of a current sheet in the direction orthogonal to the separatrix surface would be hampered. The results obtained in this paper generally confirm this prediction and demonstrate a complicated, non-self-similar structure of the electric current in a plasma.

A typical MHD singularity observed in our simulations corresponds to a current sheet directed along the separatrix surface. If the current is orthogonal to the separatrix surface, then, in the problem as formulated, the current sheet is not formed because of the forced plasma rotation and the action of the centrifugal forces, which prevent the plasma from pinching. Nevertheless, in this case, the current region has a nontrivial topology with a constriction near the null point.

ACKNOWLEDGMENTS

This work was supported in part by the Russian Foundation for Basic Research, project nos. 99-01-0167 and 00-15-96052.

REFERENCES

1. B. B. Kadomtsev, *Collective Phenomena in a Plasma* (Nauka, Moscow, 1988).
2. R. B. White, *Theory of Tokamak Plasmas* (North-Holland, Amsterdam, 1989).
3. D. Biskamp, *Nonlinear Magnetohydrodynamics* (Cambridge Univ. Press, Cambridge, 1993).
4. E. R. Priest, *Solar Flare Magnetohydrodynamics* (Gordon and Breach, New York, 1981).
5. S. I. Akasofu, *Physics of Magnetosphere* (Reidel, Boston, 1977).
6. V. S. Berezinskij, S. V. Bulanov, V. A. Dogiel, V. L. Ginzburg, and V. S. Ptushkin, *Astrophysics of Cosmic Rays* (North-Holland, Amsterdam, 1990).
7. J. W. Dungey, Philos. Mag. **44**, 725 (1953).
8. V. S. Imshennik and S. I. Syrovatskii, Zh. Éksp. Teor. Fiz. **52**, 900 (1967) [Sov. Phys. JETP **25**, 656 (1967)].
9. S. V. Bulanov and M. A. Ol'shanetskij, Fiz. Plazmy **11**, 727 (1985) [Sov. J. Plasma Phys. **11**, 425 (1985)].
10. S. V. Bulanov, I. Ya. Butov, Yu. S. Gvaladze, *et al.*, Fiz. Plazmy **12**, 309 (1986) [Sov. J. Plasma Phys. **12**, 180 (1986)].
11. S. V. Bulanov, Yu. S. Gvaladze, A. M. Zaborov, and M. A. Ol'shanetskij, Comments Plasma Phys. Controll. Fusion **12**, 125 (1989).
12. K. V. Brushlinskij, A. M. Zaborov, and S. I. Syrovatskii, Fiz. Plazmy **6**, 297 (1980) [Sov. J. Plasma Phys. **6**, 165 (1980)].
13. S. V. Bulanov, G. I. Dudnikova, T. Zh. Esirkepov, *et al.*, Fiz. Plazmy **22**, 867 (1996) [Plasma Phys. Rep. **22**, 783 (1996)].
14. R. B. Dahlburg, S. K. Antiochos, and D. Norton, Phys. Rev. E **56**, 2094 (1997).
15. S. I. Syrovatskii, Zh. Éksp. Teor. Fiz. **60**, 1727 (1971) [Sov. Phys. JETP **33**, 933 (1971)].
16. Y. Ono, V. Yamada, T. Akao, *et al.*, Phys. Rev. Lett. **76**, 3328 (1996).
17. M. R. Brown, Phys. Plasmas **6**, 1717 (1999).
18. J.-I. Sakai and C. De Jager, Space Sci. Rev. **77**, 1 (1996).
19. S. V. Bulanov and A. G. Frank, Fiz. Plazmy **18**, 1535 (1992) [Sov. J. Plasma Phys. **18**, 795 (1992)].
20. S. Yu. Bogdanov, V. B. Burilina, V. S. Markov, and A. G. Frank, Pis'ma Zh. Éksp. Teor. Fiz. **59**, 510 (1994) [JETP Lett. **59**, 537 (1994)].
21. S. V. Bulanov and J.-I. Sakai, J. Phys. Soc. Jpn. **66**, 3477 (1997).
22. S. V. Bulanov and J.-I. Sakai, Astrophys. J., Suppl. Ser. **117**, 599 (1998).
23. J. Schumaher, B. Kliem, and N. Seehafer, Phys. Plasmas **7**, 108 (2000).
24. W. K. Zwingmann, K. Schindler, and J. Birn, Solar Phys. **99**, 1331 (1985).
25. S. V. Bulanov, V. V. Pichushkin, and K. Schindler, Fiz. Plazmy **22**, 979 (1996) [Plasma Phys. Rep. **22**, 885 (1996)].
26. S. V. Bulanov, E. Yu. Echkina, I. N. Inovenkov, *et al.*, Phys. Plasmas **6**, 802 (1999).
27. S. V. Bulanov, E. Yu. Echkina, I. N. Inovenkov, *et al.*, Fiz. Plazmy **26**, 600 (2000) [Plasma Phys. Rep. **26**, 560 (2000)].

Translated by A.S. Sakharov

Plasma Physics Reports, Vol. 27, No. 4, 2001, pp. 323–329. Translated from Fizika Plazmy, Vol. 27, No. 4, 2001, pp. 343–349.
Original Russian Text Copyright © 2001 by Oraevsky, Sobolev, Zhuzgov, Afonin, Baranets.

BEAMS IN PLASMA

Magnetic Field Excitation during Electron Beam Injection from the Intercosmos-25 Satellite (APEX)

V. N. Oraevsky*, Ya. P. Sobolev*, L. N. Zhuzgov*, V. V. Afonin, and N. V. Baranets***

**Institute of Terrestrial Magnetism, Ionosphere, and Radio-Wave Propagation, Russian Academy of Sciences,*
Troitsk, Moscow oblast, 142092 Russia

***Institute for Space Research, Russian Academy of Sciences, Profsoyuznaya ul. 84/32, Moscow, 117810 Russia*

Received August 18, 2000

Abstract—Results of active experiments on electron beam injection from the Intercosmos-25 satellite into the ionospheric plasma are presented. A quasistatic magnetic field and the VLF-wave magnetic component are excited when an unmodulated electron beam with a current of $I_{be} \simeq 0.1$ A and energy of $\varepsilon_{be} = mv^2/2 \simeq 10$ keV is injected into the ambient plasma. The magnetic field excitation is attributed to the onset of plasma gradient instabilities. © *2001 MAIK "Nauka/Interperiodica".*

1. INTRODUCTION

Generally, the injection of a low-energy electron beam from a satellite into the ionospheric plasma produces only weak fluctuations in the geomagnetic field $\mathbf{B}_0$. The excitation of VLF waves was observed in many rocket experiments. The excitation of induction processes by electron helicity in a weakly collisional plasma during injection is attributed to the presence of eddy currents and various dynamo processes [1, 2]. These processes are usually responsible for the generation of a slowly growing magnetic field and the excitation of Alfvén waves (AW). When the electron flow velocity is close to the Alfvén velocity, $|\mathbf{u}| \sim |\mathbf{v}_A| = B_0/\sqrt{4\pi n_0 M_a}$ (where n_0 and M_a are the unperturbed plasma density and the ion mass of species a), the excitation of low-frequency waves may be related to either the Alfvén resonance $\omega \simeq \mathbf{k} \cdot \mathbf{v}_A$ or the electron-cyclotron resonance at $\omega \sim \omega_{ci}$ [3, 4]. In this paper, we present the results of one of the active experiments on magnetic field excitation carried out onboard the Intercosmos-25 satellite (APEX) [5] at turn no. 266. Particular attention is given to unmodulated (dc) electron beam injection.

2. SCIENTIFIC EQUIPMENT

The results presented were obtained with the help of a scientific equipment complex installed on the satellite. The complex consisted of an electron accelerator (Fig. 1, $G1$), a high-sensitivity magnetometer (the measurement accuracy was ~1 nT), and a low-frequency wave system for measuring wave amplitudes in the range $f = 8$–969 Hz and at fixed frequencies of 9.6 and 15.0 kHz. The electron T_e and ion T_i temperatures, the satellite body potential p_s, the unperturbed plasma density n_0, and the energy distributions of the thermal-plasma ion flux densities $j_{ix}(V)$ and $j_{iz}(V)$ were measured with an impedance probe and a retarding-potential analyzer (RPA). Here, j_{ix} and j_{iz} are the ion flux densities in the x and z directions, respectively, and V is the sweep voltage at the RPA grid ($0 \le V \le 12$ V).

The pitch angle of electron beam injection α_{pe}, the orientation angles of the satellite velocity vector $\mathbf{v}_s$ and the Earth's magnetic field $\mathbf{B}_0$, the angle $\beta_3 \equiv \beta_3(\mathbf{B}_0 \wedge \mathbf{Z})$, the azimuthal angle $A \equiv A(\mathbf{B}_0^* \wedge \mathbf{Y})$, and the angle of attack θ_V $(\mathbf{v}_s \wedge \mathbf{X})$ were calculated using data from the satellite-borne solar and magnetic detectors. Here, x, y, and z are the coordinates in the satellite frame of refer-

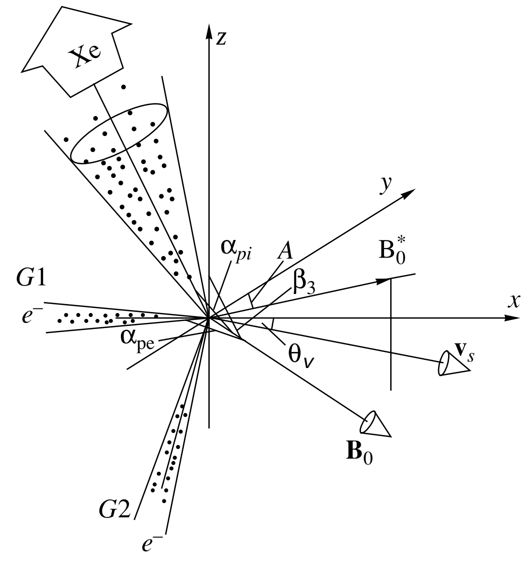

Fig. 1. Injection directions, orientation angles of the magnetic field $\mathbf{B}_0$ and velocity $\mathbf{v}_s$ in the satellite frame of reference xyz; the z-axis is directed from the Earth.

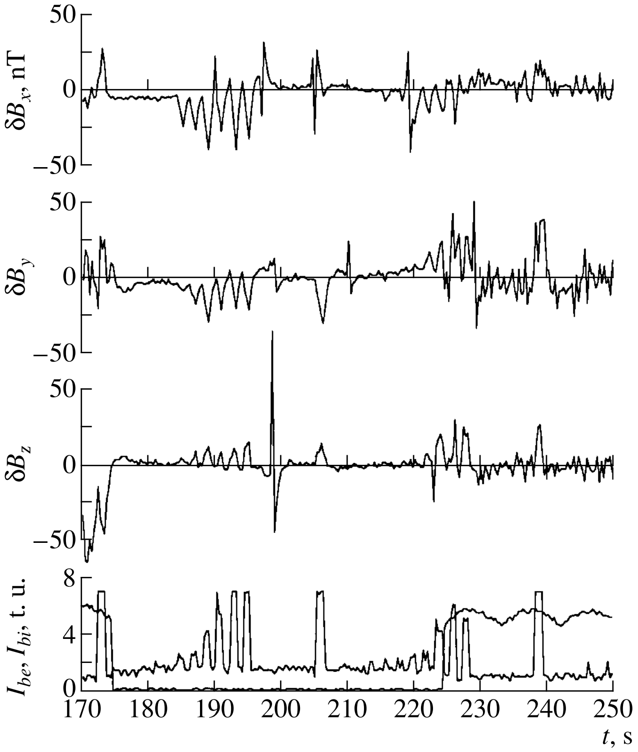

Fig. 2. Magnetic field fluctuations δB_{xyz} during two 23-s cycles of operation of an electron accelerator (without modulation at the first second; with amplitude–frequency modulation at the third, fifth, seventh, etc., second; even-numbered seconds correspond to pauses); the accelerator operates simultaneously with a plasma injector. The currents I_{be} and I_{bi} are given in telemetry units (volts).

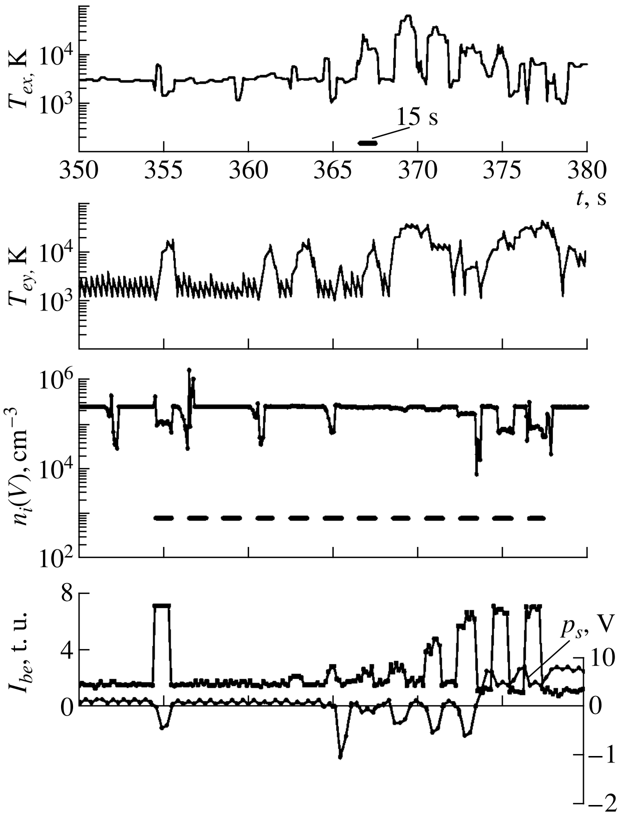

Fig. 3. Time evolution of the temperature components T_{ex} and T_{ey}, density $n_{ix}(V)$, and potential p_s during the operation of gun $G1$. The sweep duration of the RPA voltage is Δt_0 = 4 s. Horizontal bars show the time intervals of electron injection.

ence and $\mathbf{B}_0^*$ is the projection of the vector $\mathbf{B}_0$ onto the xy plane. The x-, y-, and z-axes correspond to the azimuthal (ϑ), radial (r), and axial (z) directions in cylindrical coordinates with the z-axis parallel to the magnetic field $z \parallel \mathbf{B}_0$.

3. EXPERIMENT

It is worth noting some characteristic features of the experiment. The electron beam and a quasineutral xenon plasma were simultaneously injected into the ionosphere, but the electron-beam and plasma injectors operated asynchronously, which ensured a wide choice of experimental conditions. Here, “asynchronous” operation means that different injectors were switched on and off independently of each other and the spectral measurements were not synchronized with the injector operation. The orientation of the magnetic field $\mathbf{B}_0$ was such that the pitch angles of the electron injection lay within the interval $\alpha_{pe} \simeq 74°–87°$ ($z \ge 0$) and the pitch angles of the ion injection lay within the interval $\alpha_{pi} \simeq 121°–132°$ ($z \le 0$); i.e., the electron and ion beams were injected in opposite directions with respect to the z-axis. All measurements were performed at the illuminated part of the satellite trajectory, where the electron plasma frequency and gyrofrequency varied within the intervals $\omega_{pe}/2\pi \approx 4.8–4.9$ MHz and $\omega_{ce}/2\pi \approx 1.1–1.2$ MHz, respectively. Figure 2 shows the magnetic field fluctuations $\delta\mathbf{B} = \mathbf{B} - \bar{\mathbf{B}}_0$ induced during electron beam injection, where $\bar{\mathbf{B}}_0$ is the empirical average value. The magnetic field perturbations δB_{xyz} were observed during the first second in the case of continuous (dc) injection and after the fifteenth second in the case of modulated (ac) injection (f_m = 15.625 kHz) with a pulse duration of $\tau_0 \simeq 2$ μs. Injection was accompanied by both intense transverse plasma heating (an increase in T_{ex} and T_{ey}) and density perturbations $\delta n_i \equiv n_i - \bar{n}_i$, which depended on the RPA grid potential V. Figure 3 shows the values of these parameters recorded during the operation of gun $G1$ ($t \simeq 350–380$ s). In Figs. 2 and 3, the time is counted from the beginning of the active regime, t_0 = 13 h 36 min 58.496 s UT (the altitude is $H \simeq 450–470$ km; turn no. 266; January 9, 1992).

4. ELECTRON BEAM INJECTION AT LARGE ANGLES TO THE MAGNETIC FIELD

Quasi-transverse (with respect to the magnetic field) electron injection exhibits a number of specific features and deserves special consideration. When examining the beam–plasma interaction, the decisive factors are the shape, density, and temperature of the electron beam. A certain fraction of the injected electrons returns to the satellite or moves away in the opposite direction with respect to the magnetic field, thereby decreasing the effective injection current. Therefore, we briefly consider the main features of this interaction.

4.1. Beam–Plasma Instability

In the absence of a beam–plasma discharge (BPD) at high altitudes, the main mechanism for the energy dissipation of the beam electrons is the beam–plasma instability. The efficiency of wave excitation in the RF (at ω_{ce} or ω_{pe}) and ELF–LF ($\omega \le \omega_{ci}, \omega_{pi}$) ranges and the instability growth rate γ depend strongly on the value of the relative detuning from the cyclotron resonance $n\omega_{ca}$ ($a = e, i$) [4]:

$$z_n = \frac{\omega \mp n|\omega_{ca}| - k_z u}{\sqrt{2} k_z v_{be}},$$

where the upper or lower sign is taken for the normal or anomalous Doppler effect, respectively; k_z is the projection of the wave vector onto the z-axis; and v_{be} is the thermal velocity of the beam electrons. The average (over the parameter α) flow velocity was determined from the expression $u \equiv \langle v_z \rangle_\alpha = (1/\Delta\alpha') \int_{-\Delta\alpha'/2}^{+\Delta\alpha'/2} v \cos(\alpha_{pe} + \alpha) d\alpha$, where the effective pitch-angle width of injection is $\Delta\alpha' > \Delta\alpha$ ($\simeq 4°$ at $z = 0$). The amplitude of the longitudinal-velocity fluctuations at $\gamma \longrightarrow 0$ was estimated as $\delta v_z \equiv \max\{v_z - \langle v_z \rangle_\alpha\}$. When examining the beam–plasma interaction, we assumed the electron beam to be hollow, which corresponds to a greater extent to the shape of a real electron beam not only at large z, but also in the near injection region at distances $z \ll u/\gamma$ [6]. When calculating the beam density at large pitch angles $\alpha_{pe} + \Delta\alpha'/2 > 90°$, we took into account the partial charge loss; in this case, the average density $\langle n_{be} \rangle$ was determined from the expression for the injection current I_1 into the lower hemisphere $I_1 \simeq 2\pi \int_{r_1}^{r_2} e v_z(r) n_{be}(r) r dr$, where r_1 and r_2 are the minimum and maximum radii of electron gyration at the inner and outer boundaries of the beam. For the actual beam and plasma parameters ($n_{be}/n_0 \sim 10^{-3}$–10^{-4}, $\Delta v/v \sim 10^{-1}$–10^{-2}, and $\Delta\alpha' \simeq 14°$–$16°$), the growth rate of plasma oscillations is $\gamma/\omega_{pe} \sim 10^{-2}$–$10^{-3}$. When the electric field amplitude reaches the saturation level $\delta E_f^2/4\pi \simeq n_{be} m v^2 (\gamma/\omega_{pe})$, the beam–plasma system becomes unstable [7]. Estimating the value $\eta^f = W^f/n_0 T_e \simeq (\delta E_f^2/8\pi n_0 T_e)^2$ shows that, for the above spread in the beam parameters, the turbulence level lies in the range $m/M \ll \eta^f \ll 1$ and the energy transfer toward shorter wavelengths (with a rate on the order of the modulational instability growth rate $\gamma_0/\omega_{pe} \sim 10^{-2}$–$10^{-4}$) comes into play, which ultimately results in the suppression of the beam–plasma instability due to the detuning of the resonance.

4.2. Generation of Electromagnetic Fields by the Electron Beam

During the first second of dc electron injection, the excitation of magnetic fields in the immediate vicinity of the satellite depends substantially on the development of the Langmuir and ion-acoustic turbulence in the plasma. The wave excitation in different frequency ranges may exert a focusing effect on the electron beam. When considering the wave excitation in the LF and RF ranges ($\omega \sim \omega_A$, ω_{ci} or $\sim\omega_{ce}$, ω_{pe}), we will assume the following:

(i) The level of ion-acoustic turbulence $\eta^s = W^s/n_0 T_e \simeq (\delta E_s^2/8\pi n_0 T_e)^2$ becomes higher than that of Langmuir turbulence, $\eta^s > \eta^f$, in a time of $\sim 1/\gamma_0$. Further, this inequality may be violated. At $\eta^s > \eta^f$, a slow growth of perturbations dominates: $\delta\Psi = \delta\Psi' + \delta\Psi^s$, where $\delta\Psi'$ and $\delta\Psi^s$ are the very slowly varying (on the characteristic time scale $\tau \sim \omega_A^{-1}$ or ω_{ci}^{-1}) and slowly varying (on the characteristic time scale $\tau \sim \omega_{pi}^{-1}$) parts of perturbations. Otherwise, at $\eta^s < \eta^f$, we should consider fast growing perturbations: $\delta\Psi = \delta\Psi^s + \delta\Psi^f$. Here, $\delta\Psi^s$ and $\delta\Psi^f$ are the ion-acoustic and Langmuir perturbations developing on the characteristic time scales $\tau \sim \omega_{pi}^{-1}$ and $\tau \sim \omega_{pe}^{-1}$, respectively.

(ii) The source of density perturbations $\delta n'$ ($\delta n'_{be}$) may be a parametric instability in the course of which the Alfvén pump wave decays into Alfvén and magnetoacoustic waves $a \longrightarrow a + s$; the latter causes density perturbations [8]. The action of ponderomotive forces caused by nonlinear Alfvén waves also produces a strong density perturbation $\delta n' \sim |\delta \mathbf{B}'|^2$ [9].

(iii) Magnetic field perturbations $\delta \mathbf{B}$ can be represented as a superposition of the envelope of an Alfvén wave packet and slowly varying fields induced by nonlinear plasma currents. Without taking into account the contribution from partial currents $\sim\langle \delta n'_{be} \delta \mathbf{v}' \rangle$ and $\sim\langle \delta n^s_{be} \delta \mathbf{v}^s \rangle$, the magnetic perturbation amplitude does not exceed the value $\delta B_{x,y,z} \sim I_{be}/r_{ce}$ 10–20 nT, where $\langle \ldots \rangle$ stands for the mean value of the product of two simultaneous fluctuations.

(iv) The equilibrium values of the plasma parameters are defined as $\Psi^0 = \Psi_0 + \delta\Psi$, where Ψ_0 denotes the unperturbed values and $\delta\Psi$ denotes the perturbations introduced by a steady electron beam. At small deviations from equilibrium, the fluctuation spectrum has maximums near the plasma eigenmodes. In this case, the low-frequency range makes the main contribution to suppressing instabilities.

(v) The unperturbed values of the beam density and temperature are assumed to be the equilibrium values $n_{be0} \equiv n_{be}^0$ and $T_{be0} \equiv T_{be}^0$ in the absence of perturbations ($\gamma \longrightarrow 0$). Simultaneous fluctuations of the density and temperature in a spatially uniform plasma are statistically independent; i.e., $\langle \delta n \delta T \rangle_\tau = 0$.

These assumptions on the interaction processes allow us to focus attention on a more detailed analysis of the data obtained and the mechanisms governing the excitation of low-frequency waves at injection angles of $\alpha_{pe} \simeq 74°–87°$.

5. ANALYSIS OF EXPERIMENTAL RESULTS

To analyze the experimental results, the data obtained during a series of 23-s measurement cycles were treated using an algorithm based on small variations of the parameters of an unperturbed plasma—a procedure that was best suited to the laboratory style of the experiments.

The experimental data and the numerical characteristics constituted a set of parameters for a real event $S_j(h_1, h_2, \ldots, h_i, \ldots; s_1, s_2, \ldots, s_i, \ldots; t_j)$, where h_i and s_i are the measured and calculated values, respectively. In order that the parameters h_i and s_i corresponded to the time $t_j \pm \delta t$ ($\delta t \ll \Delta t$), the "current" numerical amplitudes in the nodes of the time mesh t_j were interpolated by weighting the "old" and "new" measured values of these parameters; here, Δt is the period of telemetry polling. The instants t_j were not chosen arbitrarily, but with regard to the most frequently measured parameters. The events S_j and S_{j+1} were considered to be single events if the relaxation time of perturbed characteristics of the ionospheric plasma satisfied the inequality $\tau_r < t_{j+1} - t_j$. After selecting the set S_j of the data (records) and completing the formation of the file, the data were processed with the aim of examining certain effects during dc injection. When plotting the dependence on a certain parameter, the records S_j were arranged in ascending order of this parameter.

Figure 4 shows the density n_{ix} as a function of the parameter $V + p_s$ and the azimuthal and radial compo-

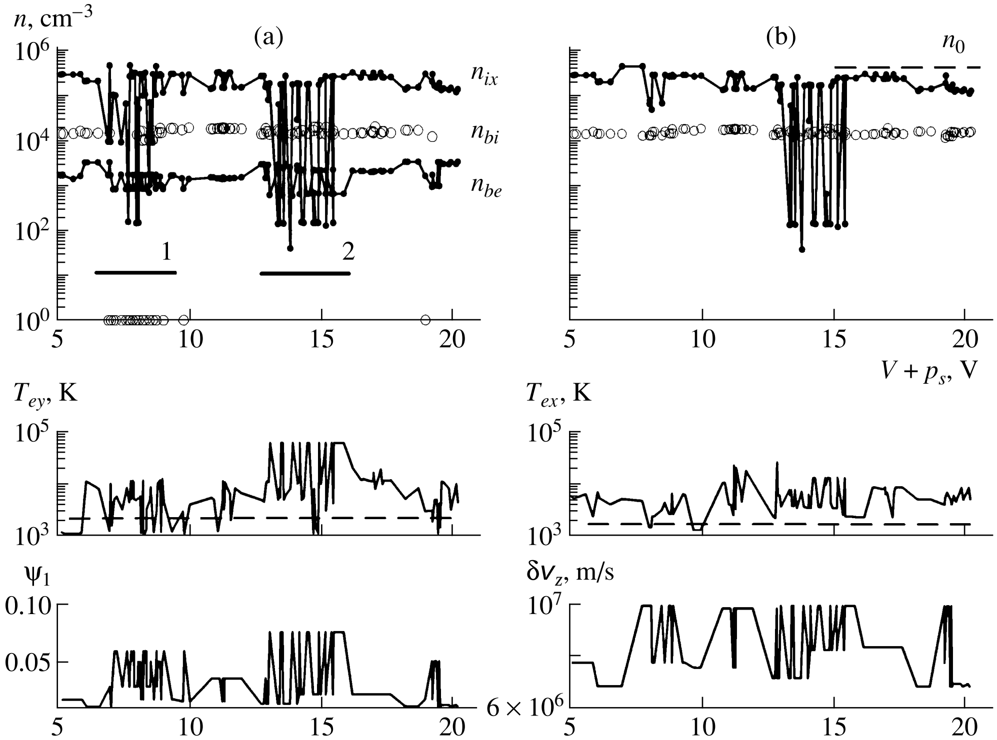

Fig. 4. Measured ion density n_{ix} as a function of the parameter $V + p_s$ and the results of simultaneous measurements of the electron temperatures T_{ex} and T_{ey} and the calculated values of the densities n_{be} and n_{bi}, quantity ψ_1, and velocity fluctuations δv_z vs. the same parameter: (a) the data obtained with the electron accelerator *G*1 independently of the plasma injector operation ($n_{bi} \geq 1$ cm^{-1}), and (b) the data obtained with simultaneous injection of the electron beam and quasineutral plasma ($n_{bi} > 1000$ cm^{-3}). Horizontal dashed lines show the unperturbed levels of T_{ex} and T_{ey} and the RPA saturation level for n_0.

nents of the electron temperature (T_{ex} and T_{ey}, respectively) and the quantity $\psi_1 = \cos^3(\alpha_{pe} - \Delta\alpha'/2) - \cos^3(\alpha_{pe} + \Delta\alpha'/2)$ versus the same parameter. Note that the parameter $V + p_s$ is the true retarding potential at the RPA grid with respect to the ambient plasma. Along with the calculated value of the electron-beam density, the estimated value of the density n_{bi} of the xenon plasma jet in the stage of free gyration is also presented, which allows us to trace the effects from the simultaneous operation of both injectors. One can see a satisfactory correlation between the increase in the xenon-plasma temperature T_{ey} and the function ψ_1 in regions *1* and *2*. This fact can be used to evaluate the increase in the electron beam temperature $\delta T'_{be} \sim \delta T'_e$, which is quite reasonable in view of the boundary conditions for thermal diffusion in the plasma. This problem requires more detailed study; here, we only formulate it: (i) electron injection at angles in the range $90° - \alpha_{pe} < \Delta\alpha'/2$ results in insignificant heating, and (ii) it causes substantial heating with respect to the transverse component at smaller injection pitch angles. The interpretation of the change in the ion composition is ambiguous. The decrease in the ion density in region *1* (or *2*) (Fig. 4a), in which $M_a(v_s \cos\theta_v)^2/2 \geq e(V + p_s) \approx 7$–$9$ eV (or 13–15 eV), where a is the ion species, is due to the depletion of the O^+ ions and the NO^+/O_2^+ group. This depletion may be attributed either to plasmochemical reactions of the form $e + NO^+ \longrightarrow NO^* + \hbar\nu$ (the Knudsen mechanism) or, most likely, to the fact that these ions are entrained by ELF and VLF waves into motion along the z-axis under conditions of the cyclotron resonance $\omega = \mathbf{k} \cdot \mathbf{v}_{ia} \pm n|\omega_{ci}|$, where $n = 0, \pm 1$. In regions *1* and *2*, one can also see strong perturbations of all the plasma parameters, which are correlated with the density of the injected electron beam (i.e., with the growth rate of the high-frequency beam–plasma instability) in spite of the fact that the parameter $V + p_s$ is an internal RPA characteristic.

Figure 5a presents the results of the wave measurements of the magnetic component of VLF and LF waves $\delta B'$ in a form similar to dependences shown in Fig. 4. It should be noted that the representation of the wave measurements versus $V + p_s$ makes sense only in connection with the data in Fig. 4 and only serves to provide additional information. The figure also shows the growth rate γ' of the Alfvén waves excited due to the cyclotron interaction via the anomalous Doppler effect ($\omega < \omega_{ci}$, $n = 1$) for a hydrogen plasma at propagation angles of $80° < \theta < \theta_r$, where $\theta_r \sim 87°$–$89°$ is the resonance angle. When calculating the growth rate, we tried to keep the detuning z_1 small ($\gamma' \neq 0$); however, this was possible only for hydrogen plasma, quasi-transverse propagation angles, and frequencies $\omega \leq \omega_{ci}$. We note certain characteristic features of VLF and LF fields for the group of data in region *2*. At frequencies $\omega \leq \omega_{ci}$, the

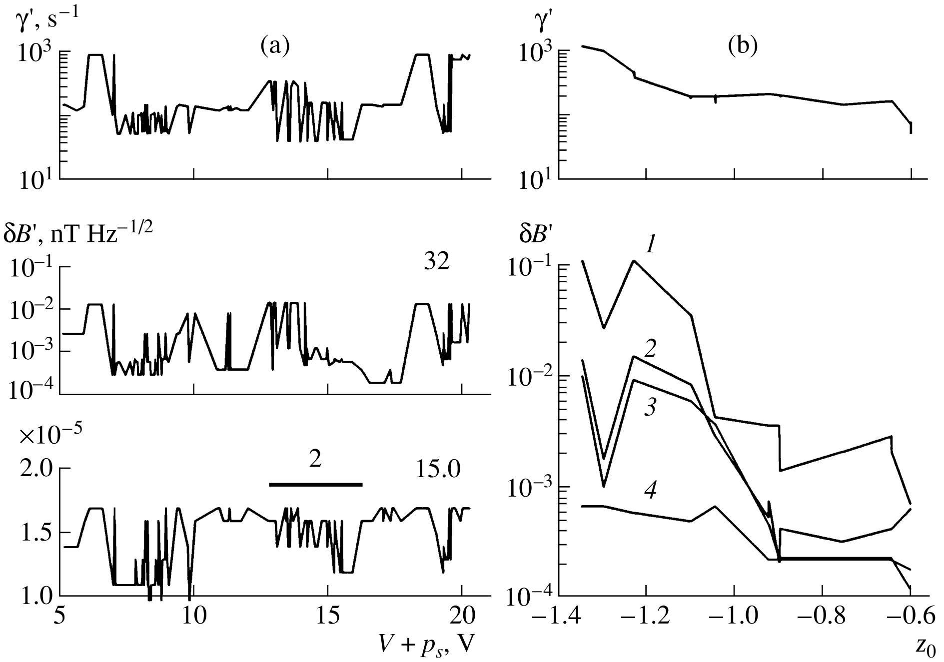

Fig. 5. (a) VLF perturbations of the magnetic field $\delta B'$ at frequencies $\omega/2\pi = 32$ and 15.0 kHz as functions of the parameter $V + p_s$; (b) the perturbations $\delta B'$ at frequencies of (*1*) 8, (*2*) 32, (*3*) 50, and (*4*) 149 Hz as functions of the parameter $z_0 \sim -u/v_{be}$ ($n = 0$). At the top of the figure, the estimated growth rate of the wave at the frequency $\omega_{ci} - \omega = 150$ Hz ($\theta = 85°$) and detuning $\delta\omega \sim 500$ Hz for $M/m = 1841$ and $\Delta v/v \sim 10^{-1}$ is shown. The data are obtained at $n_{bi} \geq 1$.

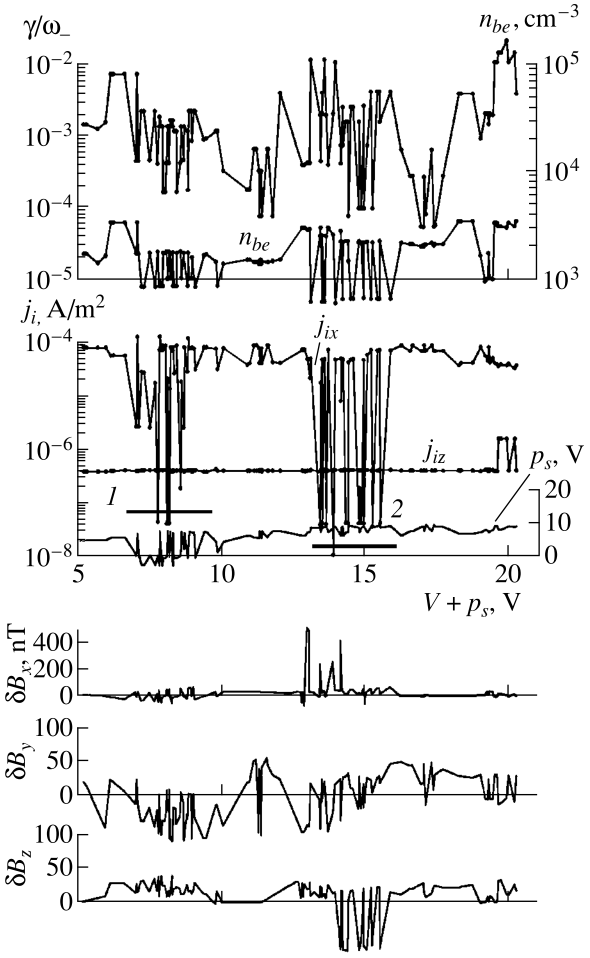

Fig. 6. Energy distributions of the ion flux densities j_{ix} and j_{iz}, magnetic field perturbations δB_{xyz}, and the satellite potential p_s as functions of $V + p_s$ for $n_{bi} \geq 1$. At the top of the figure, the growth rate γ/ω_- is shown.

magnetic component amplitude correlates well with the growth rate $\gamma' \sim n_{be}$; however, at higher frequencies (in the ion-acoustic range), we observed an appreciable attenuation of the signal. This effect can be explained based on assumption (iv) of Section 4.2 on the dominant role of low-frequency instabilities. Figure 5b shows the amplitude and growth rate of magnetic field perturbations (the same quantities as in Fig. 5a) as functions of the relative detuning $z_0 \sim u/v_{be}$, where $v_{be} \sim \Delta v \equiv (\delta v_z^2 + \delta v_\perp^2)^{1/2}$. We can infer that the excitation of LF waves is less sensitive to the thermal spread of the beam particles; this tendency is clearer at lower frequencies. This result agrees with the accepted concept of the effect, although it requires more detailed study.

The data presented in Fig. 6 demonstrate a number of effects associated with the excitation of anomalous, slowly varying magnetic fields that may be a macroscopic consequence of the development of small-scale wave processes. In the figure, we present the energy distributions of the ion flux densities j_{ix} and j_{iz}, the satellite body potential p_s, and the growth rate of potential lower hybrid plasma oscillations with the frequency ω_-. Note that, for a plasma perturbed by an electron beam, it is more adequate to interpret the RPA data in terms of the integral ion flux density j_i (the current density). The remarkable feature is the unexpectedly strong excitation of the magnetic field. By comparing the perturbations $\delta\mathbf{B}$ with the data on the magnetic components of VLF and LF waves and the growth rate γ' (at $\omega \leq \omega_{ci}$), we may suppose that there is an internal coupling among them, which can be explained based on assumption (iii) of Section 4.2. When studying this problem, attention is usually focused on the behavior of the large-scale field arising due to the interaction of kinetic (the velocity field $\mathbf{U}$) and magnetic (the field $\mathbf{B}$) modes. This interaction is described by two similar equations for the momentum and induction, the term curl($\mathbf{U} \times \mathbf{B}$) being the main source of magnetic energy [1]. In regards to microscale processes, they determine the fluctuation spectrum and the energy transfer toward short scale lengths. Based on assumptions (i) and (iv) of Section 4.2, we can suggest that these hydrodynamic processes at the equilibrium stage of interaction are responsible for weaker perturbations of the magnetic field component $\delta B_z \sim$ 70–80 nT (group *2*). To summarize the results presented, we note that the gradient character of the instability ($\nabla n \neq 0$ and $\nabla T \neq 0$) is typical of both groups *1* and *2* and may also be responsible for the excitation of anomalously large magnetic fluctuations.

6. CONCLUSION

The most remarkable experimental results obtained in turn no. 266 during electron beam injection at pitch angles $\alpha_{pe} \simeq 74°$–$87°$ are the following:

(i) The beam–plasma instability results in the excitation of waves in different frequency ranges: (a) in the frequency range $\omega \leq \omega_{ci}$, the growth of the magnetic component of VLF waves is observed, and (b) the increase in the thermal spread of the beam electrons leads to the suppression (decay) of the excited VLF waves.

(ii) The electron beam injection is accompanied by strongly anisotropic plasma heating and the modulation of the plasma (ion) flows in the vicinity of the satellite: (a) for an unmodulated injection, the efficiency of plasma (beam) heating with respect to the transverse component decreases substantially at pitch angles $\alpha_{pe} + \Delta\alpha'/2 > 90°$, where $\Delta\alpha'$ is the effective angular beam width, and (b) the decrease in the integral ion flux densities j_{ix} with energies of 7–9 and 13–15 eV is probably a consequence of the resonant coupling with the excited VLF waves.

(iii) Among the remarkable results, we can also mention (a) the anomalous resonant increase in the magnetic field δB by two orders of magnitude ($||\delta B_x|_{\max} \sim 500$ nT) as compared to the nominal value $\delta B_{\rm n} \sim I_{be}/r_{ce} \simeq 10$–20 nT and (b) magnetic field fluctuations with an amplitude of $\delta B_z \sim 70$ nT in the quasi-equilibrium case.

Some of these results confirm the results obtained previously in space experiments; however, for the most part, they are new and require further investigations.

ACKNOWLEDGMENTS

We thank our colleagues for help and fruitful discussions. We also thank V.I. Karas’ for his interest in this work.

REFERENCES

1. L. D. Landau and E. M. Lifshitz, *Electrodynamics of Continuous Media* (Gostekhizdat, Moscow, 1959; Pergamon, New York, 1984).
2. H. K. Moffatt, *Magnetic Field Generation in Electrically Conducting Fluids* (Cambridge Univ. Press, Cambridge, 1978; Mir, Moscow, 1980).
3. C. Uberoi, Phys. Fluids **15**, 1673 (1972).
4. K. N. Stepanov and A. B. Kitsenko, Zh. Tekh. Fiz. **31**, 167 (1961) [Sov. Phys. Tech. Phys. **6**, 120 (1961)].
5. V. N. Oraevsky and P. Triska, Adv. Space Res. **13**, 10103 (1993).
6. R. M. Winglee and P. L. Pritchett, J. Geophys. Res. **93**, 5823 (1988).
7. N. G. Matsiborko, I. N. Onishchenko, Ya. B. Faĭnberg, *et al.*, Zh. Éksp. Teor. Fiz. **63**, 874 (1972) [Sov. Phys. JETP **36**, 460 (1973)].
8. A. A. Galeev and V. N. Oraevsky, Dokl. Akad. Nauk SSSR **147**, 71 (1962) [Sov. Phys. Dokl. **7**, 988 (1963)].
9. S. R. Spangler, Phys. Fluids B **1**, 1738 (1989).

Translated by N.F. Larionova

Plasma Physics Reports, Vol. 27, No. 4, 2001, pp. 330–334. Translated from Fizika Plazmy, Vol. 27, No. 4, 2001, pp. 350–355.
Original Russian Text Copyright © 2001 by Kazimura, Sakai, Bulanov.

BEAMS IN PLASMA

Relaxation of an Electron Beam during the Onset of the Electromagnetic Filamentation Instability

Y. Kazimura*, J.-I. Sakai*, and S. V. Bulanov**
**Toyama University, Gofuku 3190, Toyama 930-8555, Japan*
***Institute of General Physics, Russian Academy of Sciences, ul. Vavilova 38, Moscow, 117942 Russia*

Received September 12, 2000

Abstract—Results are presented from three-dimensional particle-in-cell simulations of relaxation of an electron beam in a plasma. When penetrating into the plasma, the electron beam generates the return current carried by the plasma electrons. In a collisionless plasma, the relaxation mechanism is related to the onset of an electromagnetic filamentation instability. The instability leads to the generation of a quasistatic magnetic field, which decays due to the magnetic field reconnection in the final stage of the system evolution. *© 2001 MAIK “Nauka/Interperiodica”.*

1. INTRODUCTION

Investigations of the collective phenomena in interpenetrating collisionless plasma flows have been motivated by the important role of these phenomena in the dynamics of dense charged-particle beams [1, 2] and in the processes occurring in astrophysical [3, 4] and laser [5–9] plasmas. The interaction of plasma flows is accompanied by the generation of strong electric and magnetic fields. Even if both the plasma charge and the net plasma current vanish almost completely in the initial state, strong electric and magnetic fields arise due to the onset of electromagnetic instabilities. These instabilities are similar in character to the well-known Weibel instability [10, 11] and are caused by the anisotropy of the particle distribution function in velocity space [10–12]. This instability was incorporated in developing the theory of the generation of quasistatic magnetic fields in laser and space plasmas, whose anisotropy is related to the presence of high-energy electron flows. In laser plasmas, spontaneous magnetic fields generated by relativistically strong electromagnetic radiation result in the magnetic interaction of self-focusing channels [13, 14]. In space plasmas, an efficient mechanism for the generation of quasistatic magnetic fields is required to explain cosmological gamma-ray bursts [15]. It is supposed that cosmological gamma-ray bursts are generated in explosions with an energy release of $E \approx 10^{51}$–10^{54} erg over several seconds in a relatively small spatial region. Afterglow radiation of gamma-ray bursts are caused by the synchrotron radiation of electrons and positrons in a strong magnetic field, which, in turn, arises during the development of an electromagnetic filamentation instability [16, 17]. An analytical description of a highly nonlinear stage of the filamentation instability with allowance for kinetic effects presents significant difficulties. Hence, the necessity of numerical simulations is obvious.

The investigation described in this brief communication is related, first of all, to the problem of the nonlinear evolution of electron beams accelerated during the interaction of laser radiation with a plasma. At present, due to the advanced level of laser technology [18], experiments on the interaction of multiterawatt (or even petawatt) laser radiation with matter are being carried out in many laboratories [5–8]. One of the important directions of these studies is related to the concept of fast ignition in laser fusion research [19]. The concept of fast ignition implies that a strongly focused ultrashort laser pulse ignites a thermonuclear reaction in a precompressed target. In this case, ignition occurs in the isochoric mode (at a constant density). In contrast to the more developed concept of isobaric ignition, which occurs at a constant pressure, the fast ignition concept implies that thermonuclear burning is initiated at a much smaller energy of the laser pulse. In this model, the study of collective mechanisms for the relaxation of electron beams in a plasma is of primary importance, because, in the vicinity of the critical plasma density, the energy of laser radiation is transformed into the energy of fast electrons. Then, the energy is transferred by fast electrons deep into the plasma, where it is absorbed.

This paper presents the results from particle-in-cell (PIC) simulations of the relaxation of a fast electron beam. We used a modified version of the 3D3V-TRISTAN electromagnetic code [20], which allowed us to simulate particle distributions that depend on three spatial coordinates and three velocity components. Two configurations are investigated. In the first configuration, interpenetrating plasma flows are homogeneous at the initial instant, whereas in the second configuration, the flows are localized in a cylindrical region, outside of which the plasma is at rest. In both cases, the plasma configurations are unstable against the electromagnetic instability, the filamentation of the electric current density, and the merging of current filaments. The instability is accompanied by the generation and subsequent decay of a quasistatic magnetic field.

2. FORMULATION OF THE PROBLEM

We used the 3D3V-TRISTAN electromagnetic PIC code [20]. In the initial state, the electric charge density and electric current in a plasma are equal to zero and the electron component is represented as a sum of two interpenetrating flows with different velocities and densities. We performed numerical simulations for two different initial configurations.

In velocity space, the flows obeyed the Maxwell distribution

$$f_{ej}(v) = \frac{n_{e,j}}{(2\pi v_{e,th,j})^{3/2}} \times \exp\left(-\frac{v_x^2 + v_y^2 + (v_z - v_{e,j})^2}{2v_{e,th,j}}\right), \quad j = 1, 2; \tag{1}$$

where $v_{e,th}$ is the thermal velocity of the electrons, $v_{e,j}$ is the directed electron velocity, $n_{e,j}$ is the electron density in the jth flow. The directed electron velocities were equal to $v_{e1} = 3v_{e,th}$ and $v_{e,2} = 6v_{e,th}$. The electron densities in the flows moving in the positive and negative directions along the z-axis were equal to $n_{e1} = 2n_0/3$ and $n_{e2} = n_0/3$, respectively. Here, n_0 is the ion density in the initial state. At the initial instant, the conditions $\sum_j n_{ej} v_{ej} = 0$ and $\sum_j n_{ej} = n_0$ were satisfied, the ion temperature was equal to the electron temperature, and the directed ion velocity was equal to zero. The ion-to-electron mass ratio was equal to $m_i/m_e = 1836$.

In the second configuration, the electron beams were located in a cylindrical region whose diameter was smaller than the size of the computation region; the remaining part of the computation region was occupied by a uniform plasma with the same density.

In simulations, the size of the spatial cell was set to be $\Delta x = v_{e1}/3\omega_{pe}$. The time step was equal to $\Delta t = 0.05\omega_{pe}^{-1}$. Here, $\omega_{pe} = (4\pi n_0 e^2/m_e)^{1/2}$ is the electron Langmuir frequency. In the first case (homogeneous interpenetrating electron flows), the dimensions of the computation region were $L_x = 40\Delta x$ along the x-axis, $L_y = 40\Delta x$ along the y-axis, and $L_z = 200\Delta x$ along the z-axis. In the second case, the electron beams were inside a cylinder of radius $L_z = 20\Delta x$. In this case, the dimensions of the computation region were $80 \times 80 \times 100(\Delta x)^3$. In both cases, the periodic boundary conditions for an electromagnetic field and particles were imposed at the boundaries of the computation region. The number of particles in a cell was approximately equal to 30.

3. SIMULATION RESULTS

3.1. Homogeneous Electron Beams

In the initial state, the plasma is neutral and the net plasma current is zero, so that both the electric and magnetic fields are absent. The electric and magnetic fields arise due to the onset of instability. The transverse (with respect to the electron beam propagation direction) component of the magnetic field is mainly generated. This is seen in Fig. 1, which shows the time

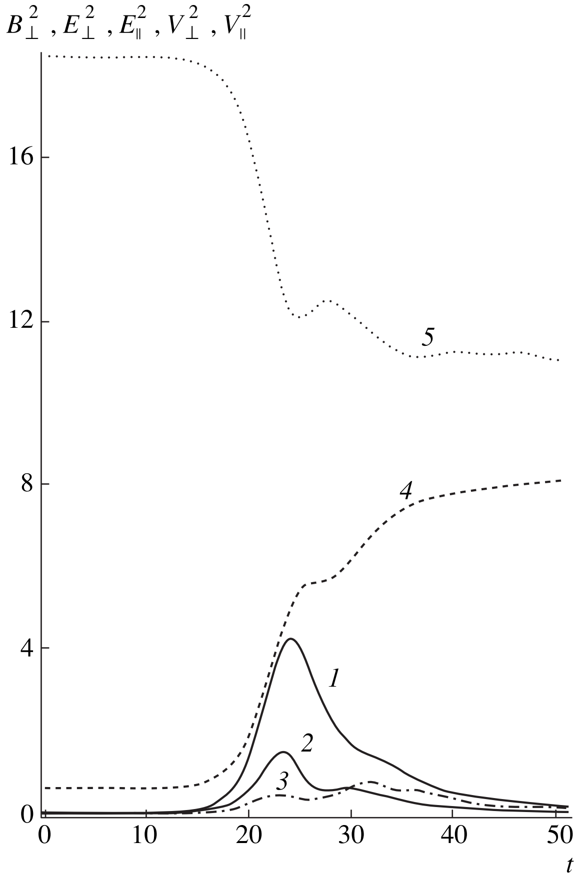

Fig. 1. Time dependences of (*1*) the square of the magnetic field strength $B_\perp^2$, squares of the (*2*) transverse $E_\perp^2$ and (*3*) longitudinal $E_\parallel^2$ components of the electric field, and averaged squares of the (*4*) transverse $V_\perp^2$ and (*5*) longitudinal $V_\parallel^2$ components of the electron velocity. The squares of the electric and magnetic fields are normalized to $8\pi n_0 v_{th,e}^2$, and the squares of the velocity components are normalized to $v_{th,e}^2$. The time is in units of ω_{pe}^{-1}. In the initial state, the electron beams are homogeneous.

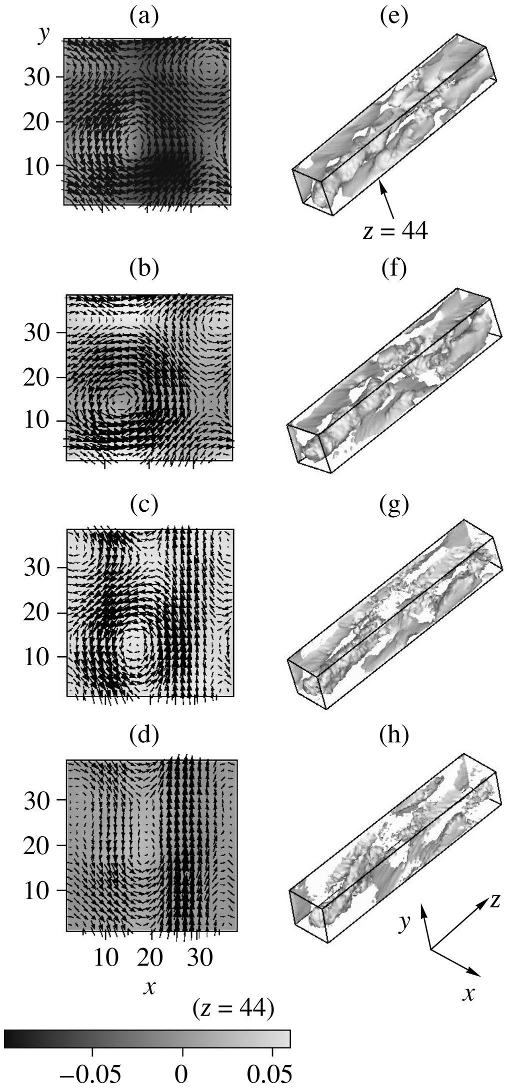

Fig. 2. (a–d) Distributions of the *z*-component of the electric field and the magnetic field in the plane $z = 44$ and (e–h) the surfaces of a constant value of the *z*-component of the electric current density j_z for different instants from $t = 25$ to 40 with a time step of $\delta t = 5$. In the initial state, the electron beams are homogeneous.

dependences of the squares of the magnetic field strength, the squares of the transverse and longitudinal components of the electric field, and the averaged squares of the transverse and longitudinal components of the electron velocity. The squares of the electric and magnetic fields are normalized to $8\pi n_0 v_{th,e}^2$, and the squares of the velocity components are normalized to $v_{th,e}^2$. The time is in units of ω_{pe}^{-1}.

It is seen that all of the quantities vary most rapidly within the time interval $15 < t < 25$, during which the isotropization of the electron velocity occurs: the longitudinal kinetic energy decreases, while the transverse energy increases. This process is accompanied by a partial transformation of the electron kinetic energy into the energy of electric and magnetic fields. Since both the transverse and longitudinal field components are generated, we may conclude that the perturbations with the wave vector directed at an angle of about 30° with respect to the electron beam propagation direction are the most unstable. This agrees with analytical results [21]. By the time $t = 20$, when the magnetic field reaches its maximum, the efficiency of transformation of the electron kinetic energy into magnetic field energy is about 20%. Then, the magnetic field decays. In this stage, the longitudinal component of the electric field appreciably increases. This fact, together with the change in the topology of the magnetic field (see Fig. 2), allows us to suppose that the magnetic field decays due to collisionless reconnection of magnetic field lines.

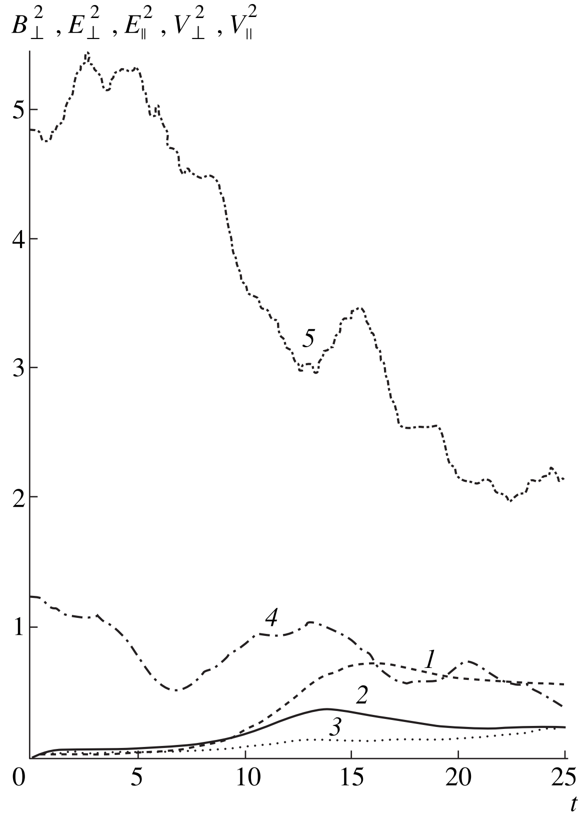

Fig. 3. Same as in Fig. 1, but for finite-size electron beams.

Figure 2 shows (a–d) the distribution of the *z*-component of the electric field (shades of gray) and the structure of the magnetic field (arrows) in the (*x*, *y*) plane at $z = 44$ and (e–h) the surfaces of a constant value of the *z*-component of the electric current density j_z for different instants from $t = 25$ to 40 with a time step of $\delta t = 5$. One can see the formation of helical current filaments and the corresponding structure of the magnetic field with X- and O-type null points in the plane $z = 44$. The magnetic field is nonsteady, and, in the vicinities of X points, current sheets arise and disappear. These current sheets are clearly seen in plot (b) at $8 < x < 22$ and $y = 35$, in plot (c) at $x = 35$ and $5 < y < 15$, and in plot (d) at $x = 17.5$ and $20 < y < 30$. During the evolution of the system, the longitudinal electric field is generated, which can lead to the acceleration of a small fraction of particles.

3.2. Finite-Size Electron Beams

In this case, the electron beams are initially located in a cylindrical region of radius $R = 20\Delta x$. As in the previous case, in the initial state, the plasma is neutral and the net plasma current is zero, so that both the electric and magnetic fields are absent. The fields arise due to the onset of instability. As previously, the transverse (with respect to the electron beam propagation direction) component of the magnetic field is mainly generated. This is seen in Fig. 3, in which the same time dependences as in Fig. 1 are shown.

It is seen that all of the quantities vary most rapidly within the time interval $12.5 < t < 17.5$. As in the previous case, both the transverse and longitudinal field components are generated. Hence, we may conclude that the perturbations with the wave vector directed at an angle of about 30° with respect to the electron beam propagation direction are the most unstable. By the time $t = 16$, when the magnetic field reaches its maximum, the efficiency of transformation of the electron kinetic energy into magnetic field energy is about 13%. The decay of the magnetic field is accompanied by an appreciable increase in the longitudinal component of the electric field.

Figure 4 shows (a–d) the structure of the magnetic field in the (x, y) plane at $z = 50$ and (e–f) the surfaces of a constant value of the z-component of the electric current density j_z for different instants: $t =$ (a, e) 5, (b, f) 10, (c, g) 15, and (d, h) 25. In the initial stage of instability (Figs. 4a, 4e), several relatively small-scale filaments with a transverse size of about the collisionless skin depth are formed. Note that similar structures were observed in 2D (with three velocity components and three electric and magnetic field components) numerical simulations of a similar problem [22]. Then, the magnetic field and electric current decay. A significant difference of 3D relaxation from 2D relaxation (which was investigated in detail in [22, 23] using numerical simulations for almost the same parameters of the problem) is that the electric current rapidly decays during 3D relaxation. In the 2D case, fairly long-lived ring structures were observed in [22, 23]. Inside these structures, the current flows in one direction, while outside of them, a neutralizing current flows in the opposite direction. In the 3D case, for the chosen parameters of the problem, such structures were not observed.

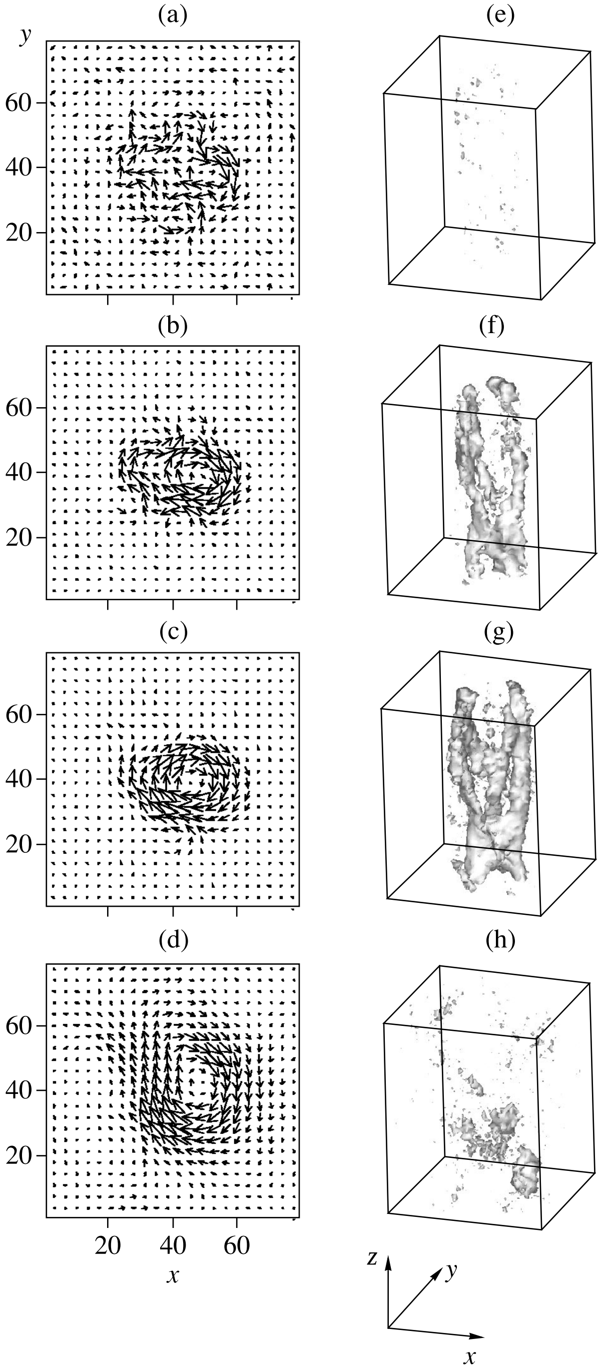

Fig. 4. (a–d) Distributions of the z-component of the electric field and the magnetic field in the plane $z = 50$ and (e–h) the surfaces of a constant value of the z-component of the electric current density j_z for different instants in the case of finite-size electron beams.

4. CONCLUSION

The collective evolution of electron beams in a plasma is investigated using 3D PIC simulations. In the initial stage, the filamentation instability develops. Then, the filaments merge. A significant difference of 3D relaxation from the previously investigated 2D relaxation is that 3D relaxation proceeds more rapidly, which is related to magnetic reconnection in a collisionless plasma. One of the possible reasons for faster reconnection may be the onset of instabilities that result in the excitation of small-scale (along the z-axis) perturbations and the anomalous plasma resistivity (as is known, this is impossible in the 2D case). Another reason may be related to the difference in the magnetic field topology in 2D and 3D geometries. A more detailed study of both the anomalous resistivity and 3D magnetic reconnection in a collisionless plasma goes beyond the scope of this brief communication and is the subject of our further study.

ACKNOWLEDGMENTS

We thank F. Pegoraro for fruitful discussions. One of the authors (S.V. Bulanov) was supported by the Russian Foundation for Basic Research, project no. 99-02-16997.

REFERENCES

1. R. B. Miller, *Intense Charged Particle Beams* (Plenum, New York, 1982).
2. J. D. Lawson, *The Physics of Charged Particle Beams* (Clarendon, Oxford, 1988).
3. V. S. Berezinskij, S. V. Bulanov, V. A. Dogiel, V. L. Ginzburg, and V. S. Ptushkin, *Astrophysics of Cosmic Rays* (North-Holland, Amsterdam, 1990).
4. T. Tajima and K. Shibata, *Plasma Astrophysics* (Addison-Wesley, Reading, 1997).
5. A. P. Fews, H. F. Norreys, F. N. Beg, *et al.*, Phys. Rev. Lett. **73**, 1801 (1994).
6. M. H. Key *et al.*, Phys. Plasmas **5**, 1966 (1998).
7. G. S. Sarkisov, V. Yu. Bychenkov, V. N. Novikov, *et al.*, Phys. Rev. E **59**, 7042 (1999); W. Yu, V. Bychenkov, and Y. Sentoku, Phys. Rev. Lett. **85**, 570 (2000).
8. S.-Y. Chen, M. Krishnan, A. Maksimchuk, and D. Umstadter, Phys. Plasmas **7**, 403 (2000).
9. S. V. Bulanov, T. Zh. Esirkepov, F. Califano, *et al.*, Pis'ma Zh. Éksp. Teor. Fiz. **71**, 593 (2000) [JETP Lett. **71**, 407 (2000)].
10. E. W. Weibel, Phys. Rev. Lett. **2**, 83 (1959); R. C. Morse and C. W. Neilson, Phys. Fluids **14**, 730 (1971).
11. V. Yu. Bychenkov, V. P. Silin, and V. T. Tikhonchuk, Zh. Éksp. Teor. Fiz. **98**, 1269 (1990) [Sov. Phys. JETP **71**, 709 (1990)].
12. F. Pegoraro, S. V. Bulanov, F. Califano, and M. Lontano, Phys. Scr. T **T63**, 262 (1996); F. Califano, F. Pegoraro, S. V. Bulanov, and A. Mangeney, Phys. Rev. E **57**, 7048 (1998); F. Califano, R. Prandi, F. Pegoraro, and S. V. Bulanov, Phys. Rev. E **58**, 7837 (1998); Y. Kazimura, F. Califano, J.-I. Sakai, *et al.*, J. Phys. Soc. Jpn. **67**, 1079 (1998).
13. G. A. Askar'yan, S. V. Bulanov, F. Pegoraro, and A. M. Pukhov, Pis'ma Zh. Éksp. Teor. Fiz. **60**, 240 (1994) [JETP Lett. **60**, 251 (1994)].
14. G. A. Askar'yan, S. V. Bulanov, F. Pegoraro, and A. M. Pukhov, Fiz. Plazmy **21**, 884 (1995) [Plasma Phys. Rep. **21**, 835 (1995)].
15. T. Piran, Phys. Rep. **314**, 575 (1999).
16. Y. Kazimura, J.-I. Sakai, T. Neubert, and S. V. Bulanov, Astrophys. J. Lett. **498**, L183 (1998).
17. M. V. Medvedev and A. Loeb, Astrophys. J. **526**, 697 (1999).
18. G. A. Mourou, C. P. J. Barty, and D. Perry, Phys. Today **51**, 22 (1998).
19. M. Tabak, J. Hammer, M. E. Glinsky, *et al.*, Phys. Plasmas **1**, 1626 (1994).
20. O. Buneman, in *Computer Space Plasma Physics, Simulation Techniques and Software*, Ed by. H. Matsumoto and Y. Omura (Terra Scientific, Tokyo, 1993), p. 67.
21. F. Galifano, R. Prandi, F. Pegoraro, and S. V. Bulanov, Phys. Plasmas **6**, 2332 (1999).
22. Y. Kazimura, J.-I. Sakai, and S. V. Bulanov, J. Phys. Soc. Jpn. **68**, 3271 (1999).
23. M. Honda, J. Meyer-ter-Vehn, and A. M. Pukhov, Phys. Plasmas **7**, 1302 (2000); Phys. Rev. Lett. **85**, 2128 (2000).

Translated by A.S. Sakharov

Plasma Physics Reports, Vol. 27, No. 4, 2001, pp. 335–339. Translated from Fizika Plazmy, Vol. 27, No. 4, 2001, pp. 356–360.
Original Russian Text Copyright © 2001 by Goretskiĭ, Soloshenko, Shchedrin.

BEAMS IN PLASMA

Space Charge Lens for Focusing Negative-Ion Beams

V. P. Goretskiĭ, I. A. Soloshenko, and A. I. Shchedrin
Institute of Physics, National Academy of Sciences of Ukraine, pr. Nauki 144, Kiev, 03028 Ukraine

Received August 18, 2000

Abstract—A space charge lens is proposed to focus intense beams of negative hydrogen ions. The focal length of the lens is determined as a function of the parameters of the beam and the gas medium. It is demonstrated experimentally that the lens efficiently focuses H^- ion beams with currents of up to ~30 mA and energies of ~10 keV. The measured focal lengths are in good agreement with the calculated ones. © *2001 MAIK “Nauka/Interperiodica”.*

1. INTRODUCTION

The idea of using space charge fields to focus beams of positive ions was first proposed by Gabor [1] and later developed by Morozov [2]. That such a lens is highly efficient was confirmed in a number of experiments (see, e.g., [3]). The main advantages are its high lens power at a relatively low energy cost and the possibility of focusing high-current beams and controlling spherical aberrations. The negative space charge of the lens is produced by electrons that either escape from the lens electrodes due to ion–electron emission or are brought to the lens from an external thermoemitter. The electrons are confined by the magnetic field, whose field lines are also the electric field equipotential lines; this fact is used to control the radial distribution of the electric field. In such a system, ionization of the residual gas by an ion beam is a parasitic process, which substantially limits the applicability of the lens in the steady-state case. At high gas pressures, this can lead to breakdowns, which destroy the structure of the focusing electric field, whereas, at low pressures, the ions accumulating on the axis can cause both high lens aberrations and specific electrostatic instabilities.

It should be noted that space charge lenses designed to focus positive-ion beams cannot be applied to negative-ion beams because, in the latter case, positive ions must be used. The idea of using a space charge lens to focus negative-ion beams is based on the employment of positive ions created during gas ionization by the beam, which is a parasitic process when focusing positive-ion beams. Since electrons are also produced during ionization, the required positive space charge can only be created if the electrons are extracted by an electric field. In this case, the positive ions stay in the system for a sufficiently long time due to their inertia. The simplest focusing system can be a metal cylinder coaxial with the beam and two electrodes at the cylinder ends. The electrodes must be transparent for the beam; i.e., they should be either gridlike or ringlike. Applying a positive (with respect to the central electrode) potential to the peripheral electrodes should result in the extraction of electrons and the formation of the required positive space charge inside the cylinder. Note that, to extract the electrons efficiently, it is necessary to apply a sufficiently high potential at which the length of the space charge sheath is comparable with the system length. Due to the relatively low density of the beam plasma (~10^8 cm^{-3}), this can be achieved at a voltage of 100–1000 V between the lens electrodes.

By supplying a gas directly to the cylinder, the required ionization can be achieved without a substantial increase in the pressure beyond the lens.

2. ESTIMATES OF THE POWER OF A SPACE CHARGE LENS

Obviously, the proposed focusing can be attained only if the space charge of the positive ions that are produced due to gas ionization exceeds that of the beam ions. This sets a lower limit on the gas pressure. The required gas density, which can be determined based on the balance equation for positive ions, is

$$n_a \geq \frac{2v_+}{v_-\sigma_i r_0}, \qquad (1)$$

where n_a is the gas density; σ_i is the cross section for gas ionization by the beam ions; v_+ and v_- are the velocities of the escaping positive ions and beam ions, respectively; and r_0 is the beam radius [4]. If the beam propagates freely and condition (1) is satisfied, then the potential of the beam is positive with respect to the periphery and its value is determined by the mean thermal energy of plasma electrons, which, in turn, is determined by Coulomb collisions with the beam ions. In this case, the focusing fields that arise in the beam with a density of ~10^8 cm^{-3} attain only several V/cm and, thus, can only be used for better transportation of weakly divergent beams.

Generally, in order to focus a beam extracted from a single hole, a lens with a focal length of about 10–20 cm is required, which calls for radial fields of ~100 V/cm.

In the system in question, such fields can only be attained if almost all of the electrons are removed from the focusing region. If this condition is satisfied, then the electron space charge can be neglected and the focusing capabilities of the lens can be relatively easily estimated.

To calculate the focusing field, we use the discontinuity equation for positive ions, Poisson's equation for the potential, and the equation of motion of positive ions in the radial electric field:

$$\frac{1}{r}\frac{\partial}{\partial r} r j_+ = e n_- n_a \sigma_i V_- = \frac{j_-}{\lambda_i}, \tag{2}$$

$$\frac{1}{r}\frac{\partial}{\partial r} r \frac{\partial}{\partial r}\varphi = -4\pi e(n_+ - n_-), \tag{3}$$

$$V_+(r_i, r) = \sqrt{\frac{2e[\varphi(r_i) - \varphi(r)]}{m_+}}. \tag{4}$$

Here, λ_i is the mean free path of the beam ions with respect to gas ionization and $V_+(r_i, r)$ is the velocity of a positive ion that is produced at the point r_i and reaches the point r.

Using Eqs. (2) and (4), we obtain the expression for the density of positive ions in a uniform negative-ion beam:

$$n_+(r) = \frac{|j_-|}{e\lambda_i r\sqrt{\frac{2e}{m_+}}}\int_0^r \frac{s\,ds}{\sqrt{\varphi(s) - \varphi(r)}}. \tag{5}$$

If the positive ion density is uniform along the radius, then the potential distribution is

$$\varphi(r) = \varphi(0) - \varphi_a\left(\frac{r}{r_0}\right)^2, \tag{6}$$

where φ_a is the radial potential drop in the beam. Then, the positive ion density is

$$n_+(r) = \left|\frac{j_- r_0}{e\lambda_i\sqrt{\frac{2e\varphi_a}{m_+}}}\right|. \tag{7}$$

From Eqs. (3) and (7), we derive the equation for the radial potential drop in the beam:

$$\varphi_a^{3/2} + \varphi_-\varphi_a^{1/2} = \varphi_-\varphi_n^{1/2}, \tag{8}$$

where $\varphi_- = \left|\frac{I_-}{\sqrt{\frac{2eU_-}{m_-}}}\right| = \frac{\Pi}{9\pi}U_-$ is the potential drop in the nonneutralized negative-ion beam, $\Pi = \left|\frac{I_-}{\frac{1}{9\pi}\sqrt{\frac{2e}{m_-}}U_-^{\frac{3}{2}}}\right|$ is the reduced beam perveance, and $\varphi_n = \frac{r_0^2 m_+}{\lambda_i^2 m_-}U_-$.

It is seen from Eq. (8) that, at

$$\varphi_- \ll \varphi_a \tag{9}$$

(i.e., under conditions of strong overneutralization of the beam space charge), the solution to Eq. (1) is

$$\varphi_a \approx \left(\varphi_-\varphi_n^{\frac{1}{2}}\right)^{\frac{2}{3}} = \left(\frac{I_- r_0}{\lambda_i\sqrt{2e/m_+}}\right)^{\frac{2}{3}}. \tag{10}$$

In the opposite case ($\varphi_- \gg \varphi_a$), which corresponds to the quasineutral mode and can be attained by increasing the beam current, we have

$$\varphi_a \approx \varphi_n = \frac{r_0^2 m_+}{\lambda_i^2 m_-}U_-. \tag{11}$$

It follows from Eqs. (9) and (10) that, as the beam current increases, the radial potential drop φ_a first increases and then reaches a maximum value, which does not depend on the beam current.

It should be noted that the relation between φ_a and φ_-, which is necessary for determining the operating mode of the lens, is not convenient in practice because φ_a is unknown. However, it is easy to show that this relation is analogous to that between the known quantities φ_n and φ_-; i.e., the quasineutral mode occurs at

$$\varphi_- \gg \varphi_n, \tag{12}$$

whereas the strong overneutralization mode takes place at

$$\varphi_- \ll \varphi_n. \tag{13}$$

It follows from the above relations that radial fields higher than 100 V/cm can be attained for the beam of negative hydrogen ions with an energy of ~10 keV in a lens with a length of ~10 cm at a gas (argon, krypton, or xenon) pressure of ~10^{-3} torr.

Using the procedure from [5], we obtain the expression for the lens power:

$$\frac{1}{f} = \frac{1}{\sqrt{U_-(0)}}\int_0^L \frac{\varphi_a\,dz}{r_0^2\sqrt{U_-(z)}} \approx \frac{\varphi_a L}{U_- r_0^2}. \tag{14}$$

Substituting expressions (10) and (11) for φ_a into Eq. (14), for high beam currents (the quasineutral mode), we obtain

$$\frac{1}{f} = \frac{L m_+}{\lambda_i^2 m_-}; \tag{15}$$

whereas, for low currents, we have

$$\frac{1}{f} = \left(\frac{\Pi}{9\pi}\right)^{\frac{2}{3}}\left(\frac{m_+}{m_-}\right)^{\frac{1}{3}}\frac{L}{(\lambda_i r_0^2)^{\frac{2}{3}}} = \left(\frac{j_-\pi}{\lambda_i\sqrt{2e/m_+}}\right)^{\frac{2}{3}}\frac{L}{U_-}. \qquad (16)$$

It follows from Eq. (15) that the required focal length of ~10 cm is attainable for the above lens parameters.

In summary, we note that the main process that limits the applicability of the lens in question is the loss of negative ions due to charge exchange in collisions with gas atoms. To minimize the ion loss, the lens length L should be shorter than the charge-exchange mean free path $-\lambda_{-0}$. According to Eq. (16), this requires that the condition

$$\frac{\Pi}{9\pi} > \sqrt{\frac{m_-}{m_+}}\frac{r_0^2\lambda_i}{(\lambda_{-0}f)^{\frac{3}{2}}}, \qquad (17)$$

be satisfied, which, in turn, limits the beam current density at a given ion energy by the value

$$j_- > \frac{1}{\pi}\sqrt{\frac{2e}{m_+}}\frac{\lambda_i U_-^{\frac{3}{2}}}{(\lambda_{-0}f)^{\frac{3}{2}}}. \qquad (18)$$

It follows from inequality (17) that, for argon at a pressure of $P \approx 10^{-3}$ torr and beam-ion energy $U_- \approx 10$ keV, the lens focal length $f \approx 10$ cm can be attained at the current density of a negative-ion beam $j_- > 4.5$ mA/cm^2.

3. EXPERIMENTS ON FOCUSING AN H$^-$ BEAM WITH A SPACE CHARGE LENS

A schematic of the experimental device is shown in Fig. 1. An H$^-$ beam with a current of ~10–30 mA and ion energy of ~10 keV was extracted from a surface plasma source *1*; the beam was formed and deflected with the help of an ~2-kG magnetic field created by magnets *2*. Collectors *7* (~10 cm in diameter) and *6* (2 cm in diameter) were used to measure the beam current and the current density, respectively. A space charge lens was placed ≈20 cm away from the source emission slit. The distance from the outlet plane of the lens to the collector was ≈30 cm. For such a system configuration, the beam radius should be minimum at a focal length of 12 cm. The lens design was as follows. Inside a grounded cylindrical stainless steel case *3* with an external diameter of 10 cm, length of 13 cm, and diameters of the inlet and outlet diaphragms of 5 cm, there was a 10-cm-long and 7-cm-diameter metal cylinder *5*. This cylinder ensured a uniform gas pressure distribution inside the lens. The cylinder was either grounded or under the potential of electrode *4* (this did not significantly affect the lens focusing properties). A cylindrical 5-cm-diameter and 10-cm-long electrode *4* made of stainless steel mesh was mounted inside electrode *5* at its ends with the help of dielectric rings. The potential of electrode *4* could be varied within a range from 0 to –1500 V. There were two pipes on the case outer wall, one of which served as a gas inlet and the other one was used to measure the pressure in the lens. This pressure differed by more than one order of magnitude from that in the beam drift chamber.

Either argon, krypton, or xenon was used as the working gas. Such a choice was dictated by both their relatively high ionization cross sections and relatively high inertia of positive ions created due to ionization. Both these factors promoted efficient focusing of the negative-ion beam.

Before considering the experimental results, we first estimate the critical pressure above which the space charge of the positive ions created due to gas ionization is greater than the space charge of the negative-ion beam. Let us assume that the mean energy of the ions created due to gas ionization is ~1 eV. Then, based on formula (1) and the cross sections taken from [6], for a beam with the above parameters, we have $P_0 \sim 1.5 \times 10^{-4}$, 4×10^{-5}, and 6×10^{-5} torr for argon, krypton, and xenon, respectively. At pressures higher than P_0, the production rate of positive ions is proportional to the pressure; however, their charge density increases more slowly because the rate with which the ions escape in the radial direction also grows due to an increase in the radial potential drop.

The experiments showed that, at pressures higher than the critical one, the negative-ion beam is focused in accordance with the above estimates. The lens focus-

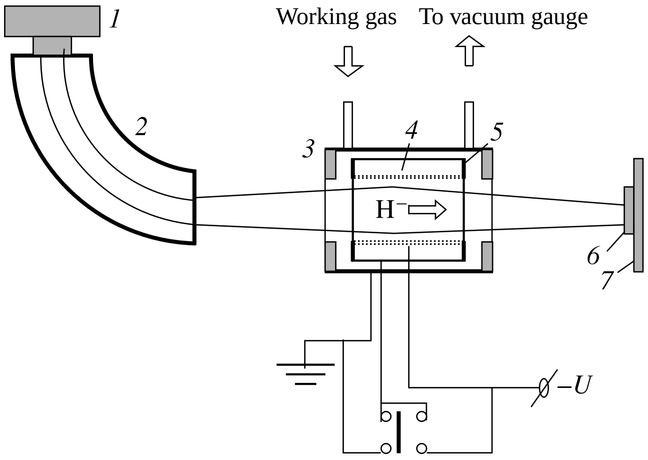

Fig. 1. Schematic of the device: (*1*) source of H$^-$ ions, (*2*) deflecting magnets, (*3*) grounded case, (*4*) 5-cm-diameter gridlike cylindrical electrode, (*5*) 7-cm-diameter metal cylinder, (*6*) 2-cm-diameter collector for measuring current density, and (*7*) 10-cm-diameter current collector.

ing capabilities are clearly demonstrated in Fig. 2, which presents the compression ratio of an H^- beam at different pressures of argon as a function of the voltage between the lens electrodes, namely, the grounded case *3* and gridlike electrode *4*. We define the compression ratio as the ratio of the maximum current density with applying the optimum potentials to the electrodes to that without applying any potential. The curves agree with the above qualitative considerations. As the voltage increases, the beam first contracts but, starting from $V \sim 200$ V, all the curves saturate. This can be explained by the fact that, at $V > 200$ V, the electron density in the beam becomes so low that the radial potential drop is determined mainly by the positive and beam ions. The higher the pressure, the stronger the dependence of the compression ratio on the voltage, which is caused by an increase in the positive space charge. The maximum compression ratio first increases (curves *1*–*3*) and then falls (curves *4*–*6*), which can be explained by the beam overfocusing. This assumption was confirmed by special experiments in which a metal plate with two holes and a fluorescent screen, which served for viewing the hole images, were placed 4 and 22 cm away from the outlet diaphragm, respectively. At the optimum potentials applied to the lens electrodes, the increase in the xenon pressure resulted in the images first approaching each other until they merged together at fairly high pressures and, then, moving apart in the direction opposite to their initial positions with respect to the center, which unambiguously evidences the beam overfocusing.

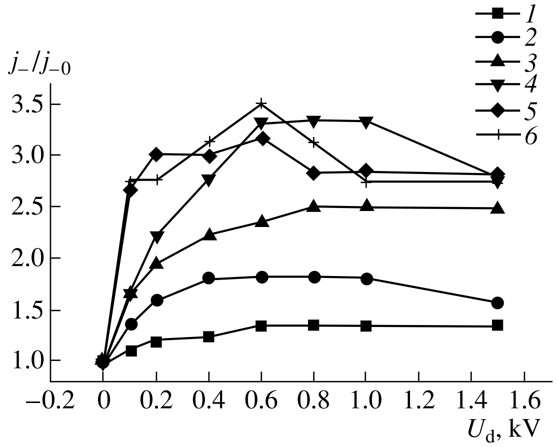

Fig. 2. Compression ratio j_-/j_{-0} of an H^- beam vs. the negative potential at the decelerating cylinder for different pressures of argon in the lens: (*1*) 3×10^{-4}, (*2*) 7.6×10^{-4}, (*3*) 1.5×10^{-3}, (*4*) 2.2×10^{-3}, (*5*) 3.6×10^{-3}, and (*6*) 6.4×10^{-3} torr.

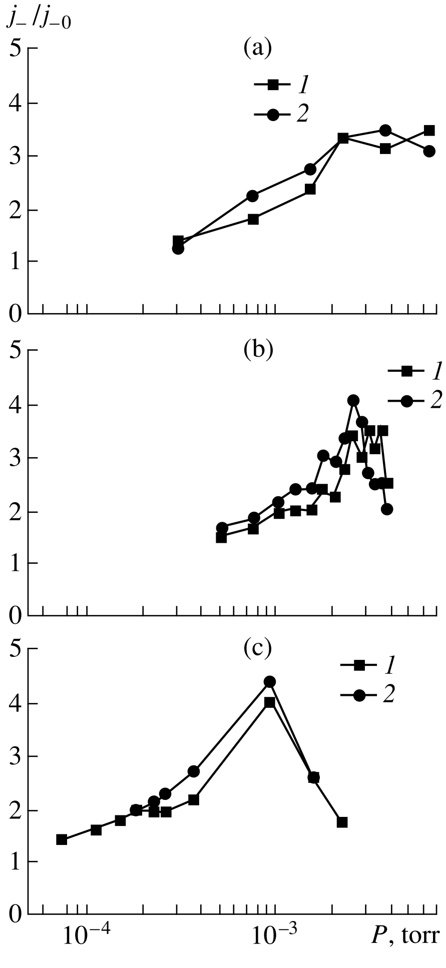

Fig. 3. Compression ratio j/j_0 of an H^- beam vs. pressure in the space charge lens for (a) argon, (b) krypton, and (c) xenon (*1*) in the case when electrode *5* is under the potential of electrode *4* and (*2*) for the grounded electrode *5*; the beam current is 15 mA, and the beam-ion energy is 10 keV.

The above considerations also agree with the dependences of the beam compression ratio on the pressure for all three gases (Fig. 3). It is seen that all of the curves are similar in character; first, the compression ratio increases, and, then, it falls.

The optimum compression ratio is approximately the same for all three gases (~4). Based on this, we may argue that the fall of the curves that occurs at high pressures in argon and krypton is related to the beam overfocusing, as is the case for xenon. The decrease in the optimum pressure upon increasing the mass of positive ions can also be easily understood. Finally, the correspondence of the maximum compression ratio to a focal length of ~12 cm at the given system configuration can be used to compare the experimental data with the calculated ones. Let us consider the case of argon, whose optimum pressure is $\sim 3 \times 10^{-3}$ torr. According to Eq. (16), for a beam current of 15 mA, the calculated focal length is ~20 cm. This value is fairly close to the measured one ($f \sim 12$ cm).

In summary, in this study, the focusing of a negative-ion beam with a space charge lens has been proposed and implemented. Such focusing is of practical importance for beams with relatively high current densities, in which a sufficient positive space charge can be accumulated without significant loss of the beam ions due to charge exchange.

ACKNOWLEDGMENTS

This work was supported by the Ukrainian Foundation for Basic Research of the Ministry of Science of Ukraine (grant no. F4/342-97-32).

REFERENCES

1. D. Gabor, Nature **160**, 89 (1947).
2. A. I. Morozov, Dokl. Akad. Nauk SSSR **163**, 1363 (1965) [Sov. Phys. Dokl. **10**, 775 (1966)].
3. A. A. Goncharov, A. N. Dobrovol'skiĭ, and A. N. Kotsarenko, Fiz. Plazmy **20**, 499 (1994) [Plasma Phys. Rep. **20**, 449 (1994)].
4. M. D. Gabovich, L. S. Simonenko, and I. A. Soloshenko, Zh. Tekh. Fiz. **48**, 1389 (1978) [Sov. Phys. Tech. Phys. **23**, 783 (1978)].
5. V. M. Kel'man and S. Ya. Yavor, *Electron Optics* (Akad. Nauk SSSR, Moscow, 1959).
6. Ya. M. Fogel', A. G. Koval', and Yu. Z. Levchenko, Zh. Éksp. Teor. Fiz. **38**, 1053 (1960) [Sov. Phys. JETP **11**, 760 (1960)].

Translated by N.N. Ustinovskiĭ

Plasma Physics Reports, Vol. 27, No. 4, 2001, pp. 340–346. Translated from Fizika Plazmy, Vol. 27, No. 4, 2001, pp. 361–368.
Original Russian Text Copyright © 2001 by Antipov, Samarian, Petrov, Nefedov.

DUSTY PLASMA

Behavior of a Dust Grain in the Double Layer of an Electric Probe in a Gas-Discharge Plasma

S. N. Antipov*, A. A. Samarian, O. F. Petrov*, and A. P. Nefedov***

**Institute for High Energy Densities, Russian Academy of Sciences, Izhorskaya ul. 13/19, Moscow, 127412 Russia*
***School of Physics, University of Sydney, NSW 2006, Australia*

Received February 1, 2000; in final form, September 22, 2000

Abstract—Equations for the motion of an individual dust grain in the double layer of a negatively charged cylindrical probe in a glow discharge plasma are derived and solved numerically. The distribution of the electric potential near the probe is determined, and the grain charge is calculated as a function of the distance from the probe for different probe potentials. The trajectories of grains with different initial energies are traced. An analysis of the grain trajectories shows that, at a certain distance from the probe, high-energy grains may be recharged; i.e., the grain charge may change sign. The grains are found to have no direct effect on the probe current in a dusty plasma of a glow discharge. *© 2001 MAIK “Nauka/Interperiodica”.*

1. INTRODUCTION

Probe diagnostics are of considerable interest for experimental investigations of dusty plasmas [1, 2] because they provide local measurements of the main plasma parameters (the electron and ion densities, the plasma temperature, and the electron energy distribution function). In dusty plasmas, the current–voltage characteristics of the probe are far more difficult to interpret because they are strongly affected by the third charged component—dust grains. Also, dusty plasmas are characterized by a new parameter, dust grain charge, which depends on both the grain size and the local parameters of the surrounding plasma.

An analysis of the probe measurements in a gas-discharge dusty plasma requires a knowledge of the behavior of dust grains in a perturbed plasma near the probe. In order to investigate this problem in more detail, it is of interest to model the behavior of an individual dust grain. The distinctive feature of the grain behavior is that the grain charge Z_d changes as the grain moves in an inhomogeneous plasma. The grain charge is governed by the potential difference between the grain surface and the surrounding plasma and thus can be affected by the local densities and temperatures of the electrons and ions.

Here, we consider an individual spherical grain moving in the field of an infinitely long, vertically oriented cylindrical probe, in which case the gravitational force can be neglected because it affects only the grain motion along the probe. We also ignore the drag and deceleration forces that are exerted on the grain by the ions and neutrals, respectively, although these forces may be important in the immediate vicinity of the probe in a high-density plasma. We assume that the dusty plasma is tenuous and nonisothermal ($T_e \gg T_i$) such that the mean free path λ of charged particles is much longer than the characteristic dimensions of the problem (this assumption corresponds to the so-called molecular regime). In the absence of emission processes, dust grains in such a plasma absorb highly mobile electrons and acquire a negative charge [3]. The dust grain is assumed to be small ($R_d \ll D \ll \lambda$, where R_d is the grain radius and D is the Debye radius), and the probe is assumed to be large enough to satisfy the condition $R_p \gg D$, where R_p is the probe radius. The probe potential relative to the plasma is assumed to be negative, which is peculiar to probe measurements in experiments with gas-discharges [4–7]. For these conditions, the theory of probe measurements is developed fairly well; in particular, the problem of determining the potential distribution and electron and ion densities in the perturbed region near the probe in a nonisothermal plasma has been solved quite thoroughly [6]. Hence, it is expedient to treat our problem using the results obtained in [6].

2. BASIC EQUATIONS

In order to systematically describe the motion of a dust grain in the perturbed region near the probe, it is necessary to solve the set of equations consisting of the equation of grain motion, the equation describing the kinetics of grain charging, and the equation for the potential distribution in the perturbed plasma (the so-called plasma–sheath equation).

Under the above assumptions, the grain experiences only an electrostatic force. Since the grain motion along the probe is unimportant, the problem as formulated reduces to a two-dimensional problem of the grain motion in the horizontal plane. Specifically, in the perturbed plasma near the probe, the dust grain moves in a centrosymmetric electric field, in which case we can use the well-known equations of motion of classical mechanics for a point particle in the field of centrosymmetric forces. In the plane of the grain trajectory, we introduce a polar coordinate system (r, θ) with the origin at the center of the probe and write the equations of grain motion in the form

$$M_d\frac{d^2r}{dt^2} = -eZ_d\frac{dU(r)}{dr} + \frac{L^2}{M_d r^3},\qquad \frac{d\theta}{dt} = \frac{L}{M_d r^2}, \tag{1}$$

where $U(r)$ is the probe potential at the point r, L is the momentum of the grain, and M_d is the grain mass. Since the grain charge Z_d is a variable quantity, it, together with the potential $U(r)$, governs the law according to which the force changes. The constants of grain motion are determined by the energy of the grain and its kinetic momentum. The latter can be conveniently expressed in terms of the kinetic energy K_0 and the impact parameter p, which is equal to the distance from the center of forces to the straight line along which the grain starts to move. In this case, the equations of grain motion (1) become

$$\frac{d^2r}{dt^2} = -\frac{eZ_d}{M_d}\frac{dU(r)}{dt} + \frac{2K_0p^2}{M_d r^3},\qquad \frac{d\theta}{dt} = \frac{p}{r^2}\left(\frac{2K_0}{M_d}\right)^{1/2}. \tag{2}$$

We will trace the trajectory of a dust grain throughout the entire perturbed region near the probe, including the space-charge layer (or the double layer), in which the potential changes abruptly, and the quasineutral (plasma) region. In contrast to [7, 9, 10], in which the plasma region and double layer were treated separately under the assumption that the potential at the plasma–layer boundary vanishes, we will solve a complete plasma–sheath equation in order to obtain a continuous distribution of the potential over the entire perturbed region. In this approach, the potential U_0 at the point r_0 from which the grain starts moving is nonzero (although it can be very low for large r_0). We assume the initial grain charge Z_{d0} to be equilibrium, i.e., to correspond to the potential U_0 at the starting point.

Probe measurements are usually performed in quasi-steady electric fields, which can be regarded as being potential and in which the displacement currents can be neglected. Under such conditions, the electric field distribution near the probe satisfies Poisson's equation, which can be written as ($\varepsilon = 1$)

$$\frac{1}{r}\frac{d}{dr}\left(r\frac{dU}{dr}\right) = -4\pi e[n_i(r) - n_e(r)]. \tag{3}$$

We can also neglect the absorption of electrons by the probe and describe the electron density by the Boltzmann distribution

$$n_e = n_0\exp\left[\frac{eU(r)}{kT_e}\right]. \tag{4}$$

In contrast, the absorption of ions by the probe cannot be neglected, so that the ion density is essentially nonequilibrium and cannot be described by the Boltzmann distribution. In order to calculate the ion density distribution, we turn to an approach that assumes the existence of an absorbing surface other than the probe surface [5–7]. We will use the terminology introduced by Kozlov [6], who called the radius of the absorbing surface the "limiting radius" and the ion motion the "limiting motion." He showed that, for $T_e \gg T_i$ and $R_p \gg D$, the ions in the field of a negative probe experience precisely the limiting motion, in which case the radius of the limiting surface is larger than the maximum radius of the space-charge layer. The limiting radius is determined by the local maximum of the effective ion potential energy

$$U_{\text{eff}}(r) = \frac{l^2}{2m_i r^2} + eU(r), \tag{5}$$

where l is the angular momentum of an ion and m_i is its mass. The plot of this function is presented in Fig. 1. The reflection point (the minimum distance from the probe) can be defined as the point at which the horizontal line corresponding to the total ion energy intersects the related curve U_{eff}. As the impact parameter (and, accordingly, the angular momentum l) decreases, the reflection point is monotonically displaced toward the probe up to the point r_L, at which the maximum (for the given l_L) value of the function U_{eff} is equal to the total

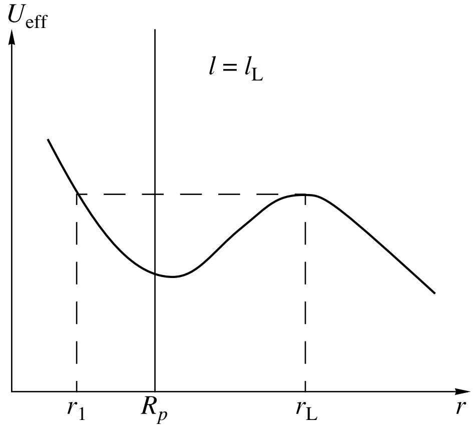

Fig. 1. Plot of the effective ion potential energy $U_{\text{eff}}(r)$ for $l = l_L$.

ion energy. As l becomes less than l_L, the minimum distance decreases from r_L to r_1 in a jumplike manner. The radius r_L can be determined from the maximum of the effective potential energy function plotted for $l = l_L$:

$$er_L^3 \frac{dU}{dr}(r_L) = \frac{l_L^2}{m_i}. \tag{6}$$

For a cylindrical probe, the key role is played by the projection v_n of the ion velocity on the plane perpendicular to the probe axis. To simplify the calculations for the case of a limiting motion, we employ the monoenergetic ion model (MIM); i.e., we switch from the real ion velocity distribution to the monoenergetic distribution [6–8]

$$f_i(v_{0n}) = \frac{m_i}{2\pi}\delta\left[\frac{m_i v_{0n}^2}{2} - E_{0n}\right], \tag{7}$$

where v_{0n} is the initial ion velocity in an unperturbed plasma, $\delta(x)$ is the delta function, and E_{0n} is equal to the plasma ion temperature to within a factor on the order of unity (although exact calculations give $E_{0n} = \pi kT_i/4$, we will not distinguish between E_{0n} and kT_i). We are justified in using a monoenergetic (rather than real) ion distribution function, because, near the probe, low-energy ($T_e \gg T_i$) ions are affected by an accelerating electric field and thereby acquire velocities much higher than the initial ones, so that the current carried by the ions is essentially unaffected by their distribution. Hence, the velocities of the ions in the plasma coincide in absolute value and are randomly oriented in space, in which case r_L is the limiting radius in terms of the ion energy E_{0n}.

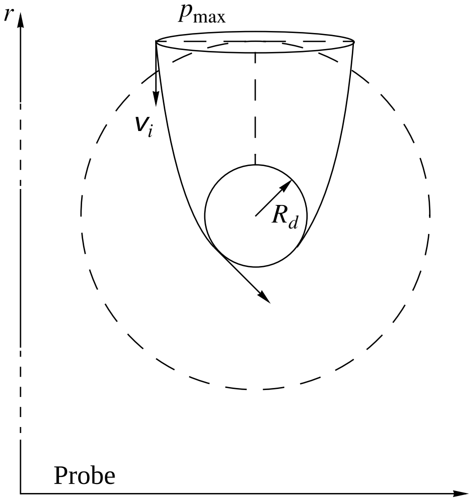

Fig. 2. Collection of the ions by a negatively charged dust grain. Shown are the grain trajectory and the cross section for collisions between the ions and the dust grain.

In accordance with the above analysis, we can specify the radial profile of the ion density as follows [6]:

$$\begin{aligned} n_i &= n_0\left\{1 - \frac{1}{\pi}\arcsin\frac{r_L}{r}\left[\frac{E_{0n} + eU(r_L)}{E_{0n} + eU(r)}\right]^{1/2}\right\} \quad \text{for } r > r_L, \\ n_i &= \frac{n_0}{\pi}\arcsin\frac{r_L}{r}\left[\frac{E_{0n} + eU(r_L)}{E_{0n} + eU(r)}\right]^{1/2} \quad \text{for } r < r_L. \end{aligned} \tag{8}$$

Here and below, $U(r)$ stands for the absolute value of the potential.

In the perturbed region near the probe, the charge of the grain is determined by the electron and ion currents onto its surface and by its radial velocity $u_r = dr/dt$:

$$u_r e \frac{dZ_d}{dr} = I_e + I_i, \tag{9}$$

where I_e and I_i are the electron and ion currents toward the grain surface at a distance r from the probe.

In the orbital motion limit (OML) [3, 5, 7, 9], the electron current is described by the equations [10]

$$\begin{aligned} I_e &= -\pi R_d^2 e n_e \left(\frac{8kT_e}{\pi m_e}\right)^{1/2} \exp\left(\frac{eU_d}{kT_e}\right) \quad \text{for } U_d < 0, \\ I_e &= -\pi R_d^2 e n_e \left(\frac{8kT_e}{\pi m_e}\right)^{1/2} \left(1 + \frac{eU_d}{kT_e}\right) \quad \text{for } U_d > 0, \end{aligned} \tag{10}$$

where n_e is the local electron density (4) and U_d is the floating potential of the grain with respect to the potential $U(r)$ of the surrounding plasma. For a spherical grain with $R_d \ll D$, the floating potential U_d and charge Z_d are related by $Z_d e = U_d R_d$.

Let us find the ion current onto the grain surface, neglecting the distortion of the probe field and assuming that the potential of the layer changes only slightly across the grain field region (i.e., in the vicinity of the grain, the layer parameters n_e, n_i, f_e, f_i are constant). We again assume (as we did in deriving the radial profile of the ion density) that the ion energies in an unperturbed plasma are the same, $E_0 \approx kT_i$; i.e., we again employ the MIM. With the absorbing surface in the perturbed region, no grains whose trajectories are screened by the probe can occur at the point r. The ion current onto the grain surface is equal to the ion flux through the surface element of area $\pi p_{\max}^2$, where $p_{\max}$ is the maximum impact parameter at which the ions can reach the grain surface (Fig. 2). Since, in the OML, the role of the absorbing surface is played by the grain surface, we have

$$p_{\max}^2 = R_d^2\left(1 - \frac{2Z_d e^2}{R_d m_i v_i^2}\right), \tag{11}$$

$$v_i = \left\{\frac{2}{m_i}[E_0 + eU(r)]\right\}^{1/2}, \tag{12}$$

in which case the ion current is equal to

$$I_i = \pi p_{\max}^2 e n_i v_i, \tag{13}$$

where the ion density n_i is defined by formulas (8).

3. NUMERICAL SOLUTION AND DISCUSSION OF THE RESULTS

Let us formulate the initial and boundary conditions for our problem. The first boundary condition determines the value of the potential at the probe surface:

$$U(R_p) = U_p. \tag{14}$$

At the limiting surface, we have

$$\begin{gathered} U(r_\mathrm{L}) = U_\mathrm{L}, \\ \frac{dU}{dr}(r_\mathrm{L}) = -\frac{2}{er_\mathrm{L}}(E_{0n} + eU_\mathrm{L}). \end{gathered} \tag{15}$$

Here, the condition on the radial derivative of the potential is derived from expression (6) and the energy conservation law. Now, the plasma–sheath equation (3) can be solved by the shooting method: we must find the value of U_L at which the solution to the equation in the region $r < r_\mathrm{L}$ satisfies condition (14). The resulting value of U_L gives the explicit boundary conditions (15), with which the plasma–sheath equation (3) can be readily solved for the region $r > r_\mathrm{L}$ by using, as the initial conditions, the polar radius, radial velocity, and polar angle of the grain at $t = 0$:

$$\begin{gathered} r(t=0) = r_0, \quad u_r(t=0) = -\left[\frac{2K_0}{M_d}\left(1 - \frac{p^2}{r_0^2}\right)\right]^{1/2}, \\ \theta(t=0) = \arcsin\frac{p}{r_0}. \end{gathered} \tag{16}$$

Then, using Eqs. (2)–(4) and (8)–(13) with the boundary and initial conditions (14)–(16), we can describe the grain motion in the perturbed region near the probe. To simplify the solution of the problem, we convert the equations to the dimensionless form. We adopt the limiting radius r_L and Debye radius $D = (kT_e/4\pi n_0 e^2)^{1/2}$ as scale lengths and also the electron temperature kT_e and potential kT_e/e as energy and potential scales, respectively. The dimensionless variables introduced in such a way are as follows:

$$x = \frac{r}{r_\mathrm{L}}, \quad \gamma = \frac{T_i}{T_e}, \quad \gamma_d = \frac{K_0}{kT_e}, \quad \varphi = \frac{eU(r)}{kT_e}. \tag{17}$$

Note that numerical calculations were carried out with the equations normalized to the (most suitable) limiting radius r_L, whereas, in plotting the diagrams, we expressed the length scales of the problem in units of the Debye radius.

We numerically traced the trajectories of a dust grain with a radius of 1 μm and a mass of 4.2×10^{-12} g in an argon plasma ($m_i = 6.63 \times 10^{-23}$ g) with 1-eV electrons, the ion temperature being equal to the room temperature ($\gamma = T_i/T_e = 0.026$). In this case, the value of the variable γ_d is the grain energy in electronvolts and the value of the variable φ is the absolute value of the space potential in volts. In calculations, we also put $R_p/D = 10$ and $R_d/D = 0.01$. For the above values of R_d and kT_e, the latter relationship also determines the Debye radius and plasma density: $D = 0.01$ cm and $n_0 = 5.5 \times 10^9$ cm^{-3}.

The calculated radial profiles of the electric field near the probe are illustrated in Fig. 3. From Fig. 3a, we can see that, for a sufficiently high probe potential ($\varphi_p = eU_p/kT_e \gg 1$), the limiting radius is larger than the maximum radius of the space-charge layer. This result confirms the estimates made in [6].

Let us consider the grain motion in the probe field with the potential $\varphi_p = 10$. Let the grains start moving at the point $x_0 = 4$, at which $\varphi_0 = 0.02$ and $Z_{d0} = -2117$. The trajectories of grains with different initial energies are shown in Fig. 4. That the shape of trajectories *1* and *2* is characteristic of grains scattered by a centrosymmetric repulsive force is explained as being due to the negative initial grain charge. Trajectories *5*–*8* demonstrate that the probe can attract grains with sufficiently high initial energies. This possibility is illustrated by the plots in Figs. 5 and 6.

Figure 5 demonstrates how the charge of the grain changes as it moves near the probe and also presents radial profiles of the electron and ion densities, n_e and n_i, as well as the steady-state grain charge calculated from the equation $I_e + I_i = 0$ as a function of distance from the probe. In the range $Z_d < 0$, the grain charge is seen to have a minimum; this indicates that the charge of the grain that starts moving in the quasineutral region decreases (i.e., increases in absolute value). This result was obtained by exact calculation of the electron and ion charging currents along the entire grain trajectories by using formulas (10) and (13). We can see that, in the perturbed region far from the probe, $(r - R_p)/D > 10$ for $\varphi_p = 10$, the ion current (13) onto the grain surface decreases at a faster rate than the electron current. As the grain approaches the so-called ion sheath, in which the electron density is negligibly low and the electron current sharply decreases, the grain charge begins to increase (i.e., to decrease in absolute value). Note that, at a certain distance from the probe, the charge of the moving grain changes sign: a negatively charged grain becomes positively charged. We will call this distance the “recharging distance.” The grain is recharged in the region where the ion current dominates over the elec-

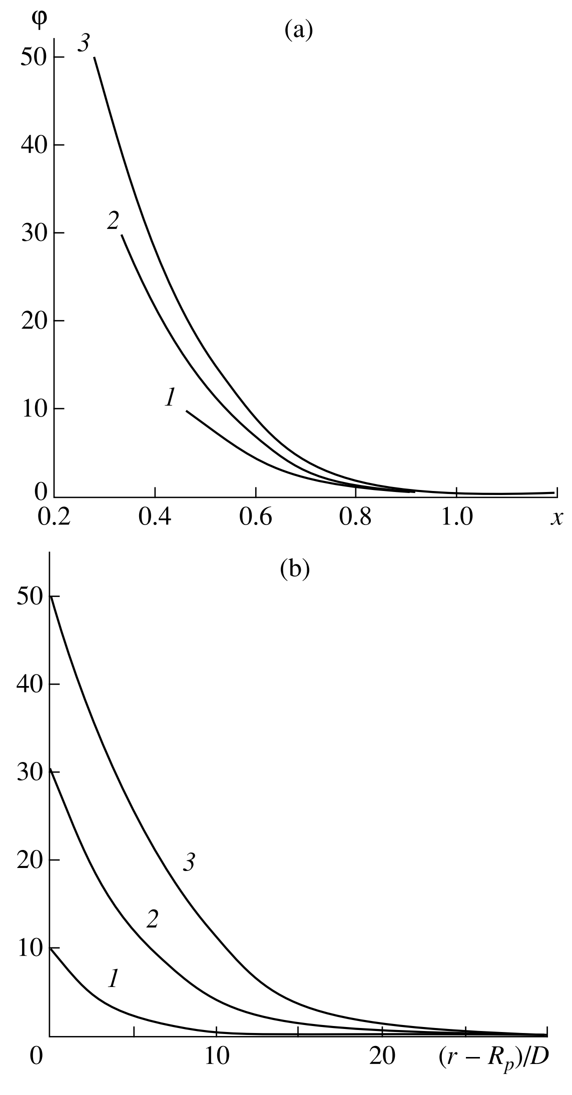

Fig. 3. Distribution of the electric potential near a cylindrical probe for different probe potentials $\varphi_p = eU_p/kT_e$ = (*1*) 10, (*2*) 30, and (*3*) 50.

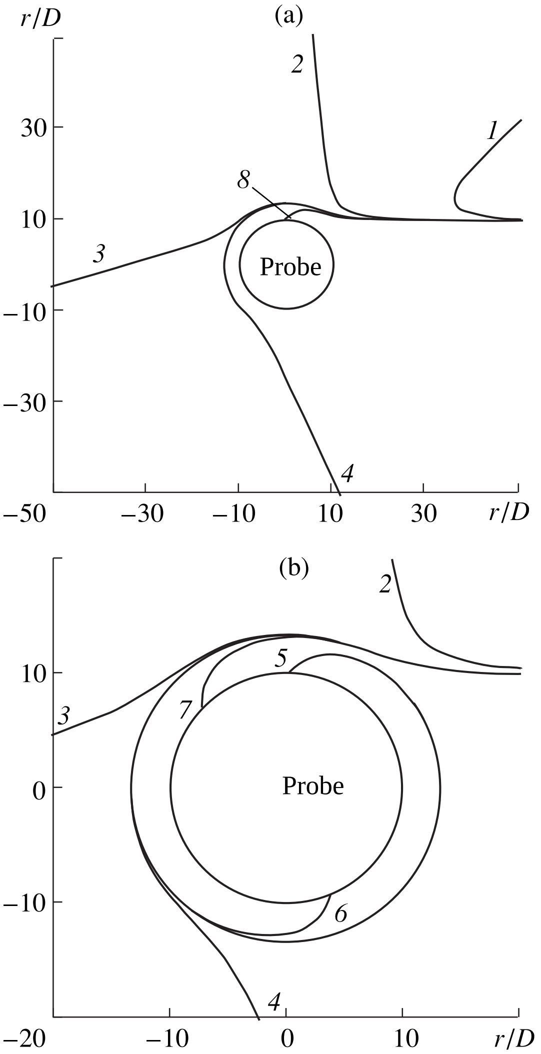

Fig. 4. Trajectories of a dust grain in the perturbed region near the probe with the potential $\varphi_p = 10$ for $p = R_p$ and different initial kinetic energies of the grain: $\gamma_d = K_0/kT_e$ = (*1*) 500, (*2*) 5000, (*3*) 12600, (*4*) 12685, (*5*) 12690, (*6*) 12692, (*7*) 12800, and (*8*) 15000.

tron current. A comparison between the steady-state grain charge and the charge obtained in solving Eq. (9) allows us to determine the applicability range of the steady-state approximation for calculating the dust grain charge. We can clearly see that the steady-state approximation is valid at distances longer than the recharging distance. At shorter distances, the grain charge differs from that obtained in the steady-state approximation because of the delay in the charging process. The delayed charging can be explained by the fact that, within the ion sheath, the grain charge is governed not by the electrons (as is the case in an unperturbed plasma) but by far less mobile ions. As a result, there is not enough time for a sufficiently fast dust grain to acquire a steady-state charge corresponding to the given spatial point.

However, according to Fig. 4, the energies of the grains that can reach the probe surface (and generally can move in a double layer) should be very high, much higher than those observed in real experiments. The grains with energies corresponding to the experimentally observed ones (usually up to 20 eV [11–13]) cannot reach the probe nor can they enter the double layer, which thus restricts the region where the dust grains tend to distribute themselves around the probe. The same result can also be obtained by estimating the height of the potential barrier that the grain with energy K_0 and charge Z_d can overcome. In fact, for $K_0 \sim 1$ eV and $Z_d \sim -10^3$, the relationship $U[\mathrm{B}] \sim K_0[\mathrm{eV}]/Z_d$ gives a rather insignificant potential difference, $U \sim -10^{-3}$ V. Analogously, the energy required for a grain to

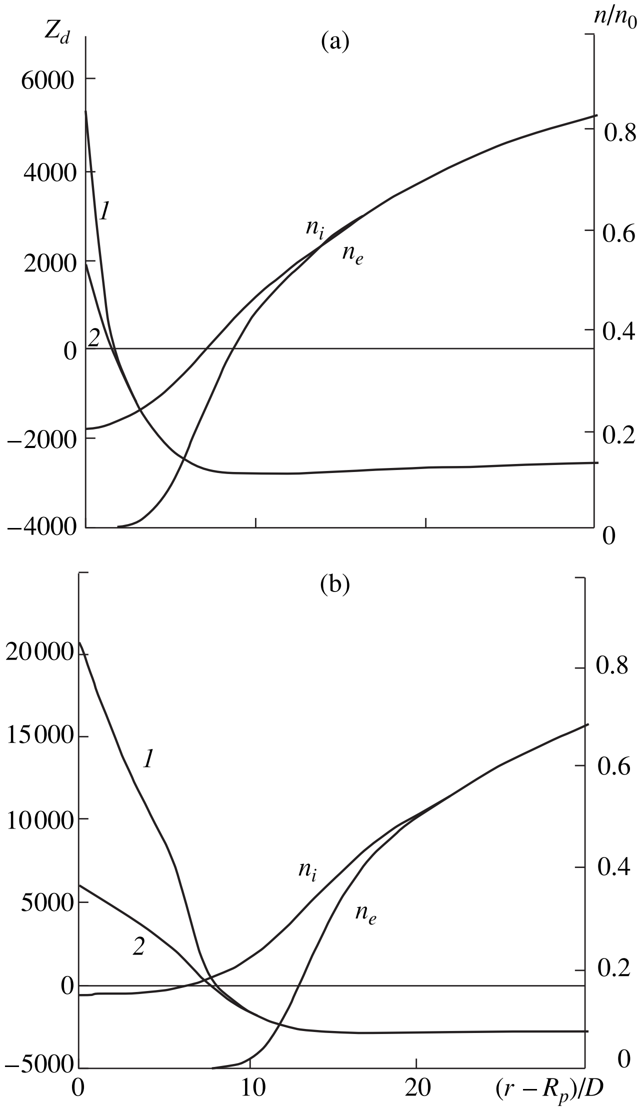

Fig. 5. Radial profiles of (*1*) the steady-state grain charge and (*2*) the grain charge calculated for γ_d = 15000 with allowance for a delay in the charging process. The profiles were obtained for the probe potentials φ_p = (a) 10 and (b) 30.

approach a probe with a potential of –10 V is estimated as K_0[eV] ~ $Z_d U$[V] ~ 10^4 eV. Hence, we can conclude that, for negative probe potentials, dust grains do not directly affect probe measurements in gas-discharge dusty plasmas, because they do not contribute to the total probe current.

The dust grain that manages to acquire enough energy (e.g., under the action of an external force) to enter the double layer moves along a trajectory similar to those shown in Fig. 4. Hence, we can determine the charge of a dust grain (the ratio T_i/T_e is to be determined in advance) by analyzing its trajectory in the following way. First, the experimentally recorded grain trajectory should be compared with the calculated trajectories in order to find the ratio T_i/T_e. Then, the grain charge Z_d at an arbitrary point of the trajectory can be determined in the OML. According to Fig. 6, in plasmas with different values of T_i/T_e, the trajectories of a grain capable of approaching the "recharging" surface can be markedly different. This circumstance allows us to achieve the desired accuracy in comparing the calculated and experimental trajectories and, accordingly, in determining the dust grain charge.

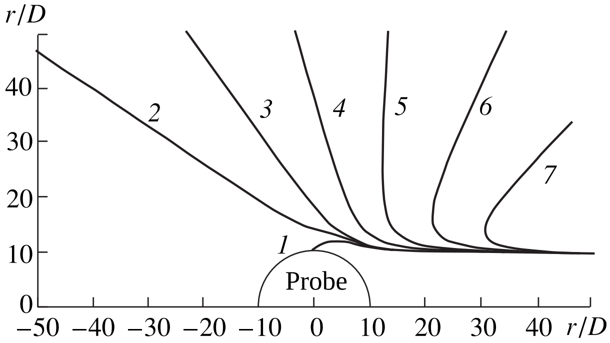

Fig. 6. Trajectories of a dust grain near the probe for U_p = 10 V, $p = R_p$, and K_0 = 15 keV and for different electron temperatures kT_e: (*1*) 1, (*2*) 1.1, (*3*) 1.2, (*4*) 2, (*5*) 3, (*6*) 5, and (*7*) 10 eV.

4. CONCLUSION

We have derived a set of equations for the motion of a dust grain in the perturbed plasma region near the probe. Solving these equations numerically, we have determined the potential distribution around the probe and the radial profiles of the dust grain charge for different probe potentials. We have traced the trajectories of dust grains having different initial kinetic energies and moving in the perturbed region. Dust grains with a negative charge of about 10^3 electron charges are strongly repulsed by the probe electric field, so that grains with low kinetic energies have no direct effect on the probe current. An analysis of the grain trajectories shows that high-energy grains may experience recharging; i.e., at a certain distance from the probe, the grain charge may change sign. We have shown that the steady-state approximation for calculating the dust grain charge is valid on the outside of the recharging surface, where the grain charge is negative. Also, an analysis of the grain trajectories calculated for different values of the ratio T_i/T_e enabled us to propose a new method for determining the grain charge in a dusty plasma.

In deriving the equation for the grain charge, we assumed that the ions and electrons move in the centrosymmetric electric field of the grain and neglected the effects of the probe electric field and collective processes associated with the asymmetry of the grain field [14]. This approach is valid under the condition $R_d \ll D$, in which case the grain electric field at small distance from the grain is described by Coulomb's law, $U \sim U_d R_d / r$, because the space charge comes into play at distances of about the Debye radius D from the grain and farther out. The potential of the grain electric field decreases to nearly zero over a very short distance (smaller than the Debye radius) from the grain; the change in the potential of the layer over this distance is insignificant and can be neglected. For the same reason, we can also ignore the distortion of the probe field by a dust grain.

In addition, we neglected the drag and deceleration forces that are exerted on the grain by the ions and neutrals, respectively, although these forces may be important in certain situations. The ion drag force acting upon a dust grain is important in examining the grain motion in a layer around a probe with a high negative potential such that the ions move preferentially in the radial direction and the grain velocity is high. In this situation, the ion drag force may act to push the grains in the layer toward the probe and to partially counterbalance the repulsive force exerted by the probe on the grains in the region where the grain charge is negative ($Z_d < 0$). In turn, the neutrals act to decelerate the grains, especially at high gas pressures. In order to further improve the model proposed here, it is necessary to correctly account for the effect of the ion drag force and the grain deceleration by neutrals on the motion of dust grains in systems with different parameters.

ACKNOWLEDGMENTS

This work was supported in part by the Russian Foundation for Basic Research, project nos. 98-02-18628 and 98-02-18625. One of the authors (A.A. Samarian) was supported by the Australian Research Council.

REFERENCES

1. A. P. Nefedov, O. F. Petrov, and V. E. Fortov, Usp. Fiz. Nauk **167**, 1215 (1997) [Phys. Usp. **40**, 1163 (1997)].
2. V. E. Fortov, V. I. Molotkov, A. P. Nefedov, and O. F. Petrov, Phys. Plasmas **6**, 1759 (1999).
3. V. N. Tsytovich, Usp. Fiz. Nauk **167**, 57 (1997) [Phys. Usp. **40**, 53 (1997)].
4. V. I. Demidov, N. B. Kolokolov, and A. A. Kudryavtsev, *Probe Methods for Researching Low Temperature Plasma* (Énergoatomizdat, Moscow, 1996).
5. B. V. Alekseev and V. A. Kotel'nikov, *Probe Method for Diagnostics of Plasma* (Énergoatomizdat, Moscow, 1988).
6. O. V. Kozlov, *Electrical Probe in Plasma* (Atomizdat, Moscow, 1969).
7. P. M. Chung, L. Talbot, and K. J. Touryan, *Electric Probes in Stationary and Flowing Plasmas* (Springer-Verlag, New York, 1975; Mir, Moscow, 1978).
8. Yu. M. Kagan and V. I. Perel', Usp. Fiz. Nauk **81**, 409 (1963) [Sov. Phys. Usp. **6**, 767 (1964)].
9. J. E. Allen, Phys. Scr. **45**, 497 (1992).
10. T. Nitter, Plasma Sources Sci. Technol. **5**, 93 (1996).
11. H. Thomas and G. E. Morfill, Nature **379**, 806 (1996).
12. A. Melzer, A. Homann, and A. Piel, Phys. Rev. E **53**, 2757 (1996).
13. J. B. Pieper and J. Goree, Phys. Rev. Lett. **77**, 3137 (1996).
14. F. Melandso and J. Goree, Phys. Rev. E **52**, 5312 (1995).

Translated by O.E. Khadin

Plasma Physics Reports, Vol. 27, No. 4, 2001, pp. 347–354. Translated from Fizika Plazmy, Vol. 27, No. 4, 2001, pp. 369–377.
Original Russian Text Copyright © 2001 by Khomkin, Vorob'ev, Mulenko, Oleĭnikova.

LOW-TEMPERATURE PLASMA

Construction of Chemical Models of a Partially Ionized Atomic Plasma Based on Exact Asymptotic Expansions

A. L. Khomkin, V. S. Vorob'ev, I. A. Mulenko, and E. N. Oleĭnikova

Associated Institute for High Temperatures, Russian Academy of Sciences,
ul. Izhorskaya 13/19, Moscow, 127412 Russia

Received June 16, 2000; in final form, August 7, 2000

Abstract—Chemical models of an atomic plasma based on exact asymptotic expansions are considered. It is shown that, when developing the chemical models of a weakly nonideal plasma, taking into account highly excited atoms results in corrections to the thermodynamic functions and a decrease in the ionization potential that are quite different from those predicted by the Debye theory. © *2001 MAIK "Nauka/Interperiodica".*

1. INTRODUCTION

Let us consider a weakly nonideal (with respect to the Coulomb interaction) partially ionized plasma consisting of electrons, ions, and atoms. In [1–4], an expansion of thermodynamic functions in power series in the activity (z_e of electrons and z_i of ions) up to the terms $z_k^{5/2}$ and $z_k^{5/2}\ln z_k$ (where $z_k = g_k\lambda_k^{-3}e^{\beta\mu_k}$, $k = e, i$; $\beta = 1/T$ is the inverse temperature; and $\lambda_k = (2\pi\beta\hbar^2/m_k)^{1/2}$, g_k, and μ_k are the thermal wavelength, statistical weight, and chemical potential of the particles of kth species, respectively) was obtained for such a plasma. The expansion is based on the physical model [1, 3, 4] in which the atomic plasma is assumed to be a mixture of positively and negatively charged particles, namely, nuclei and electrons interacting with each other via the Coulomb potential. A grand canonical ensemble is considered. No assumptions about the initial atomic component are made; it arises as a result of the pair quantum mechanical interaction between the oppositely charged particles. The final result is obtained by summing the convergent sequences of the ring and ladder diagrams in perturbation theory. For the thermodynamic potential Ω ($\Omega = -PV$, where P is the pressure and V is the system volume) and the total charge density n, one can obtain

$$-\beta\Omega/V = \beta P$$
$$= (z_e + z_i)\left(1 + \frac{\alpha}{3} + \frac{\alpha^2}{8}\right) + z_e z_i \frac{\lambda_e^3}{2}\Sigma_P, \tag{1}$$

$$n = z_e\left(1 + \frac{\alpha}{2} + \frac{\alpha^2}{4}\right) + z_e z_i \frac{\lambda_e^3}{2}\Sigma_P. \tag{2}$$

Here, $\alpha = \beta e^2\chi$ is the plasma parameter; $\chi = \sqrt{4\pi\beta e^2(z_e + z_i)}$ is the inverse Debye radius in terms of the electron and ion activities; and Σ_P is the convergent Planck–Larkin partition function,

$$\Sigma_P = \sum_{n=1}^{\infty} g_n(e^{\beta E_n} - 1 - \beta E_n), \tag{3}$$

where g_n and E_n are the statistical weight and the energy of the bound atomic state with the principal quantum number n. Relations (1) and (2) are written correct to the terms z^2 without taking into account quantum corrections on the order of $\lambda_e\chi$. This significantly simplifies subsequent calculations with no loss of generality. At high temperatures, the equations of state (1) and (2) describe a fully ionized plasma ($\beta P = 2n$), whereas at lower temperatures, they describe an atomic gas ($\beta P = n$). Relations (1) and (2) are rarely used in calculations because they require the determination of an intermediate quantity (the activity z_k) and cannot be generalized to a plasma with a more complex composition.

In practice, in order to calculate the thermodynamic functions and composition of a partially ionized plasma, a chemical model in which the plasma is assumed to be a mixture of weakly interacting electrons (N_e), ions (N_i), and atoms (N_a) contained in a volume V at a temperature T is most widely used [5]. For such a mixture, it is possible to write the free energy F with a correction ΔF, which accounts for the interaction between free charges (in this paper, we do not consider interatomic interactions or interactions between atoms and charged particles). We know more than 20 versions of the plasma chemical model. They differ in both the method for calculating the contribution from the Coulomb interaction to thermodynamic quantities and the form of the atomic partition function. Twelve versions were used in [6] to calculate the thermodynamic functions and the composition of an atomic cesium plasma and to analyze the scatter in the results obtained using these models. Later on, a series of other plasma chemical models [7–12] were developed. In most of the

1063-780X/01/2704-0347$21.00 © 2001 MAIK "Nauka/Interperiodica"

models, either the classical Debye theory [13] or its modification for the grand canonical ensemble [2, 14] was used to take into account the interaction between free charged particles. Various methods for calculating the atomic partition function may be conventionally divided into three groups: (i) calculations according to formula (3), (ii) the use of the so-called “nearest neighbor” approximation (NNA) or the Fermi method [15] (the models of the critical microfield [16] and confluence of lines may also be included in this group), and (iii) calculations of the atomic partition function with allowance for all the bound electronic states whose energies exceed in absolute value the decrease in the atomic ionization potential obtained with one of the modifications of Debye theory [6]. Obviously, each of the existing versions of the chemical model depends on the way the electronic states in an atomic plasma are separated into free and bound states. Nevertheless, the existence of exact asymptotic expansions (1) and (2) requires that the final result be independent of the chosen way of separating the electronic states into free and bound states, because all of the versions of the chemical model of an atomic plasma under conditions when the plasma is weakly nonideal with respect to the Coulomb interaction describe the same plasma states as relations (1) and (2) do. The way of choosing the atomic partition function is studied in most detail in [16]. It is shown that the partition function (3) significantly underestimates the number of observed states, whereas the calculations according to the third version greatly overestimate it.

In our opinion, there is a paradoxical situation in the theory of a nonideal atomic plasma: despite the existence of exact asymptotic expansions (1) and (2), tens of different modifications of the plasma chemical model are employed in calculations. Naturally, the question arises as to what version is the most accurate consequence of the exact physical model based on the expansion in power series in the activity in the grand canonical ensemble.

In this paper, we derive several nonideal plasma chemical models based on the exact asymptotic expansions (1) and (2) of thermodynamic quantities in power series in the activity in the grand canonical ensemble. We deduce expressions for the free energy F and relate the profile of the atomic partition function to the correction for the Coulomb interaction between free charged particles. It is shown that the Debye asymptotics for both the decrease in the ionization potential and corrections to thermodynamic functions is only valid if the atomic partition function is determined by Eq. (3); for any other version, such an asymptotics is absent. The relative contribution of both corrections for the Coulomb interaction in the equation of state and the decrease in the atomic ionization potential is shown to be much less than the corrections predicted by the Debye theory.

2. RING DEBYE APPROXIMATION IN THE GRAND CANONICAL ENSEMBLE

This approximation was first proposed in [2] and then in [4, 8]. Let us determine the free energy for this model in terms of the densities of free electrons (ions) $n_{e,\,i}$ and atoms n_a. This is convenient for subsequent analysis because most of the chemical models of a nonideal plasma are formulated in terms of the free energy. Here and below, the basic point is the separation of the total density of the plasma charged particles, defined by Eq. (2), into two components, namely, the densities of free charged particles and atoms. Following [4, 8], we define the densities of free charged particles and atoms as follows:

$$n_{e,\,i} = z_{e,\,i}\left(1 + \frac{\alpha}{2} + \frac{\alpha^2}{4}\right), \tag{4}$$

$$n_a = z_e z_i \frac{\lambda_e^3}{2}\Sigma_P. \tag{5}$$

Let us consider the relation that links the grand thermodynamic potential Ω to the free energy F:

$$\frac{\beta F}{V} = \frac{\beta\Omega}{V} + (n_e + n_a)\beta\mu_e + (n_i + n_a)\beta\mu_i. \tag{6}$$

Eliminating the activities $z_{e,\,i}$ and using the above relations for the chemical potentials $\mu_{e,\,i}$, we obtain

$$\begin{aligned}\frac{\beta F}{V} = -\Bigg\{& n_a \ln\frac{e\Sigma_P}{n_a\lambda_a^3} + n_i \ln\frac{e}{n_i\lambda_i^3} + n_e \ln\frac{2e}{n_e\lambda_e^3} \\ &+ (n_i + n_e)\left[\ln(1 + \alpha/2 + \alpha^2/4) - \frac{\alpha/6 + \alpha^2/8}{1 + \alpha/2 + \alpha^2/4}\right]\Bigg\}.\end{aligned} \tag{7}$$

The parameter α in Eq. (7) is related to the densities of free charged particles $n_{e,\,i}$ by the expression that follows from Eq. (4):

$$\Gamma^2 = \alpha^2(1 + \alpha/2 + \alpha^2/4), \tag{8}$$

where $\Gamma = (\beta e^2)^{3/2}\sqrt{4\pi(n_e + n_i)}$ is the coupling parameter characterizing the degree to which the plasma is nonideal.

Using the conventional thermodynamic relations, from Eq. (7), we obtain the equations of state and ionization equilibrium:

$$\beta P = (n_e + n_i)\left(1 - \frac{\alpha/6 + \alpha^2/8}{1 + \alpha/2 + \alpha^2/4}\right) + n_a, \tag{9}$$

$$n_a = n_e n_i \frac{\lambda_e^3}{2}\Sigma_P e^{-2\ln(1 + \alpha/2 + \alpha^2/4)}. \tag{10}$$

In the limit in which the plasma is weakly nonideal with respect to the Coulomb interaction ($\alpha \longrightarrow 0$) relations (7)–(10) have the Debye asymptotics. Indeed, the solution to Eq. (8) is $\Gamma \approx \alpha$; then, for the correction to the free energy and for the equations of state and ionization equilibrium, we obtain

$$\frac{\beta\Delta F}{V} = -(n_e + n_i)\frac{\Gamma}{3}, \tag{11}$$

$$\beta P = (n_e + n_i)\left(1 - \frac{\Gamma}{6}\right) + n_a, \tag{12}$$

$$n_a = n_e n_i \frac{\lambda_e^3}{2}\Sigma_P e^{-\Gamma}. \tag{13}$$

Here, the most important result is that the ionization equilibrium equation (13) contains the Planck–Larkin partition function (3). As was mentioned above, this sum incorrectly describes the contribution from highly excited atomic states [16]; for this reason, some versions of the chemical model use the corrections to thermodynamic functions and the decrease in the ionization potential described by expressions (9) and (10), whereas the partition function is calculated according to the second or third version (see Introduction) [6]. Such a modification of the ring Debye approximation is not valid because it would lead to a discrepancy with Eqs. (1) and (2) when calculating thermodynamic functions.

3. DERIVATION OF THE CHEMICAL MODEL BASED ON THE EXPANSION IN THE GRAND CANONICAL ENSEMBLE WITH ALLOWANCE FOR HIGHLY EXCITED ATOMIC STATES

Let us consider another version of the plasma chemical model that is based on the NNA for the atomic component. In [17], using as an example the electron state density determined for an atomic plasma in the same approximations as for Eqs. (1) and (2), it was shown that the sum Σ_P in the expansions of thermodynamic functions appears as a result of an integrable state-density singularity that stems from the divergent contributions from both the highly excited atomic states and free charged particles.

In [18], this state-density singularity was eliminated by substituting the pair approximation with the NNA and taking into account the Debye correlations. It was rigorously shown that the integration of the finite state density does not influence the expansion thermodynamic functions in power series in the activity up to the terms z^2. It was revealed that the highly excited atomic states are naturally present in the plasma, but their influence is neutralized if both the bound and free electronic states are taken into account. The Planck–Larkin partition function appears as a result of such neutralization.

Let us derive the chemical model of an atomic plasma from expansions (1) and (2) (which are accurate up to the terms z^2), using a definition for the atom density n_a based on the NNA, which is different from definition (5). From a physical standpoint, this way of truncating the atomic partition function is the most adequate because it determines the characteristic atom size using a simple physical rule formulated by Fermi [15]: there are no charged particles inside an atom or, in other words, an electron can form a bound state only with the nearest ion [19]. This definition might be refined but the main results obtained below will be the same. The state density obtained in the NNA [18] corresponds to the following atomic partition function:

$$\Sigma_N = \sum_{n=1}^{\infty} g_n e^{\beta E_n}\omega_n, \tag{14}$$

$$\omega_n = \exp\left(-\frac{4}{3}\pi(z_e + z_i)r_n^3\right), \tag{15}$$

where $r_n = a_0 n^2$ is the radius of an electron orbit with the principal quantum number n and $a_0 = \hbar^2/me^2$ is the Bohr radius. The quantity ω_n is the Poisson probability that there are no charges inside a sphere of radius r_n.

Before deriving the chemical model, we make some transformations of the partition function Σ_N that will be called for later. We rewrite sum (14) in the form of a sum of the two summands

$$\Sigma_N = \sum_{n=1}^{\infty} g_n(e^{\beta E_n} - 1 - \beta E_n)\omega_n + \sum_{n=1}^{\infty} g_n(1 + \beta E_n)\omega_n. \tag{16}$$

The main contribution to the first summand in expression (16) is provided by the terms with the bound state energies $E_n \geq T$ and, accordingly, orbit sizes less than the Landau length βe^2. For these states, provided that $\beta e^2 \ll r_{\rm m}$ (where $r_{\rm m}$ is the mean interparticle distance defined by the relation $3/4\pi(z_e + z_i)r_{\rm m}^3 = 1$), we may assume that $\omega_n \approx 1$; hence, the first summand is close to the Planck–Larkin partition function (3). Taking into account that ω_n differs from 1 when calculating this summand would lead to an excessive accuracy because the correction is proportional to z^3. Conversely, in the second summand, the states with large principal quantum numbers n play a major role, because the state statistical weight increases proportionally to n^2. If the number of the excited states taken into account by partition function (14) is large enough ($n_{\max} \sim \sqrt{r_{\rm m}/a_0} \gg 1$), we may pass over to integration in the second summand in Eq. (16) instead of summation over n:

$$\sum_{n=1}^{\infty} g_n(1 + \beta E_n)\omega_n = \int_0^{\infty} g_n(1 + \beta E_n)\omega_n dn. \tag{17}$$

Substituting expression (15) into Eq. (17), we obtain

$$\sum_{n=1}^{\infty} g_n(1+\beta E_n)\omega_n = \int_0^{\infty} 2n^2(1+\beta Ry/n^2)\exp\left[-\frac{4}{3}(z_e+z_i)a_0^3 n^6\right]dn. \qquad (18)$$

Taking the integral in Eq. (18), we have for Σ_N

$$\Sigma_N = \Sigma_P + \frac{4}{(z_e+z_i)\lambda_e^3} f_1(\alpha), \qquad (19)$$

where

$$f_1(\alpha) = \frac{\pi\sqrt{6}}{24}\alpha + \frac{\sqrt{2\pi}\times 3^{1/6}\Gamma(1/6)}{48}\alpha^{5/3}. \qquad (20)$$

In expression (19), the function $f_1(\alpha)$ describes the contribution from highly excited atomic states to the partition function. For brevity, we will omit the argument of the function $f_1(\alpha)$.

To derive a chemical model, we again define the densities of atoms and free charged particles using the NNA partition function for the atoms:

$$n_a = \frac{z_e z_i}{2}\lambda_e^3 \Sigma_N, \qquad (21)$$

$$n_e = n - n_a = z_e\left(1 + \frac{\alpha}{2} + \frac{\alpha^2}{4} - f_1\right). \qquad (22)$$

It is important to note that the sum of these expressions coincides with expression (2). In other words, when defining the atom density n_a, any modification of the partition function certainly changes the expression for the density of free charged particles n_e. Next, repeating the same calculations as for Eq. (6), we obtain for the free energy

$$\frac{\beta F}{V} = -\left\{ n_a \ln\frac{e\Sigma_N}{n_a\lambda_a^3} + n_i \ln\frac{e}{n_i\lambda_i^3} + n_e\ln\frac{2e}{n_e\lambda_e^3} + (n_i+n_e)\left[\ln\left(1+\frac{\alpha}{2}+\frac{\alpha^2}{4}-f_1\right) - \frac{\frac{\alpha}{6}+\frac{\alpha^2}{8}-\frac{f_1}{2}}{1+\frac{\alpha}{2}+\frac{\alpha^2}{4}-f_1}\right]\right\}. \qquad (23)$$

Using conventional thermodynamic relations, we obtain the equations of state and ionization equilibrium:

$$\beta P = (n_e+n_i)\left(1 - \frac{\alpha/6+\alpha^2/8-f_1/2}{1+\alpha/2+\alpha^2/4-f_1}\right) + n_a, \qquad (24)$$

$$n_a = n_e n_i \frac{\lambda_e^3}{2}\Sigma_N e^{-2\ln(1+\alpha/2+\alpha^2/4-f_1)}. \qquad (25)$$

Unlike Eq. (8), here, the parameter α is related to the parameter Γ by a relation that follows from Eq. (22):

$$\Gamma^2 = \alpha^2(1+\alpha/2+\alpha^2/4-f_1(\alpha)). \qquad (26)$$

The expressions for the internal energy E and enthalpy H are as follows:

$$E = TV\left\{\frac{3}{2}(n_a+n_i+n_e) - \frac{n_a E_a'}{T\Sigma_N} - (n_i+n_e)\frac{\frac{\alpha}{2}+\frac{3}{8}\alpha^2-\frac{3}{4}\alpha\frac{\partial f_1}{\partial\alpha}}{1+\frac{\alpha}{2}+\frac{\alpha^2}{4}-f_1}\right\}, \qquad (27)$$

$$H = TV\left\{\frac{5}{2}(n_a+n_i+n_e) - \frac{n_a E_a'}{T\Sigma_N} - (n_i+n_e)\frac{\frac{2\alpha}{3}+\frac{\alpha^2}{2}-\frac{f_1}{2}-\frac{3}{4}\alpha\frac{\partial f_1}{\partial\alpha}}{1+\frac{\alpha}{2}+\frac{\alpha^2}{4}-f_1}\right\}. \qquad (28)$$

Since $f_1(\alpha) \approx 0.32\alpha$ at small values of α, it follows from Eqs. (23)–(28) that taking into account excited atoms radically changes the corrections for the Coulomb interaction to all the thermodynamic functions and decreases the atom ionization potential. Below, we will consider this problem in more detail.

The partition function Σ_N entering expression (23) for the free energy depends on the volume V and densities $n_{e,i}$. Some versions of the chemical model also use partition functions similar to Σ_N. Deriving the equations of state and ionization equilibrium from the free energy equation brings up the question of differentiating Σ_N over the volume and particle densities. Usually, it is not recommended to carry out this differentiation. However, in the version of the chemical model in question, this differentiation is required to obtain the equations of state and ionization equilibrium consistent with relations (1) and (2), the more so as formulas (24) and (25) can be derived directly from relations (1) and (2). When deriving Eqs. (24)–(28), the derivative of any function $\varphi(\alpha)$ with respect to the variables V, $n_{e,i}$, and T can be represented as

$$\partial\varphi(\alpha)/\partial x = (\partial\varphi/\partial\alpha)(\partial\alpha/\partial\Gamma)(\partial\Gamma/\partial x). \qquad (29)$$

4. INFINITE-COMPONENT CHEMICAL MODEL OF AN ATOMIC PLASMA

In [12], a chemical model was developed in which the atomic component was considered as a mixture of an infinite number of components corresponding to atoms in certain excited states. The atomic component in the expression for the free energy is taken into account as follows [12]:

$$\frac{\beta F_a}{V} = -\sum_{k=1}^{\infty} n_k \ln\frac{e g_k e^{\beta E_k}}{n_k \lambda_k^3} - \sum_{k=1}^{\infty} n_k \ln\omega_k, \tag{30}$$

where n_k, λ_k, g_k, and E_k are the density, thermal wavelength, statistical weight, and energy of an atom in the bound state k, respectively, and ω_k is a Poisson probability [analogous to probability (15)] that there are no particles inside the atomic orbit with the principal quantum number k. After minimizing the free energy over the densities, n_k becomes proportional to ω_k, which ensures the convergence of the partition function, which is nearly the same as Σ_N defined by expression (14).

In [12], the last term on the right-hand side of Eq. (30) is referred to as an "entropy" term. Note that such a term was first introduced in the Fermi model; however, including it in the expression for the free energy in [12] looks somewhat artificial because all the additions to F are determined only by the virial coefficients.

Let us derive the so-called infinite-component model from relations (1) and (2). The densities of free charged particles and atoms in the state with the principal quantum number k are

$$n_k = \frac{z_e z_i}{2}\lambda_e^3 g_k e^{\beta E_k}\omega_k, \tag{31}$$

$$n_e = z_e\left(1 + \frac{\alpha}{2} + \frac{\alpha^2}{4} - f_1\right). \tag{32}$$

In Eq. (31), ω_k coincides with that defined by expression (15); hence, the sum of all n_k coincides with n_a defined by expression (21) and the overall particle density coincides with that defined by expression (2).

Let us consider in more detail the origin of the atomic constituent of free energy in formula (6):

$$\begin{aligned} -\frac{\beta F_a}{V} &= \sum_{k=1}^{\infty} n_k\left(1 + \ln\frac{2}{z_e\lambda_e^3} + \ln\frac{1}{z_i\lambda_i^3}\right) \\ &= \sum_{k=1}^{\infty} n_k \ln\frac{2e}{z_e\lambda_e^3 z_i\lambda_i^3} = \sum_{k=1}^{\infty} n_k \ln\frac{2e g_k e^{\beta E_k}\omega_k}{n_k\lambda_k^3} \\ &= \sum_{k=1}^{\infty} n_k \ln\frac{e\Sigma_k}{n_k\lambda_k^3} + \sum_{k=1}^{\infty} n_k\omega_k, \end{aligned} \tag{33}$$

where $\Sigma_k = g_k e^{\beta E_k}$. For the free energy, we obtain

$$\begin{aligned} \frac{F}{TV} &= -n_e\ln\frac{2e}{n_e\lambda_e^3} - n_i\ln\frac{e}{n_i\lambda_i^3} \\ &\quad - \sum_k n_k\ln\frac{e\Sigma_k}{n_k\lambda_k^3} - \sum_k n_k\ln\omega_k \\ &\quad - (n_e + n_i)\left[\ln\left(1 + \frac{\alpha}{2} + \frac{\alpha^2}{4} - f_1\right) - \frac{\alpha/6 + \alpha^2/8 - f_1/2}{(1 + \alpha/2 + \alpha^2/4 - f_1)}\right]. \end{aligned} \tag{34}$$

It is seen from Eq. (34) that the entropy term originates naturally and the correction for the Coulomb interaction coincides with the above correction (23), which differs from the Debye correction. In [12], the Debye correction was used to take into account the Coulomb interaction, which would lead to a result different from relations (1) and (2). Expressing the free energy in form (34) is more preferable than in form (23) because, in the former case, the atomic statistical weights are independent of the density and it is possible to take into account the interaction of the excited atoms with a plasma [12].

In our opinion, the entropy term has a more obvious physical meaning. Let us present the Poisson probability (15) in the form

$$\omega_k = e^{-(z_e + z_i)v_k}, \tag{35}$$

where v_k is a volume occupied by an atom in the kth quantum state. Substituting ω_k into the entropy term and taking into account expression (32), we obtain

$$\begin{aligned} \sum_k n_k\ln\omega_k &= -(z_e + z_i)\sum_k n_k v_k \\ &= -\frac{n_e + n_i}{1 + \alpha/2 + \alpha^2/4 - f_1}\sum_k n_k v_k. \end{aligned} \tag{36}$$

Since summation over all the quantum states provides the total atom density in a plasma

$$\sum_k n_k = n_a, \tag{37}$$

the quantity

$$\sum_k n_k v_k = n_a v_0 \tag{38}$$

can be regarded as a fraction of the plasma volume occupied by atoms in all of the states and the parameter

$$v_0 = \sum_k n_k v_k / \sum_k n_k \tag{39}$$

can be regarded as an averaged (effective) volume of an atom. Using Eqs. (36) and (38), the sum $-n_e \ln \frac{2e}{n_e \lambda_e^3} - n_i \ln \frac{e}{n_i \lambda_i^3} - \sum_k n_k \ln \omega_k$ in (34) can be represented in the linear approximation in α as

$$-n_e \ln \frac{2e(1 - n_a v_0)}{n_e \lambda_e^3} - n_i \ln \frac{e(1 - n_a v_0)}{n_i \lambda_i^3}. \tag{40}$$

Representation (40) has a clear physical meaning: free electrons and ions in an atomic plasma move in a volume reduced by the volume occupied by atoms. This statement agrees completely with the NNA; i.e., there cannot be free charged particles inside an excited atom. Although the fraction of the volume occupied by the atoms is relatively small, it is the terms related to this volume that ensure convergence of the partition function in the model of [12]. We will refer to the corrections for the volume occupied by atoms as configuration corrections in contrast to correlation corrections related to the particle interaction.

Note that the thermodynamic models obtained in Sections 3 and 4 are completely equivalent. It can be shown that expressions (24)–(28) follow from expression (34) for the free energy in the infinite-component model without any additional assumptions. However, their derivation is rather lengthy and we do not present it here.

5. DISCUSSION OF THE RESULTS

Let us consider the version of the chemical model from Section 3 and limit ourselves to the terms linear in the coupling parameter. It follows from Eq. (26) that, in this case, $\alpha \simeq \Gamma$; in addition, according to Eq. (20), we have

$$f_1 \approx \frac{\pi\sqrt{6}}{24}\alpha = a\alpha, \quad \alpha\frac{\partial f_1}{\partial \alpha} = a\alpha, \quad a \simeq 0.32. \tag{41}$$

The expressions for the plasma thermodynamic functions and the equation of ionization equilibrium take the form

$$F = -TV\left\{n_a \ln \frac{e\Sigma_N}{n_a \lambda_a^3} + n_i \ln \frac{e}{n_i \lambda_i^3} + n_e \ln \frac{2e}{n_e \lambda_e^3} + (n_e + n_i)\frac{\Gamma}{3}\left(1 - \frac{3}{2}a\right)\right\},$$

$$E = TV\left\{\frac{3}{2}(n_a + n_e + n_i) - \frac{n_a E'_a}{T\Sigma_N} - (n_e + n_i)\frac{\Gamma}{2}\left(1 - \frac{3}{2}a\right)\right\},$$

$$H = TV\left\{\frac{5}{2}(n_a + n_e + n_i) - \frac{n_a E'_a}{T\Sigma_N} - (n_e + n_i)\frac{2}{3}\Gamma\left(1 - \frac{15}{8}a\right)\right\}, \tag{42}$$

$$P = T\left\{n_a + (n_e + n_i)\left[1 - \frac{\Gamma}{6}(1 - 3a)\right]\right\},$$

$$n_a = \frac{n_e n_i}{2}\lambda_e^3 \Sigma_N e^{-\Gamma(1 - 2a)}.$$

The corrections for "nonideality" to the thermodynamic functions differ from the Debye corrections by the value of the numerical factor at the parameter Γ. Thus, the correction to the pressure is reduced by a factor of nearly 25 compared to the Debye correction, and the decrease in the ionization potential is reduced threefold. This result qualitatively explains the fact that, in experiments [13], a nonideal plasma behaved as an ideal gas.

The corrections for nonideality in Eqs. (42) are not related to each other by the main thermodynamic relations [20]; for example, $\Delta P \neq -\partial(\Delta F)/\partial V$ because the numerical factors at Γ in Eqs. (42) are different. This is caused by the fact that the corrections consist of components of different natures, namely, configuration and correlation components. If we separate them, then the main thermodynamic relations will hold for all of the thermodynamic quantities and the factor $(1 - 3a/2)$ at Γ will appear in all of the expressions. The configuration correction (38), which is equal to the fraction of the volume occupied by atoms, can be calculated analytically; in the linear approximation in Γ, it is equal to

$$\sum_k n_k v_k = n_a v_0 = a\Gamma/4. \tag{43}$$

Separating the configuration and correlation corrections in Eqs. (42) and restricting ourselves to the terms linear in Γ, we obtain

$$F = -TV\left\{n_a \ln \frac{e\Sigma_N}{n_a \lambda_a^3} + n_i \ln \frac{e}{n_i \lambda_i^3} + n_e \ln \frac{2e}{n_e \lambda_e^3} + (n_e + n_i)\frac{\Gamma}{3}\left(1 - \frac{3}{2}a\right)\right\},$$

$$P = T\left\{n_a + \frac{n_e + n_i}{1 - n_a v_0} - (n_e + n_i)\frac{\Gamma}{6}\left(1 - \frac{3}{2}a\right)\right\},$$

$$\begin{aligned} E &= TV\left\{\frac{3}{2}(n_a+n_e+n_i)-\frac{n_aE_a'}{T\Sigma_N}\right. \\ &\qquad \left. -(n_e+n_i)\Gamma\left(1-\frac{3}{2}a\right)\right\}, \\ H &= TV\left\{\frac{3}{2}(n_a+n_e+n_i)+\frac{n_e+n_i}{1-n_av_0}\right. \\ &\qquad \left. -\frac{n_aE_a'}{T\Sigma_N}-(n_e+n_i)\frac{2}{3}\Gamma\left(1-\frac{3}{2}a\right)\right\}, \\ n_a &= \frac{n_en_i}{2}\frac{\lambda_e^3\Sigma_N}{(1-n_av_0)^2}e^{-\Gamma\left(1-\frac{3}{2}a\right)}. \end{aligned} \tag{44}$$

It is seen from Eqs. (44) that the factor $(1 - 3a/2)$ appears in all of the correlation corrections. Equations (42) and (44) can be regarded as a chemical model of a weakly ionized plasma, which is fully consistent with the exact asymptotic expansions (1) and (2). None of the chemical models mentioned in the Introduction corresponds to the obtained results.

Thus, the contribution from highly excited atomic states to the plasma thermodynamic functions is shared between the configuration and correlation terms. The correlation term differs from the Debye term even in the limit $\Gamma \longrightarrow 0$. The configuration term does not contribute to the plasma internal energy and can be regarded as a contribution from a certain volume occupied by atoms; however, this contribution differs from the Van der Waals contribution because it does not follow from interatomic (or atom–ion) repulsion.

Now, let us discuss how the transition to the Debye asymptotics occurs. We consider a high-temperature ($\beta Ry \ll 1$) weakly ionized plasma. In this case, partition function (19) contains only the second summand and the equation of ionization equilibrium takes the form

$$n_a = \frac{2n_en_i}{(n_e+n_i)}f_1(\Gamma). \tag{45}$$

Using the electroneutrality condition, we express the densities $n_{e,i,a}$ through the total density of nuclei $n = n_i + n_a$ in the linear approximation in the parameter Γ:

$$\begin{aligned} n_{e,i} &= n(1-a\Gamma), \\ n_a &= na\Gamma. \end{aligned} \tag{46}$$

When deriving (46), we used linear approximation (41) for the function $f_1(\Gamma)$.

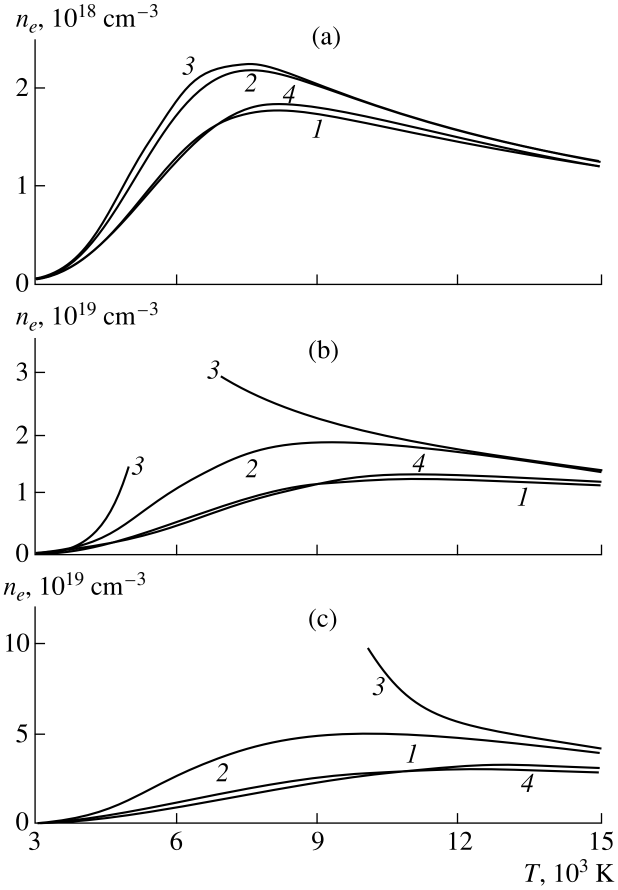

Electron density vs. temperature at pressures P = (a) 5, (b) 50, and (c) 150 atm for different thermodynamic models: (*1*) ideal gas model, (*2*) ring Debye approximation, (*3*) Debye theory, and (*4*) present paper [calculation by formulas (24)–(29)]; curves *1–3* correspond to the Plank–Larkin partition function and curve (*4*) correspond to the NNA partition function calculated by formula (15).

Substituting expressions (46) into Eqs. (42), in the linear approximation in Γ, we obtain for the pressure

$$\beta P = n_a + (n_e+n_i)\left(1-\frac{\Gamma}{6}(1-3a)\right) = 2n\left(1-\frac{\Gamma}{6}\right), \tag{47}$$

which corresponds to the classical Debye result. It follows from Eqs. (46) that a nonideal plasma is always partially ionized. Even at high temperatures, a nonideal plasma contains excited atoms, which contribute to the classical Debye correction. Applying the Debye theory directly to the chemical model of an atomic plasma is incorrect because the excited atoms would be taken into account twice. It can only be applied to an atomic plasma in the version of the chemical model considered in Section 2 and can only be used to calculate the thermodynamic functions of an atomic plasma. In this model, the density of free charged particles is overestimated; hence, applying the model to multicomponent plasmas (in which the corrections for interatomic interaction, as well as the interaction between atoms and free charged particles, should be taken into account) is also incorrect.

The figure presents isobaric dependences of n_e on the temperature T in a cesium plasma, calculated using the models with different equations of state. It is seen that the NNA and taking into account the highly excited atomic states substantially decrease the influence of the Coulomb interaction on the plasma composition. The electron density is close to that in an ideal gas (curves *1* and *4*) within a large region of the phase diagram.

6. CONCLUSION

Several versions of the chemical model of a weakly nonideal atomic plasma are accurately derived based on the exact asymptotic expansions of thermodynamic quantities in the grand canonical ensemble. The contribution of the Coulomb interaction between free charged particles to the thermodynamic quantities of an atomic plasma is found in the NNA for the atomic partition function. Actually, this result corresponds to applying the Hill theory [21] of virial coefficients for systems with chemical reactions to the Coulomb interaction. The revealed strong decrease in the contribution of the Coulomb interaction to the equations of state and ionization equilibrium stems from the existence of highly excited atomic states. It is shown that none of the existing versions of the chemical model of an atomic plasma, except that considered in Section 2, correspond to asymptotic expansions (1) and (2). Chemical models of an atomic plasma (see Sections 3 and 4) corresponding to asymptotic expansions (1) and (2) are proposed.

ACKNOWLEDGMENTS

This work was supported by the grant “School of L.M. Biberman and V.S. Vorob’ev.”

REFERENCES

1. A. A. Vedenov and A. I. Larkin, Zh. Éksp. Teor. Fiz. **36**, 1139 (1959).
2. A. A. Likal’ter, Zh. Éksp. Teor. Fiz. **56**, 241 (1969) [Sov. Phys. JETP **29**, 133 (1969)].
3. Yu. G. Krasnikov, Zh. Éksp. Teor. Fiz. **73**, 516 (1977) [Sov. Phys. JETP **46**, 270 (1977)].
4. W.-D. Kraeft, D. Kremp, W. Ebeling, and G. Röpke, *Quantum Statistics of Charged Particle Systems* (Plenum, New York, 1986; Mir, Moscow, 1988).
5. *Essays of Plasma Physics and Chemistry*, Ed. by L. S. Polak (Nauka, Moscow, 1971).
6. V. E. Fortov, B. N. Lomakin, and Yu. G. Krasnikov, Teplofiz. Vys. Temp. **9**, 869 (1971).
7. V. K. Gryaznov, M. V. Zhernokletov, V. N. Zubarev, *et al.*, Zh. Éksp. Teor. Fiz. **78**, 573 (1980) [Sov. Phys. JETP **51**, 288 (1980)].
8. Yu. G. Krasnikov and V. I. Kucherenko, Teplofiz. Vys. Temp. **16**, 43 (1978).
9. A. S. Kaklyugin and G. É. Norman, Teplofiz. Vys. Temp. **25**, 209 (1987).
10. I. A. Mulenko and A. L. Khomkin, Teplofiz. Vys. Temp. **29**, 72 (1991).
11. D. Saumon and G. Chabrier, Phys. Rev. A **46**, 2084 (1992).
12. A. Y. Potekhin, Phys. Plasmas **3**, 4156 (1996).
13. V. E. Fortov and I. T. Yakubov, *Nonideal Plasma* (Énergoatomizdat, Moscow, 1994).
14. V. K. Gryaznov, I. L. Iosilevskiĭ, Yu. G. Krasnikov, *et al.*, in *Thermophysical Properties of Operating Environment of Gas-Phase Nuclear Reactor*, Ed. by V. M. Ievlev (Atomizdat, Moscow, 1980).
15. L. P. Kudrin, *Statistical Plasma Physics* (Atomizdat, Moscow, 1974).
16. V. S. Volokitin and N. N. Kalitkin, Preprint No. 11 (VTsMM Akad. Nauk SSSR, Moscow, 1991).
17. V. S. Vorob’ev, Teplofiz. Vys. Temp. **13**, 245 (1975).
18. V. S. Vorob’ev and A. L. Khomkin, Teor. Mat. Fiz. **26**, 364 (1976).
19. G. Ecker, *Theory of Fully Ionized Plasmas* (McGraw-Hill, New York, 1972; Mir, Moscow, 1974).
20. L. D. Landau and E. M. Lifshitz, *Statistical Physics* (Nauka, Moscow, 1976; Pergamon, Oxford, 1980).
21. T. L. Hill, *Statistical Mechanics: Principles and Selected Applications* (McGraw-Hill, New York, 1956; Inostrannaya Literatura, Moscow, 1960).

Translated by N.N. Ustinovskiĭ

Plasma Physics Reports, Vol. 27, No. 4, 2001, pp. 355–361. Translated from Fizika Plazmy, Vol. 27, No. 4, 2001, pp. 378–384.
Original Russian Text Copyright © 2001 by Magunov.

LOW-TEMPERATURE PLASMA

Kinetics of Heat Release during the Interaction of a Low-Temperature Oxygen Plasma with a Catalytically Active Surface

A. N. Magunov

Institute of General Physics, Russian Academy of Sciences, ul. Vavilova 38, Moscow, 117942 Russia

Received April 4, 2000; in final form, July 3, 2000

Abstract—The method of differential scanning calorimetry is applied to determine the temperature dependence of the power transferred to a solid surface during the deactivation of excited molecular states and atomic recombination on the surface of a platinum film in a low-pressure (40 Pa) capacitive RF discharge in oxygen. Temperature scanning within the range 300–600 K is performed under the action of the heat flux from the discharge. The total heat flux is separated into the components associated with different heat transfer mechanisms. The effective activation energy for the heat release related to the relaxation of the excited states of particles on the platinum surface is about 75 meV. *© 2001 MAIK “Nauka/Interperiodica”.*

1. INTRODUCTION

Catalytic processes occurring in the interaction of a weakly ionized plasma with a surface and accompanied by heat release are usually studied with the aim of developing discharge diagnostic techniques [1–3]. Traditionally, the object under investigation is the gas phase of a discharge and the aim of the study is to determine the densities of the excited particles, radicals, etc. from thermal effects on catalytically active surfaces [4, 5]. However, since the thermal methods are nonselective with respect to different particles or excited states and the information provided by the conventional thermal diagnostics is insufficient, these methods fail to resolve the problem of separating the contributions from different particles to the heat transfer onto the surface or to determine the density of the excited particles in the discharge volume. Spectral methods of diagnostics of the gas phase of a discharge are more informative.

Thermal effects occurring in the interaction of a gas-discharge plasma with catalytically active materials are of interest for aircraft engineering [6] and microtechnology because the catalytic energy release may result in undesired heating of a solid body (for instance, an aircraft body or a substrate on which the surface microstructures are etched) due to deactivation of the excited particles. The relaxation rate of the metastable excited levels of particles colliding with a surface increases as the surface temperature increases, which leads to both a positive feedback in the “temperature–heat release rate” chain and an avalanche-like growth of the temperature [7, 8]. To forecast the temperature regime of the surface, one needs information on the catalytic heat release rate. This and other problems on the heat exchange between a plasma and a surface can be resolved only with the help of thermal measurements.

The problem of studying thermal catalytic processes consists in distinguishing the heat power related to deactivation of the excited states against the background of several mechanisms for heat exchange between a plasma and a surface. When applying stationary diagnostic methods [4], one has no information about the main characteristic of the heat transfer mechanism under study—the temperature dependence of the temperature growth rate of a solid body in a discharge (or the power transferred from a discharge to the surface). For this reason, attempts to determine the characteristic features of different heat transfer mechanisms and experimentally identify the presence of individual mechanisms have been unsuccessful.

In this paper, it is shown that the nonstationary diagnostic method allows one to distinguish between the contributions from different mechanisms for heating a solid body in a discharge and to determine the heat power related to the activation of the excited states on a catalytically active surface over a wide temperature range.

2. EXPERIMENT

The experiment was carried out with a cylindrical quartz reactor 19 cm in diameter and 45 cm in length. An oxygen discharge at pressures of 0.1–1 torr was excited in a continuous gas flow (with a flow rate of ~100 sccm) by external RF electrodes at a frequency of 13.56 MHz. The input power was equal to P_0 = 100–300 W. Under these conditions, the discharge occurs in the low-current (or α) form [9]; a characteristic feature of such a discharge is that the power is dissipated in the discharge volume (rather than in the electrode sheaths) and the gas temperature is rather high. The degree of dissociation of oxygen molecules was $\leq 10^{-2}$; the degree of gas ionization was no more than 10^{-6}. The gas temperature at the axis was 500–800 K. The discharge emission spectrum in the range 300–900 nm was measured with the help of a KSVU-23 computerized spectral complex. The design of the plasmochemical reactor was described in detail in [10].

Scanning calorimetry in a discharge implies continuous measurements of the heat power transferred to the calorimeter under conditions when its temperature varies in time in a given fashion under the action of the heat flux from the discharge. The temperature measurements are based on recording the time-dependent temperature $T(t)$ from the start of the discharge up to the stage in which the calorimeter temperature reaches a steady-state value. After differentiating the dependence $T(t)$, we obtain the calorimeter heating power $P \sim dT/dt$ as a function of time. Since the heating process is quasisteady, the time can be excluded from consideration and the data can be represented in the "temperature–power" coordinates (in this case, the power transferred from the discharge to the surface depends explicitly on the surface temperature rather than on time). The quasisteady character of the process is determined by the relation between two characteristic times: the short relaxation time of the temperature and particle density distributions in a boundary sheath around the calorimeter ($\tau_1 \sim 1$ ms and the long time of calorimeter heating ($\tau_2 \sim 100$ s) in the discharge.

The differential version of scanning calorimetry was used to determine the difference power [11]. To find the contribution from the energy release due to the relaxation of excited states on a catalytically active surface, we compared the dependences $P(T)$ for two calorimeters identical in shape, but with different surface properties. As calorimeters, we used 0.8- to 0.9-mm-thick polished silicon single crystals 2.5×2.5 cm in size. The catalytically active surface of one calorimeter was produced by depositing a thin (0.2 μm) platinum film by magnetron sputtering. The surface of the second (reference), catalytically inert calorimeter was covered by a natural oxide film approximately 5–10 nm thick. The formation of the oxide film on the cold surface occurs according to the Cabrera–Mott mechanism and ends when the film becomes thick enough to prevent the tunneling of an electron from the crystal to oxygen adsorbed on the film surface [12]. The further growth of the oxide film occurs only due to diffusion of oxygen through the film. This process is characterized by a high activation energy ($\Delta E \geq 1.5$ eV) and takes place at high temperatures (≥1300 K) [13]. For this reason, the properties of a silicon single crystal in a low-pressure oxygen plasma change only slightly. The constancy of the silicon properties was tested experimentally by exposing the crystal to the action of an oxygen discharge for several tens of minutes. The oxide film thickness was measured by an IFS-88 Bruker Fourier-spectrometer and an LEF-3M laser ellipsometer at a wavelength of 633 nm. In an oxygen plasma, platinum also oxidizes to form volatile compounds [14]. However, under our experimental conditions, the oxidation rate of the platinum film was negligibly small, which was ascertained by weighing the sample accurate to 0.1 mg with an analytical balance. Hence, we believe that chemical reactions on the silicon and platinum surfaces do not occur and, consequently, the heat release related to these reactions is absent.

The time-dependent temperature of the calorimeters was measured using laser interference thermometry [15] at a wavelength of 1.15 μm (the He–Ne laser line, lying in the transparency band of the silicon crystal). In the case of the calorimeter with a metal film on one of its surfaces, the laser beam fell on the opposite crystal surface. The calorimeters were placed inside the reactor in turn; in both cases, the discharge was initiated at the same wall temperature and at the same gas pressure and was maintained by the same input power. The dependence $T(t)$ was also measured during the calorimeter cooling after the discharge was switched off. The kinetics of cooling allowed us to determine the radiative power loss for each calorimeter. This is necessary because one of the calorimeters was covered with a metal film, so that the emitting properties of the calorimeters were different. In addition, the temperature dependences of the emissivities of optically thin semiconductors differed substantially from the dependences characteristic of blackbody and graybody radiation. Note that the power (rather than the exponential) temperature dependence of the emitted power is characteristic of 1-mm-thick weakly doped semiconductor crystals in the range of low temperatures $T \leq 0.05(E_g/k)$, where E_g is the band gap energy of the crystal and k is the Boltzmann constant [16].

3. RESULTS AND DISCUSSION

Figure 1 shows the dependences $T(t)$ during heating of the inert and active calorimeters in the discharge for two levels of the input power. It is seen that, in both cases, the heating rate of the calorimeter with a platinum film is higher, although its mass is greater by 12% (the thickness of the active calorimeter is 0.9 mm, whereas that of the inert calorimeter is 0.8 mm). We carried out a test experiment on the heating a calorimeter whose surface was covered by a thin (0.2 μm) aluminum film. The dependences $T(t)$ for the calorimeter with an aluminum film and reference calorimeter coincided. Hence, the additional heat release on the platinum surface is related to its catalytic properties, i.e., to the capability of substantially increasing the rates of some elementary processes. This heat release may be attributed to the recombination of oxygen atoms as well as deactivation of the $b^1\Sigma_g^+$ (the excitation energy is $\varepsilon \approx$ 1.6 eV and the radiation lifetime is $\tau \approx 7$ s) and $a^1\Delta_g$ ($\varepsilon \approx$ 1 eV and $\tau \approx 3 \times 10^3$ s) excited singlet levels of molecular oxygen on the active surface. The emission spectra of both atomic and singlet oxygen in the discharge were recorded. The fraction of energy transferred from the excited particles to the solid body is usually unknown; it is believed that, in the interaction of singlet oxygen with platinum, this fraction is close to unity [17].

Figure 2 shows the kinetics of cooling the calorimeters in a cold gas (the cooling time of the reactor gas after switching off the discharge is equal to 0.1 s). The temperature dependences of the calorimeter heating power in the discharge and the cooling power after switching off the discharge were calculated by numerically differentiating the curves $T(t)$ (Fig. 3). The temperature–power dependence is analogous to a phase trajectory on the coordinate–momentum plane used in mechanics.

When calculating the derivative dT/dt, it is necessary to eliminate the noise associated with both fluctuations in the power input in the discharge and errors in determining the instants corresponding to interference extremums in thermometry measurements. For this reason, when processing the experimental data, the dependences $T(t)$ were approximated by polynomials in order to smooth fluctuations in the heating and cooling rates.

The equations of energy conservation for the active and inert calorimeters have the form

$$D_1 \equiv c\rho h(dT/dt)_1 = 2\alpha(T_g - T) + D_h - (D_r)_1, \quad (1)$$

$$D_2 \equiv c\rho h(dT/dt)_2 = 2\alpha(T_g - T) - (D_r)_2, \quad (2)$$

where c, ρ, and h are the specific heat, mass density, and thickness of the crystal, respectively; α is the heat transfer coefficient; T_g is the gas temperature outside the thermal boundary layer; and the terms D_h and D_r are related to the heat release via deactivation of excited states and radiative heat loss, respectively.

The first terms on the right-hand sides of Eqs. (1) and (2) describe the heat flux caused by both heat conduction in gas and relaxation of the translational and rotational degrees of freedom of the particles impacting the surface. The power transferred to the surface linearly decreases with calorimeter temperature. If the inequality $NuKn \ll \gamma$ is satisfied, this heat flux is independent of the surface material (here, $Nu = \alpha L/\lambda$ is the Nusselt number, $Kn = L_0/L$ is the Knudsen number, γ is the heat accommodation coefficient of the energy of the translational degrees of freedom of a particle impacting the surface, L is the characteristic size of the calorimeter, λ is the thermal conductivity of the gas, and L_0 is the mean free path of neutrals). The heat-exchange rate is limited by the energy transfer through the thermal boundary layer [18]. The largest temperature drop $(\Delta T)_b$ occurs in the boundary layer, whose thickness is comparable with the characteristic size of the calorimeter. The temperature drop across the Knudsen layer $(\Delta T)_k$, which depends on the heat accommodation coefficient and, consequently, on the surface properties, is negligibly small as compared to $(\Delta T)_b$. The Knudsen layer thickness is comparable with the mean free path of the gas particles.

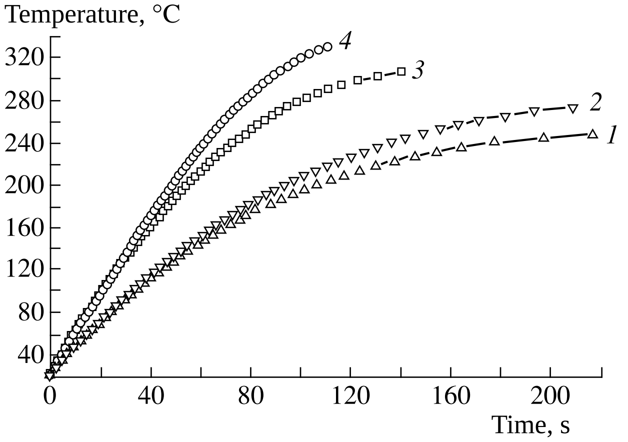

Fig. 1 Time dependences of the calorimeter temperatures after the initiation of an RF discharge at a pressure of 50 Pa. The power input in the discharge is (*1*, *2*) 140 and (*3*, *4*) 280 W. The inert calorimeter is made of a silicon single crystal 2.8 × 1.5 cm in size and 0.8 mm thick (*1*, *3*). The active calorimeter has an area of 2.8 × 1.5 cm and a thickness of 0.9 mm; one of its surfaces is covered by a platinum film (*2*, *4*).

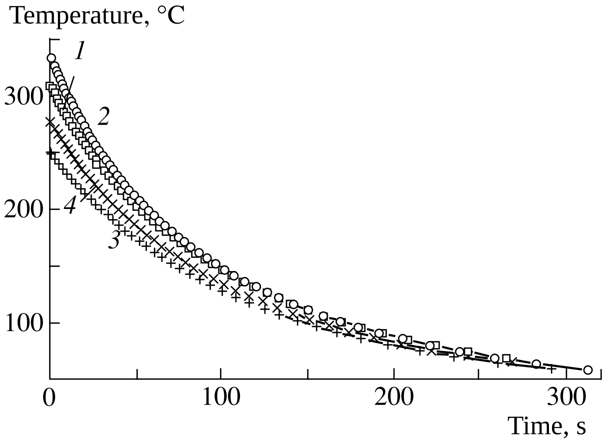

Fig. 2. Cooling kinetics of (*1*, *3*) the inert and (*2*, *4*) active calorimeters after switching off an RF discharge. The input power is (*1*, *2*) 280 and (*3*, *4*) 140 W.

We assume that the temperature profiles in the boundary layers and, consequently, the heat transfer coefficients α are the same for inert and active calorimeters. However, if the excited particles partially transfer their energy to the gas after the interaction with the active surface, the temperature profile can be distorted because of an additional heating of the gas near the calorimeter. In this case, the heat transfer coefficients of the two calorimeters may be different. This question is still unclear.

The gas temperature in the discharge, the heat transfer coefficient, and the heating rate are determined from the heating kinetics of the inert calorimeter [19]. The gas temperature equals 310°C at P_0 = 140 W and 470°C at P_0 = 280 W. The heat transfer coefficient α at

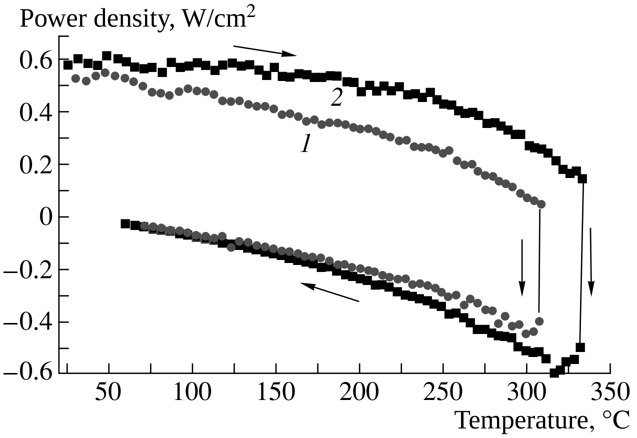

Fig. 3. Temperature dependence of the power density D during heating the calorimeter by the discharge ($D > 0$) and cooling it ($D < 0$) after switching off the discharge for (*1*) the inert and (*2*) active calorimeters. The input power is 280 W. Arrows show the evolution in time: after the initiation of the discharge, D abruptly increases from zero; then, it decreases as the calorimeter heats up; after switching off the discharge, it jumps to a lower half-plane; and, finally, due to heat loss, returns to the temperature of the reactor wall ($T \approx$ 40–50°C).

P_0 = 140 W is equal to 6.4×10^{-4} W/(cm^2 K); at P_0 = 280 W, this coefficient is equal to $\alpha \approx 6.5 \times 10^{-4}$ W/(cm^2 K). The characteristic heating time of the inert calorimeter is $\tau = c\rho h/2\alpha$; for heating in the discharge, we have $\tau \approx 110$ s at P_0 = 140 W and $\tau \approx 105$ s at P_0 = 280 W.

The cooling kinetics of the calorimeters gives the values of the gas temperature in the reactor and the heat transfer coefficients after switching off the discharge. The gas temperature is equal to 42–44°C and coincides with the wall temperature. The heat transfer coefficients of the inert and active samples are the same and equal to $\alpha \approx 6.2 \times 10^{-4}$ W/(cm^2 K). The cooling time constant at low temperatures (at which the thermal emission of the sample plays a lesser role as compared to molecular heat conduction) after switching off the discharge is equal to $\tau \approx 120$ s for any sample.

The contribution from charged particles to heat transfer is three orders of magnitude smaller than the contribution from neutral particles because of the low degree of gas ionization and the low floating potential of the surface (nearly 10 V). The effect of discharge emission was tested by depositing antireflecting films on the crystal surface. SiO_2 and Si_3N_4 films with thicknesses in the range from 0.2 to 0.5 μm decrease the coefficient of light reflection from the surface in the 200- to 1000-nm range by a factor of 1.5–2. In this case, the heating rate of the crystal does not increase, which indicates the negligible role of optical radiation in the calorimeter heat balance. The absence of RF heating of a metal film was proved experimentally in [20].

Since the first terms on the right-hand sides of Eqs. (1) and (2) are the same, we obtain

$$D_h = D_1 - D_2 + (D_r)_1 - (D_r)_2. \quad (3)$$

The values of $(D_r)_1$ and $(D_r)_2$ are determined from the cooling kinetics of the calorimeters after switching off the discharge:

$$(D_c)_1 = 2\alpha(T_g - T) - (D_r)_1, \quad (4)$$

$$(D_c)_2 = 2\alpha(T_g - T) - (D_r)_2. \quad (5)$$

When the condition $\mathrm{Nu} \cdot \mathrm{Kn} \ll \gamma$ is satisfied, the term $2\alpha(T_g - T)$ is the same for both calorimeters and is determined from the low-temperature part of the curve $D(T)$ because the contribution of radiation to the cooling rate is negligibly small in this temperature range. The radiation power of an optically thin, weakly doped silicon single crystal in the range $T \le 800$ K increases with temperature more rapidly than by the Stefan–Boltzmann law, $D_r \sim T^4$ (apparently, the thermal emission power of the crystal is lower than the blackbody radiation power in this case). The reason for this is that the main mechanism for heat transfer in the intermediate and far infrared regions is related to free charge carriers (electrons in the conduction zone and holes in the valence zone), whose density is related to the temperature by the expression $n_n \approx n_p \sim \exp(-\Delta E/kT)$, where the activation energy is close to the half of the band gap energy of the crystal, $\Delta E \approx E_g/2$.

Approximating the experimental temperature dependence of radiative heat loss of the silicon calorimeter without a film in the range $T \approx$ 170–300°C by the Arrhenius dependence, we obtain $(D_r)_1 \approx 3.7 \times 10^4 \exp(-7070/T)$; in this case, the activation energy is equal to $\Delta E \approx 0.6$ eV, which is very close to the half of the band gap energy. In fact, the obtained dependence is determined by the difference between two energy fluxes, one of which is emitted and the other (emitted by the wall and other reactor components) is absorbed by the sample.

The thermal emission of the calorimeter with a metal film on one of the calorimeter surfaces consists of three summands: on the side of the uncovered surface, both the film and the single crystal emit (the former emits through the optically thin crystal), whereas only the film emits on the opposite calorimeter surface. The power of radiative heat loss of the calorimeter with a platinum film is higher than that of the crystal without a film and differs substantially from the Arrhenius temperature dependence (Fig. 4).

The temperature dependences of the power transferred from the discharge to the surface of the inert and active calorimeters are shown in Fig. 5. With radiative heat loss taken into consideration, both of the dependences $D(T)$ are almost linear. The difference between them is described by expression (3). The temperature dependences $D_h(T)$ plotted in Arrhenius coordinates fit a straight line (Fig. 6). The power transferred to the calorimeter due to the relaxation of excited states on the surface increases as the input power in the discharge increases. The mean square method was used to determine the parameters of the Arrhenius temperature dependence $D_h = (D_h)_0\exp(-\Delta E_h/kT)$ characterizing the kinetics of catalytic heat release on the surface:

$$D_h\ (\mathrm{W/cm^2}) \approx 1.5\exp(-888/T)\ \text{for}\ P_0 = 280\ \mathrm{W},$$

$$D_h\ (\mathrm{W/cm^2}) \approx 0.5\exp(-845/T)\ \text{for}\ P_0 = 140\ \mathrm{W}.$$

The activation energies in these expressions are almost the same: $\Delta E_h \approx 0.076$ eV for $P_0 = 280$ W and $\Delta E_h \approx 0.073$ eV for $P_0 = 140$ W. The error is ±0.01 eV. Such low values of the activation energy mean that the relaxation of excited states does not require a high temperature of the active surface; the efficiency of the process can be high even at low temperatures. It is this effect in which the catalytic properties of platinum manifest themselves: platinum substantially decreases the activation energy and increases the probability of elementary processes. The same processes occur at a low rate on the SiO_2 surface and, for this rate to increase, it is necessary to heat the surface to very high temperatures [21]. The apparent small increase in the activation energy, which is observed when increasing the input power, may be the consequence of both the additional gas heating in the boundary layer and the increase in the heat transfer coefficient.

Plotting the temperature dependence in Arrhenius coordinates makes sense only when the catalytic heat release is limited by the rate of relaxation processes on the surface (the kinetic limitation of heat transfer). In this case, the density of particles with excited internal degrees of freedom near the surface differs only slightly from their density in the discharge volume. The slowest stage of heat transfer is associated with one of the elementary surface processes (adsorption, reaction, or desorption), which is of activation character (i.e., it is accompanied by overcoming the energy barrier ΔE_h) and is characterized by a low probability.

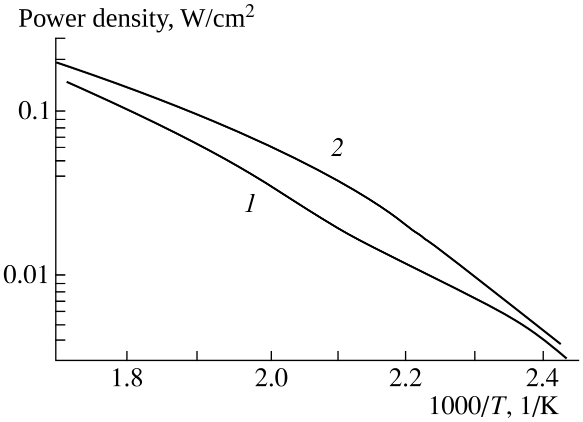

Fig. 4. Temperature dependence of the radiative power loss of (*1*) the inert and (*2*) active calorimeters in Arrhenius coordinates.

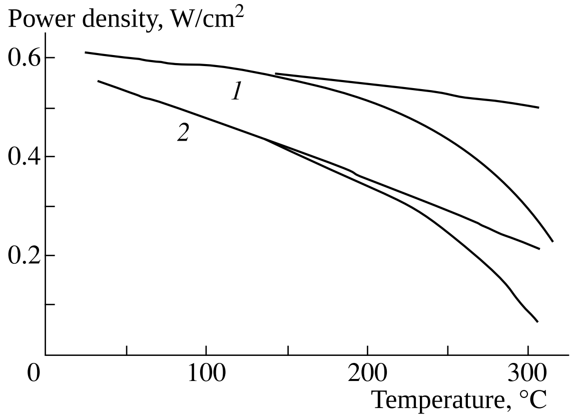

Fig. 5. Temperature dependence of the power density transferred to (*1*) the inert and (*2*) active calorimeters in the discharge at a power of 280 W. The lines deflecting down at high temperatures are obtained by smoothing the experimental data. The straight lines are obtained by taking into account the radiative heat loss of each calorimeter. Extrapolating the straight lines until they intersect the abscissa gives $T \approx 470$°C for the inert calorimeter (this is the gas temperature T_g in the discharge) and $T \approx 1540$°C for the active calorimeter (this is a fictitious temperature that can take any value $T \geq T_g$, including infinity, and even a negative value in the case of instability).

There may be one more type of limitation associated with the finite rate of particle diffusion from the unperturbed discharge to the surface. If the probability of energy relaxation in each collision event is high, then almost every particle colliding with a surface transfers the energy of the excited state to this surface. In this case, the density of particles with excited internal degrees of freedom near the surface is low (compared to their density in the discharge volume). The heat power D_h depends on the rate at which the loss of excited particles near the surface is balanced by the diffusion flux from the discharge. The diffusion in low-pressure gases is not of activation nature (i.e., $\Delta E = 0$). However, even in the absence of kinetic limitations, the temperature dependence of the power D_h is related to an increase in the mean gas temperature $\bar{T}_g \approx (T_g + T_s)/2$ in the thermal boundary layer, whose thickness is comparable with the characteristic size of the calorimeter, and the increase in the particle diffusion coefficient, which is proportional to $\bar{T}_g^{3/2}$ (here, T_g is the gas temperature outside the thermal boundary layer and T_s is the temperature of the calorimeter surface). If the temperature dependence measured in a relatively narrow range of temperatures and related to the diffusion limitations is plotted in Arrhenius coordinates, then we can formally determine the parameters $(D_h)_0$ and ΔE_h, although such a representation makes no definite physical sense.

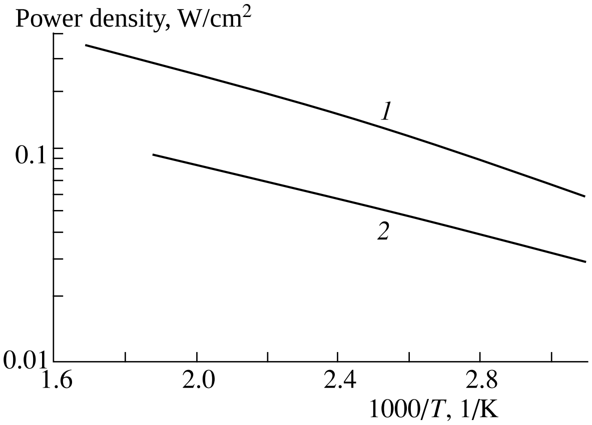

Fig. 6. Temperature dependence of the power of catalytic heat release on the platinum surface in an oxygen discharge. The input power is (*1*) 280 and (*2*) 140 W. The slope of the straight lines in Arrhenius coordinates corresponds to an activation energy of (*1*) 0.076 and (*2*) 0.073 eV.

Let us consider the facts that confirm the kinetic character of the limitations and the activation character of the temperature dependence $D_h(T)$. Immediately after igniting the discharge (for example, in 0.1 s), the mean gas temperature in the boundary layer is $\bar{T}_g \approx 520$ K; when the calorimeter temperature increases to T_s = 590 K, we have $\bar{T}_g \approx 670$ K. Hence, during calorimeter heating, the particle diffusion coefficient in the boundary layer increases by a factor of no more than ≈1.5. If heat transfer is limited to the diffusion stage, the power transferred to the calorimeter by excited particles should increase by the same factor. At P_0 = 280 W and a calorimeter temperature in the range 290–590 K, the heat flux D_h increases by a factor of more than 5. Consequently, in this case, the rate of energy relaxation of excited states on the platinum surface is limited by the surface processes, rather than by the particle transport in the gas.

For heat explosion (i.e., the avalanche deactivation of excited states on the active surface) to occur, it is necessary to satisfy two inequalities: $2\alpha(T_g - T) + D_h - (D_r)_1 > 0$ and $(dD_h/dT) - 2\alpha - (dD_r/dT) > 0$. An increase in the input power results in an increase in both the density of excited particles in the discharge and the gas temperature. In this case, D_h grows rapidly, whereas α grows only slightly. Therefore, as the input power in the discharge increases, surface heating inevitably will pass over to the self-acceleration regime.

The reason why it is difficult to determine the fluxes of excited particles from the measured heat flux related to catalytic heat release is the reversible character of the catalyst action. On the platinum surface, not only does the exothermic atomic recombination reaction $O + O \longrightarrow O_2$ accelerate, but the reverse endothermic dissociation reaction $O_2 \longrightarrow O + O$ (which, however, has a higher activation energy) also accelerates. For this reason, the measured heat power characterizes the rate difference of the direct and reverse reactions.

4. CONCLUSION

The purpose of thermal measurements is to determine both the contributions from different heat transfer mechanisms to the integral heat flux onto the surface and the characteristic features of each mechanism. In particular, such features include the temperature dependence of the power transferred to the surface and the character of the limiting heat-exchange stage. For the two mechanisms governing the interaction between an oxygen discharge and a catalytically active surface (namely, heat conduction of the neutral gas and relaxation of internal degrees of freedom), these features differ substantially: as the surface temperature increases, the power related to the former mechanism linearly decreases, while the power related to the latter mechanism exponentially increases. For the former mechanism, the diffusion heat-exchange stage is limiting; for the latter mechanism, the kinetic stage is limiting. For both inert and active calorimeters, the power of radiative heat loss was determined experimentally, which was impossible when using stationary thermal measurements in discharges (e.g., with the help of thermocouples). To increase the reliability of the results obtained with differential scanning calorimetry, it is necessary to investigate both the effect of incomplete accommodation of the energy of the excited states on gas heating in the boundary layer and the dependence of the heat transfer coefficient on the temperature profile in the boundary layer.

Standard thermal measurements do not allow one to determine the particles and excited states responsible for heat release on a catalytically active surface. These particles and states can be identified by using scanning calorimetry and optical spectrometry. Near the active calorimeter, variations in its temperature should lead to variations in the density n of the particles whose energy is released on the surface, in which case $D_h(t)$ and dn/dt are proportional to each other.

To evaluate the efficiency with which the energy of the excited particles is transferred to the surface due to collisions, it is expedient to use a reference catalytic surface capable of completely absorbing the energy of the internal degrees of freedom of the particles. The kinetic energy of a particle leaving such a “black” surface after colliding with it corresponds to the surface temperature. Probably, a porous silicon structure can be used as such a “black” surface, because 70% of its volume is occupied by nanometer-sized pores in which a particle may remain during a time sufficient for the energies of all the degrees of freedom to relax.

REFERENCES

1. M. R. Carruth, Jr., R. F. DeHaye, J. K. Norwood, and A. F. Whitaker, Rev. Sci. Instrum. **61**, 1211 (1990).

2. F. Nguen-Xuan, S. Cavadias, and J. Amouroux, in *Proceedings of the XII International Symposium on Plasma Chemistry, Minneapolis, 1995*, Vol. 3, p. 1425.
3. M. Mozetič, M. Drobnič, and A. Zalar, in *Proceedings of the XXIV International Conference on Phenomena in Ionized Gases, Warsaw, 1999*, Vol. 5, p. 55.
4. F. K. McTaggart, *Plasma Chemistry in Electrical Discharges* (Elsevier, Amsterdam, 1967; Atomizdat, Moscow, 1972).
5. Yu. A. Ivanov, Yu. A. Lebedev, and L. S. Polak, *Methods of Contact Diagnostics in Nonequilibrium Plasmochemistry* (Nauka, Moscow, 1981).
6. V. D. Berkut, V. M. Doroshenko, V. V. Kovtun, and N. N. Kudryavtsev, *Nonequilibrium Physicochemical Processes in Hypersonic Aerodynamics* (Énergoatomizdat, Moscow, 1994).
7. M. Mozetič, in *Proceedings of the 2nd International Symposium on Heat and Mass Transfer under Plasma Conditions, Tekirova, Turkey, 1999*, p. 23.
8. A. N. Magunov, Fiz. Plazmy **25**, 704 (1999) [Plasma Phys. Rep. **25**, 646 (1999)].
9. Yu. P. Raizer, M. N. Shneider, and N. A. Yatsenko, *Radio-Frequency Capacitive Discharge* (Nauka–Mosk. Fizikotekh. Inst., Moscow, 1995; CRC, London, 1995).
10. A. N. Magunov, Prib. Tekh. Éksp., No. 5, 131 (1995).
11. A. N. Magunov, Prib. Tekh. Éksp., No. 1, 92 (1999).
12. N. Cabrera and N. F. Mott, Rep. Prog. Phys. **12**, 163 (1949).
13. *Low Temperature Plasma*, Vol. 4: *Plasmochemical Technology*, Ed. by M. F. Zhukov (Nauka, Novosibirsk, 1991), p. 343.
14. C. H. Chou and J. Phillips, J. Appl. Phys. **68**, 2415 (1990).
15. A. N. Magunov and E. V. Mudrov, Teplofiz. Vys. Temp. **30**, 372 (1992).
16. A. N. Magunov, Pis'ma Zh. Tekh. Fiz. **20** (7), 65 (1994) [Tech. Phys. Lett. **20**, 289 (1994)].
17. Yu. A. Kulagin, L. A. Shelepin, and V. N. Yarygina, Tr. Fiz. Inst. Akad. Nauk SSSR **212**, 121 (1991).
18. A. N. Magunov, Fiz. Plazmy **23**, 1018 (1997) [Plasma Phys. Rep. **23**, 940 (1997)].
19. A. N. Magunov, A. Yu. Gasilov, and O. V. Lukin, Teplofiz. Vys. Temp. **37**, 202 (1999).
20. A. N. Magunov, Pis'ma Zh. Tekh. Fiz. **20** (4), 36 (1994) [Tech. Phys. Lett. **20**, 149 (1994)].
21. O. V. Krylov and B. R. Shub, *Nonequilibrium Processes in Catalysis* (Khimiya, Moscow, 1990).

Translated by N.F. Larionova